Doctoral Dissertation
Doctoral Program in Mechanical Engineering (34th Cycle)

Electromechanical Modelling and Analysis of Piezoelectric Smart Structures: Energy Harvesting, Static and Dynamic Problems

By:

Mahmoud Askari

******

Supervisor(s):

Prof. Cristiana Delprete, Supervisor
Prof. Eugenio Brusa, Co-Supervisor

Doctoral Examination Committee:

Prof. Flavia Libonati, Università di Genova
Prof. Gabriele Cricri, Università degli Studi di Napoli Federico II

Politecnico di Torino
2022

Declaration

I hereby declare that the contents and organization of this dissertation constitute my own original work and does not compromise in any way the rights of third parties, including those relating to the security of personal data.

Mahmoud Askari
2022

* This dissertation is presented in partial fulfillment of the **Ph.D. degree** in the graduate school of Politecnico di Torino (ScuDo).

Dedication

I would like to dedicate this thesis to my loving parents who have always given me their infinite love, kindness, and support without any expectation!

Acknowledgment

This dissertation is the product of the passionate encouragement and assistance I received from numerous individuals, both directly and indirectly. I owe them a great deal for their guidance, advice, assistance, and contributions to the production of this work.

First and foremost, I would like to express my sincere gratitude and special appreciation to my supervisors Prof. Cristiana Delprete and Prof. Eugenio Brusa, who placed their trust in me, and provided the space for me to develop both personally and professionally. Their bold characters have persuaded me to regard them as mentors on several occasions over the last few years, and I wish I could replicate more of their characteristics. I consider myself really fortunate to work under their supervision and will always be indebted to them for their support and assistance.

During my Ph.D. course at Politecnico di Torino, I had the privilege of meeting some of the most amazing people, namely Maria Grazia Angelillo, Nicola Ruggiero and Vilma Boaglio, those who were always available to provide me with any help and support.

Special thanks go to my favorite Italian, Prof. Elvio Bonisoli, who has been a wonderful friend to me since the first days I started my work at Politecnico di Torino. Despite his hectic schedule, he always tried to make time for discussions and guiding me toward the development of my career.

Selfishly, I would like to thank me for long working hours that are illegal under labor laws, and for never giving up when situation became tight on occasion. The experience I have gained as a graduate student in the Department of Mechanical

and Aerospace Engineering (DIMEAS) of Politecnico di Torino is invaluable. I know that I am only at the beginning of my academic career but my appreciation of Mechanical Engineering as a part of my life has increased significantly after attending this university, as well as multiple classes presented by the pioneers of this field.

I also would like to extend my appreciation to Coffee Espresso, which played a critical part in keeping me alive and energized throughout the last three years.

Last but not least, my sincere appreciation to my family for their continuous love, assistance, and support. I am forever beholden to my parents; they instilled in me the confidence to venture outside my comfort zone and pursue my own destiny. Without them, this journey would not have been possible, and I dedicate this milestone to them.

Summary

Piezoelectric materials are capable of converting mechanical deformation to electric voltage and vice versa. Due to these features, they have been widely used in many engineering applications such as vibration energy harvesting, sensing and actuation technology. This dissertation is divided into two parts. Following the introduction, Part 1 consists of Chapters 2 and 3 dealing with analytical and numerical electromechanical modelling and analysis of different piezoelectric smart structures proposed for vibration energy harvesting. Part 2 consists of Chapters 4 to 7 covering analytical modeling of dynamic and static problems for piezoelectrics bimorph/unimorph structural elements such as beams, plates, and shells with substrates made of functionally graded materials (FGMs) and porous materials.

Piezoelectric vibration energy harvesting has been investigated by many researchers from different disciplines throughout the last two decades. The ultimate goal of this line of research is to power small electronic components by harvesting the ambient vibration available in their environment. Taking into account the issues and shortcomings of available studies, the former part of this present work is focused on developments of reliable piezoelectric energy harvesting models for a unimorph cantilevered beam, a novel multi-beam smart structure, and a bimorph plate harvester with porous substrate, by means of both analytical and numerical techniques. First of all, analytical modeling of the unimorph piezoelectric harvester is presented based on the thin-beam theory, followed by its numerical model simulated in the commercial software of COMSOL Multiphysics®. Using several of this unimorph harvester, as well as two identical proof masses, a novel multi-beam piezoelectric structure is then proposed for harvesting vibration from low frequency applications (below 100 Hz). Moreover, regarding the bimorph plate harvesters with substrate containing porosities, an exact electromechanical model

based on shear deformation theories is presented, which can be used for analyzing moderately thick and thick plate-like energy harvester configurations. For each of such piezoelectric scavengers, the respective electromechanical response to external harmonic excitation is extracted, reliability of the models is verified, and finally detailed parametric studies are presented to demonstrate the performance of the scavengers.

On the other hand, developing computationally efficient but accurate electromechanical models is of great importance to the research community of the rapidly growing and multi-disciplinary area of piezoelectric smart structures. Therefore, the focus in the latter part of this thesis is placed on proposing comprehensive analytical solutions for the particular problems of free vibration, wave propagation and buckling analysis of beam-, plate-, and shell-like smart sandwich structures consisting of functionally graded or porous substrates, and integrated piezoelectric layer(s). Analytical methods, as long as they are available, are usually much faster than the numerical solution techniques such as the finite element modeling and other energy-based discretization techniques. To study the above-mentioned problems analytically, the governing equations of each system are first derived based on higher-order shear deformation theories, and through the use of Hamilton's principle and Maxwell's equation. Depending on the type of boundary conditions, the obtained governing equations, that are highly coupled, are solved using Navier's approach, state space approach and Galerkin method. As the systems response, closed-form expressions have been extracted for the wave characteristics, free vibration, and buckling problems of the systems of interest, providing the opportunity to study the effects of the systems parameters explicitly, and understand the physics of the problem clearly. Finally, the effects of variety of the systems parameters such as characteristics of selected materials, mechanical and electrical boundary conditions, as well as geometrical properties are studied in detail. The analytical models presented in this part of the thesis not only furnish benchmark solutions of shear deformation theories for the piezoelectric coupled structures but also provide insight into the significance of shear deformation on the response. The exact results obtained from those analytical models can also be used for verification of the numerical approaches.

Keywords: Smart Structures; Piezoelectricity; Energy Harvesting; Electromechanical Modeling; Structural Analysis; Vibration Analysis; Analytical Solutions; FGMs; Porosity.

Table of Contents

List of Figures

List of Tables

Chapter 1

Introduction

1.1 An Overview of Smart Structures

Numerous definitions have been presented in the literature for smart or intelligent structures, which differ in many aspects from one engineering or science discipline to another. In spite of such varieties, it is widely accepted that a smart structure is a system containing multifunctional components which have both *life features* and *artificial intelligence* (see Fig. 1.1). The life features concern with the fact that intelligent structures can perform sensing, actuation and control, the characteristics that exist in every living thing. These functions or features can either be inherent properties of the smart structure or be synthetically embedded in it. On the other hand, the artificial intelligence feature is concerned with the notion that each intelligent structure possesses unique capabilities, via computers, microprocessors, and so on, to adapt to environmental changes/conditions and external stimuli in order to accomplish the stated objectives and provide adaptive functionality. Smart materials, which are used to design intelligent structures, refer to those materials that are capable of changing their structure or composition, electrical and/or mechanical properties, or even their functions in response to some environmental stimuli such as temperature, pressure, magnetic and electric fields. For instance,

piezoelectrics, magnetostrictive, and shape memory alloys (SMAs) are some examples of smart materials that convert various types of energy into mechanical deformation and vice versa. Other examples include magneto- and electro-rheological materials whose rheological properties are controlled by application of external magnetic and electric fields, respectively. In Table 1.1 are presented a list of some smart materials alongside their corresponding stimulus and response forms. The listed materials are classified into two categories of sensors and actuators applications. A critical property of the change or response of smart materials to environmental stimuli is reversibility, which indicates that the beneficial physical impact can be easily adjusted by simply altering the condition of the environmental stimulation. Due to their great features and wide applications, the design and analysis of intelligent structures has been a hot topic for many years among researchers from different disciplines. A comprehensive description of smart materials/structures and their applications can be found in [1].

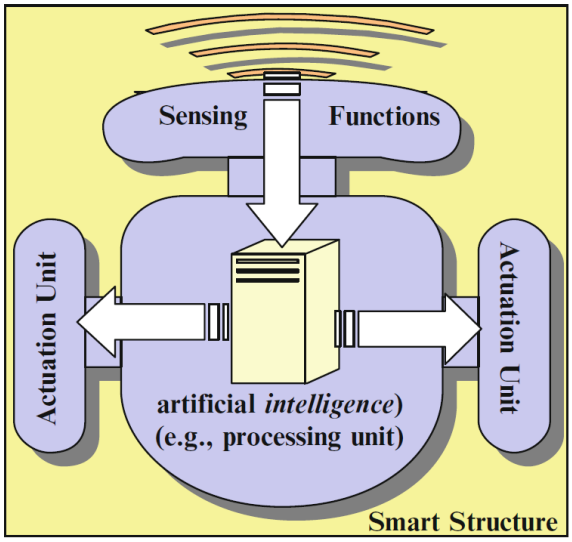

Fig. 1.1: Conceptual definition and attributes of intelligent structures [2]

Among various types of intelligent materials, piezoelectrics have gained much importance and stand out as the most commonly used active material in many applications such as vibration control and energy harvesting, the areas that are of great importance to the subject of this dissertation. Piezoelectrics are a class of smart materials being capable of converting mechanical deformation into electrical charge and vice versa. The former effect is called direct piezoelectric effect and the

latter is the converse piezoelectric effect. Piezoelectrics have a wide range of applications and can be used as sensors (such as many accelerometers), actuators (provide a voltage to create a motion) and energy scavengers because the charge generated from motion can be harvested and stored. Leaving much of the details to the next subsection, it was briefly discussed here the significance of piezoelectrics in design of sensors and actuators. From the structural point of view, it is worth noting that piezoelectric materials are often used in the forms of patches or layers attached to host structures made of different materials such as metals, composites, and functionally graded materials (FGMs). However, since the smart structures investigated in the present dissertation are assumed to be composed of either FGM or porous structural elements integrated with piezoelectric layers, the definitions, properties, and constitutive equations of such materials are presented in the next subsections. The specific applications/capabilities of such smart structures will be highlighted in the respective chapters.

Table 1.1: Some of smart materials used in sensor and actuator technology [3]

	Material Class	Stimulus	Response
Sensors	Pyroelectrics	Temperature Change	Electric Polarization
	Piezoelectrics	Mechanical Strain	Electric Polarization
	Electrostrictors	Mechanical Strain	Electric Polarization
	Magnetostrictors	Mechanical Strain	Change in Magnetic Field
	Electroactive Polymers	Mechanical Strain	Electric Polarization
	Electroluminescent	Electric Field	Light Emission
	Photoluminescent	Incident Light	Light Emission
	Electrochromic	Electric Field	Color Change
Actuators	Piezoelectrics	Electric Current	Mechanical Strain
	Electrostrictors	Electric Current	Mechanical Strain
	Magnetostrictors	Magnetic/Electric Field	Mechanical Strain
	Shape Memory Alloys	Temperature Change	Mechanical Strain
	Electroactive Polymers	Electric Field/pH change	Mechanical Strain
	Electrorheological Fluids	Electric Field	Viscosity Change
	Magnetorheological Fluids	Magnetic Field	Viscosity Change

1.2 Piezoelectric Materials

Piezoelectricity, as a research field in crystal physics, was discovered by the brothers Jacques Curie and Pierre Curie in 1880 [2]. The term “piezo” derives from a Greek word meaning for pressure; therefore, piezoelectricity translates as pressure electricity. As mentioned earlier, the direct piezoelectric effect (also called piezoelectric effect) is used in design of sensors while the converse effect is the basis of piezoelectric actuating devices. In Fig. 1.2 are schematically shown both direct and converse piezoelectric effects, in which mechanical and electric fields are converted to each other. For clarity, the magnitude of deformations has been exaggerated in both cases. As seen from Figure 1.2a, an electric charge is generated when a compressive load is applied to piezoelectric material due to the coupling between the electrical and mechanical fields. On the actuation side, Fig. 1.2b displays that application of an electric voltage to the piezoelectric element results in mechanical strain in its structure, again because of the mechanical and electrical fields coupling. It is important to note that both direct and converse effects usually co-exist in a piezoelectric material. This means that in an application of piezoelectric materials where the direct effect is of specific interest (e.g. in the case energy harvesting), ignoring the existence of the converse effect would not be consistent thermodynamically.

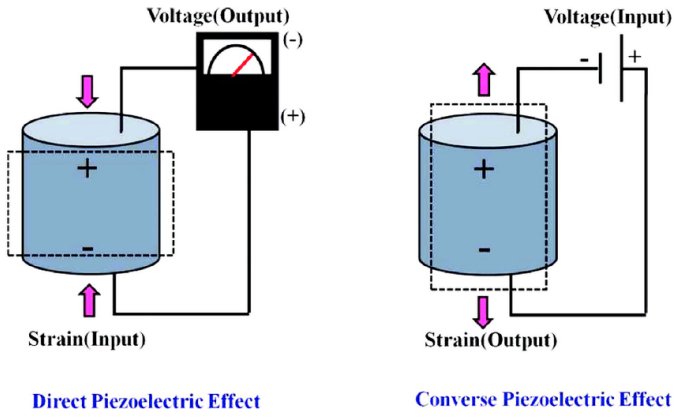

Fig. 1.2: Schematic representation of direct and converse piezoelectric effects [2]

Piezoelectricity is found in materials either naturally or by artificial means. Crystals such as ceramics, polymers and composites are some examples of man-made piezoelectrics. On the other hand, quartz, ammonium, bone and even wood

are some of the common natural piezoelectric materials. The most commonly produced piezoelectric material is lead zirconate titanate (so-called PZT), a ceramic perovskite material which is manufactured via a complicated process [4]. Some other known piezoelectric ceramics (or piezoceramics) are barium titanate and lead titanate as well. Another typical piezoelectric material is polyvinylidene fluoride (so-called PVDF), which is not a ceramic but a polymeric material. Piezoceramics are widely chosen for different applications due to their physical strength, chemical inertness, and their relatively low manufacturing cost. More specifically, PZTs are the most popular piezoceramics because not only they offer an even higher sensitivity and greater operating temperature as compared to other piezoceramics but also their properties can be optimized by appropriate adjustment of the zirconate-titanate ratio to suit specific applications. Some examples of PZT ceramics include PZT-2, PZT-4, PZT-5A and PZT-5H whose mechanical and electrical properties are listed in Table 1.2. To prepare a piezoelectric ceramic, fine powders of the component metal oxides are combined in precise quantities and then heated until a homogeneous powder is formed. The powder is combined with an organic binder and molded into required structural elements such as discs, beams, plates, and shells. After cooling, the elements are shaped or cut to the desired dimensions, and electrodes are placed to the appropriate surfaces. Above a specific temperature, referred to as the *Curie temperature*, each perovskite crystal in the fired ceramic element exhibits a simple cubic symmetry devoid of a dipole moment.

Most piezoelectric materials are naturally isotropic and do not have the dipole effect to generate piezoelectricity so that an important process called *poling* is required. Usually, the direction of polarization in the elemental crystals, that comprise a piezoelectric domain, are different from each other (see Fig. 1.3a), such that at a global level the domain is not polarized. Hence, a strong electric field is applied to the material, therefore, each crystal changes its polarization direction along the applied field, and when the external field is removed, the material retains a degree of polarization. (see Fig. 1.3b). It is worth noting that, because each crystal has only six possible polarization directions, the level of domain's polarization can never equal that of a single crystal. In Figure 1.3 is observed that, after polarization, the direction of the elemental poling is typically aligned with the direction of the coercive field. Depending on the material anisotropy, the produced polarization can be in any direction, which can lead to displacements of varying amplitude and

direction. This feature allows manufacturers to fabricate piezoelectric materials in such a manner that the resultant displacement can be selectively controlled in a particular direction. A piezoelectric material can lose its piezoelectric effect when it undergoes the following severe conditions: (i) being subjected to high mechanical stresses, which leads to distortion of dipoles alignment, (ii) applying a significant electric field in the opposite direction of the polarization and (iii) heating the material above its Curie temperature. Accordingly, in most practical cases, the operating temperature of the piezoelectric material has to be kept below its Curie temperature to avoid permanent damage to the material.

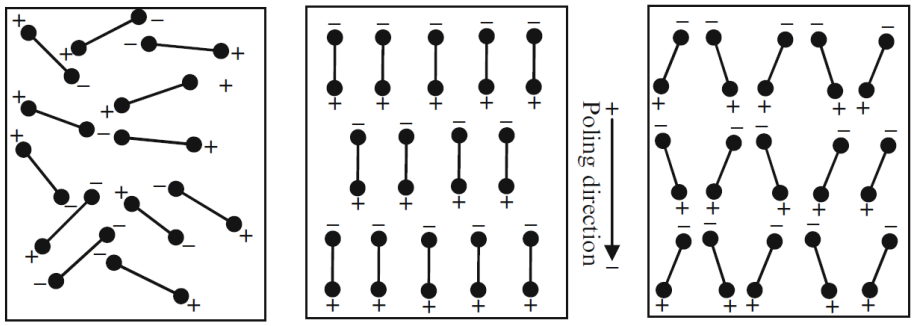

(a) (b) (c)

Fig. 1.3: Schematic representation of electric dipoles in a piezoelectric domain (a) prior to poling, (b) poling under a constant electric field, and (c) after poling

Due to the coupling between mechanical and electrical fields, the constitutive equations of piezoelectric materials are expressed as a combination of both mechanical and electrical characteristics. The respective constitutive equations, which connect the electrical domain (with electric field $\{E\}$ and displacement $\{D\}$) to the mechanical domain (with stress field $\{\sigma\}$ and strain field $\{\varepsilon\}$) are expressed in the following general form for linear piezoelectric materials:

$$\{\varepsilon\} = [s]^E\{\sigma\} - [d]^T\{E\} \tag{1.1a}$$

$$\{D\} = [d]\{\sigma\} + [\epsilon]^\sigma\{E\} \tag{1.1b}$$

in which $[s]^E$ is the matrix of compliance coefficients under a constant electrical filed, $[\epsilon]^\sigma$ is the dielectric permittivity under a constant stress, and $[d]$ and $[d]^T$ are the matrices of the electromechanical coefficients for direct and converse piezoelectric effects, where T stands for the transpose.

Table 1.2: Mechanical and electrical properties of some PZT materials [5]

	PZT Material			
Property	PZT-2	PZT-4	PZT-5A	PZT-5H
Elastic moduli (GPa)				
c_{11}	134.9	139.0	99.2	127.2
c_{12}	67.9	77.8	54.0	80.2
c_{33}	113.3	115.0	86.9	117.4
c_{13}	68.1	74.3	50.8	84.7
c_{55}	22.2	25.6	21.1	23.0
c_{66}	33.4	30.6	22.6	23.5
Piezoelectric moduli (C/m^2)				
e_{31}	-1.82	-5.2	-7.2	-6.6
e_{33}	9.05	15.1	15.1	23.2
e_{15}	9.8	12.7	12.3	17.0
Dielectric moduli (nF/m)				
Ξ_{11}	4.46	6.75	15.30	15.10
Ξ_{22}	4.46	6.75	15.30	15.10
Ξ_{33}	2.4	5.90	15.00	12.70
Mass density (kg/m^3)				
ρ	7600	7500	7750	7500
Curie temperature (^{o}C)	NA	328	365	193

The constitutive equations (1.1) can also be written in the following forms:

$$\{\sigma\} = [c]\{\varepsilon\} - [e]^T\{E\} \tag{1.2a}$$

$$\{D\} = [e]\{\varepsilon\} + [\Xi]\{E\} \tag{1.2b}$$

where:

$$\begin{aligned} [c] &= [s]^{-1} \\ [e] &= [s]^{-1}[d] \\ [\Xi] &= [\epsilon] - [d][s]^{-1}[d] \end{aligned} \tag{1.3}$$

In Eq. (1.2), $[c]$, $[e]$, $[\Xi]$ are the matrices of stiffness, piezoelectric, and permittivity coefficients, respectively. It is worthy to note that the first equation in (1.1) or (1.2) denotes the converse piezoelectric effect (i.e., actuation mechanism) whilst the second equation represents the direct effect (i.e., sensing mechanism). In the present dissertation, the piezoelectric materials are considered to be *transversely isotropic*.

PZTs belong to this class of piezoelectric materials. Hence, the constitutive equations (1.2) can be simplified and rewritten in particular matrix forms for such materials. To that, first, consider a piezoelectric domain as shown in Fig. 1.4:

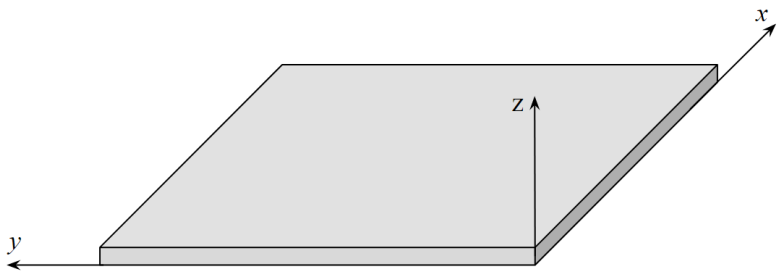

Fig. 1.4: A 3D piezoelectric domain

Depending on the direction of polarization, Eq. (1.2) can be rewritten in the following forms for transversely isotropic piezoelectric materials:

With z being the direction of polarization (see Fig. 1.4):

$$\begin{Bmatrix}\sigma_{xy}\\ \sigma_{yy}\\ \sigma_{zz}\\ \sigma_{yz}\\ \sigma_{xz}\\ \sigma_{xy}\end{Bmatrix} = \begin{bmatrix} c_{11} & c_{12} & c_{13} & 0 & 0 & 0\\ c_{12} & c_{11} & c_{13} & 0 & 0 & 0\\ c_{13} & c_{13} & c_{33} & 0 & 0 & 0\\ 0 & 0 & 0 & c_{55} & 0 & 0\\ 0 & 0 & 0 & 0 & c_{55} & 0\\ 0 & 0 & 0 & 0 & 0 & c_{66}\end{bmatrix} \begin{Bmatrix}\varepsilon_{xy}\\ \varepsilon_{yy}\\ \varepsilon_{zz}\\ \gamma_{yz}\\ \gamma_{xz}\\ \gamma_{xy}\end{Bmatrix} - \begin{bmatrix} 0 & 0 & e_{31}\\ 0 & 0 & e_{31}\\ 0 & 0 & e_{33}\\ 0 & e_{15} & 0\\ e_{15} & 0 & 0\\ 0 & 0 & 0\end{bmatrix} \begin{Bmatrix}E_x\\ E_y\\ E_z\end{Bmatrix} \tag{1.4a}$$

$$\begin{Bmatrix} D_x \\ D_y \\ D_z \end{Bmatrix} = \begin{bmatrix} 0 & 0 & 0 & 0 & e_{15} & 0 \\ 0 & 0 & 0 & e_{15} & 0 & 0 \\ e_{31} & e_{31} & e_{33} & 0 & 0 & 0 \end{bmatrix} \begin{Bmatrix} \varepsilon_{xy} \\ \varepsilon_{yy} \\ \varepsilon_{zz} \\ \gamma_{yz} \\ \gamma_{xz} \\ \gamma_{xy} \end{Bmatrix} + \begin{bmatrix} \Xi_{11} & 0 & 0 \\ 0 & \Xi_{11} & 0 \\ 0 & 0 & \Xi_{33} \end{bmatrix} \begin{Bmatrix} E_x \\ E_y \\ E_z \end{Bmatrix} \tag{1.4b}$$

The constitutive equations of the piezoelectric materials poled in the other directions (i.e., x and y directions) can be obtained by applying some mathematical operations (i.e., transformation or rotation) to the matrices presented in the constitutive equations of transversely polarized piezoelectric materials. For instance, for the piezoelectric materials poled in the x-direction, the respective equations can be derived through a 90° degree rotation around the y-direction, followed by a 180° rotation around the z-direction. A similar procedure has to be adopted for those poled though the y-direction. Accordingly, the resulting constitutive equations are given below:

For the piezoelectrics poled through the x-direction (see Fig. 1.4):

$$\begin{Bmatrix} \sigma_{xy} \\ \sigma_{yy} \\ \sigma_{zz} \\ \sigma_{yz} \\ \sigma_{xz} \\ \sigma_{xy} \end{Bmatrix} = \begin{bmatrix} c_{33} & c_{13} & c_{13} & 0 & 0 & 0 \\ c_{13} & c_{11} & c_{12} & 0 & 0 & 0 \\ c_{13} & c_{12} & c_{11} & 0 & 0 & 0 \\ 0 & 0 & 0 & c_{66} & 0 & 0 \\ 0 & 0 & 0 & 0 & c_{55} & 0 \\ 0 & 0 & 0 & 0 & 0 & c_{55} \end{bmatrix} \begin{Bmatrix} \varepsilon_{xy} \\ \varepsilon_{yy} \\ \varepsilon_{zz} \\ \gamma_{yz} \\ \gamma_{xz} \\ \gamma_{xy} \end{Bmatrix} - \begin{bmatrix} e_{33} & 0 & 0 \\ e_{31} & 0 & 0 \\ e_{31} & 0 & 0 \\ 0 & 0 & 0 \\ 0 & 0 & e_{15} \\ 0 & e_{15} & 0 \end{bmatrix} \begin{Bmatrix} E_x \\ E_y \\ E_z \end{Bmatrix} \tag{1.5a}$$

$$\begin{Bmatrix} D_x \\ D_y \\ D_z \end{Bmatrix} = \begin{bmatrix} e_{33} & e_{31} & e_{31} & 0 & 0 & 0 \\ 0 & 0 & 0 & 0 & 0 & e_{15} \\ 0 & 0 & 0 & 0 & e_{15} & 0 \end{bmatrix} \begin{Bmatrix} \varepsilon_{xy} \\ \varepsilon_{yy} \\ \varepsilon_{zz} \\ \gamma_{yz} \\ \gamma_{xz} \\ \gamma_{xy} \end{Bmatrix} + \begin{bmatrix} \Xi_{33} & 0 & 0 \\ 0 & \Xi_{11} & 0 \\ 0 & 0 & \Xi_{11} \end{bmatrix} \begin{Bmatrix} E_x \\ E_y \\ E_z \end{Bmatrix} \tag{1.5b}$$

For the piezoelectrics poled through the y-direction (see Fig. 1.4):

$$\begin{Bmatrix} \sigma_{xy} \\ \sigma_{yy} \\ \sigma_{zz} \\ \sigma_{yz} \\ \sigma_{xz} \\ \sigma_{xy} \end{Bmatrix} = \begin{bmatrix} c_{11} & c_{13} & c_{12} & 0 & 0 & 0 \\ c_{13} & c_{33} & c_{13} & 0 & 0 & 0 \\ c_{12} & c_{13} & c_{11} & 0 & 0 & 0 \\ 0 & 0 & 0 & c_{55} & 0 & 0 \\ 0 & 0 & 0 & 0 & c_{66} & 0 \\ 0 & 0 & 0 & 0 & 0 & c_{55} \end{bmatrix} \begin{Bmatrix} \varepsilon_{xy} \\ \varepsilon_{yy} \\ \varepsilon_{zz} \\ \gamma_{yz} \\ \gamma_{xz} \\ \gamma_{xy} \end{Bmatrix} - \begin{bmatrix} 0 & e_{31} & 0 \\ 0 & e_{33} & 0 \\ 0 & e_{31} & 0 \\ 0 & 0 & e_{15} \\ 0 & 0 & 0 \\ e_{15} & 0 & 0 \end{bmatrix} \begin{Bmatrix} E_x \\ E_y \\ E_z \end{Bmatrix} \tag{1.6a}$$

$$\begin{Bmatrix} D_x \\ D_y \\ D_z \end{Bmatrix} = \begin{bmatrix} 0 & 0 & 0 & 0 & 0 & e_{15} \\ e_{31} & e_{33} & e_{31} & 0 & 0 & 0 \\ 0 & 0 & 0 & e_{15} & 0 & 0 \end{bmatrix} \begin{Bmatrix} \varepsilon_{xy} \\ \varepsilon_{yy} \\ \varepsilon_{zz} \\ \gamma_{yz} \\ \gamma_{xz} \\ \gamma_{xy} \end{Bmatrix} + \begin{bmatrix} \Xi_{11} & 0 & 0 \\ 0 & \Xi_{33} & 0 \\ 0 & 0 & \Xi_{11} \end{bmatrix} \begin{Bmatrix} E_x \\ E_y \\ E_z \end{Bmatrix} \tag{1.6b}$$

1.3 Functionally Graded Materials (FGMs)

In late 1980's, Japanese scientists discovered a type of multifunctional composites, called functionally graded materials (FGMs), which contain a spatial variation in composition, aiming to control variations in thermal, structural, or functional properties. The properties of FGMs can vary smoothly with respect to their dimensions based on a specific graduation. In other words, the microstructure of FGMs vary from one material to another, enabling the structure to have the best of both materials (see Fig. 1.5). For instance, when FGMs are designed for the purpose of thermal or corrosive resistance, both strengths of materials may be taken into account to avoid fracture, fatigue, and stress corrosion cracking. To fabricate FGMs, various procedures such as bulk (particulate processing), preform processing, layer processing, and melt processing are used [6]. The aircraft and aerospace industries, as well as the computer circuit industry are interested to develop materials capable of withstanding extremely high thermal gradients. This is often accomplished by using a ceramic layer connected with a metallic layer [7–11].

Fig. 1.5: Composition of materials in microstructure of FGMs

In structures made of FGMs, the volume fractions of two or more materials are varied continuously as a function of position along certain dimension(s) of the structure to achieve a required function. For example, thermal barrier plate structures for high-temperature applications may form from a mixture of ceramic and a metal. The composition is varied from a ceramic-rich surface to a metal-rich

surface, with a desired variation of the volume fractions of the two materials in between the two surfaces. The ceramic constituent of the material provides the high-temperature resistance due to its low thermal conductivity. The gradual change of material properties can be tailored to different applications and working environments. This makes FGMs preferable in many applications.

Consider a plate of total thickness $2h$ and composed of functionally graded material through the thickness. It is assumed that the material is isotropic, and the grading is assumed to be only through the thickness. The profile for volume fraction variation can be expressed by [8]

$$P(z) = P_b + (P_t - P_b)V(z) \tag{1.7a}$$

$$V(z) = \left(\frac{1}{2} + \frac{z}{2h}\right)^N \tag{1.7b}$$

where $P(z)$ denotes a generic material property such as modulus and mass density, P_t and P_b denote the property of the top and bottom faces of the plate, respectively, and N is a parameter that dictates the material variation profile through the thickness. Here we assume that moduli E and G, and density vary according to equation (1.7). In case the constituents of the FGM structure are ceramic and metal, Eq. (1.7) can be rewritten as:

$$P(z) = P_m + (P_c - P_m)\left(\frac{1}{2} + \frac{z}{2h}\right)^N \tag{1.8}$$

in which P_m and P_c denote the property of the metal and ceramic constituents. One can simply realize from Eq. (1.8) that setting $N = 0$ results in a structure only made of a ceramic while it is made of only metal when very large values are considered for the power-law index (i.e., $N \cong \infty$). This can be achieved during fabrication of FGMs.

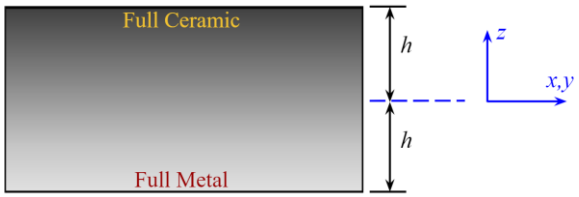

Fig. 1.6: Cross-section of an FGM plate

Despite great features of FGMs, it is recently realized that micro pores occur in their structure as defects due to technical problems during their fabrication [12]. To include the effect of such undesired porosities, which significantly influence the mechanical response of FGMs (under various loading conditions), the modified rule of mixture is introduced to describe and approximate the corresponding effective material properties. To that, two types of porosity distribution, namely *Even* and *Uneven* patterns (see Fig. 1.7), have been usually considered in the literature, as:

Even porosity distribution:

$$P(z) = P_m + (P_c - P_m)\left(\frac{1}{2} + \frac{z}{2h}\right)^N - \frac{e_0(P_c + P_m)}{2} \tag{1.9}$$

Uneven porosity distribution:

$$P(z) = P_m + (P_c - P_m)\left(\frac{1}{2} + \frac{z}{2h}\right)^N - e_0(P_c + P_m)\left(\frac{1}{2} - \frac{|z|}{2h}\right) \tag{1.10}$$

where the dimensionless parameter e_0 $(0 \leq e_0 < 1)$ denotes the porosity volume fraction of the *Porous FGM* substrate. It is worth noting that zero value for this parameter (i.e., $e_0 = 0$) represents a FGM structure with no porosity, which is called *Perfect FGM* in the literature.

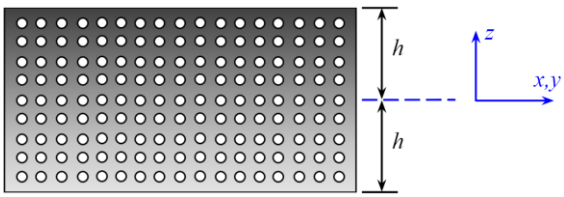

(a) Even porosity distributiuon

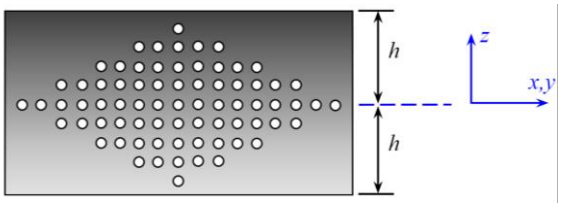

(b) Uneven porosity distributiuon

Fig. 1.7: Schematic representation of Even and Uneven porosity distributions in FGMs

To provide a better illustration of the varying properties in FGM structures, variation of the effective Young's modulus versus the power-law index is plotted in Fig. 1.8, for an FGM domain with the cross-section given in Fig. 1.6. The respective constituents are, for instance, assumed to be Aluminum (as the metal part) and Alumina (as the ceramic part) with the following properties:

Aluminum: $E_m = 70$ GPa, $\rho_m = 2700$ kg/m^3, $\nu = 0.3$
Alumina: $E_c = 380$ GPa, $\rho_c = 3800$ kg/m^3, $\nu = 0.3$

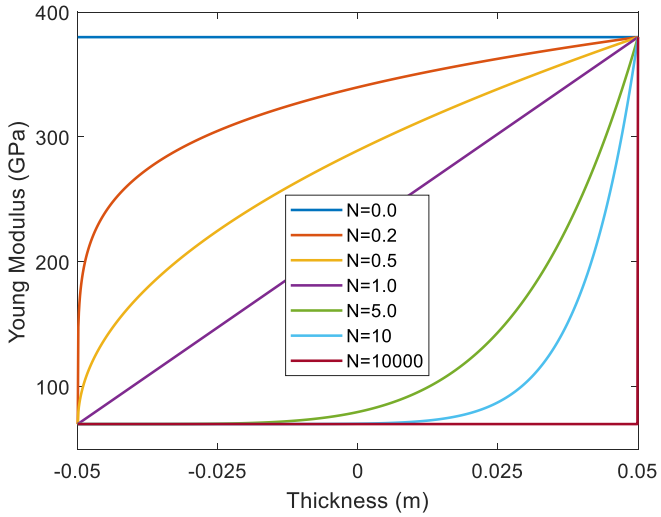

Fig. 1.8: Variation of Young's modulus with respect to the power-law index in perfect FGMs ($2h = 100mm$)

Since FGMs are isotropic materials, their constitutive stress-strain relations simply obey the Hooke's law, and can be expressed in the general form of:

$$\{\sigma_{ij}\} = [Q_{ij}]\{\varepsilon_{ij}\} \tag{1.11}$$

where σ_{ij} and ε_{ij} are the components of the stress and strain fields, respectively, and Q_{ij} represents the elastic coefficients. For the plane stress condition, Eq. (1.11) can be expressed in the following form:

$$\begin{Bmatrix}\sigma_{xx}\\ \sigma_{yy}\\ \sigma_{yz}\\ \sigma_{xz}\\ \sigma_{xy}\end{Bmatrix}=\begin{bmatrix}Q_{11} & Q_{12} & 0 & 0 & 0\\ Q_{12} & Q_{22} & 0 & 0 & 0\\ 0 & 0 & Q_{44} & 0 & 0\\ 0 & 0 & 0 & Q_{55} & 0\\ 0 & 0 & 0 & 0 & Q_{66}\end{bmatrix}\begin{Bmatrix}\varepsilon_{xx}\\ \varepsilon_{yy}\\ \gamma_{yz}\\ \gamma_{xz}\\ \gamma_{xy}\end{Bmatrix} \tag{1.12}$$

where, for FGMs with varying properties through the thickness direction (which is usually considered as z-direction), Q_{ij}'s are given as:

$$Q_{11}=Q_{22}=\frac{E(z)}{1-\nu^2},\quad Q_{12}=\nu Q_{11},\quad Q_{44}=Q_{55}=Q_{66}=\frac{E(z)}{2(1+\nu)} \tag{1.13}$$

1.4 Porous Materials

Porous materials refer to those materials containing internal pores. Their properties are basically controlled by the internal micro pores (or voids) that are distributed in their structure. The internal pores are classified into two major types: open and closed pores. Open pores connect to the outside of the material while closed pores are isolated from the outside and may contain a fluid (see Fig. 1.9). For most industrial applications of porous materials, open pores are required. Porosity, either closed or open, is therefore a characteristic of porous media that strongly defines the properties of the material, such as density, stiffness, and specific surface area. Porous materials can be either natural such as rocks and soil, wood, and biological tissues (e.g., bone) or man-made such as ceramics, foams, and cellular metals (e.g. cellular Aluminum) [13]. Porous metals, ceramics and glasses are particularly important for industrial applications, in chemistry, mechanical engineering, biotechnology and electronics.

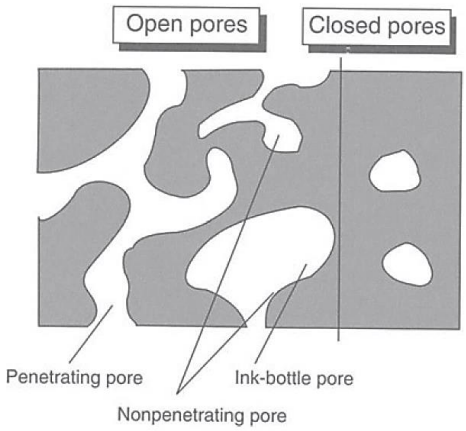

Fig. 1.9: Schematic illustration of different morphology of pores

Foams and other porous materials with a cellular structure are known to have many interesting combinations of physical and mechanical properties, such as high stiffness in conjunction with very low specific weight or high gas permeability combined with high thermal conductivity. For this reason, nature frequently uses cellular materials for constructional or functional purposes (e.g. wood or bones). Metallic cellular materials (or porous metals) have the general attractive features of metals, such as high flow stress and toughness, solid state mechanical formability, resistance to thermal exposure and to many environments, coupled with high thermal and electrical conductivity, combined with the attributes of cellular materials. Microcellular metals are now commercially available; thus, these are nowadays an area of intense current research and development, in both academia and industry. Compared to dense solid metals, porous metals have low density, large specific surface area, good energy absorption, and greater specific strength and stiffness. A complete discussion on porous materials and their applications is beyond the scope of this chapter but comprehensive descriptions concerning fabrication techniques, characterization and application of cellular metals and metal foams can be found in [14,15].

The basic theory of poroelasticity, first developed by Biot [16], describes the coupling between changes in stress, strain, pore compressibility, and the material properties that relate these three variables. Based on this theory, the constitutive equations of the linear poroelastic materials can be expressed in the following form:

$$\sigma_{ij} = 2G\varepsilon_{ij} + \lambda_u \varepsilon_{kk}\delta_{ij} - \alpha p \delta_{ij} \tag{1.14}$$

where G is the shear modulus, λ_u is the Lame's parameter, p represents pore fluid pressure, δ_{ij} indicates the Kronecker delta, and α is the Biot coefficient of effective stress $(0 \leq \alpha < 1)$, which is the ratio of the increment in fluid content to the volumetric strain at constant pore pressure. The volumetric strain is shown by ε_{kk}, and equals to $\varepsilon_{kk} = \varepsilon_{xx} + \varepsilon_{yy} + \varepsilon_{zz}$. The mentioned parameters are defined as

$$\begin{aligned} \lambda_u &= \frac{2\nu_u G(z)}{1-2\nu_u} \\ p &= M(\zeta - \alpha\varepsilon_{kk}) \end{aligned} \tag{1.15}$$

where:

$$\begin{aligned} M &= \frac{2G(z)(\nu_u - \nu)}{\alpha^2(1-2\nu_u)(1-2\nu)} \\ \nu_u &= \frac{3\nu + \alpha B(1-2\nu)}{3-\alpha B(1-2\nu)} \end{aligned} \tag{1.16}$$

In the above relations, M is the Biot modulus and is defined as the increase of the amount of fluid, ν_u is the undrained Poisson's ratio $(\nu \leq \nu_u < 0.5)$, ζ is the variation of fluid volume content, and B is the Skempton's coefficient and has a value between 0 and 1 $(0 < B < 1)$, showing the fluid compressibility of the internal pores in cellular structures. A key feature of the response of fluid-infiltrated porous material is the difference between two different modes, namely undrained and drained conditions. These two modes represent limiting behaviors of the material: the undrained response characterizes the condition where the fluid is trapped in the porous solid such that $\zeta = 0$, while the drained response corresponds to zero pore pressure $p = 0$ [16].

Various models have been presented in the literature for the distribution of porosities in porous structures [148,149,154]. In most cases, the mechanical properties of porous structures are assumed to vary along their thickness direction (usually defined by z-direction) based on various symmetric/asymmetric patterns. In Fig. 1.10, the most commonly used porosity patterns are schematically presented.

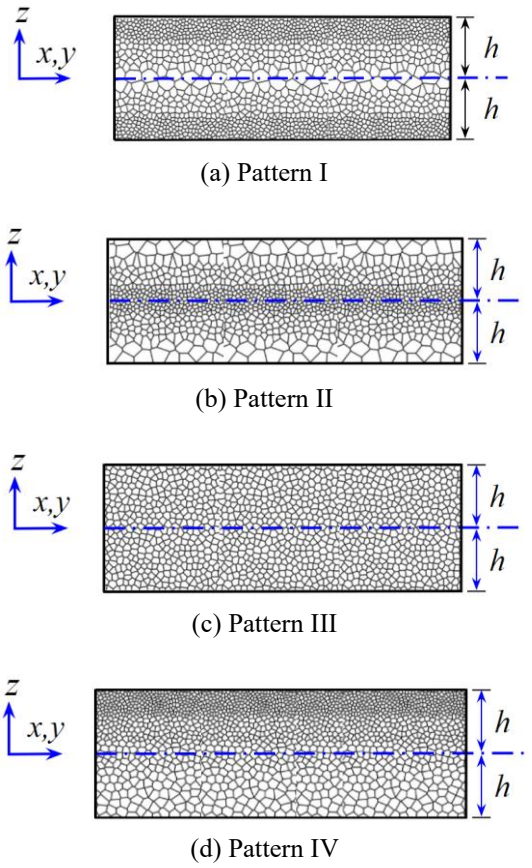

(a) Pattern I

(b) Pattern II

(c) Pattern III

(d) Pattern IV

Fig. 1.10: Cross-section of a porous structure with various porosity distributions ($2h$ is the constant thickness of the structure)

As it is seen from Fig. 1.10, the presented porosity distributions are here called as *Pattern I*, *Pattern II*, *Patterns III* and *Patterns IV* three of which (i.e., the first three profiles) are symmetric with respect to the mid-plane, while the last case is an asymmetric pattern. The effective mechanical properties of porous structures with such porosity distributions can be expressed as [148,149,154]:

$$\begin{aligned} E(z) &= E_0[1 - e_0\psi(z)] \\ G(z) &= G_0[1 - e_0\psi(z)] \\ \rho(z) &= \rho_0[1 - e_m\psi(z)] \end{aligned} \tag{1.17}$$

where $E(z)$, $G(z)$ and $\rho(z)$ are Young's modulus, shear modulus and the mass density at any point of the porous structure, respectively. Moreover, E_0, G_0 and ρ_0 are also the properties of the parent material of the porous structure. The parameter

e_0 (in the range of $0 \leq e_0 < 1$) represents the porosity coefficient, and e_m is a dimensionless parameter related to the effective mass density and is equal to $e_m = 1 - \sqrt{1 - e_0}$.

The function $\psi(z)$ in Eq. (1.17) is defined according to the type of porosity pattern, as follows:

Pattern I: $$\psi(z) = \cos\left(\frac{\pi z}{2h}\right) \tag{1.18a}$$

Pattern II: $$\psi(z) = \cos\left(\left|\frac{\pi z}{2h}\right| - \frac{\pi}{2}\right) \tag{1.18b}$$

Pattern IV: $$\psi(z) = \cos\left(\frac{\pi z}{4h} + \frac{\pi}{4}\right) \tag{1.18c}$$

For the porosity *Pattern III*, in which the internal pores are *uniformly* distributed within the structure, the respective mechanical properties do not vary along the thickness direction and are dependent on the porosity parameter only, as:

$$\begin{aligned} E(z) &= E_{max}[1 - e_0\psi_0] \\ G(z) &= G_{max}[1 - e_0\psi_0] \\ \rho(z) &= \rho_{max}\sqrt{1 - e_0\psi_0} \end{aligned} \tag{1.19}$$

in which the parameter ψ_0 is obtained based on the equivalent mass of the porous structure for any of the cases given in Fig. 1.10, and is:

$$\psi_0 = \frac{1}{e_0}\left(1 - \left(\frac{2}{\pi}\sqrt{1 - e_0} - \frac{2}{\pi} + 1\right)^2\right) \tag{1.20}$$

1.5 Piezoelectric-Based Systems: Applications and State of the Art

As briefly mentioned in the preceding sections, piezoelectricity exists in materials either naturally or synthetically. If not all, most engineering applications of piezoelectric materials consist of synthetic piezoelectric materials such as PZTs, and PVDFs. Although PVDFs have found diverse uses in industrial applications such as ultrasonic transducers, microphones, hydrophones, and vibration damping

[17,18], their low stiffness and electromechanical coupling coefficients (when compared to PZTs) have limited their utilization. PZTs, on the other hand, are the most popular piezoceramics for engineering applications due to their strong electromechanical coupling. Moreover, they have the ability to optimize their properties to suit specific applications (by appropriate adjustment of the zirconate-titanate ratio). As a result, PZTs (in particular PZT-5H and PZT-5A) are today the most commonly used piezoceramics and are found to be ideal for a variety of electromechanical transducers such as generators (e.g., spark ignition, solid-state batteries), sensors (e.g., acceleration and pressure), actuators (e.g., pneumatic, and hydraulic valves), and energy harvesters [4]. Piezoceramics are usually integrated with elastic substrates, and are not often used as pure piezo structures due to their fragile nature. In the following subsections, some of the main applications of smart structures with piezoelectric elements, which are of interest to the subject of this dissertation, are discussed.

1.5.1 Piezoelectric-Based Energy Harvesters

Recent advancements in low-power, small-sized, and remote electronic devices have led to the introduction of non-conventional power sources during the past decades. Batteries are considered conventional power sources, yet suffer from severe problems such as limited lifetime, and low power efficiency and energy storage capacity, requiring frequent recharging or replacement [19]. Another serious concern with chemical batteries is the environmental panorama of battery disposal around the world. Millions of batteries are discarded into sanitary landfills, where heavy metals can result in groundwater contamination [20]. Thus, solutions that minimize or prevent battery discarding will certainly lead to massive environmental advantages. A promising solution to these shortcomings has been found in harvesting ambient energies available in the environment. Energy harvesters not also provide the chance to extend the working life of small-sized and low-power electronics but also offer specific application to inaccessible electronics or those subject to costly maintenance. Variety of abundant and consistent sources of energy in thermal, chemical, and mechanical forms available for energy harvesters exist in environment [21], ranging from the industrial machinery to vehicles, from the human body to wild animals, from large-scale buildings to

bridges, and from water flow to wind. These ambient energies can be harvested to be used immediately or stored for later use. Mechanical vibration, kinetic energy or deformation energy is a widespread source of ambient energy existed in many applications, where energy scavenging can be beneficial. The unused vibration energy can be converted to usable voltage by means of piezoelectric materials based on their direct effect [22,23,205-209]. Although there are some other basic mechanisms such as electromagnetic [24–26] and electrostatic [27,28] transductions for the vibration-to-electricity energy conversion, piezoelectric transduction has received the greatest attention during recent years. Over the last decade, several books [20,29] and review articles [5,30–37] have appeared on the use of all these three transduction mechanisms covering the theoretical and experimental research works for low power generation from ambient vibrations. The main advantages of piezoelectric energy harvesters are their high power density, architectural simplicity, and scalability. They can be produced both in macro-scale to micro-scale due to the well-established thick-film and thin-film fabrication methods [23,38]. It is however demonstrated that piezoelectric energy harvesting (PEH) usually focuses on harvesting low-level energy, on the order of microwatts to milliwatts [32]. The motivation in this research field is owing to the decreasing power requirement of small electronic components, such as low-power micro-electromechanical systems (MEMS) (e.g. MEMS sensors) used in wireless sensor networks (WSNs). Therefore, along with the rapid advancements in low-power integrated circuits and high-efficiency energy storage devices, the ultimate objective of the energy harvesting concept is to reach autonomous operation of the small-sized electronics used for healthcare, automotive applications, and environmental monitoring. Basically, appropriate applications for the piezoelectric vibration energy harvesting (PVEH) should meet some general requirements; there needs to be a consistent source of vibration in the selected application, battery replacement has to be impractical, and there must be a need to sense something valuable. Several applications such as WSNs, shoes, implantable pacemakers, tire pressure monitoring systems, and bridge and building monitoring systems have been identified as the most promising and widely studied applications of PEH systems [5,39] (see Fig. 1.10).

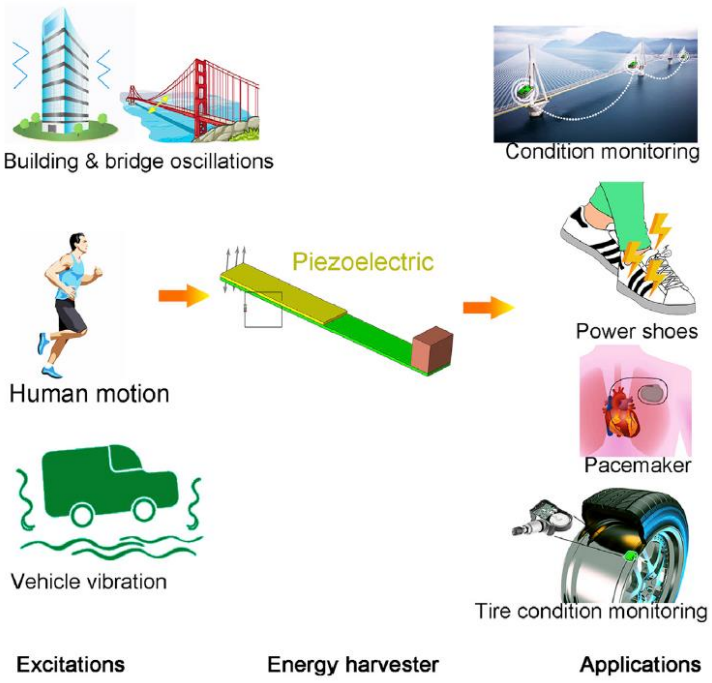

Fig. 1.11: Widely considered applications of piezoelectric energy harvesters [5]

Piezoelectric materials, that are usually used for kinetic energy harvesting, include Aluminum Nitride (AlN), ZnO, $BaTiO_3$, PVDF, PZT, PMN-PT, PZN-PT, and various piezoelectric composites such as piezoelectric macro-fiber composites (MFCs) [40]. Even the concept of FGMs has been considered for the piezoelectric materials to improve the electromechanical response of PEHs [41–44]. In some other studies, piezoelectric materials containing porosities have been used to design particular energy scavengers for applications where lightweight is a concern [45–53]. Nevertheless, it appears from the literature that, as far as PEH research is concerned, PZT-5H and PZT-5A are the most widely implemented piezoceramics in design of energy harvesting systems. It is known that for most piezoceramics, usually $d_{15} \gg d_{33} > d_{13}$ where d_{ij}'s are the electromechanical coupling coefficients (for PZTs, $d_{33} \approx 2d_{31}$). According to the direction of polarization and mechanical stress, piezoelectric energy scavengers can be categorized into three main operation modes, namely d_{31}, d_{33} and d_{15}. As represented in Fig. 1.11(a), in the d_{31} mode (or transverse mode), the direction of polarization (i.e., the electric field direction, which is "3") is perpendicular to the direction of the applied mechanical force/stress (which is "1"). This is the most commonly implemented

piezoelectric operation mode for energy harvesting, and extensively exists in bending-beam scavengers. On the contrary, in the d_{33} mode (or axial mode), the direction of polarization and the applied stress are identical (see Fig. 1.11(b)). This mode is usually employed in tensile/compressive piezoelectric harvesters or scavengers with interdigitated electrodes [54,55]. The last case is the d_{15} mode (or the so-called shear mode), in which the polarization direction is perpendicular to the direction of applied electric filed. In this mode, the electrodes are made *parallel* to the poling direction while they are made *perpendicular* to the poling direction in both d_{31} and d_{33} modes (i.e., the electric field is aligned with the polarization). However, because the d_{15} piezoelectric shear coefficient is the highest coefficient compared to the commonly used axial and transverse modes (that utilize the d_{33} and the d_{31} piezoelectric strain coefficients, respectively), some researchers have employed the shear operation mode to design piezoelectric harvesters with higher power generation [56–58].

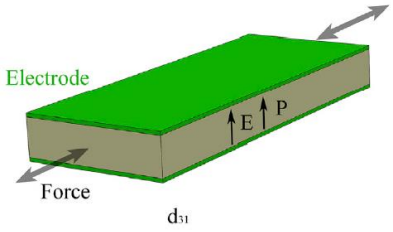

(a) d_{31} mode

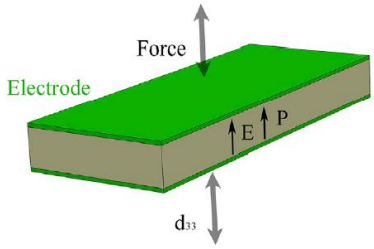

(b) d_{33} mode

Fig. 1.12: Schematic illustration of d_{31} and d_{33} operation modes [5]

Typically, in its simplest form, a PEH system is a cantilevered beam with one or two piezoelectric layers (a unimorph or a bimorph, respectively), as shown in Fig. 1.12 (referred from Chapter 2) along with its equivalent electrical circuit model.

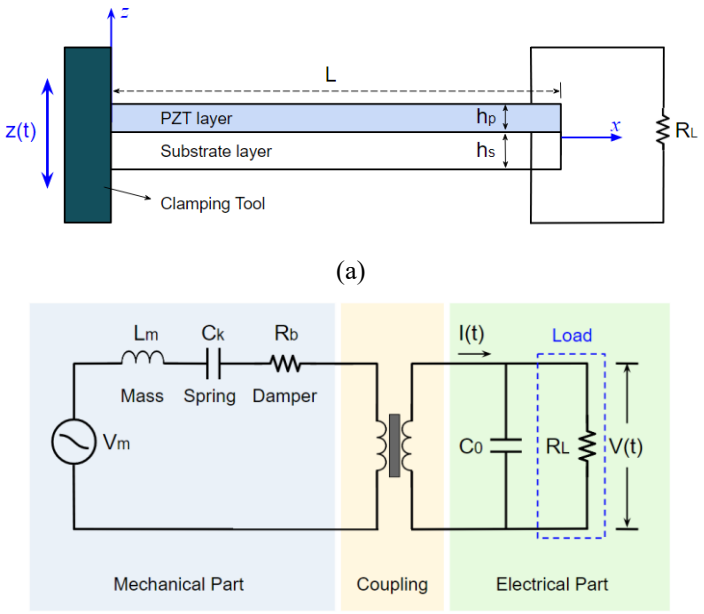

Fig. 1.13: (a) Unimorph cantilever energy harvester (b) equivalent electrical circuit model (referred from Chapter 2)

The piezoelectric harvester device is supposed to be placed on a vibrating host structure (e.g. a vibratory machinery), so that the piezoelectric layer(s) undergoes the dynamic strain, and an electric charge will be generated across the connected electrodes through the direct effect of piezoelectric materials. It is a common practice to the research community focused on the PEH field to consider a simple resistive load (indicated by R_L in Fig. 1.12) in the electrical domain for estimating the performance of the system in term of power generation [22,23,27]. This assumption is also included in the cases investigated in the present dissertation. From the particular viewpoint of electronic engineering or similar subjects, the conversation of the alternating voltage output to a constant voltage is often required. This can be achieved by using a rectifier bridge (AC-to-DC converter) and a smoothing capacitor so that the harvested energy can be stored in a rechargeable small battery or a capacitor. Because the voltage levels used to charge batteries and capacitors are not random, it is frequently necessary to utilize a DC-to-DC converter (step-up or step-down) to adjust the rectified voltage output of the piezoceramic to the voltage required for the specific charging application. These electrical engineering and power electronics aspects are beyond the scope of this dissertation

and the relevant electrical engineering research works can be found in the literature [59–61].

Research in the rapidly growing area of PVEH requires an insight into different aspects of this Multiphysics problem, which includes mechanics of vibrating structures, constitutive behaviors of selected materials, and basic electrical circuit theories. Starting with the early work of Williams and Yates [24] in 1996, this promising way of energizing small-sized electronics and remote sensors has received significant attention by researchers from different engineering disciplines [30,32,33,35–37,39]. So far, mechanical, electrical, and civil engineers and even researchers from the field of material science have considerably focused their attention on this field, as summarized in the following.

As can be realized from Fig. 1.13, the objective of modeling piezoelectric energy harvesters is to estimate the output voltage $V(t)$ across the electrical resistance load R_L in terms of the mechanical input (base motion). The output power generated by the harvester can then be obtained from the calculated output voltage and the applied electrical load through the use of Ohm's law. In the early mathematical modelling of PVEH systems, different researchers employed lumped-parameter solution to electromechanically model the energy harvesters [62,63]. Later, the lumped-parameter modelling was also used for studying the maximum power generation and parameter optimization in PVEH structures [64,65]. While lumped-parameter modeling provides an initial insight into the problem by allowing for simple expressions, it is a simplified approximation that is limited to a single vibration mode and ignores critical aspects of the coupled physical system, such as dynamic mode shapes and accurate strain distribution information, as well as their effects on the electrical response. For this, Sodano et al. [66] and duToit et al. [67] used an improved modeling approach, the Rayleigh-Ritz type discrete formulation originally derived by Hagood et al. [68] for piezoelectric actuation, to model cantilevered piezoelectric energy harvesters (based on the Euler-Bernoulli beam theory). The Rayleigh-Ritz model gives a discrete model of the distributed parameter system, and it is a more accurate approximation compared to lumped-parameter modeling with a single degree of freedom. It can be seen that the modeling the force acting on the beam due to base excitation in the distributed-parameter formulation caused some confusion [66]. The Rayleigh-Ritz model gives

an approximate representation of the distributed-parameter system (Fig. 1.1) as a discretized system by reducing its mechanical degrees of freedom from infinity to a finite dimension and usually it is computationally more expensive than the analytical solution (if available). A comprehensive work was done by Erturk and Inman [69], in which they developed analytical solutions for bimorph cantilever harvesters with both series and parallel electrical connections. A novel composite multi-layer PVEH device consisted of piezoelectric layers, carbon fiber and glass fiber composite laminates was proposed by Lu et al. [70], to improve the efficiency of linear harvesters. Benasciutti et al. [71] studied vibration energy harvesting via piezoelectric resonant bimorph beams of optimized shapes. The aim of their study was to increase the power generated per unit scavenger volume, by optimizing the shape of the cantilever beam. They used different analytical approaches as well as finite element modeling for the analysis of the systems of interest and verified the analytical and numerical results by performing experimental examinations. Some other important contributions concerning the design of optimized PVEH systems were identified in literature [72–75]. In most research works focused on design of PVEH devices, researchers have used PZTs as the material of piezoelectric layer(s). Since PZTs are brittle in nature, some other researchers have presented energy harvesters made of FGPMs [41,43,44,76–80]. In FGPMs, the mechanical and electrical properties vary continuously in the thickness directions, and they enable piezoelectric harvesters to produce larger displacements with smaller stress concentrations and therefore increase the lifetime of piezoelectric devices. Hundreds of other works (available in review articles, e.g., in Refs. [32]) have been published in the literature, dealing with analytical and numerical modelling, experimental investigations, and optimization techniques for piezoelectric energy harvesters.

Due to the fact that this dissertation is devoted to electromechanical modeling of piezoelectric energy harvesters (in Chapters 2 and 3), available articles on experimentation, materials research, and circuit design for piezoelectric energy harvesters are not reviewed here; such works can be found in existing review papers [5,30,33,34,81]. Based on the literature review presented in this section, it is clear that throughout the previous two decades, a variety of modeling methodologies and piezoelectric smart layouts/structures have been proposed for vibration energy harvesting. These works originated from different engineering disciplines,

including mechanical, electrical, civil, and materials engineering. When one takes into consideration the rapidly growing applications of piezoelectric harvesters that are being used for vibration-to-electricity conversion in a variety of environments, it appears that it is necessary to propose new designs as well as reliable electromechanical piezoelectric energy harvester models for use by this particular research community from a variety of engineering disciplines.

1.5.2 Structural Elements with Integrated Piezoelectric Layers

Piezoelectric materials embedded into beams, plates and shells make the structures being capable of sensing and actuation, which directly relate electrical signals to material strains and vice versa. Such smart structures are frequently used for shape and vibration control, noise control, health monitoring, and energy harvesting. From the viewpoint of structural mechanics, a plate is a structural element with substantial plane form dimensions relative to its thickness and is subjected to loads that produce both bending and stretching deformation. The thickness is typically about one-tenth of the smallest in-plane dimension. Due to the smallness of the thickness dimension, it is frequently unnecessary to model the plate using three-dimensional elasticity equations. Beams are also one-dimensional counterparts of plates. Additionally, a shell structure is a thin, curved plate structure shaped to transmit applied forces through compressive, tensile, and shear stresses acting in the plane of the surface. Essentially, a shell can be formed from a plate in two ways: by initially forming the middle surface as a singly or doubly curved surface, and by applying coplanar loads to the plane of the plate that cause considerable stresses. The governing equations of such structural elements under various loading conditions can be derived using either vector mechanics or energy and variational principles. In vector mechanics, the forces, and moments on a typical element of the structure are summed to obtain the equations of equilibrium or motion. In energy methods, the principles of virtual work or their derivatives, such as the principles of minimum potential energy, are employed to obtain the equations. While both approaches can give the same equations, the energy methods have the advantage of providing information on the form of the boundary conditions.

To the subject of the second part of this dissertation is important to provide reliable and comprehensive electromechanical models to give a precise prediction of static and dynamic behavior of structural elements including piezoelectric patches/layers. It appears from the literature that, so far, a number of laminate theories, and computational models have been reported for analysis of smart or adaptive structures involving piezoelectric patches or layers [82–85]. Some other examples include the analytical modeling and analysis of a beam equipped with surface-bonded or embedded piezoelectric sensors and actuators [86,87], the incorporation of piezoelectric materials into composite laminates, and the use of piezoelectric materials for vibration control [88,89]. The challenge of developing a basic mechanics model for the piezoelectric coupled structure has been met by many researchers. Crawley and de Luis [90] established a uniform strain model for a beam with surface bonded and embedded piezoelectric actuator patches, that took into consideration the shear lag effects of the adhesive layer between the piezoelectric actuator and the beam. A model to account for the coupling effect was later proposed by the same authors based on the Euler beam assumption [91]. Ding et al [92] obtained the general solutions for the coupled dynamic equations of a transversely isotropic piezoelectric medium. Models for composite structures with piezoelectric materials as sensors and actuators have also been published [93,94]. In most published literature on the mechanics model for the analysis of the coupled structure, the distribution of the electric potential is assumed to be uniform in the longitudinal direction of the piezoelectric actuator and linear in its thickness direction, which may violate the Maxwell static electricity equation. Wang and Quek [95,96] presented their research on the free vibration of a piezoelectric sandwich beam and circular plate structure, in which the piezoelectric effect on the resonance frequencies of the structure and the distribution of the electric potential are studied and analyzed. A potential application of piezoelectric material is to use it as an actuator in an ultrasonic motor. An analytical model for this application has been proposed by Hagood and McFarland [97]. They assumed that the distribution of electric potential is uniform in the radial direction of the circular plate and showed that resonance response in the plate structure will be initiated if the external electric voltage is well designed. Heyliger and Ramirez [98] studied the free vibration characteristics of laminated circular piezoelectric plates using a discrete-layer model of the weak form of the equation of period motion. A general purpose

design scheme of actively controlled smart structures with piezoelectric sensors and actuators was presented by Xu and Koko [99].

Some other studies have dealt with FGM structures integrated with piezoelectric patches or layers. As was mentioned earlier, FGMs are generally nonhomogeneous composites consisting of ceramic and metal with high coupling in bending and stretching. Besides having the properties of both ceramic and metal, a combination of functionally graded structures with piezoelectric layers results in FGMs with controllable characters and, therefore, with unique applications in industry. Indeed, the electromechanical coupling characteristic in piezoelectric materials, which leads to mechanical deformation in electric field and electrical polarization under mechanical loads, make them good candidates for a variety of electromechanical devices. One of the primary research works on analysis of piezoelectric coupled FGM plates was done by He et al. [100], in which the free vibration response of the coupled plates was extracted through the use of classical plate theory and finite element approach. Hwang and Shen [101] studied the nonlinear vibration of FG plates with surface bonded piezoelectric layers in thermal environments. In this work, the problem, which was formulated based on higher order shear deformation plate theory (HSDT), was solved for the special case of simply supported plates. Vibration of a simply supported FG rectangular plate with piezoelectric rectangular patches on its top and/or bottom surfaces was analyzed by Kargarnovin et al. [102]. The use of refined plate theories on the analysis of functionally graded piezoelectric plates was investigated by Brischetto and Carrera [103]. Refined models with higher-orders of expansion in the thickness direction were implemented and their effectiveness on the static response in comparison with classical theories was studied. The effects of thickness, mass density and stiffness of the piezoelectric layer on the plate natural frequency were investigated by Liang and Batra [104] for a simply supported laminated plate with embedded piezoelectric layers. Furthermore, the role of electrical surface conditions on effective stiffness of piezoelectric materials was studied by Davis and Lesieutre [105]. Jin and Batra [106] showed that the natural frequency would change significantly when the closed circuit condition changed to the open one. Askari Farsangi and Saidi [107] presented an analytical approach for free vibration analysis of moderately thick functionally graded rectangular plates coupled with piezoelectric layers. Active vibration control of functionally graded beams with upper and lower surface-

bonded piezoelectric layers was studied by Bendine et al. [108]. The static and dynamic behavior of functionally graded sandwich structures with piezoelectric skins, using B-spline finite strip models, were investigated by Loja et al. [109].

Mechanical analysis of porous structural elements with integrated piezoelectric patches/layers have also been the subject of research in recent years. Having special capabilities, metal foams have been widely used in lightweight structures in aerospace, automotive, energy absorbing, and civil engineering. Introducing internal pores into the microstructure of porous media allows tailoring the local density of the structure to improve the structural performance and achieve the desired properties. Therefore, integrating piezoelectric layers with porous beams, plates, and shells results in smart bimorphs or unimorphs, with controllable characters and, consequently, with unique applications in industry. Limited works have been carried out to study mechanical problems of porous structures coupled with piezoelectric layers. For instance, Jabari et al. [50,51,52,53,54] studied the elastic and thermal buckling analysis of circular plates made of saturated porous materials integrated with piezoelectric patches, using linear and nonlinear displacement models, respectively. In their studies, they exploited several plate theories, such as the classical, the first-order, and the higher-order shear deformation displacement models, to write the governing equations of motion. Arshid et al. [55] used the classical plate theory to study the free vibration response of porous circular plates integrated with piezoelectric actuators by means of the differential quadrature method. There is a paucity of investigations dealing with the free vibration problem of porous shells integrated with piezoelectric layer. Furthermore, since employing shear deformation theories leads to highly-coupled and complicated governing equations, most of the published papers studied dynamic response of smart coupled structures through numerical methods, and analytical approaches are mostly limited to classical theories.

Based on the literature review given in this subsection, it can be seen that most of the previous works have dealt with analysis of structural elements with piezoelectric layers based on the classical (Euler-Bernoulli/Kirchhoff) theories, but few include shear deformation theories. The classical beam/plate theory is not adequate in providing accurate bending, buckling, and vibration results when the thickness-to-length ratio of the beam/plate is relatively large. This is because the

effect of transverse shear strains, neglected in the classical theory, becomes significant in deep beams and thick plates. In such cases, shear deformation theories provide accurate solutions compared to the classical theory. Equations governing shear deformation theories are typically more complicated than those of the classical theory. Hence it is desirable to have exact relationships between solutions of the classical theory and shear deformation theories so that whenever classical theory solutions are available, the corresponding solutions of shear deformation theories can be readily obtained. Such relationships not only furnish benchmark solutions of shear deformation theories but also provide insight into the significance of shear deformation on the response.

1.6 Objectives of the Dissertation

Commonly used designs for piezoelectric-based devices employ cantilevered beam geometries subjected to base excitations from an ambient source. While this is an attractive option due to its simplicity in design, it still suffers from higher-than-expected natural frequencies that require further tuning. The increasing demand to build a compact yet flexible energy harvester highlights the need for designs having low natural frequencies and higher power densities for a given footprint area. To achieve this goal, in the first part of this dissertation is presented a novel two-dimensional piezoelectric energy harvester design of disc-like geometry. With the increased flexibility of the novel proposed geometry, this design has successfully achieved a smaller natural frequency and larger power density compared to the literature. Moreover, it provides high flexibility in matching its resonance frequency with those of variety of applications, yet offering high power density.

For the specific research community of the multi-disciplinary and rapidly growing area of piezoelectric smart structures, development of computationally efficient but precise electromechanical models has always been of great importance both in academia and industry. Moreover, as long as analytical solutions are available, they are usually much faster compared to the numerical approaches such as finite element method (FEM) or other energy-based discretization techniques. In addition to this, the closed-form expressions extracted from the analytical solutions give the opportunity to explicitly understand the influences of the systems'

parameters and the physics of the problem of interest. Thus, this dissertation is aimed to develop comprehensive analytical models for electromechanical energy harvesting, static and dynamic problems of smart structural elements such as beams, plates, and shells made of piezoelectric and FGM/porous materials. If not all, most of the existing models for studying electromechanical behavior of various structural elements (e.g., beams, plates, and shells) have been developed either based on classical theories or for simply supported boundary conditions. Classical theories ignore the effect of shear deformations, which are very important when analyzing moderately-thick or thick structures. On the other hand, the models based on higher-order theories are mostly limited to either simply supported boundary conditions or coupled structures consisting of homogenous substrates (e.g., made of metals) and PZT layers. Therefore, in this dissertation, both conventional higher-order theories, and higher-order refined theories (which results in less governing equation) are used to establish the electromechanical models of the systems of interest, and reliable analytical solutions are presented to solve the governing equations for variety of boundary conditions. Considering its objectives, a major part of this dissertation is indeed covered by analytical formulations and equations, as well as the exact solution techniques that are developed for solving the respective equations.

In addition to the above-mentioned objectives, it is also aimed to study the effects of various design parameters such as materials and geometrical properties of both substrate and piezoelectric layers, as well as the mechanical and electrical boundary conditions on the systems response. In the problems concerned with the hot topic of piezoelectric energy harvesting (presented in Chapters 2 and 3), the closed-form expressions obtained from the electromechanical models provide the chance to quickly and accurately calculate the optimum electrical load resistance, which results in the maximum power generation.

1.7 Layout of the Dissertation

The main body of the present dissertation is composed of seven chapters, that are divided into two parts. Part 1 consists of Chapters 2 and 3 dealing with analytical and numerical energy harvesting models of different piezoelectric smart structures proposed for vibration-to-electricity conversion. Part 2 consists of Chapters 4 to 7

covering dynamic and static problems of various structural elements such as beams, plates and shells integrated with piezoelectric layer(s). Starting with the second chapter, the main body of this dissertation is covered by the following contents:

The **Second Chapter** starts with development of analytical energy harvesting model of a unimorph cantilevered beam, which is subjected to harmonic base excitation. The model is established based on the Euler-Bernoulli beam assumptions, and closed-form solutions are obtained as the harvester response to the harmonic base excitation. Next, the finite element model of the harvester is developed using COMSOL Multiphysics® software. Verification studies are conducted first by comparing the results of both analytical and numerical models to each other, then by updating the present COMSOL model, and comparing the respective results with experimental and numerical works reported in the literature. In the latter case, the 3D COMSOL model developed by the authors is updated to build the FE model corresponded to unimorph/bimorph harvesters investigated by others (analytically/numerically/experimentally). Once the model is verified, a novel multi-beam piezoelectric structure of disc-like geometry is proposed for vibration energy harvesting, and its numerical model is created in COMSOL through updating the FE model developed for the former case (i.e., the unimorph harvester). Finally, extensive parametric studies are conducted for different case studies of the novel layout, and its performance in terms of power generation is examined.

The **Third Chapter** is concerned with analytical modeling and analysis of plate energy harvesters consist of porous substrates integrated with two piezoelectric layers under both parallel and series electrical connections. Plate-like piezoelectric harvesters can be used in many applications such as energy generation from pressure sources. Three different porosity patterns are considered for the distribution of porosities within the porous substrate. The energy harvesting model of the plate harvester is established based on the conventional shear deformation plate theories, and through the use of Hamilton's principle and Gauss's law. Such theories allow for consideration of transverse shear deformations, therefore, deriving a highly accurate model that can be used for analysis of relatively-thick and thick plate-like piezoelectric harvesters. An analytical solution is then applied to the governing equations, and closed-form expressions are obtained for the

voltage, current and power outputs as the scavenger response to harmonic excitation. Comparing the present results with some available in the literature, the proposed model is validated, and extensive parametric studies are then presented. The effects of design parameters such as the electrical load, porosity characteristics and geometrical parameters are studied in detail, and the results are presented with an eye toward guidelines for design of useful energy harvesting structures to be used in various applications.

In **Chapter 4**, a higher-order beam theory is used to develop the electromechanical free vibration model of piezoelectric bimorph beams. It is assumed that the substrate layer of the bimorph beam is made of FGMs containing porosities, although the model allows to consider different types of material (with properties varying through the thickness), for this layer. The motivation is related to the effect of porosities, which occur in FGMs, being rarely investigated in the literature of piezoelectric coupled FGM structures. This is included in the present modeling by adopting the modified rule of mixture for variation of effective material properties within the FGM substrate. Besides, both thickness-poled and length-poled piezoelectric layers are considered in this smart structure. For the beam with each type of piezoelectric layers (i.e., either transversely or axially polarized), the governing equations are derived through the use of Hamilton's principle and Maxwell's electrostatic equation. Navier's approach is then employed, and applied to the governing equations for extracting the natural frequencies of the beam with simply supported boundary condition. The developed model does not only allow to extract the analytical results for the free vibration response of the beam, but it also provides the opportunity to investigate the effect of the system parameters.

Chapter 5 aims to present an accurate electromechanical model for the both problems of wave propagation and free vibration in/of plate-like structures with integrated piezoelectric layers. The model is derived, through the use of Hamilton's principle and Maxwell's equation, and based on a higher-order four-variable theory, which results in fewer governing equations compared to those of the conventional shear deformation theories. Again, the developed model allows to assign to the substrate layer different types of material with mechanical properties varying through the thickness (e.g., FGMs and porous materials). The refined plate theory

used in this study drops the need of any shear correction factor, and results in highly accurate results in comparison with the 3D solutions available in the literature for the simple counterparts. After deriving the governing equations in term of displacements and electric potential function, analytical solutions are applied to such equations for extracting the exact numerical results for two investigations: (I) the plane wave propagation of infinite smart plates and (II) the free vibration of smart rectangular plates with different boundary conditions. The solution approach proposed for the latter case provides the opportunity to compute the results for various combinations of the classical boundary conditions including simply supported, clamped and free edge conditions. After verifying the model, extensive numerical results are presented covering the effects of material properties, geometrical parameters on the wave and free vibration characteristics of the smart plate structure.

In **Chapter 6**, the linear buckling problem of piezoelectric bimorph plates under various in-plane mechanical loading conditions is studied. The refined higher-order shear theory used in the previous chapter is herein employed to derive the governing equations of the loaded plate. A generalized Levy-type solution in conjunction with the *State Space* concept is then used to solve the respective equations for the smart coupled plate. The exact analytical solutions are obtained for thick and moderately thick plates as well as for thin plates. Although the model allows to consider the substrate layer to be made of materials with varying properties along the thickness, the case of saturated porous materials is of interest in this chapter. Accordingly, the constitutive equations of porous materials are considered based on Biot's poroelasticity theory, which takes into account the effect of pore fluid compressibility, playing a critical role in tailoring the value of critical buckling load. For comparison, different symmetric and asymmetric patterns are considered for the distribution of porosities within the porous substrate. Exact buckling loads of the system are obtained for the system under different loading conditions, and arbitrary boundary conditions.

For relatively complicated structural configurations, i.e., piezoelectric bimorph/unimorph doubly-curved panels, which are usually studied through numerical solutions, an analytical solution using Navier's method is given in **Chapter 7**. The problem of free vibration of such structures with porous substrate

is considered, and the respective governing equations are derived based on the first-order shear deformation theory (FSDT). The formulation given here should be preferred for thin, and moderately-thick shells, due to the assumptions of the adopted theory concerning the effect of transverse shear deformations. Once the proposed exact model is verified through conducting several comparison examples, extensive numerical results are presented for the smart bimorph/unimorph panel having different geometries such as spherical, cylindrical, hyperbolic paraboloidal, and plate shapes. In those tabulated results, the effect of piezoelectric characteristics, porosity, and other design parameters are studies.

Finally, **Chapter 8** summarizes the results of this work, draws conclusions from the chapters, and discuss the impact of the research works presented in the thesis. A summary of the scientific articles published in international journals and conferences as the outcomes of this dissertation is also provided in this chapter.

Chapter 2

Piezoelectric Vibration Energy Harvesting via A Cantilevered Beam and A Novel Multi-beam Structure

2.1 Overview

In this chapter, electromechanical vibration energy harvester models of two systems including a piezoelectric unimorph cantilevered beam, and a novel multi-beam piezoelectric smart structure are presented. The content of the chapter is accordingly organized as follows: in section 2.3, the electromechanical energy harvesting model of the unimorph cantilevered beam is established by means of both analytical modeling based on Euler-Bernoulli assumptions, as well as numerical finite element modeling in COMSOL Multiphysics® software. Then, in section 2.4, using several of the unimorph beams represented in section 2.3, as well as two identical proof masses, a novel multi-beam reference configuration is proposed, aiming to design an energy scavenger for harvesting vibratory motion

from low frequency applications. In section 2.5, Verification studies are conducted first by comparing the results of both analytical and numerical models to each other, and then by updating the present COMSOL model, and comparing the respective results with experimental and numerical works reported in the literature. Then, different case studies of the reference multi-beam configuration are considered, the effects of various design parameters involved on the systems' response are studied, and the obtained numerical results are deeply discussed. Finally, section 2.6 concludes the work and highlights the main findings.

The results of the research work presented in this chapter is published in the journal *Mechanics of Advanced Materials and Structures* [110].

2.2 State of the Art

In recent years, different designs and harvesting materials, nonlinear methods, and optimization techniques (both in mechanical and electrical aspects) have been presented for vibration-to-electricity conversion. As was mentioned in the previous chapter, vibratory motion is a widely-available source of ambient energy, which can be effectively converted into useful electric charge or power, through the use of piezoelectric energy harvesters. The generated electric charge can be used for powering a wide range of small-sized devices in many applications. This interesting research topic has gained much attention of many researchers from different disciplines during the last decade. Various piezoelectric energy scavengers have been designed and proposed for either specific applications or in a general manner. The commonly used designs for piezoelectric-based energy harvesters employ cantilevered beam geometries subjected to base excitation. Although this layout is an attractive structure due to its simplicity in design and fabrication, it suffers from higher-than-expected natural frequencies and deficient power generation. Therefore, to expand the working frequency range and to maximize the power generation, variety of non-conventional piezoelectric structures have been introduced for vibration energy harvesting. For instance, Wu et al [111] proposed a compact two degree of freedom layout for harvesting mechanical vibration from its first and second vibrational modes. Their design consisted of a main cantilever and an inner secondary beam, both equipped with piezoelectric patches, for tuning the

resonance frequencies of the whole device to achieve a wide bandwidth. Toyabur et al. [112] presented a new configuration of a piezoelectric vibration energy harvester that utilizes both fundamental mode and high mode resonant frequencies of the structure, to be used for harnessing energy at lower frequency ranges. A novel trident-shaped multimodal piezoelectric energy harvester was designed by Upadrashta and Yang [113]. Their device was able to achieve three close resonant peaks, thereby being useful for broadband energy harvesting. Sun and Tse [114] presented T-folded and E-folded designs of vibration-based energy harvester model whose resonance frequencies were tunable. The main contribution of their work was to make optimal structures being able of scavenging the destructive vibration into the highest possible electric energy even when the attached machine is running at a low rotational frequency. Later, the same authors proposed another new horizontal U-shaped PVEH, and used COMSOL Multiphysics® to analyze the performance of their proposed device [115]. Fractal-inspired piezoelectric structures were introduced by Castagnetti [116,117] for harvesting vibration at frequencies below 100 Hz. Their proposed structures exhibited wideband frequency response and good energy conversion, specifically at the fundamental eigenfrequency. Several other configurations such as fan-folded structure, zigzag layout, spiral-shaped layout, S-shaped layout, and V-shaped layout, have been introduced by researchers [118–122] for harvesting ambient vibrational energy from various environments, in which the objectives were to increase the power density and/or to maintain the resonance frequency of the proposed device, to be compatible with characteristics of the target application.

Although many geometries and layouts have been introduced by many researchers, there is still a need for new designs to be used for harvesting vibration in various environments. Not only such designs should be able to provide high power densities, but they also should offer variability in design, to be simply adjusted to a selected application (in terms of resonance frequency, for instance). To meet these targets, a novel multi-beam configuration composed of several unimorph beams and proof masses is proposed in this work. As a great advantage, the resonance frequency of this layout can be simply tailored through either altering the number of the unimorphs or modifying their shapes. Besides, it can generate relatively high amount of power density. However, one limitation of linear vibration energy harvesters is that they are only effective near resonance. This means that

even if the amplitude and frequency of the environmental vibration are known, the energy harvester needs to be accurately manufactured exactly at that resonance, to avoid any reduction in the maximum output power. Nevertheless, rapid advances in the relevant technologies allow accurate fabrication of such structures.

2.3 Vibration Energy Harvesting via A Piezoelectric Unimorph Cantilevered Beam

The schematic drawing of the unimorph cantilever beam, with length L and width b , is shown in Fig. 2.1(a). The composite beam consists of a metallic substrate of thickness h_s integrated with a thickness-poled piezoelectric layer of thickness h_p. The origin of the reference coordinate system is located on the neutral surface of the beam. Once the beam vibrates due to its base excitation, mechanical strain is induced inside the piezoelectric layer, that is then converted, through electromechanical coupling, into an electric charge distribution, so that inducing an electric field between the electrodes connected to the piezoelectric layer. Since the thickness of the electrodes is negligible, it is never shown in the sketch given in Fig. 2.1. The upper and lower electrodes attached to the piezoelectric layer are assumed to be connected to an electrical resistive load represented by R_L. Most researchers have considered only a resistive electrical load in the read-out circuit, to come up with a simple model for predicting the electrical outputs for a given base excitation. The implementation of piezoelectric energy scavenging for charging a real battery in an efficient way is more sophisticated, owing to the AC-to-DC transformation process [59,123,124].

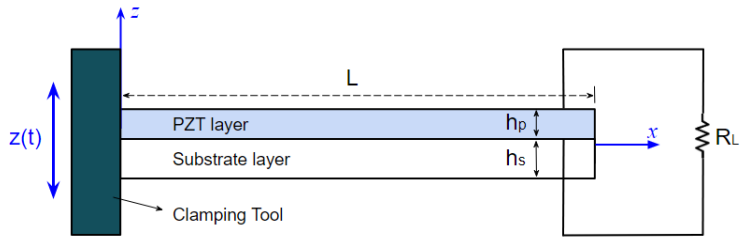

(a)

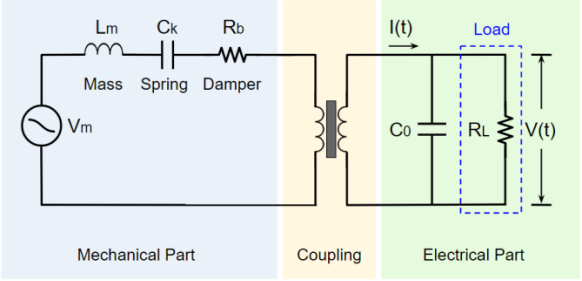

(b)

Fig. 2.1: (a) Unimorph cantilever energy harvester (b) equivalent electrical circuit model

In Fig. 2.1(b), the equivalent electrical circuit model of the cantilevered energy scavenger is represented, in which C_0 denotes the capacitance of the piezoelectric layer that is considered as an external element parallel to the resistive load R_L. Later in future sections, it will be observed that the piezoelectric constitutive equations generate the electrical capacitance term in the circuit equation. Note that, in the right part of Fig. 2.1(b), $V(t)$ represents the electric voltage across the resistive load and $I(t)$ shows the current in the piezoelectric layer. Besides, in the left part of the figure, the inductor L_m indicates the mass, the capacitor C_k signifies the stiffness of the piezoelectric beam, the resistor R_b shows the parasitic damping and V_m simulates an alternating input force.

2.3.1 Analytical Modelling

2.3.1.1 Euler-Bernoulli Beam Theory

It is assumed that the thickness of the beam is small compared to its length so that the shear deformation and rotary inertia can be neglected. For such as thin beam, Euler-Bernoulli beam theory can sufficiently be used to establish the analytical energy harvesting model of the considered unimorph cantilever. Typically, the maximal thickness of the beam is limited by assumptions of thin-beam theory, and on the contrary, the minimal thickness is given by manufacturing limitations.

Since the electrodes attached to the piezoelectric layer are assumed to be perfectly conductive and fully cover the top and bottom surfaces of the piezoelectric layer, the electric potential function ϕ has no dependency on x and y coordinates

[125]. Moreover, due to small thickness of piezoelectric layers in practical cases, the variation of the electric potential within the beam thickness is assumed to be linear, hence, the applied electric field is only along the thickness direction as [125]:

$$E_x = E_y = 0, \;\; E_z = -\frac{V(t)}{h_p} \tag{2.1}$$

According to the Euler-Bernoulli beam theory, the displacement field within the smart cantilevered beam can be expressed as [126]:

$$U_x = -z\frac{\partial w}{\partial x}, \;\; U_y = 0, \;\; U_z = w(x,t) \tag{2.2}$$

Here, (U_x, U_y, U_z) are the total displacements at any point of the beam and $w(x,t)$ is the relative deflection of the beam with respect to its base, thus, $w(0,t) = 0$. From the linear strain-displacement relationship, the strain field is obtained as:

$$\varepsilon_{xx} = -z\frac{\partial^2 w}{\partial x^2}, \;\; \varepsilon_{yy} = \varepsilon_{zz} = \gamma_{xy} = \gamma_{xz} = \gamma_{yz} = 0 \tag{2.3}$$

2.3.1.2 Constitutive Equations

Based on the Euler-Bernoulli assumptions (i.e., Eqs. (2.2) and (2.3)), the constitutive equations of the metallic substrate and piezoelectric layer can be expressed as:

$$\begin{aligned}
\sigma_{xx}^s &= Y^s \varepsilon_{xx} = -Y^s z\frac{\partial^2 w}{\partial x^2} \\
\sigma_{xx}^p &= Y^p(\varepsilon_{xx} - d_{31}E_z) = Y^p\left(-z\frac{\partial^2 w}{\partial x^2} + d_{31}\frac{V(t)}{h_p}\right) \\
D_z &= d_{31}Y^p\varepsilon_{xx} + \epsilon_{33}^S E_z = -d_{31}Y^p z\frac{\partial^2 w}{\partial x^2} - \epsilon_{33}^S\frac{V(t)}{h_p}
\end{aligned} \tag{2.4}$$

Here, Y^s and Y^p are Young's moduli of the materials of the substrate and piezoelectric layers, respectively, d_{31} is the piezoelectric constant and ϵ_{33}^S is the permittivity at constant strain.

2.3.1.3 Equation of Motion

The governing equation of motion for the cantilevered beam subjected to the base excitation $z(t)$ can be written as [29]:

$$\frac{\partial^2 M(x,t)}{\partial x^2} + c_s I \frac{\partial^5 w(x,t)}{\partial x^4 \partial t} + c_a \frac{\partial w(x,t)}{\partial t} + m \frac{\partial^2 w(x,t)}{\partial t^2} = -m \frac{d^2 z(t)}{dt^2} - c_a \frac{dz(t)}{dt} \tag{2.5}$$

in which, $M(x,t)$ is the internal bending moment, $z(t)$ is the base displacement due to the input vibration. Two types of damping mechanisms, i.e., the strain-rate (or the so-called Kelvin-Voigt) damping and the viscous air damping, are included in Eq. (2.5), hence, the coefficients c_s and c_a denote the strain-rate and the viscous air damping coefficients, respectively. These damping mechanisms satisfy the proportional damping criterion, and they are mathematically convenient for the modal analysis solution procedure. The strain-rate damping accounts for the structural damping of the system owing to the internal friction of the beam particles, while the viscous air damping corresponds to the force acting on the beam due to the air particles displaced by the beam during the vibratory motion. Other beam damping mechanisms and the identification procedures of their respective damping parameters from experimental measurements are discussed by Banks and Inman [127]. However, since the considered damping mechanisms are introduced separately in the present modeling, a damping term is hence added to the inertial term in the resulting forcing function of the base excitation expression on the right side of Eq. (2.5). Moreover, m in Eq. (2.5) is the mass per unit length of the beam and can be expressed as:

$$m = b\left(\rho^s h_s + \rho^p h_p\right) \tag{2.6}$$

in which ρ^s and ρ^p are the mass densities of the substrate and piezoelectric layer, respectively.

The internal moment $M(x,t)$ along the unimorph cantilever beam can be obtained by integration of the first moment of the axial stress σ_{xx} over the cross section A, as:

$$
\begin{aligned}
M(x,t) &= -\iint_A \sigma_{xx}\, z\, dA = -b\int_{h_a}^{h_c} \sigma_{xx}\, z\, dz \\
&= -b\left[\int_{h_a}^{h_b} \sigma_{xx}^{s}\, z\, dz + \int_{h_b}^{h_c} \sigma_{xx}^{p}\, z\, dz\right] \\
&= -b\left[\int_{h_a}^{h_b} -Y^{s}\frac{\partial^2 w}{\partial x^2} z^2\, dz \right. \\
&\left. + \int_{h_b}^{h_c} Y^{p}\left(-z\frac{\partial^2 w}{\partial x^2} + d_{31}\frac{V(t)}{h_p}\right) z\, dz\right] \\
&= \frac{\partial^2 w}{\partial x^2}\left(\int_{h_a}^{h_b} Y^{s} b\, z^2 dz + \int_{h_b}^{h_c} Y^{p} b\, z^2\, dz\right) \\
&+ V(t)\int_{h_b}^{h_c} -\frac{Y^{p} b d_{31}}{h_p} z\, dz \\
&= YI\frac{\partial^2 w}{\partial x^2} + \varrho\, V(t)[H(x) - H(x-L)]
\end{aligned}
\tag{2.7}
$$

To avoid the omission of electrical term after substituting in Eq. (2.5), the electrical term of Eq. (2.7) is multiplied by $[H(x) - H(x-L)]$ (where H is the Heaviside function). In Eq. (2.7), h_a is the position of the bottom of the substructure layer from the neutral axis, h_b is the position of the bottom of the piezoelectric layer from the neutral axis, and h_c is the position of the top of the piezoelectric layer from the neutral axis. The mathematical calculations of h_a, h_b and h_c are given in Relation (A.1) of Appendix A. Moreover, the effective transverse stiffness EI and the electromechanical coupling term ϱ are obtained as:

$$
\begin{aligned}
YI &= \int_{h_a}^{h_b} Y^{s} b\, z^2 dz + \int_{h_b}^{h_c} Y^{p} b\, z^2\, dz = \frac{Y^{s} b(h_b^3 - h_a^3) + Y^{p} b(h_c^3 - h_b^3)}{3} \\
\varrho &= -\int_{h_b}^{h_c} \frac{Y^{p} b d_{31}}{h_p} z\, dz = -\frac{Y^{p} b d_{31}(h_c^2 - h_b^2)}{2h_p}
\end{aligned}
\tag{2.8}
$$

Thus, the motion equation of the system can be derived by employing Eqs. (2.6) and (2.7) into Eq. (2.8), as:

$$
\begin{aligned}
YI\frac{\partial^4 w(x,t)}{\partial x^4} + c_s I\frac{\partial^5 w(x,t)}{\partial x^4 \partial t} + c_a\frac{\partial w(x,t)}{\partial t} \\
+ b\left(\rho^s t_s + \rho^p t_p\right)\frac{\partial^2 w(x,t)}{\partial t^2} \\
+ \varrho\, V(t)\frac{d}{dx}[\delta(x) - \delta(x-L)] \\
= -b\left(\rho^s t_s + \rho^p t_p\right)\frac{d^2 z(t)}{dt^2} - c_a\frac{dz(t)}{dt}
\end{aligned}
\tag{2.9}
$$

in which δ is the Dirac delta function, which is the first derivative of Heaviside function. Eq. (2.9) constitutes the motion equation of the electromechanical system presented in Fig. 2.1.

2.3.1.4 Electrical Circuit Equation

The electric displacement equation, coupled with the induced mechanical strain throughout the smart beam, can be derived from the balance of applied and generated electric charge in the piezoelectric layer of the harvester. Therefore, the generated charge $q(t)$ due to the deformation in the beam can be expressed as:

$$
\begin{aligned}
q(t) = \iint_A \vec{D}.\vec{n}\, dA = \iint_A D_3\, dA \\
= b\int_0^L \left(-d_{31} Y^p h_z \frac{\partial^2 w}{\partial x^2} - \epsilon_{33}^S \frac{V(t)}{h_p}\right) dx \\
= -\int_0^L b d_{31} Y^p h_z \frac{\partial^2 w}{\partial x^2} dx - C_0 V(t)
\end{aligned}
\tag{2.10}
$$

in which, $\vec{n}$ denotes the unit outward normal and A is the electrode area. Note that $C_0 = bL\epsilon_{33}^S/h_p$ is the internal capacitance of the piezoelectric layer and is parallelly connected to the resistive load R_L, as shown in Fig. 2.1(b). Moreover, h_z is generated due to averaging in z-direction since the average transverse strain is used to calculate the electrical displacement at position x and time t. In fact, h_z is measured as the distance from the neutral axis to the center of the piezoelectric layer. The corresponding calculations of h_z are given in Relation (A.1) of Appendix A.

One can simply obtain the current generated by the piezoelectric layer as:

$$I(t) = \frac{dq(t)}{dt} = -\int_0^L bd_{31}Y^p h_z \frac{\partial^3 w}{\partial x^2 \partial t} dx - C_0 \frac{dV(t)}{dt} \tag{2.11}$$

Here, the current generated is a function with two components: the first component is due to the vibratory motion of the beam and the second component includes the voltage across the piezoelectric layer. The voltage across the resistive load could be simply obtained from Ohm's law (i.e., $V(t) = R_L I(t)$), thus:

$$V(t) = -R_L \left[\int_0^L bd_{31}Y^p h_z \frac{\partial^3 w}{\partial x^2 \partial t} dx + C_0 \frac{dV(t)}{dt} \right] \tag{2.12}$$

Or:

$$C_0 \frac{dV(t)}{dt} + \frac{1}{R_L} V(t) = -\int_0^L bd_{31}Y^p h_z \frac{\partial^3 w}{\partial x^2 \partial t} dx \tag{2.13}$$

Eqs. (2.9) and (2.13) are the coupled electromechanical equations of motion for the cantilevered piezoelectric energy harvester subjected to the base excitation $z(t)$.

2.3.1.5 Modal Analysis

The most common method of solving the coupled Eqs. (2.9) and (2.13) is to assume that the relative vibratory motion of the beam can be expressed as a series expansion with multiplying functions of separate variables:

$$w(x,t) = \sum_{i=1}^{\infty} \phi_i(x)\eta_i(t) \tag{2.14}$$

where $\phi_i(x)$ is the ith transverse mode normalized eigenfunction and $\eta_i(t)$ is the ith modal displacement of the uniform clamped-free beam. Because the system is proportionally damped, the eigenfunctions represented by $\phi_i(x)$ are the mass normalized eigenfunctions of the corresponding undamped free vibration problem, so that employing Eq. (2.14) and the boundary conditions of the clamped-free beam

in the reduced form of Eq. (2.9) corresponded to the undamped free vibration problem, yield:

$$\phi_i(x) = \sqrt{\frac{1}{mL}}\left(\cos\frac{\lambda_i x}{L} - \cosh\frac{\lambda_i x}{L} + \frac{\sinh\lambda_i - \sin\lambda_i}{\cosh\lambda_i - \cos\lambda_i}\left[\sin\frac{\lambda_i x}{L} - \sinh\frac{\lambda_i x}{L}\right]\right) \tag{2.15}$$

Eq. (2.15) represents the mode shape of the cantilevered beam at ith vibrational mode. In Eq. (2.15), the λ_i's are the dimensionless frequency numbers obtained from the following characteristic equation:

$$1 + \cos\lambda\cosh\lambda = 0 \tag{2.16}$$

The ith modal short circuit natural frequency (i.e., $V(t) = 0$) of the system can be determined as:

$$\omega_i = \lambda_i^2\sqrt{\frac{YI}{mL^4}} \tag{2.17}$$

Substituting Eq. (2.14) into Eq. (2.9) and taking advantage of the orthogonally conditions of the mode shapes, the electromechanically coupled ordinary equation including the modal damping term for the influence of the proportional damping can be obtained as:

$$\frac{d^2\eta_k(t)}{dt^2} + 2\zeta_k\omega_k\frac{d\eta_k(t)}{dt} + \omega_k^2\eta_k(t) + \Theta_k V(t) = -m\gamma_k\frac{d^2z(t)}{dt^2} \tag{2.18}$$

where ζ_k is the modal mechanical damping ratio, the coefficient Θ_k is the modal electromechanical coupling coefficient for all k, and γ_k denotes the modal influence coefficient of the base excitation. These coefficients are given by the following expressions:

$$\Theta_k = \varrho\left.\frac{d\phi_k(x)}{dx}\right|_{x=L} \tag{2.19a}$$

$$\gamma_k = \int_0^L \phi_k(x)\, dx \tag{2.19b}$$

$$\zeta_k = \frac{c_s I \omega_k}{2YI} + \frac{c_a}{2m\omega_k} \tag{2.19c}$$

As seen from Eq. (2.19c), the damping ratio ζ_k includes the influences of both viscous air damping and strain-rate damping, and it can be expressed as $\zeta_k = \zeta_k^s + \zeta_k^a$ where the strain-rate and the air damping components of the damping ratio are $\zeta_k^s = c_s I \omega_k / 2YI$ and $\zeta_k^a = c_a / 2m\omega_k$, respectively. It is clear from Eq. (2.19c) that the strain-rate damping coefficient is proportional to the effective structural stiffness and the viscous air damping is proportional to mass per unit length of the beam. It is also worth mentioning that obtaining the value of the damping ratio (hence, the damping coefficients c_s and c_a) should be conducted through experimental measurements, which is generally difficult to assess. Consequently, in the present analytical modeling, all sources of mechanical damping are represented by a single damping ratio (i.e., ζ_k) and its value will be evaluated with reference to literature data for the selected materials. A comprehensive discussion on this very important parameter is provided in Ref. [29].

The electrical equation of motion can be rewritten in terms of the modal coordinates by employing Eq. (2.14) into Eq. (2.13), as:

$$\frac{dV(t)}{dt} + \frac{1}{R_L C_0} V(t) = \frac{1}{C_0} \sum_{i=1}^{\infty} \psi_i \frac{d\eta_i(t)}{dt} \tag{2.20}$$

where

$$\psi_i = -\int_0^L b d_{31} Y^p h_z \frac{d^2 \phi_i(x)}{dx^2} dx = -b d_{31} Y^p h_z \left. \frac{d\phi_i(x)}{dx} \right|_{x=L} \tag{2.21}$$

Eq. (2.18) together with Eq. (2.20) provides a complete system of modal equations for the vibration energy harvesting model of the unimorph cantilevered beam.

2.3.1.6 Response to Harmonic Excitation

In this subsection, the application of the above electromechanical model, established for energy harvesting from a unimorph cantilevered beam, is investigated. In a prototypical piezoelectric energy harvesting system, the cantilevered beam is subjected to base excitations in a wide band. Here, the case of harmonic base motion is taken into account, so that $z(t) = Z_0 e^{j\omega t}$, where Z_0 is the amplitude of the base excitation (considered real), ω is the deriving frequency, and $j = \sqrt{-1}$. It is also remembered that the external electrical load attached to the energy harvester device is assumed to be represented by a simple resistor with resistance load R_L, (see Fig. 2.1). Because the system of Eqs. (2.18) and (2.20) is linear, the output voltage and modal response are harmonic at the deriving frequency, therefore, $V(t) = V_0 e^{j\omega t}$ and $\eta_k(t) = H_k e^{j\omega t}$, for all k, where V_0 and H_k are complex. Substitution of these expressions into Eqs. (2.18) and (2.20) gives the magnitude of the modal response and the output voltage, as follows:

$$H_k = \frac{m\gamma_k\omega^2 Z_0 - \Theta_k V_0}{\omega_k^2 - \omega^2 + 2j\zeta_k\omega_k\omega} \tag{2.22a}$$

$$V_0\left(j\omega + \frac{1}{R_L C_0}\right) = \frac{1}{C_0}\sum_{i=1}^{\infty}\varphi_i j\omega H_i \tag{2.22b}$$

One can simply observe from Eq. (2.22) that the two responses are coupled, so that to express V_0 explicitly, the modal response has to be omitted from Eq. (2.22b), thus:

$$V_0 = \frac{S_1/C_0}{j\omega + \frac{1}{R_L C_0} + \frac{S_2}{C_0}} \tag{2.23}$$

where the functions S_1 and S_2 are here defined for the simplification of the function representing the output electric voltage, as follows:

$$S_1 = \sum_{i=1}^{\infty}\frac{j\omega\, m\, \gamma_i\, \psi_i(\omega^2 Z_0)}{\omega_i^2 - \omega^2 + 2j\zeta_i\omega_i\omega} \tag{2.24a}$$

$$S_2 = \sum_{i=1}^{\infty} \frac{j\omega\, \Theta_i\, \psi_i}{\omega_i^2 - \omega^2 + 2j\zeta_i\omega_i\omega} \tag{2.24b}$$

Now, the amplitude of the voltage frequency response can be simply obtained by determining the absolute value of the complex expression of V_0 in Eq. (2.23). It is also very simple to determine the current I and the power frequency response P using the Ohm's law and the power equation as well, as follows:

$$I = \frac{|V_0|}{R_L}, \qquad P = \frac{|V_0|^2}{R_L} \tag{2.25}$$

The obtained output voltage V_0 can also be substituted into the modal response in Eq. (2.22a), to calculate the transverse displacement in each vibrational mode, and subsequently the modal response as a function of the excitation frequency ω and the time t.

At this stage, a code is provided by using MATLAB® R2020a software, in which the data listed in Tables 2.1 and 2.2 are used as the material and geometrical parameters of the unimorph harvester. That code is then used to extract the numerical results of the analytical model developed for the unimorph PVEH device. In the next section, the FE modeling of the same PVEH system is performed in COMSOL Multiphysics® 5.5, and the modeling and the simulation procedure is explained in detail.

2.3.2 Numerical Modelling

COMSOL Multiphysics® 5.5. is used here for the development of the FE modeling. This software gives the opportunity of coupling different domains of physics to simply study their effects on each other, when analyzing Multiphysics problems. In order to analyze the PVEH systems in COMSOL, the *Solid Mechanics* module is coupled with *Electrostatics* and *Electrical Circuit* modules, to create the coupled electromechanical model. Modal analysis of the system is first performed using the *Eigenfrequency* study to obtain the resonant frequencies, the corresponding mode shapes, and the strain plots. Once the eigenfrequencies of the system are computed,

Frequency-Domain studies are carried out within confined frequency bands (which include the obtained resonance frequencies of the harvester) to extract the frequency response of the system. Note that frequency-domain study performs the FE analysis of the system for each given frequency, which is then used to extract extensive results presented in frequency response plots.

Following the above procedure and adopting the material and geometrical parameters given in Tables 2.1 and 2.2, the 3D model of the cantilevered beam is created in COMSOL, as shown in Fig. 2.2.

Table 2.1: Materials properties

Property	Substrate				PZT layer
	Aluminum	Steel	Bronze	Titanium	PZT-5A
Young modulus (GPa)	70	210	105	115.7	66
Mass density (kg/m^3)	2700	7800	9000	4506	7800
Poisson's ratio	0.30	0.30	0.30	0.32	-
Coupling coefficient, d_{31} (pm/V)	-	-	-	-	-190
Permittivity, ϵ_{33}^{s} (nF/m)	-	-	-	-	15.93

Table 2.2: Geometrical parameters of the typical unimorph cantilever

Parameter	Substrate	PZT layer
Length (mm), L_b, L_p	40	40
Width (mm), b	7	7
Thickness (mm), h_s, h_p	0.3	0.3

The geometry of the unimorph beam consists of two subdomains of the substrate and the piezoelectric layer. To model the clamped boundary condition, *Fixed Constraint* is applied to the left boundaries of both layers of the beam (at $x = 0$), while remaining boundaries are left free. The harmonic base excitation is modeled by applying a *Body Load*, along the z-direction, to the whole geometry (i.e. all subdomains). The substrate material is selected as the linear elastic material while the PZT layer is selected in the piezoelectric material subsection. The value

of the mechanical damping ratio, which represents a parameter that is generally difficult to assess, is evaluated with reference to literature data, thus, an *Isotropic Damping Loss Factor* of 5% is considered for both materials of substrate and piezoelectric layer [74,75,128,129]. Electrostatics module is used to match the nodes to the electrodes. In this module, the bottom surface of the piezoelectric layer (that is in contact with the substrate) is attached to a Ground electrode and the top surface is attached to a Terminal electrode. The type of terminal is chosen as circuit type, to be linked to the electrical load resistor in the Electrical Circuit module for obtaining the electrical response of the energy harvester. As the last step, the design is meshed to discretize the geometry for the FE analysis. It is true that using more mesh elements leads to more accurate approximation and solution, but it requires longer solution time. Therefore, a mesh convergence study is done first, to adequately select the type and number of mesh elements. According to what is just said, pre-defined tetrahedral elements with normal size is selected to mesh the unimorph beam for the FE simulations.

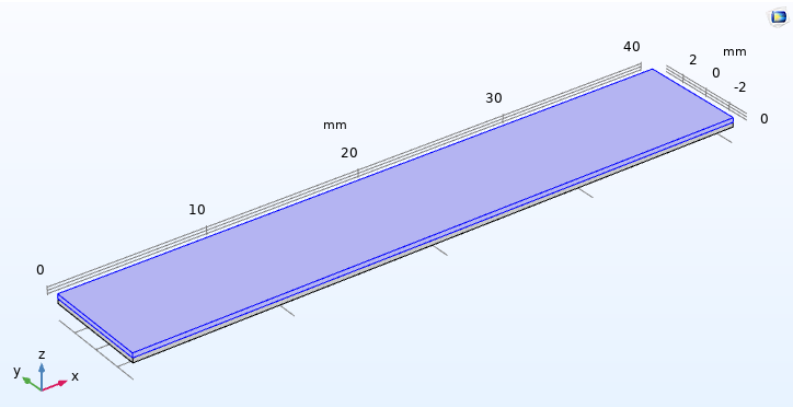

Fig. 2.2: 3D COMSOL model of the unimorph cantilevered beam

2.4 Vibration Energy Harvesting via A Novel Multi-beam Piezoelectric Smart Structure

2.4.1 Harvester Layout

In the previous section, both analytical and FE models of the unimorph piezoelectric energy harvester were established. In this section, a novel multi-beam smart

structure, composed of several of the unimorph beams investigated in the previous section as well as two identical proof masses, is proposed. A reference layout of the proposed energy scavenger, resting on its housing, is shown in Fig. 2.3, where 8 unimorph beams are attached to an octagon-shaped part at the center of the structure. In fact, this smart structure is supposed to be consisted of n unimorph beams attached to all sides of a regular n-sided polygon-shaped disc integrated by two proof masses at its top and bottom faces. Therefore, the layout shown in Fig. 2.3 represents the structure for the particular case of $n = 8$. As seen from Fig. 2.3(a), all the beams are clamped to a housing case at their outer edges. For clarification, the proposed system is divided into three different parts including the *Substrate Structure*, the *PZT Patches*, and the two *Proof Masses*. The substrate structure consists of a regular n-sided polygon of side length a, that is located at the center of the layout, and is surrounded by n identical unimorph beams of length L_b, widths b_i (at center) and b_o (at clamped edge), and thickness h_b. The substrate structure is, in fact, a continuous part, as is depicted in Fig. 2.3(b). Thickness-poled piezoelectric layers of length L_p, width b_p and thickness h_p, are attached to the substrate structure on the beams, to be used for the mechanical deformation-to-electricity conversion. Moreover, two identical proof masses with the same shape of the regular n-sided polygon and having a thickness of h_m (for each mass) are also attached to the center of the layout on both top and bottom sides. The proof masses can be properly selected to adapt the resonance frequency of the harvester to that of ambient vibration source, therefore maximizing transmissibility. The proposed energy harvester is supposed to be attached to a vibrating machinery by bolting or gluing its housing part to the host structure. Once the harvester is excited along its thickness direction, the proof masses oscillate with respect to the housing, thus significant stress/strain is induced inside the piezo patches, which in turn electric voltage is generated. Similar to the case of the unimorph harvester in the previous subsection, the electrodes attached to the PZT patches of the new proposed device are assumed to be connected to an electrical resistive load R_L, for measuring the electrical outputs.

2.4.2 Numerical Modelling

Following the same procedure used to model the unimorph harvester (presented in subsection 2.2.2), and using the provisional data listed in Table 2.3, the FE model of the proposed PVEH device is created in COMSOL software. Aluminum, Steel and PZT-5A (properties are given in Table 2.1) are considered as the materials of the substrate structure, the proof masses and the PZT patches, respectively. Also, in the meshing step of the FE simulations for this multi-beam layout, the type and size of mesh elements for discretizing the geometry are appropriately selected after performing mesh convergence studies. The mesh is accordingly built using tetrahedral elements with normal/fine size.

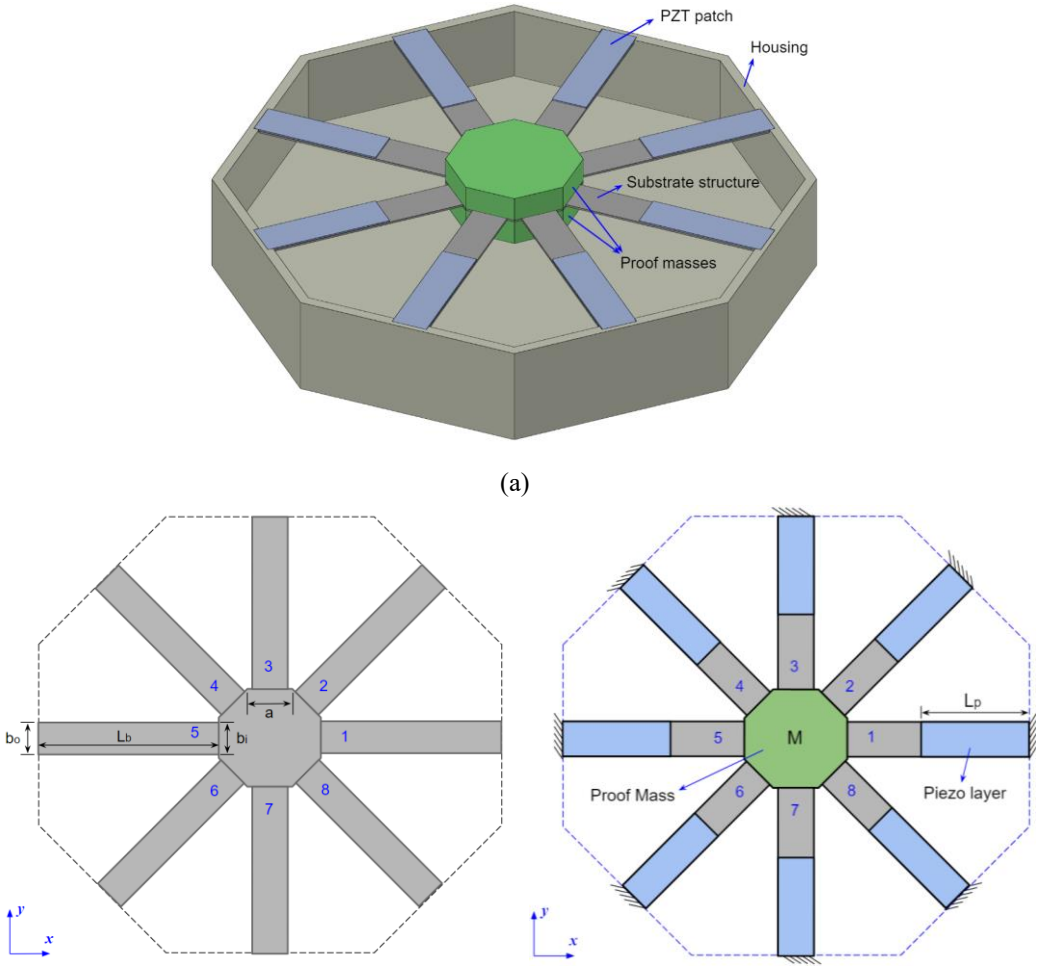

Fig. 2.3: (a) 3D sketch of the proposed multi-beam energy harvester resting on its housing (for $n = 8$) (b) 2D sketch of the substrate structure (c) 2D sketch of the substrate structure equipped with PZT patches and proof masses

Table 2.3: Provisional dimensions of the novel multi-beam energy harvester

Parameter	Substrate	PZT layer	Central mass
Side length of the central part (mm), a	-	-	10
Length (mm), L_b, L_p	40	40	-
Inner width (mm), b_i	7	7	-
Outer width (mm), b_o	7	7	-
Thickness (mm), h_b, h_p, h_m	0.3	0.3	5

2.5 Parametric Studies and Discussion

This section provides numerical results of both unimorph and the novel multi-beam energy harvesters. Because the fundamental vibration mode of the scavengers is of the highest practical importance for energy harvesting, attention is therefore given to this mode. In addition to frequency response functions, variations of the electrical outputs with load resistance and other design parameters are also investigated here, for excitations at short circuit (SC) and open circuit (OC) resonant frequencies.

2.5.1 Numerical Results for the Unimorph Harvester

The accuracy of the analytical modeling and the FE simulations is first evaluated in this subsection. To that, the resonance frequencies of the unimorph beam calculated from the analytical model and the FE COMSOL simulation are presented in Table 2.4, in which different materials are assigned to the substrate layer of the harvester. Moreover, the transverse displacement and the strain plots associated to the first vibrational mode of the unimorph harvester are also extracted from the COMSOL simulations and given in Figure 2.4. It is noted that in the MATLAB computations, only stiffness, mass density and dimensions are considered, so that involved in the slight differences observed from Table 2.4. Nonetheless, one can observe from the table that the relative differences are less than 1%, confirming reliability of the FE COMSOL models and simulations for accurate prediction of resonance frequencies.

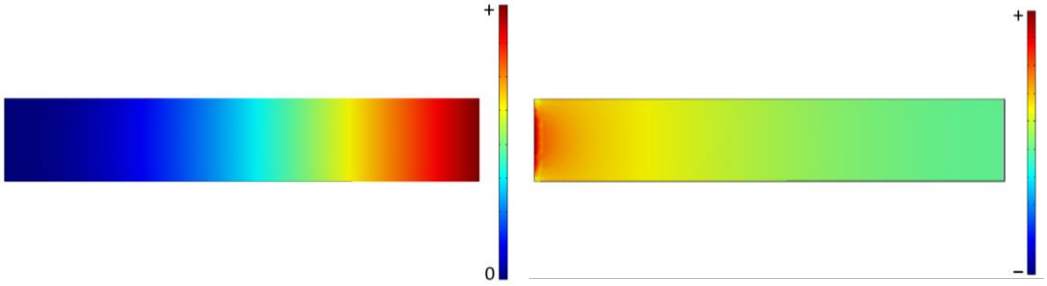

(a) Transverse displacement plot (b) Strain plot

Fig. 2.4: Fundamental mode shape of the unimorph beam (top view–the beam is clamped at its left end)

Table 2.4: Fundamental resonance frequency (Hz) of the unimorph beam calculated by MATLAB and COMSOL

Reference	Substrate material			
	Aluminum	Steel	Bronze	Titanium
MATLAB code	217.95	227.31	189.46	226.14
COMSOL simulation	216.62	225.32	188.01	224.49
Relative difference (%)	+ 0.61	+ 0.88	+ 0.77	+ 0.73

Based on the geometrical properties given in Table 2.2, the developed analytical and FE COMSOL models are used to obtain the voltage, current and power response to base excitation for the unimorph harvester made of Aluminum and PZT-5A. Because the electrical load resistance R_L is an important parameter which has a great influence on the dynamic behavior of the PVEH device, the first peak in the output electrical response of the unimorph beam is plotted in Figs. 2.5 to 2.7, for different values of load resistance R_L: 10^2, 10^3, 10^4, 10^5, 10^6, 10^7 and 10^8 Ω. These plots represent the magnitude of the output voltage, current and power for unimorph energy harvester when subjected to a harmonic base excitation with an amplitude of $0.4g$ (i.e., $\omega^2 Z_0 = 0.4g$), where g is the acceleration of gravity ($g \approx 9.81\ m/s^2$). It can be noticed that level of 0.4g is significant, in terms of applied acceleration, but it is remarkable that the PVEH system is aimed to recover at least a portion of energy dissipated in case of evident loss in the host structure and is compatible with some assumptions already made in the literature as well as in some specific application (see for instance rolling mill vibration or in

steelmaking plants [130,131]). As known, the SC condition is expected for low values of load resistance (i.e., $R_L \to 0$), whereas the PVEH device is expected to shift toward the OC condition for large values of R_L (i.e., $R_L \to \infty$).

From Figs. 2.5 to 2.7, again, excellent agreement between the results of MATLAB and COMSOL simulations, both in terms of values and overall trends, is seen, which clearly shows the consistency of the electromechanical models proposed here. Some other important points can be realized from these figures. For instance, Fig. 2.5 indicates that as R_L increases from low values to large values, the amplitude of the voltage output rises monotonically for all the excitation frequencies until it reaches its maximum value at $R_L = 10^6$ and then remains constant for $R_L \geq 10^6$. Moreover, with increasing the load resistance R_L, the resonance frequency of the unimorph moves from the SC resonance frequency to the OC frequency. The two important excitation frequencies are the SC and the OC resonance frequencies of the unimorph PVEH device, which can be calculated simply from Figs. 2.5 to 2.7. From Fig. 2.6, in which the output current is plotted against the driving frequency, it is observed that the amplitude of the electric current goes down monotonically (similar to output voltage) as the value of R_L increases, which is the opposite of the output voltage behavior presented in Fig. 2.5. It is also obvious that for every considered driving frequency, the maximum amount of the electric current is achieved when the PVEH system is close to the SC condition. Fig. 2.7 shows that the output power does not represent a monotonic behavior when the value of R_L increases. In fact, as the load resistance gets larger, the power output increases until it reaches its maximum value, which corresponds to $R_L = 10^5$ (among the sample values considered), then drops due to the large resistance value in the denominator which reduces the electric current. Using the frequency response plots given in Figs. 2.5 to 2.7, the SC and OC resonance frequencies, the maximum peak power, and its corresponding excitation frequency as well as the power density of the unimorph harvester, are extracted and listed in Table 2.5. It is noted that the maximum power output reported in Table 2.5 is achieved for $R_L = 10^5$, which is among the sample values of the load resistance considered for plotting the frequency response plots. Therefore, the obtained value of the maximum peak power is not necessarily the maximum possible or the optimized power output that can be generated by the unimorph energy harvester. It is, however, a straightforward

practice to compute the optimum value of R_L and its respective resonance frequency for the present unimorph energy harvester and it is beyond the discussion of this subsection, which intends to address more general points.

Table 2.5: Dynamic and electric outputs of the unimorph cantilever PVEH device

Parameter	MATLAB Code	COMSOL Simulations
SC resonance frequency (Hz)	218.0	219.6
OC resonance frequency (Hz)	221.6	223.0
Total volume of the proposed PEH (mm^3)	168	168
Total volume of the PZT patches (mm^3)	84	84
Peak power at $R_L = 10^5\Omega$ (μW)	21.08	20.65
Excitation frequency at the peak power (Hz)	221.0	222.2
Power density 1 ($\mu W/mm^3$)	0.125	0.123
Power density 2 ($\mu W/mm^3$)	0.251	0.246
Power density 1 = Peak power per total volume of the energy harvester		
Power density 2 = Peak power per total volume of the PZT patches		

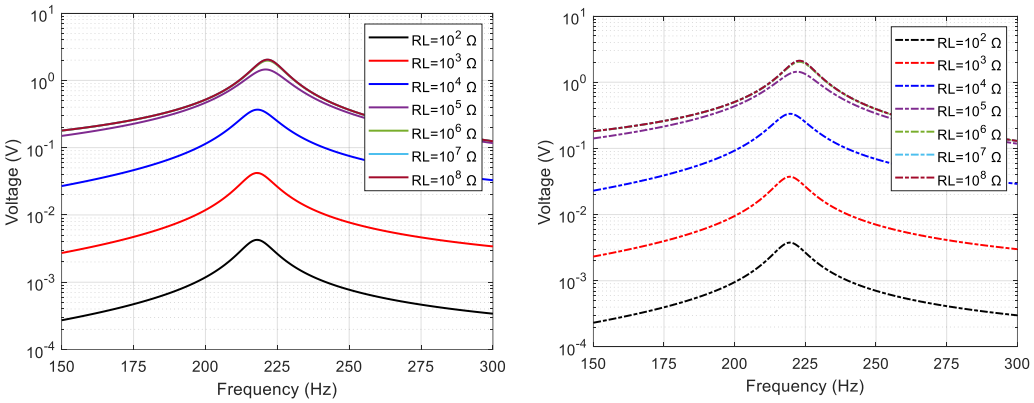

(a) MATLAB Code (b) COMSOL Simulations

Fig. 2.5: Voltage response to base excitation for the typical unimorph beam

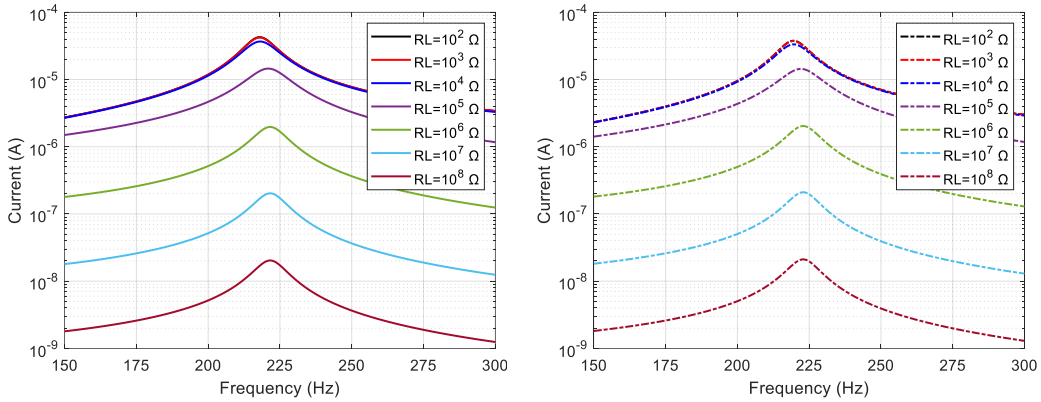

(a) MATLAB Code (b) COMSOL Simulations

Fig. 2.6: Current response to base excitation for the typical unimorph beam

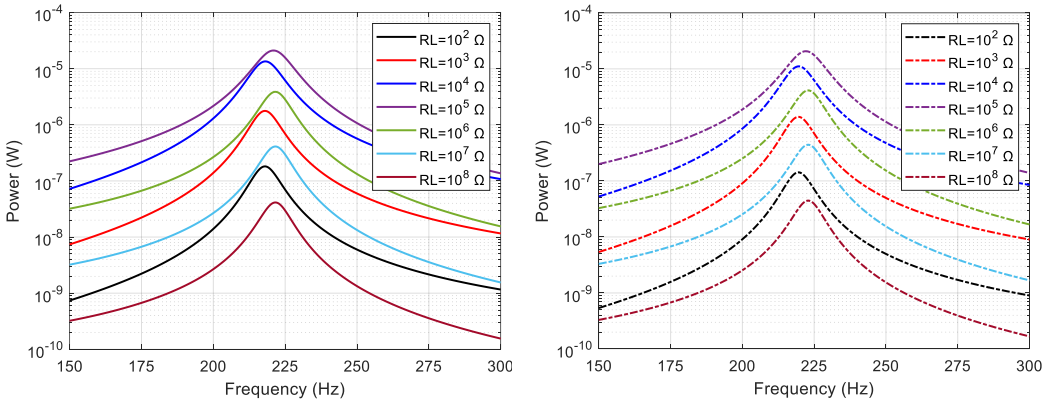

(a) MATLAB Code (b) COMSOL Simulations

Fig. 2.7: Power response to base excitation for the typical unimorph beam

Although the good agreement between the results of the present analytical and FE numerical models (observed from Table 2.4 and Figs. 2.5 to 2.7) clearly shows the reliability of both developed models, the accuracy of the present FE model is further investigated by making some other comparison examples, with the help of some relevant numerical and experimental works available in literature. To that end, the present numerical COMSOL models are slightly modified and updated to build the FE model of some other PVEH layouts presented in literature. The first example is concerned with analysis of the cantilevered unimorph energy harvester proposed in Ref. [128], which is studied both numerically and experimentally. The present FE model is modified to build the 3D COMSOL model of that unimorph,

for comparing the results. Using this updated COMSOL model, the results of numerical modeling and experimental measurements of modal and frequency domain analyses presented in Ref. [128] (given in Figs. 2 and 4, and also Table 2 of Ref. [128]) are recalculated, and given here in Table 2.6 and Fig. 2.8 alongside their counterparts. Good agreement between the obtained results is observed, which clearly shows the consistency of the FE electromechanical model proposed in the current contribution.

Table 2.6: Comparison example between the results of the present simulations with those of Ref. [128]

Parameter	Ref. [128]		
	Numerical	Experimental	Our FE model
Location of the PZT patch	0	0	0
OC voltage (V)	24.21	23.05	23.69
Resonance frequency (Hz)	94.5	93.7	94.4

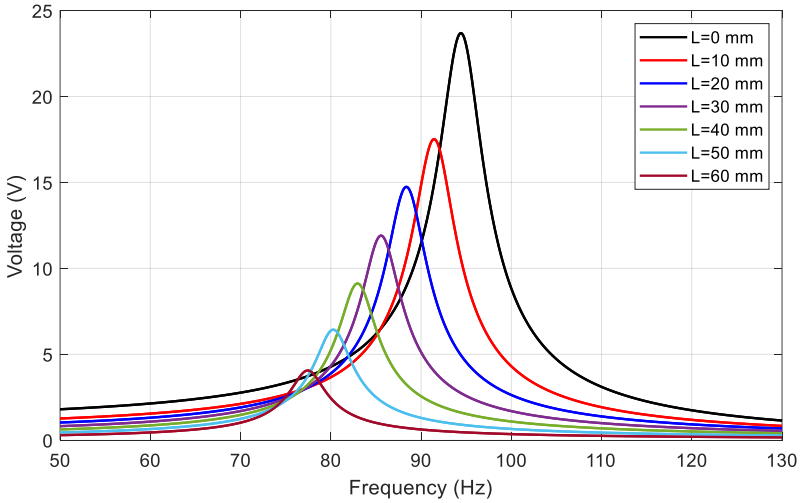

Fig. 2.8: OC voltage versus driving frequency for the unimorph beam proposed in Ref. [128] (here, L is the distance of PZT patch from the fixed end of the beam)

In a second comparison example, the authors have updated the present FE COMSOL model and simulated the bimorph harvester presented in Ref. [132], and listed in Table 2.7 the obtained results alongside their counterparts reported in Ref. [132]. The concurrence of the results listed in Table 2.7, once again, confirms that

the developed FE simulations exhibit good reliability in prediction of the dynamic and electric response of PVEH systems.

Table 2.7: Comparison example between the results of the present simulations with those of Ref. [132]

Parameter	Ref. [132]	Our FE model
SC resonance frequency (Hz)	99.80	99.74
OC resonance frequency (Hz)	105.50	106.6
Displacement of the tip mass at optimal load (μm)	127	131
Harvested power at optimal load (mW)	0.323	0.334

2.5.2 Numerical Results for the Novel Multi-beam Harvester

The FE COMSOL model developed for the unimorph harvester was verified through the comparison examples presented in the previous subsection. This reliable model is here used and modified (in terms of geometry) to build the numerical model of the proposed multi-beam structure. Here and hereafter, different case studies of the multi-beam layout are considered, and comprehensive parametric studies are performed to assess the performance of the proposed device and to realize the effect of various design parameters. First, three different structures with $n = 4$ (4-beam layout), $n = 6$ (6-beam layout) and $n = 8$ (8-beam layout) are selected the case studies of our interest for conducting the FE electromechanical analyses. In COMSOL Multiphysics® software, the FE models of these three cases are created, as depicted in Fig. 2.9. Aluminum, Steel and PZT-5A (properties are given in Table 2.1) are considered as the materials of the substrate structure, the proof masses and the PZT patches, respectively. The geometrical dimensions are also considered based on the data listed in Table 2.3.

In a first step, Eigenfrequency studies are carried out in COMSOL to obtain the resonance frequencies and the corresponding eigenmodes of the three considered layouts. As a result, in Figs. 2.10 to 2.12 are shown the obtained results of the fundamental mode shapes for all the considered layouts. From the figures, the existence of two curves throughout the length of each beam is observed, which shows the existence of two regions in which mechanical strain can be created when the fundamental mode of each layout is excited. Obviously, one should attach the

piezoelectric patches to the substrate structure within these two regions, so that considerable mechanical strain can be induced inside the PZT patches, which in turn leads to generation of electrical voltage.

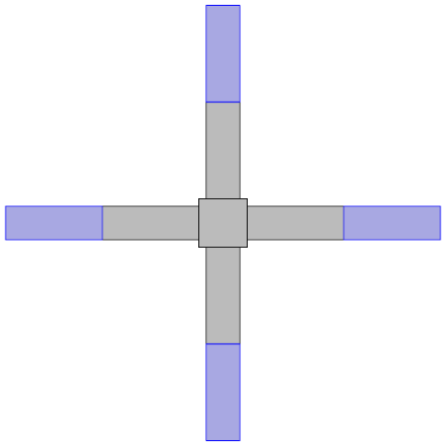

(a) The 4-beam layout

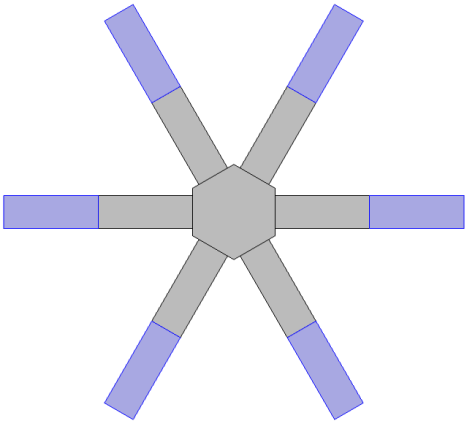

(b) The 6-beam layout

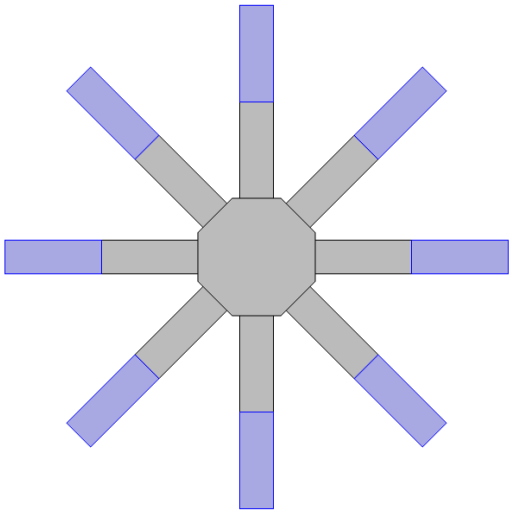

(c) The 8-beam layout

Fig. 2.9: FE COMSOL models of the proposed energy harvester for $n = 4, 6, 8$

The next step is to perform Frequency-Domain simulations in COMSOL to determine the voltage and power generated by the considered layouts. Excitation of sinusoidal form is thus applied at the fixed ends of the selected layouts assuming constant excitation acceleration amplitude. In the following subsections, a number of frequency-domain studies are conducted to investigate how different design

parameters such as the length of piezoelectric patches, the proof masses, the type of electrical connection (i.e., parallel or series among the piezoelectric patches), as well as the selected materials influence the electric response of the layouts presented in Fig. 2.9. In the frequency-domain analyses presented in the future subsections, an isotropic damping loss factor of $\eta_s = 0.05$ is considered for both materials of the substrate structure and PZT patches, with reference to the literature data for the same materials [74,128,129,133]. Moreover, the system is assumed to be subjected to a harmonic base acceleration of 0.4g.

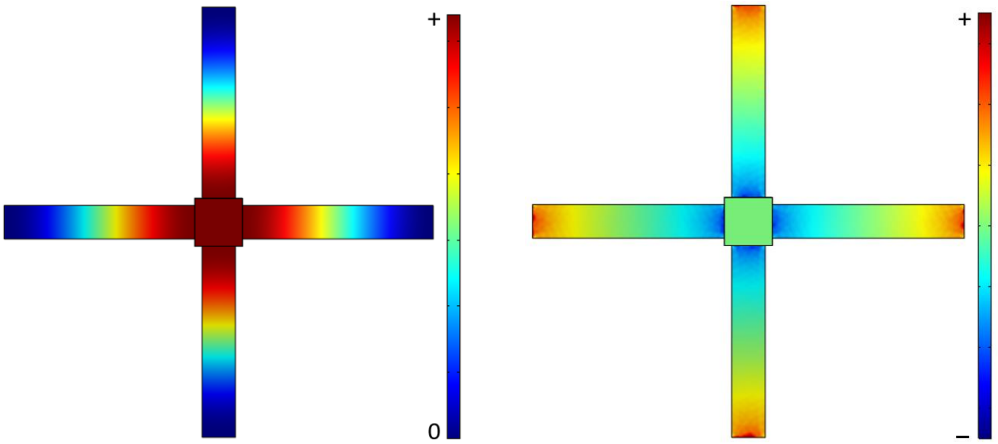

(a) Transverse displacement (top view) (b) Strain distribution (top view)

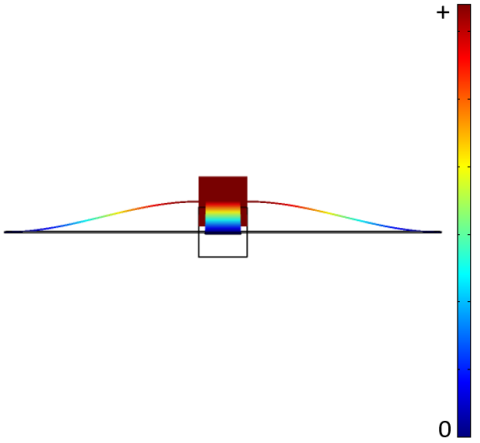

(c) Transverse displacement (side view)

Fig. 2.10: First mode shape corresponded to the fundamental frequency of 4-beam layout (133 Hz)

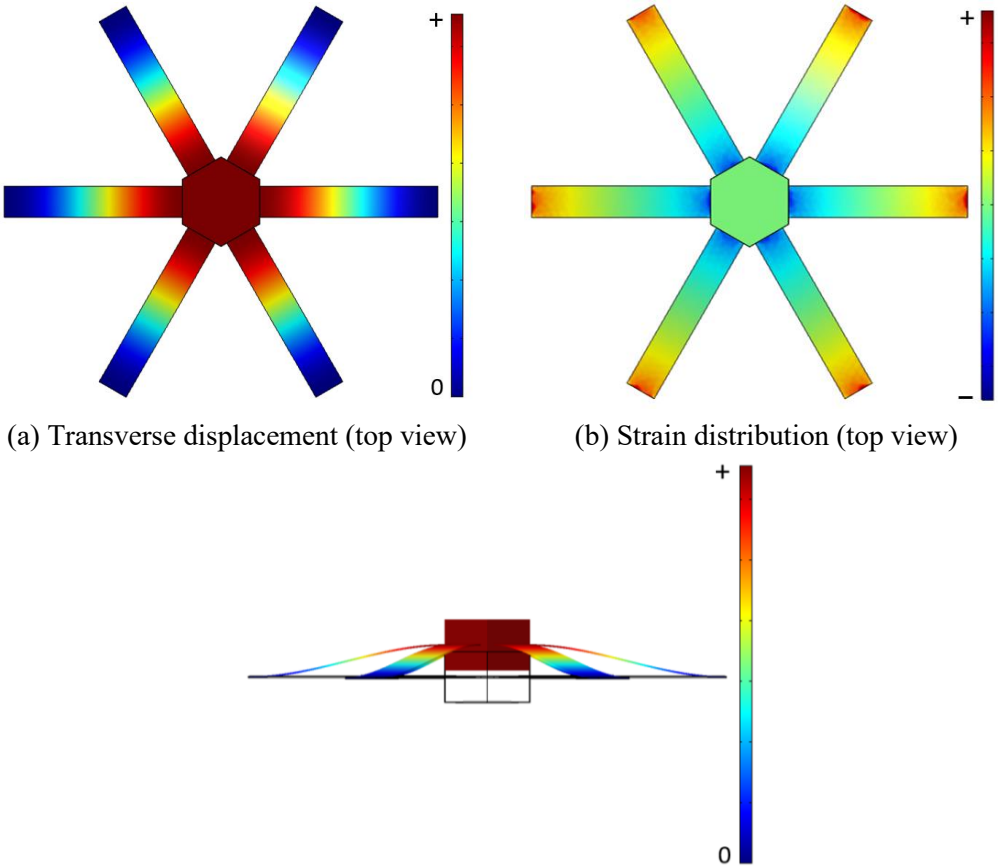

(a) Transverse displacement (top view)

(b) Strain distribution (top view)

(c) Transverse displacement (side view)

Fig. 2.11: First mode shape corresponded to the fundamental frequency of 6-beam layout (104.3 Hz)

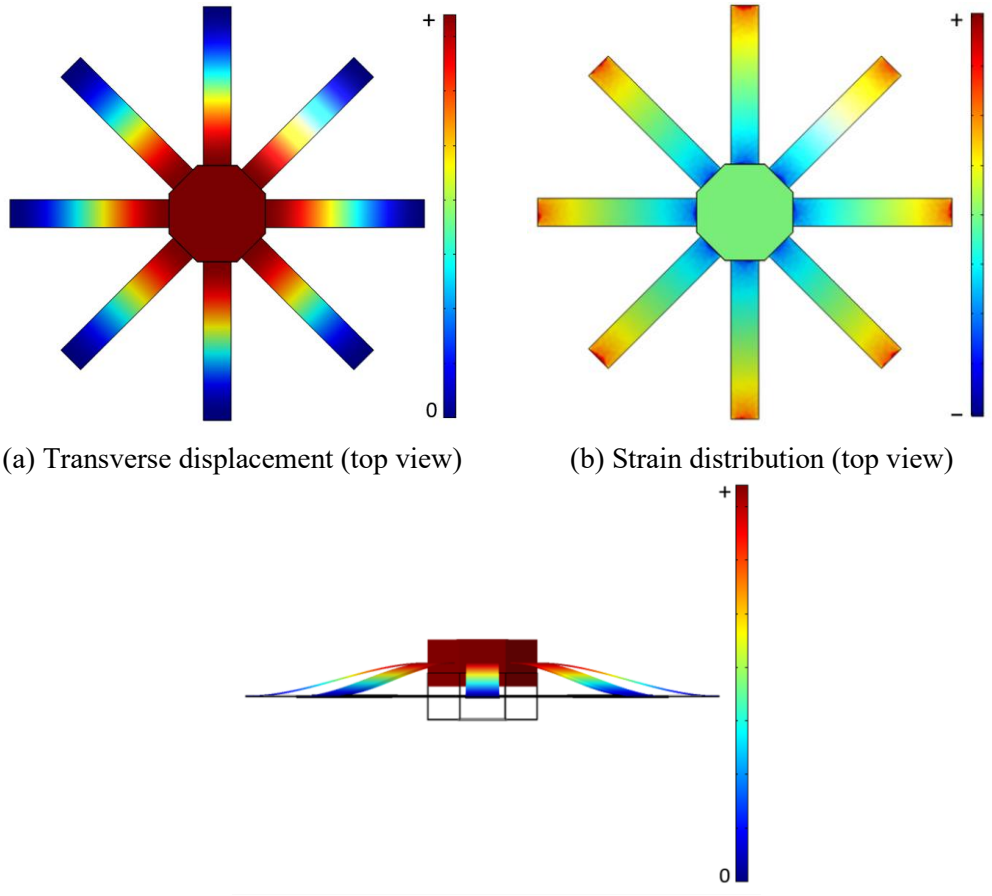

(a) Transverse displacement (top view) (b) Strain distribution (top view)

(c) Transverse displacement (side view)

Fig. 2.12: First mode shape corresponded to the fundamental frequency of 8-beam layout (89.5 Hz)

2.5.2.1 Effect of length of the PZT Patches

Assuming different values for the length of the PZT patches L_p, ranging from 6 to 38 mm (with a step of 2 mm), Frequency-Domain studies are performed for the three cases of interest, and the obtained results are given in Fig. 2.13, where the effects of variation of L_p on resonance frequency of the harvester, peak voltage and peak power are illustrated. Note that parallel connection is used here for wiring the piezoelectric patches, in which the bottom surfaces of all the PZT patches are attached to a Ground electrode while all the top surfaces are connected to a Terminal electrode. An electrical load of $R_L = 10^5\Omega$ is also considered as a fixed sample

value of the electrical load resistance, to extract the general trends of mechanical and electrical outputs against the length of PZT patches.

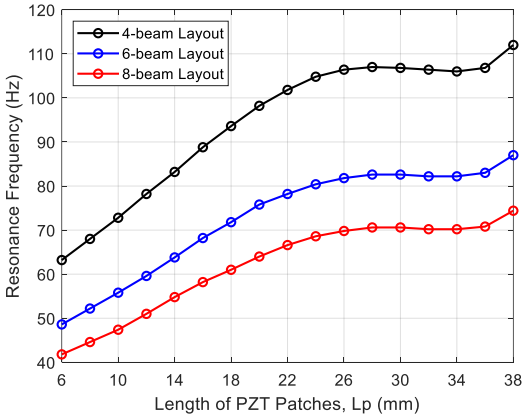

(a)

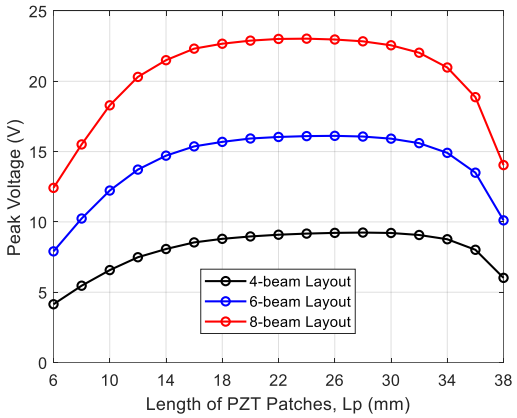

(b)

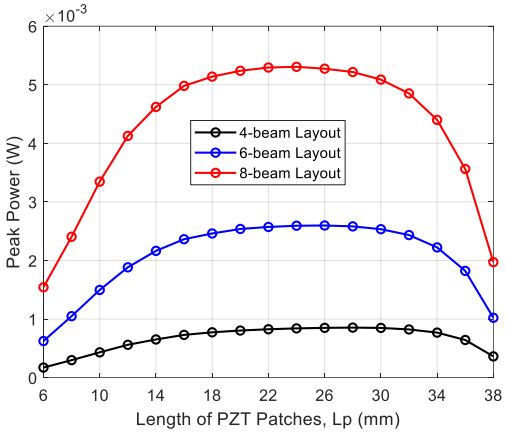

(c)

Fig. 2.13: Variation of resonance frequency and electric outputs of the 4-Beam, 6-beam, and 8-beam harvesters versus the length of PZT patches

As a primary observation, it is abundantly clear from Fig. 2.13 that the more are the number of the adopted beams in the multi-beam harvester, the less is the resonance frequency of the harvester, and the more is its output voltage/power. Moreover, one can observe that changing the length of the piezo patches significantly affects the resonance frequency and the peak voltage/power for all the considered multi-beam harvesters. In fact, the resonance frequency of each of the considered smart layouts increases by increasing the length of the PZT patches. On the other hand, as the length of the piezo patches increases, the peak voltage (and also the peak power) in frequency response plots increases until it reaches its maximum value then drops dramatically. The physical reason behind the increasing/decreasing trends of the voltage/power peaks could be attributed to the bending strain distribution throughout the length of the beams. Actually, as we move from the clamped end of each beam to the center of the layout, the bending strain distribution changes sign (see Figs. 2.10(b), 2.11(b) and 2.12(b)), which indicates the existence of a Strain Node through the length of each beam. Note that a Strain Node corresponds to a location, in a mode shape, where the strain distribution (or the beam curvature) changes sign [134]. According to the definition of piezoelectric materials, the voltage produced on the electrodes of a piezoelectric layer is proportional to the strain induced in the piezoelectric layer. In fact, if an element of piezoelectric material has positive strain (tension) in one location and negative strain (compression) in another location (simultaneously), negative and positive voltages will be produced across the piezoelectric material, therefore, when a continuous electrode covers the entire piezoelectric layer, the negative and positive voltages will tend to cancel. This phenomenon results in significant reduction of the power output. Due to this phenomenon, it is therefore not efficient (in terms of the maximum voltage and power generation) to cover the entire length of the beams with continues piezoelectric patches.

Optimal values are seen from Fig. 2.13 for the length of the PZT patches (among the considered values), in which the maximum peak voltage/power can be achieved from each of the considered layouts. These values and their respective frequencies, maximum peak powers and power densities (peak power per unit volume of the energy harvester) are extracted and listed in Table 2.8, for the three considered smart layouts. The results listed in Table 2.8 demonstrate that the 8-beam harvester exhibits the lowest resonance frequency, which is 68.8 Hz, followed

by the 6-beam and the 4-beam layouts (81.8 and 107 Hz, respectively). Among the three considered layouts, the maximum peak voltage/power as well as the maximum power density are also achieved by the 8-beam structure, when the same harmonic base excitation is applied. Comparing the obtained results presented in Tables 2.5 and 2.8, it can be found that when the same base excitation (i.e., 0.4g) and the same load resistance (i.e., $R_L = 10^5\Omega$) are applied, the 4-beam, 6-beam, and 8-beam layouts provide power densities of almost 3.3, 5 and 6.3 times greater than that of the typical unimorph cantilever, respectively. Note that the value of load resistance used to obtain the plots presented in Fig. 2.13, was taken arbitrarily as a sample value to observe the general trends only, thereby, the maximum voltage and power outputs reported above, are for this sample value and they are not necessarily the maximum possible or the optimized power outputs.

Table 2.8: Optimal length of the piezo patches and the respective output voltage/power for different multi-beam structures

	Structure		
Parameter	4-beam layout	6-beam layout	8-beam layout
Optimal length of the PZT patches (mm)	28	26	24
Resonance frequency of the harvester (Hz)	107	81.8	68.6
Total weight of the whole harvester (gr)	10.62	24.39	43.01
Total volume of the harvester (mm^3)	1601.2	3507.6	5903.6
Total volume of the PZT patches (mm^3)	235.2	327.6	403.2
Peak voltage (V)	9.2	16	23
Peak power (mW)	0.85	2.6	5.3
Power density 1 ($\mu W/mm^3$)	0.53	0.74	0.90
Power density 2 ($\mu W/mm^3$)	3.61	7.94	13.14

Power density 1 = Peak power per total volume of the energy harvester

Power density 2 = Peak power per total volume of the PZT patches

2.5.2.2 Effect of Parallel and Series Connections

In this subsection, the 8-beam PVEH device investigated in the preceding subsection (with $L_p = 24$ mm) is selected as the case of our interest due to its highest power density compared to the other layouts, therefore, the FE COMSOL parametric studies are continued for this system only. For wiring the electrodes attached to the eight piezoelectric patches in the 8-beam smart layout, both parallel and series connections are used and simulated in COMSOL. The parallel connection is simulated in COMSOL simply by assigning a ground node to the bottom electrodes of all the PZT patches, and a terminal node to all the top electrodes. Regarding the configuration with series connection, the bottom electrode of the PZT patch of the first smart beam (beam No. 1 in Fig. 2.3c) is assigned to a ground node. Then, its top electrode is considered as a terminal node, shared with the bottom electrode of the PZT patch of the second smart beam. This pattern is repeated for the following patches as well. Eventually, the last remaining electrode of the smart beam No. 8 is attached to a separate terminal node. The type of this last terminal is considered as circuit, to be connected to the electrical circuit in electrical circuit module, for the measurement of the voltage generated across the load resistance. In order to investigate the effect of the type of electrical connection among the piezo patches, the frequency response of voltage and power outputs of the 8-beam PVEH system are plotted in Figs. 2.14 and 2.15, for different values of load resistance ranging from 100Ω (SC condition) to 100MΩ (OC condition).

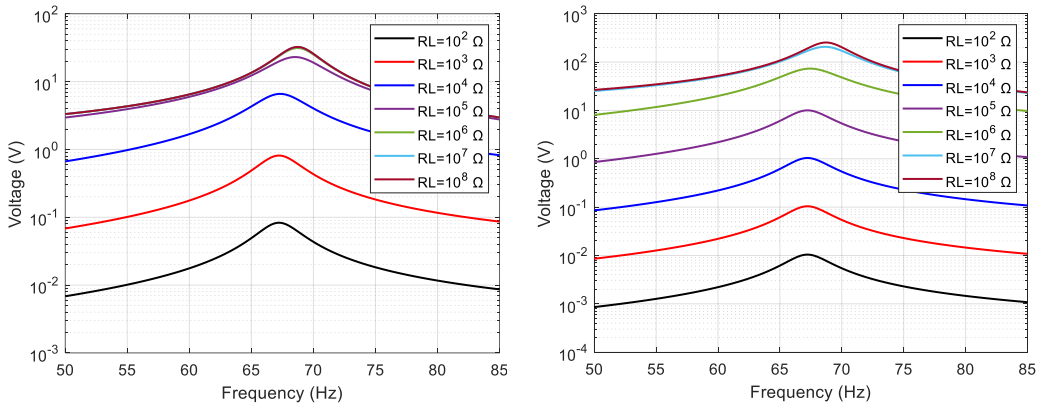

(a) Parallel connection (b) Series connection

Fig. 2.14: Voltage response to base excitation for the 8-beam layout

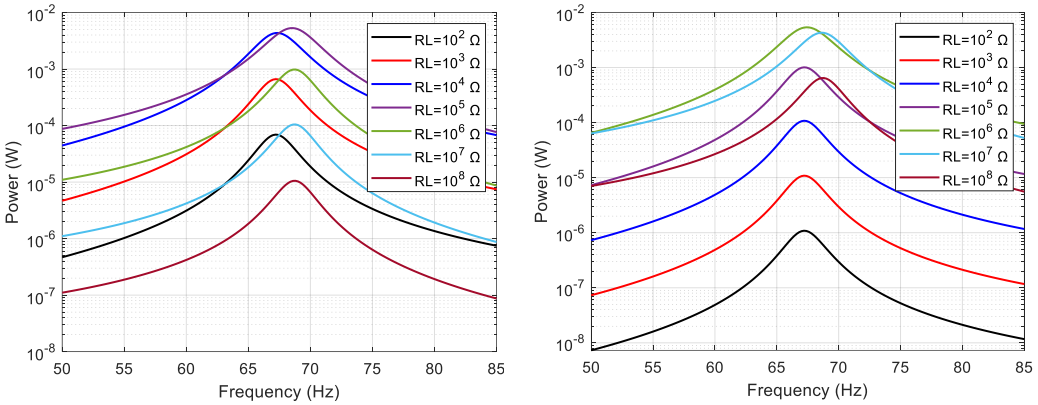

(a) Parallel connection (b) Series connection

Fig. 2.15: Power response to base excitation for the 8-beam layout

The trends observed from Figs. 2.14 and 2.15 are expectedly similar to those presented for the unimorph harvester. However, Fig. 2.15 indicates that although the output voltage increases with increasing the value of R_L for both types of electrical connections, a larger resistance load has to be applied to the PVEH system under series connection to reach its OC condition, compared to when the parallel connection is used. The output voltage rises with increasing the load resistance first, and then it remains constant in the OC voltage for $R_L \geq 10^6\Omega$ in parallel connection, while for $R_L \geq 10^8\Omega$ in series connection. As expected, the amount of the OC voltage provided by the series electrical configuration is much higher compared to the parallel configuration. It is also worth noticing that the type of electrical connections has no effect on the resonance frequencies corresponded to the SC and OC conditions of the PVEH system. From Fig. 2.14, the SC and OC resonance frequencies of the 8-beam layout are found to be 67.2 Hz and 68.8 Hz, respectively. On the other hand, Figs. 2.15(a) and 2.15(b) represent that among the sample values considered for R_L, the values of the maximum output power generated by the PVEH device under parallel and series connections correspond to $R_L = 10^5\Omega$ and $R_L = 10^6\Omega$, respectively, which are close to the OC condition of the system. Another interesting point, that can be seen from Fig. 2.15, is that some of the curves corresponded to various frequency response cross each other at different values of R_L, in which the crossing points are around the resonance frequency of the harvester. At these crossing frequencies, the two respective values of R_L result in the same amount of power output.

To provide a deeper insight into the load resistance effect, variations of the voltage, current and power outputs with load resistance for excitations at the SC and OC resonance frequencies are plotted in Figs. 2.16 to 2.18, for the 8-beam PVEH system.

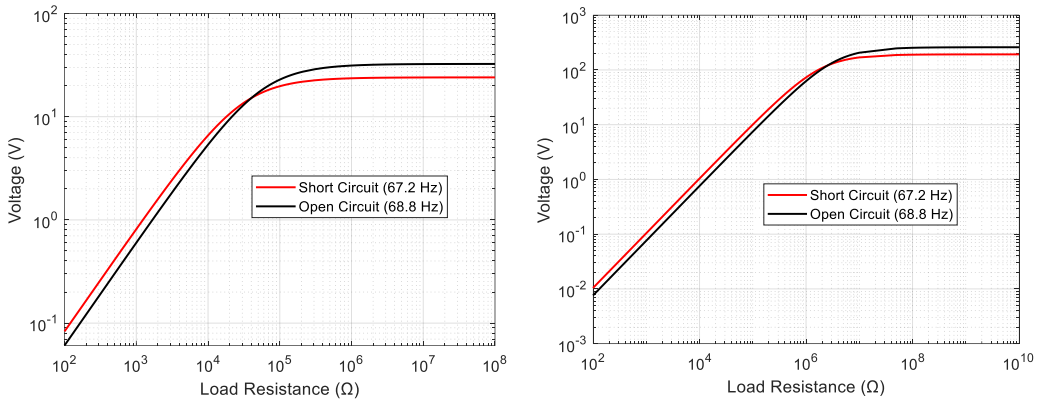

(a) Parallel connection (b) Series connection

Fig. 2.16: Variation of the voltage output with resistance load for the 8-beam PVEH device

Fig. 2.16 indicates that for low values of load resistance R_L, the voltage output at the SC resonance frequency is higher than that of the OC excitation since the system is close to SC conditions. However, the SC and OC curves intersect at a certain value of R_L (about 40.1 kΩ for parallel connection, and 2.6 MΩ for series connection), and for the values of R_L greater than the value at the point of intersection, the voltage output at the OC resonance frequency becomes higher expectedly. Finally, the voltage output remains constant and insensitive to the variations of R_L at OC conditions (i.e., for very large amounts of R_L).

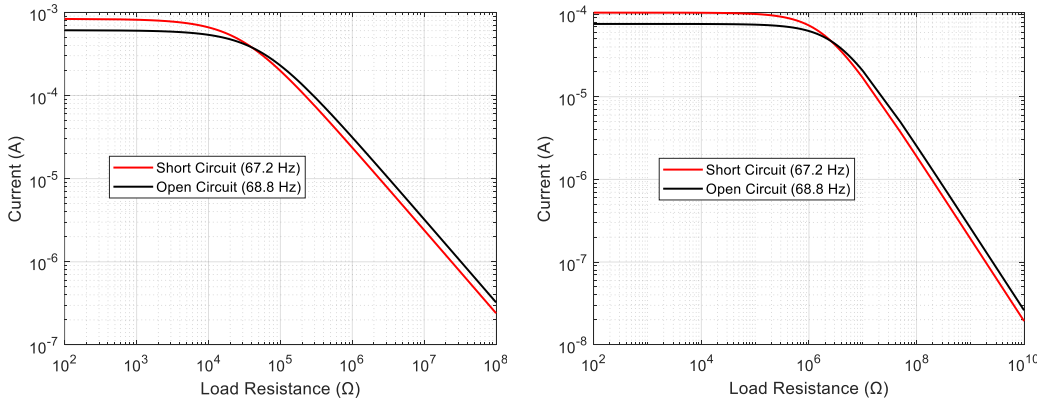

(a) Parallel connection (b) Series connection

Fig. 2.17: Variation of the current output with resistance load for the 8-beam PVEH device

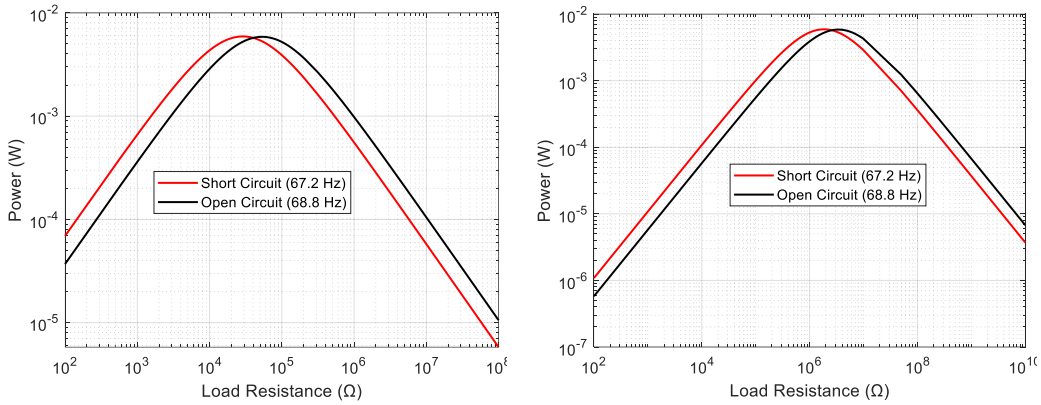

(a) Parallel connection (b) Series connection

Fig. 2.18: Variation of the power output with resistance load for the 8-beam PVEH device

Concerning the current output, one can simply observe from Fig. 2.17 that, for both parallel and series connections, the current is very insensitive to the changes in R_L when it varies at the range of its low values. Since in this relatively low resistance domain the system is close to the SC conditions, higher current output is obtained at the SC resonance frequency compared to the OC one, similar to the case of voltage output. After, the output current starts declining with further increase in R_L, until both the curves (in both Figs. 2.17(a) and 2.17(b)) cross each other at a certain value of load resistance (again, around 40.1 kΩ for parallel connection, and 2.6 MΩ for series connection). For the values of R_L greater than

the value at the crossing point, the output current corresponded to the excitation at the SC resonance frequency becomes higher than that of the OC resonance frequency.

In regard to the power output, it is also realized from Fig. 2.18 that the same intersection points (around 40.1 kΩ for parallel connection, and 2.6 MΩ for series connection) are appeared for the curves associated to the power outputs of excitation at the SC and OC resonance frequencies. For both parallel and series types of connection among the PZT patches, the trends of the power output at the SC and the OC resonance frequencies in the regions before and after the crossing load resistance are similar to those of the voltage output plots. More important are the observed peak power values in both Figs. 2.18(a) and 2.18(b), that are corresponded to the optimum values of load resistance in both parallel and series connections, respectively. It is realized that when the optimum values of R_L are used for each of the SC and OC excitations, the same values of maximum power output are obtained. In particular, from Fig. 2.18(a), when the parallel connection is used, the maximum power output generated by the 8-beam PVEH device is 5.9 mW across the optimum resistance loads of $R_L^{opt} = 29.10$ kΩ and $R_L^{opt} = 53.10$ kΩ, for excitation at the SC and OC resonance frequencies, respectively. The same amount of peak power (i.e., 5.9 mW) is also obtained from Fig. 2.19(b) for the case of series connection, but at optimum resistance loads of $R_L^{opt} = 1.84$ MΩ and $R_L^{opt} = 3.42$ MΩ for the SC and OC excitations, respectively. Therefore, the amounts of power output for these resistive loads are identical for excitation at the SC and the OC resonance frequency, as well as for the parallel and the series connections, separately.

In Fig. 2.19, the relative motion frequency response of the central part of the 8-beam harvester (i.e., the proof masses) is plotted for different values of R_L, for both parallel and series configurations. Although the relative motion response can be obtained for any point throughout the volume of the proposed layout, the motion of the central part of the layout is of particular interest since it is the position of the maximum transverse displacement when the system oscillates due to applying the base excitation. Therefore, the vibratory motion of the central part of the PVEH device plays an important role while deciding on the volume of the proposed energy scavenger. Fig. 2.19 represents that there are significant variations around the

resonance frequencies extracted from the plots corresponded to different resistance loads. However, the same SC and OC resonance frequency behaviors (62.7 Hz and 68.8 Hz, respectively) are observed. According to the figure, as the value of resistance load increases from $10^2\Omega$ to $10^5\Omega$ for the parallel configuration (and from $10^2\Omega$ to $10^6\Omega$, for the series configuration), the vibration amplitude decreases remarkably, and when R_L is further increased to $10^8\Omega$, the amplitude of vibration starts increasing sharply. Thus, it can be concluded that the dynamic response of the PVEH system is highly influenced by variation of load resistance, and the vibration amplitude does not necessarily represent a monotonic behavior with increasing or decreasing the value of load resistance, as was also seen in the plots corresponding to the voltage/current output.

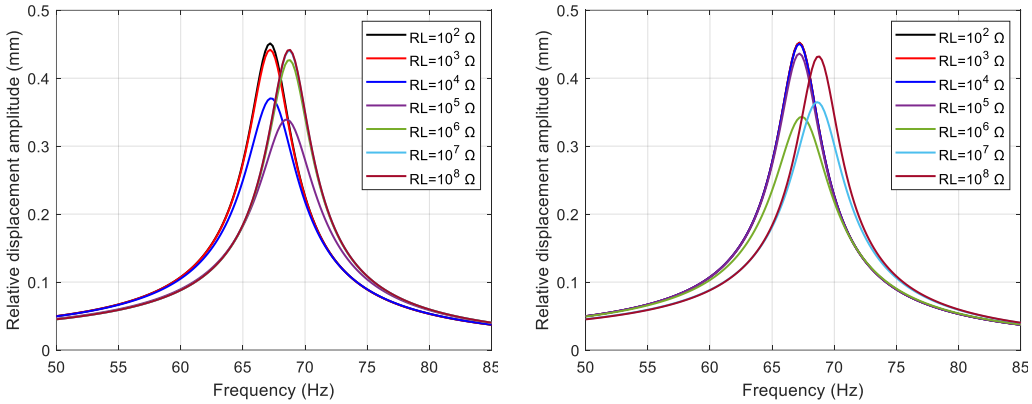

(a) Parallel connection (b) Series connection

Fig. 2.19: Relative displacement response to base excitation for the 8-beam layout

2.5.2.3 Effect of Proof Masses

Generally speaking, proof masses are used in PVEH designs to match the resonance frequency of the harvester to that of ambient vibration available at the selected application. It also helps increasing the power output of the scavenger by increasing the amplitude of oscillation, which raises the level of mechanical strain induced in the active layers. In this subsection, to have a better understanding of the proof mass effect, the voltage and power frequency response are plotted in Fig. 2.20, for the 8-beam PVEH system without/with proof masses having different thicknesses. Note

that a sample value of load resistance, equal to $R_L = 10^5\Omega$, is used here to obtain the voltage and power response. However, one can simply observe from the figure that the resonance frequency of the scavenger as well as the corresponding peak voltage/power in the obtained plots are significantly influenced by changing the thickness of the proof masses. In absence of the proof masses, the proposed structure has a resonance frequency of 353.5 Hz and produces a maximum power of 23.2 μW. As expected, equipping the energy harvester with proof masses leads to a PVEH device with lower resonance frequency and higher output power. In particular, when the energy scavenger is equipped with the proof masses of 5 mm thickness, its resonance frequency reduces to 68.5 Hz, and its peak power touches the value of 5.3 mW, which is much more than that of the same harvester without proof masses.

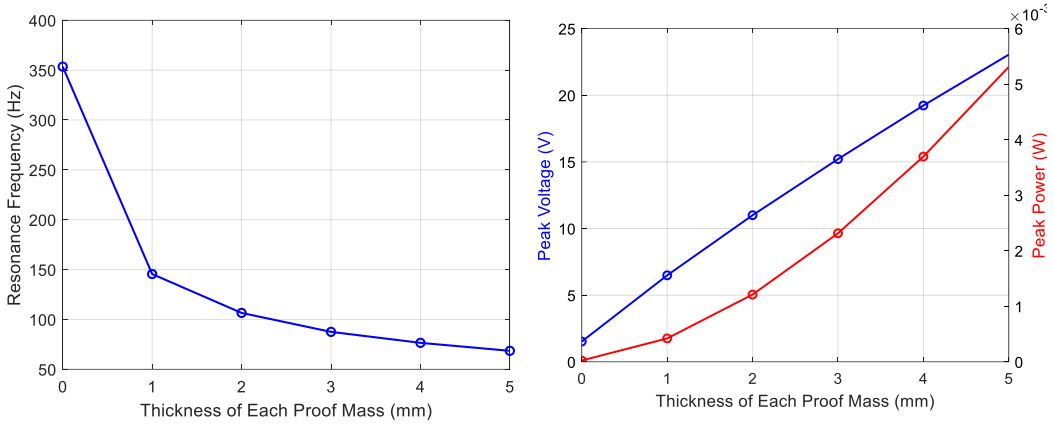

(a) (b)

Fig. 2.20: Variation of resonance frequency and electric outputs of the 8-beam harvester versus the thickness of proof masses ($R_L = 10^5\Omega$, Excitation amplitude $= 0.4g$)

2.5.2.4 Effect of Selected Materials

In this subsection, the effect of materials used for the proof masses and the PZT patches on the performance of the energy scavenger is investigated. Note that in the analyses performed in this subsection, the material of the substrate structure is kept constant as Aluminum, and the dimensions of the Steel proof masses are also kept constant and are considered according to Table 2.3. A load resistance of $R_L = 10^5\Omega$ is also adopted to measure the voltage and power outputs.

First, Bronze, Steel, Titanium and Aluminum are separately assigned to the proof masses in the FE COMSOL models developed for the 8-beam PVEH structure, and the corresponding voltage and power outputs are computed and presented in Fig. 21. Note that in this comparison example, PZT-5A is adopted as the material of the PZT patches. However, as seen from Fig. 2.21, for the proof masses made of Bronze, the scavenger generates the highest power output, that is 6.7 mW, at a resonance frequency of approximately 63.8 Hz. In another comparison example, while keeping constant the materials the proof masses (which is Steel), the voltage and power frequency response of the PVEH system are plotted in Fig. 2.22 for different materials of the PZT patches such as PZT-2, PZT-4, PZT-5H and PZT-5A. Among the systems made of the adopted piezoelectric materials, the one having PZT-5A patches exhibits the lowest resonance frequency (68.6 Hz) while giving the highest peak power (5.3 mW), when the same base excitation is applied to the PVEH device.

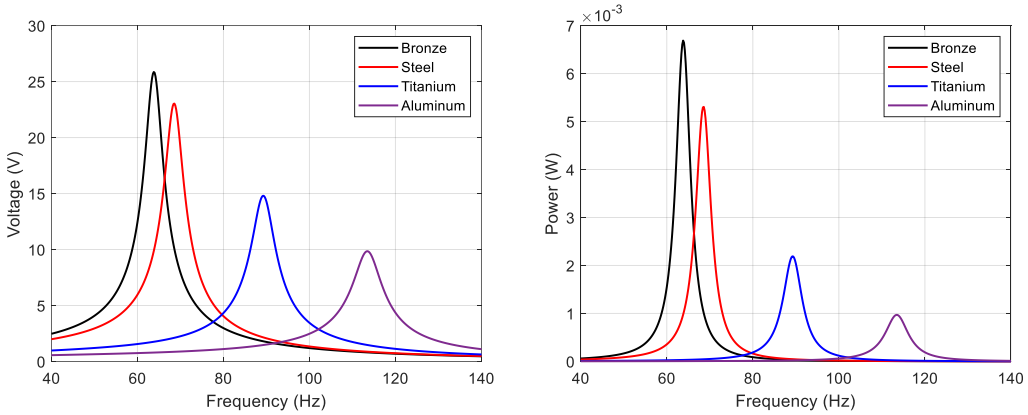

Fig. 2.21: Voltage and power frequency response for the 8-beam layout with different materials assigned to the proof masses ($R_L = 10^5\Omega$, base acceleration $= 0.4g$)

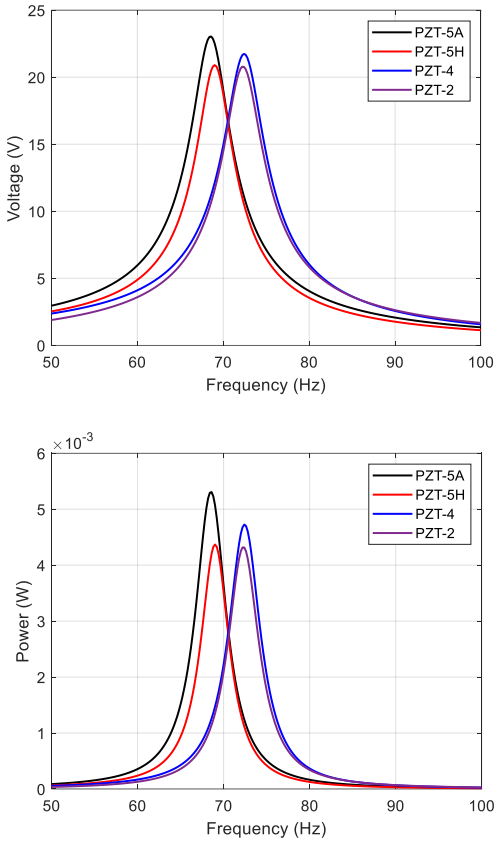

Fig. 2.22: Voltage and power frequency response for the 8-beam layout with different materials assigned to the PZT patches ($R_L = 10^5\Omega$, base acceleration $= 0.4g$)

2.5.2.5 Effect of Shape of the Unimorph Beams

This last investigation is concerned with the effect of the shape of the unimorph beams on the dynamic behavior and the electric response of the proposed multi-beam PVEH system. Using trapezoidal beams instead of rectangular beams in the proposed layout, various designs including 8, 10 and 12 smart beams as well as the case of a pure PZT-5A disc with Steel proof masses at the middle are considered and investigated here. These layouts are shown in Fig. 2.23, and their geometrical properties are given in Tables 2.9 and 2.10. Note that all the considered designs are clamped at their outer edges, so that when the base acceleration is applied to each of the systems, the proof masses can oscillate transversely.

Table 2.9: Geometrical properties of Designs 1, 2 and 3 presented in Figs. 2.23(a-c)

PVEH system	Design 1	Design 2	Design 3
Number of the trapezoidal beams	8	10	12
Side length of the central part a (mm)	10	10	10
Length of the Aluminum substrate L_b (mm)	40	40	40
Length of the PZT-5A patches L_p (mm)	32	34	32
Inner width of the substrate beams b_{ib} (mm)	7	7	7
Inner width of the PZT patches b_{ip} (mm)	13.3	15.575	14.35
Outer width b_o (mm)	38.5	31.5	28
Thickness of the Aluminum substrate h_b (mm)	0.3	0.3	0.3
Thickness of the PZT-5A patches h_p (mm)	0.3	0.3	0.3
Thickness of the Steel proof masses h_m (mm)	7	7	7

Table 2.10: Geometrical properties of the pure PZT disc presented in Fig. 2.23(d)

Parameter	
Radius of the PZT-5A disc (mm)	60
Thickness of the PZT-5A disc (mm)	0.3
Radius of the Steel proof masses (mm)	19
Thickness of the Steel proof masses (mm)	7

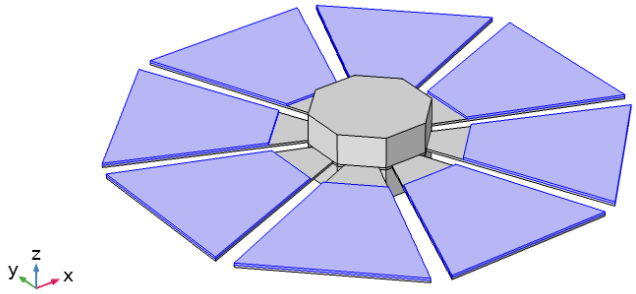

(a) Design 1: 8-beam layout with trapezoidal shape

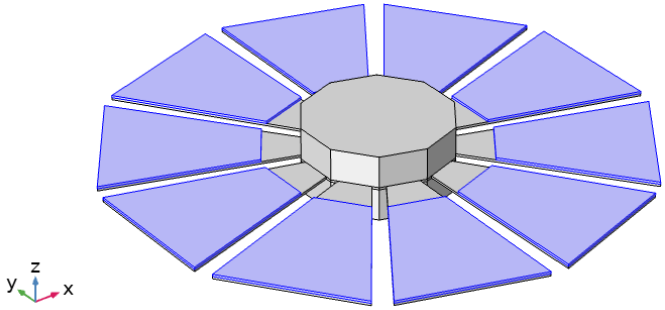

(b) Design 2: 10-beam layout with trapezoidal shape

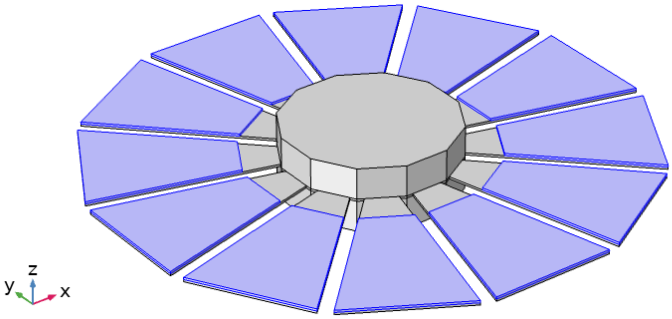

(c) Design 3: 12-beam layout with trapezoidal shape

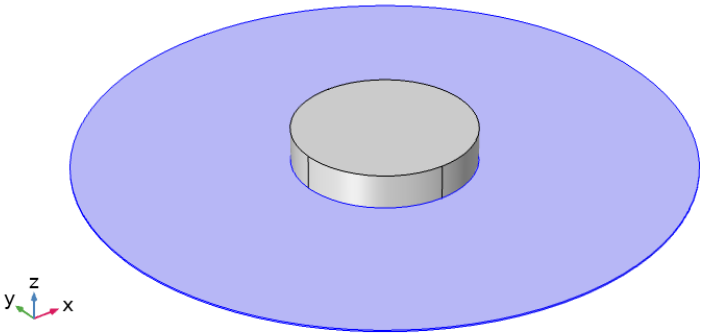

(d) Pure PZT-5A disc with Steel proof masses in the middle

Fig. 2.23: The proposed layout with trapezoidal unimorph beams and the pure PZT disc with proof masses at the middle

Frequency-domain studies are performed in COMSOL for the layouts presented in Fig. 2.23, and the corresponding vibration and electric outputs are obtained and given in Table 2.11. From the table, it is realized that the more beams are used in the proposed PVEH system the lower resonance frequency has the smart device and the higher power density is achieved. It is also concluded that, for the fixed harmonic base excitation of $0.4g$, the power densities provided by Designs 1, 2 and 3 are much higher than that of the considered pure PZT disc.

Table 2.11: Resonance frequencies and electric outputs of the systems presented in Fig. 2.23

Design property	Design 1	Design 2	Design 3	Pure PZT disc
Resonance frequency (Hz)	106.6	88.4	77.8	43.35
Total volume (mm^3)	11078	15149	20512	18921
Total volume of the PZT patches (mm^3)	1989	1835.9	1982	3052.3
Maximum power output (mW)	1.83	3.76	6.35	65.29×10^{-3}
Power density 1 ($\mu W/mm^3$)	0.17	0.25	0.31	0.003
Power density 2 ($\mu W/mm^3$)	0.92	2.05	3.20	0.021

Power density 1 = Peak power per total volume of the energy harvester

Power density 2 = Peak power per total volume of the PZT patches

Last but not least, it must be noted that all the analyses performed in the previous subsections assumed that the excitation amplitude is not large enough to cause failure in any of the studied PVEH systems. It is well known that the piezoceramic materials such as PZT-5A are very brittle compared to the classical engineering materials such as Aluminum and Steel. As reported in [135], the PZT-5A commercial product has an ultimate tensile strength of about 140 MPa and a fatigue strength of 55 MPa, at 5×106 cycles. Besides, Aluminum exhibits an ultimate tensile strength of about 483 MPa [136]. Because the maximum stress reached at the resonance frequency of any of those layouts was calculated and observed to be less than 20 MPa, both PZT-5A and Aluminum elements in the studied systems exhibit high safety factors, which ensures safe operation of the proposed devices in practice.

2.6 Summary and Conclusions

In this chapter, analytical and numerical energy harvesting models were first developed for a unimorph cantilevered beam. Then, a novel multi-beam energy scavenger composed of several of that unimorph, and two identical proof masses was introduced, aiming to propose a scavenger with a resonance frequency of less than 100 Hz, still capable of providing high power density. For the case of harmonic base excitation, the performance of both PVEH systems was investigated through conducting comprehensive parametric studies. The existence of strain nodes was identified in the fundamental mode of the new structure; therefore, preliminary optimization studies were performed to efficiently equip the system with the PZT patches, and consequently, to avoid any voltage cancellation. The results demonstrated that this new multibeam harvester offers high flexibility in matching its resonance frequency to that of a target application, simply by changing the number/shape of the smart beams or altering the proof masses used to design the structure. It was also found that increasing the number of the smart beams significantly improves the electric outputs and reduces the resonance frequency of the scavenger. Under the same base excitation, the novel harvester was able to generate a power density of up to six times greater than that of the simple unimorph. Finally, among all those cases studied in previous section, the 8-beam structure demonstrated the lowest resonance frequency and could generate several milliwatts of power across its optimum load resistance, when a harmonic base acceleration of 0.4g as applied.

Chapter 3

Kinetic Energy Harvesting Via Piezoelectric Bimorph Plates

3.1 Overview

As an alternative to piezoelectric cantilevers, plate-like energy harvesters can be much more effective in marine, aerospace, and automotive applications. For instance, they can be used for energy generation from pressure sources. This chapter is concerned with exact electromechanical modelling and analysis of piezoelectric bimorph plate energy harvesters with substrates made of either homogenous or porous materials. For the case of plate harvester with porous substrate, three different porosity distributions across the thickness of the core layer are inspected, and the piezoelectric layers are considered to be wired in both parallel and series configurations. Rayleigh damping assumptions are also used to model the structural damping of the harvesting system. The energy harvesting model of the plate harvester is established based on the conventional shear deformation plate theories, and through the use of Hamilton's principle and Gauss's law. Such theories allow for consideration of transverse shear deformations, therefore, deriving a highly accurate model that can be used for analysis of relatively-thick and thick plate-like

piezoelectric harvesters. An analytical solution is then applied to the governing equations, and closed-form steady-state response expressions are obtained for the voltage, current and power outputs as the scavenger response to harmonic excitation. Comparing the present results with some available in the literature, the proposed model is validated, and extensive parametric studies are then presented. The effects of design parameters such as the electrical load, porosity characteristics and geometrical parameters are studied in detail, and the results are presented with an eye toward guidelines for design of useful energy harvesting structures to be used in various applications.

3.2 State of the Art

The theory behind cantilever-type piezoelectric scavengers is clear, but the plate-like piezoelectric harvesters, which can be used in many applications such as energy generation from pressure sources, is not yet fully developed, and only very few studies (dealing with plate harvesters) are available in the literature. For instance, Kim et al. [137] studied power generation via a pressure-loaded unimorph circular plate harvester with clamped boundaries and investigated the effects of electrode patterns and the thickness ratio on the energy generation of the harvester. They also validated the results through experimental studies [138]. Junior et al. [136] used the Generalized Hamilton's principle to develop an electromechanical finite element model based on Kirchhoff theory for the piezoelectric energy harvester plates. A bistable composite plate having piezoelectric patches was proposed and investigated by Arrieta et al. [139] to be used for broadband nonlinear energy harvesting. A detailed analysis was performed by Solovyev and Duong [140] for optimization of bimorph piezoelectric circular plate energy harvesters through a reduced order finite element analysis. Abadi et al. [141] developed analytical solutions by means of Classical plate theory and Rayleigh-Ritz method for the analysis of annular sectorial piezoelectric plate harvesters made of elastic substrates integrated with piezoelectric layers. Vibration energy harvesting via a disk-type piezoelectric bimorph structure was studied by Darabi et al. [142]. The bimorph disk with free edge conditions was mounted on a vibrating base from its center, and the focus was placed on the fundamental axisymmetric vibration mode for energy

harnessing. Using the classical laminate plate theory, an exact analytical solution was presented by Paknejad et al. [143] for a piezoelectric patch energy harvester attached to a thin multilayer orthotropic composite plate. The author then used finite element analysis in ANSYS for the verification of their proposed analytical model. Yoon et al. [144] proposed an electromechanically-coupled analytical model based on Kirchhoff plate theory for a rectangular surface-bonded piezoelectric energy harvesting skin considering the inertia and stiffness effects. Shukla and Pradyumna [145] proposed a variable stiffness composite laminate (VSCL) bimorph energy harvester, used the first-order shear deformation theory to establish the respective energy harvesting model, and extracted the results through the use of the finite element method.

Recently, piezoelectric energy harvesters with elements containing porosities are introduced by several researchers [45–53,146,147], aiming to improve the respective voltage/power generation. Porosity, either closed or open, is a characteristic that strongly defines the properties of a given material, such as its density and stiffness. A properly engineered porous material, for instance, can provide the same performance as its bulk counterpart, but for a fraction of the weight, which is crucial for its use in applications where lightweight is a concern. Martínez-Ayuso et al. [50] developed an analytical model of impact energy harvester consisting of a cantilever beam with integrated porous piezoelectric patches. The material chosen to extract the energy was porous PZT, a composite material made of two phases: air and PZT. Very recently, Moradi-Dastjerdi and Behdinan [147] proposed a bridge-type piezoelectric energy harvester made of an advanced porous nanocomposite substrate activated by two piezoceramic layers. The results of their study demonstrated that embedding pores into the substrate layers leads to higher deflection/voltage peaks and consequently higher power generation. A lumped parameter model was used by Mahesh [53] to represent the dynamic behavior of a multifunctional composite harvester consisting of functionally graded materials with porosities.

To the best of authors' knowledge, so far, highly different modeling approaches have appeared in the literature of vibration energy harvesting for piezoelectric beam-based harvesters while plate-like scavengers are rarely investigated despite their broad applications. Even though piezoelectric energy

harvesters are usually designed and manufactured as thin structures for larger flexibility and larger power, there might be need to use configurations where the structure might have moderate thickness (e.g., due to the limitations in the active material dimensions) where the shear deformation and the rotary inertia effects are pronounced. However, considering the issues in the existing literature, there seems to be an urgent need to develop reliable piezoelectric energy harvester models that can be used for analysis of thin, moderately thick, and thick plate-like scavengers. In this chapter, it is therefore aimed to use the higher-order shear deformation theories to develop a comprehensive analytical energy harvesting model for the bimorph plate harvesters. Another objective is to study the effect of utilizing porous substrates on the performance of piezoelectric energy harvesters. To that end, the case of plate harvester with substrate containing porosities is also considered, and three different porosity patterns are inspected for the distribution of internal pores. If not all, most of the previous works dealing with the analysis of porous plate structures have been focused on the problems of free vibration, bending, and buckling analysis [148–157], and a distinct lack of comprehensive studies on analyzing porous piezoelectric plate harvesters is observed. However, the electromechanical governing equations of the harvester are derived for both parallel and series connections between the piezoelectric layers. The obtained equations are then solved analytically, and closed-form steady-state response expressions are derived for the coupled electrical outputs and the structural vibration response. Finally, the model is validated, and the effects of a wide range of design parameters are studied in detail.

3.3 Bimorph Plate Harvester

Consider a rectangular bimorph plate harvester with two identical piezoelectric layers, as shown in Fig. 3.1. In the figure, a, b, $2h$ and h_p indicate the length, width, substrate thickness, and the thickness of each piezoelectric layer, respectively. The piezoelectric layers are assumed to cover all the surface of the substrate and to be poled along the thickness direction. Therefore, the d_{31} mode of piezoelectric materials is here utilized for the conversion of vibratory energy. The electrodes covering the opposite faces of piezoelectric layers are assumed to be very thin when

compared to the overall thicknesses of the plate harvester so that their contribution to the thickness dimension is negligible. The origin of the reference coordinate system is located on the neutral surface of the plate (at $z = 0$). Once the smart plate is subjected to external excitations (here along z-direction), mechanical strain is induced inside the smart layers, which is then converted into an electric charge distribution so that inducing an electric field between the electrodes connected to the smart layers. Deformations are assumed to be small, and the composite structure exhibits linear-elastic material behavior. Both parallel and series connections between the piezoelectric layers are considered (see Fig. 3.2), and the electrodes are assumed to be connected to an external resistive load R_L. The condition of having a pure resistive load, although not necessarily the most realistic one (electric load often consists of rechargeable batteries or other capacitive loads), is very useful for an immediate comparison of the harvested power levels [158]. In Fig. 3.2, $V(t)$ represents the electric voltage across the resistive load, which is applied to the piezoelectric layers. From the viewpoint of electrical engineering, it is often required to convert the alternating voltage output to a constant voltage using a rectifier bridge (AC-to-DC converter) and a smoothing capacitor in order to reach a constant level of voltage for charging a small battery or a capacitor using the harvested energy. Since the voltage levels for charging batteries and capacitors are not arbitrary, it is usually required to use a DC-to-DC converter (step-up or step-down) in order to regulate the rectified voltage output of the piezoceramic according to the voltage requirement of the specific charging application. These electrical engineering and power electronics aspects are beyond the scope of this work and the relevant electrical engineering work can be found in the literature.

It is assumed that the electrodes covering the piezoelectric layers are perfectly conductive so that the electric potential is only dependent on z-coordinate and time t and has no dependency on the in-plane coordinates. Moreover, due to the small thickness of piezoelectric layers in practical cases, the electric potential in the thickness direction can be assumed to have linear distribution. In the case of parallel configuration, the inner electrodes (i.e., at $z = \pm h$) are assumed to be connected to a Ground node while the outer electrodes of both piezoelectric layers (i.e., at $z = \pm\left(h + h_p\right)$) are connected to a single terminal node. Thus, in this case, the electric potential may have the following form:

$$\phi_p(x,y,z,t) = \begin{cases} +\dfrac{V(t)}{h_p}(z-h), & +h \le z \le +h+h_p \\ -\dfrac{V(t)}{h_p}(z+h), & -h-h_p \le z \le -h \end{cases} \tag{3.1}$$

On the other hand, for the case of series configuration, the electric potential function may have the form of:

$$\phi_s(x,y,z,t) = \begin{cases} \dfrac{V(t)}{2h_p}(z-h), & +h \le z \le +h+h_p \\ \dfrac{V(t)}{2h_p}(z+h), & -h-h_p \le z \le -h \end{cases} \tag{3.2}$$

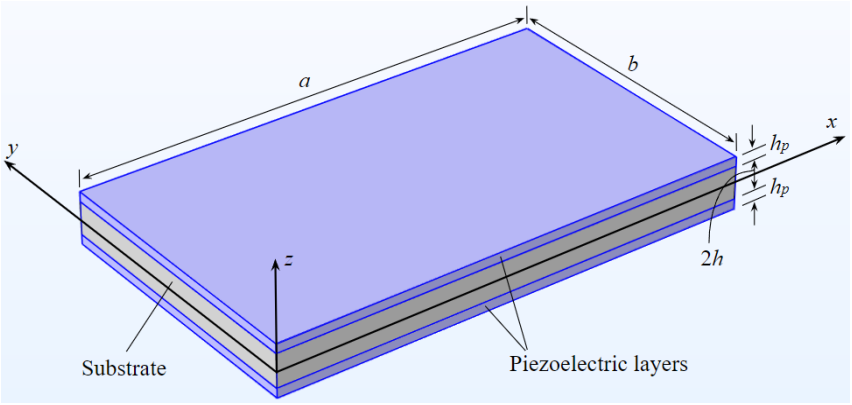

Fig. 3.1: 3D sketch of the piezoelectric bimorph plate harvester

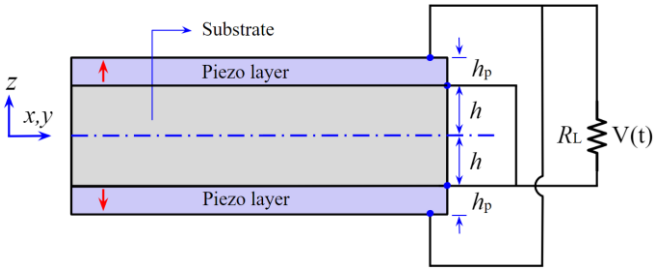

(a)

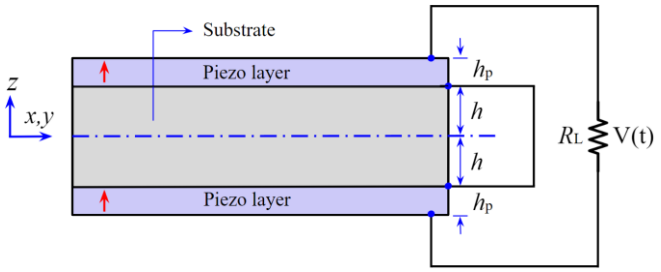

(b)

Fig. 3.2: Cross section of the bimorph harvester with (a) parallel and (b) series connections (red arrays show the polarization directions)

Considering the relation between electric potential function ϕ and electric field $\vec{E}$ (i.e., $\vec{E} = -\vec{\nabla}\phi$ where $\vec{\nabla}$ is the gradient vector), one can simply derive (from Eqs. (3.1) and (3.2)) the only non-zero component of electric field for both types of electrical configurations, as follows:

For parallel connection:

$$E_z(t) = \begin{cases} -\dfrac{V(t)}{h_p}, & +h \le z \le +h + h_p \\ +\dfrac{V(t)}{h_p}, & -h - h_p \le z \le -h \end{cases} \tag{3.3}$$

For series connection:

$$E_z(t) = \begin{cases} -\dfrac{V(t)}{2h_p}, & +h \le z \le +h + h_p \\ -\dfrac{V(t)}{2h_p}, & -h - h_p \le z \le -h \end{cases} \tag{3.4}$$

On the other hand, the substrate layer is considered to be made of either homogenous metals (such as Aluminum, Steel, Bronze etc.) or materials containing porosities (such as cellular Aluminum etc.), according to the *symmetric* profiles (*Pattern* I, *Pattern* II, and *Pattern* III) given in Fig. 1.10 of Chapter 1. Therefore, the material properties in this layer (when it contains porosities) vary through the thickness direction, as were already defined in Eqs. (1.17) to (1.20) in Chapter 1. Note that for a given porosity, the masses of the three types of porous substrates are

equal, and is however less than that of the homogenous substrate. It is also important to note that due to both geometrical and material symmetry along the z-axis (with respect to the mid-plane of the plate), the neutral surface of the bimorph plate is located on the mid-plane (i.e., at $z = 0$).

3.4 Governing Equations

3.4.1 Governing Equations in Physical Coordinates

3.4.1.1 Displacement Model and Constitutive Equations

Both the first-order (so-called FSDT) and the third-order shear deformation theories (so-called TSDT) are employed here, to derive the governing equations of the plate harvester. The components of the mechanical displacement filed can therefore be expressed as:

$$\begin{aligned} U_x(x,y,z,t) &= u_0 + z\psi_x - \alpha z^3\left(\psi_x + w_{0,x}\right) \\ U_y(x,y,z,t) &= v_0 + z\psi_y - \alpha z^3\left(\psi_y + w_{0,y}\right) \\ U_z(x,y,z,t) &= w_0 \end{aligned} \tag{3.5}$$

where U_x, U_y and $U_z(x,y,z,t)$ are the components of total displacement at any point of the smart plate along x-, y- and z-direction, respectively. Also, u_0, v_0, w_0, ψ_x and $\psi_y(x,y,t)$ are displacements and rotations of the mid-plane of the plate. The coefficient α must be set to zero for the case of FSDT ($\alpha = 0$), while it equals to $\alpha = 4/[3h_t^2]$ for the TSDT case (h_t is the total thickness of the bimorph harvester and equals to $h_t = 2h + 2h_p$). Here and hereafter, all the mathematical formulations and expressions are first derived based on the model given in Eq. (3.5), and later the values corresponding to FSDT or TSDT will be assigned to this parameter for the computation of numerical results. it is however easy to set $\alpha = 0$ in the following mathematical expressions and equations, to simplify them for the case of FSDT.

Considering Eq. (3.5), the linear strain components ε_{ij}'s, are obtained as:

$$\varepsilon_{xx} = u_{0,x} + z\psi_{x,x} - \alpha z^3\left(\psi_{x,x} + w_{0,xx}\right) \tag{3.6}$$

$$\varepsilon_{yy} = v_{0,y} + z\psi_{y,y} - \alpha z^3\left(\psi_{y,y} + w_{0,yy}\right)$$
$$\gamma_{xy} = u_{0,y} + v_{0,x} + z\left(\psi_{x,y} + \psi_{y,x}\right) - \alpha z^3\left(\psi_{x,y} + \psi_{y,x} + 2w_{0,xy}\right)$$
$$\gamma_{xz} = (1 - 3\alpha z^2)\left[\psi_x + w_{0,x}\right]$$
$$\gamma_{yz} = (1 - 3\alpha z^2)\left[\psi_y + w_{0,y}\right]$$

According to the linear elasticity, the constitutive equations of the porous materials (in which the pores are free of fluid) simply obey the Hooke's law, as was already discussed for FGMs in Eqs. (1.11) to (1.13) in Chapter 1. However, due to the consideration of a shear correction factor in the models based on FSDT, such constitutive equations are rewritten here, as:

$$\begin{aligned}
\sigma_{xx} &= Q_{11}\varepsilon_{xx} + Q_{12}\varepsilon_{yy} \\
\sigma_{yy} &= Q_{21}\varepsilon_{xx} + Q_{11}\varepsilon_{yy} \\
\sigma_{yz} &= {K_s}^2 Q_{44}\gamma_{yz} \\
\sigma_{xz} &= {K_s}^2 Q_{55}\gamma_{xz} \\
\sigma_{xy} &= Q_{66}\gamma_{xy}
\end{aligned} \tag{3.7}$$

in which ${K_s}^2$ denotes the shear correction factor that has to be considered in FSDT-based analyses, for vanishing the shear stresses on the outer surfaces of the plate. In this study, the value of this coefficient is assumed to be ${K_s}^2 = 5/6$ [150] for the case of FSDT. However, TSDT does not require any shear correction factor, therefore, setting ${K_s}^2 = 1$ in Eq. (3.7) for this case. Note that the expressions related to Q_{ij}'s were given earlier in Eq. (1.13).

On the other hand, since the piezoelectric layers are assumed to be polarized through the thickness direction (z-direction), the respective electromechanically-coupled stress-strain relations are considered based on Eq. (1.4). However, considering $\sigma_{zz} = 0$, and applying such assumption to Eq. (1.4), the piezoelectric constitutive equation can be expressed as:

$$\begin{aligned}
\sigma_{xx} &= \bar{C}_{11}\varepsilon_{xx} + \bar{C}_{12}\varepsilon_{yy} - \bar{e}_{31}E_z \\
\sigma_{yy} &= \bar{C}_{12}\varepsilon_{xx} + \bar{C}_{11}\varepsilon_{yy} - \bar{e}_{31}E_z \\
\sigma_{yz} &= {K_s}^2 C_{44}\gamma_{yz}
\end{aligned} \tag{3.8}$$

$$\sigma_{xz} = {K_s}^2 C_{55}\gamma_{xz}$$
$$\sigma_{xy} = C_{66}\gamma_{xy}$$
$$D_x = e_{15}\gamma_{xz}$$
$$D_y = e_{15}\gamma_{yz}$$
$$D_z = \bar{e}_{31}\varepsilon_{xx} + \bar{e}_{31}\varepsilon_{yy} + \bar{\Xi}_{33}E_z$$

in which $\bar{C}_{11}$, $\bar{C}_{12}$, $\bar{e}_{31}$ and $\bar{\Xi}_{33}$ are the reduced coefficients and are given as:

$$\bar{C}_{11} = C_{11} - \frac{{C_{13}}^2}{C_{33}}, \bar{C}_{12} = C_{12} - \frac{{C_{13}}^2}{C_{33}}, \bar{e}_{31} = e_{31} - \frac{C_{13}e_{33}}{C_{33}}, \bar{\Xi}_{33} = \Xi_{33} + \frac{{e_{33}}^2}{C_{33}} \tag{3.9}$$

In the following subsections, the energy harvesting model of the bimorph plate is established by means of both Hamilton's principle and the integral form of Gauss's law.

3.4.1.2 Hamilton Principle

The Hamilton's principle for the present problem is of the form:

$$\delta U + \delta\Omega = 0 \tag{3.10}$$

where δ is the variational operator, and U and Ω represent the strain energy of the smart plate and the potential energy of the external loads, respectively. In Eq. (3.10), the terms δU and $\delta\Omega$ can be obtained with the help of the definition of strain energy and the virtual work done by the applied loads. However, using Eq. (3.10), the electromechanical equations of motion of the plate harvester are derived based on the displacement filed given in Eq. (3.5) and are expressed as:

$$N_{xx,x} + N_{xy,y} = I_0\ddot{u}_0 + J_1\ddot{\psi}_x - \alpha I_3\ddot{w}_{0,x} \tag{3.11a}$$
$$N_{xy,x} + N_{yy,y} = I_0\ddot{v}_0 + J_1\ddot{\psi}_y - \alpha I_3\ddot{w}_{0,y} \tag{3.11b}$$
$$M_{xx,x} + M_{xy,y} - Q_{xz} - \alpha\left(P_{xx,x} + P_{xy,y}\right) + 3\alpha R_{xz} = J_1\ddot{u}_0 + K_1\ddot{\psi}_x - \alpha J_4\ddot{w}_{0,x} \tag{3.11c}$$

$$M_{xy,x} + M_{yy,y} - Q_{yz} - \alpha\left(P_{xy,x} + P_{yy,y}\right) + 3\alpha R_{yz} = J_1\ddot{v}_0 + K_1\ddot{\psi}_y - \alpha J_4\ddot{w}_{0,y} \tag{3.11d}$$

$$Q_{xz,x} + Q_{yz,y} + \alpha\left(P_{xx,xx} + 2P_{xy,xy} + P_{yy,yy}\right) - 3\alpha\left(R_{xz,x} + R_{yz,y}\right) + F_z(t) = I_0\ddot{w}_0 - \alpha^2 I_6\left(\ddot{w}_{0,xx} + \ddot{w}_{0,yy}\right) + \alpha I_3\left(\ddot{u}_{0,x} + \ddot{v}_{0,y}\right) + \alpha J_4\left(\ddot{\psi}_{x,x} + \ddot{\psi}_{y,y}\right) \tag{3.11e}$$

In Eq. (3.11), $F_z(t)$ is the mechanical load intensity per unit area. Moreover, N_{ij}, M_{ij}, P_{ij}, Q_{ij} and R_{ij} are the stress resultants, and I_i and J_k are the inertia terms, with the following definitions:

$$\left\{N_{ij}, M_{ij}, P_{ij}\right\} = \int_{-h-h_p}^{+h+h_p} \sigma_{ij}\{1, z, z^3\}\, dz\,, \qquad ij = (xx, xy, yy)$$

$$\left\{Q_{ij}, R_{ij}\right\} = \int_{-h-h_p}^{+h+h_p} \sigma_{ij}\{1, z^2\}\, dz\,, \qquad ij = (xz, yz)$$

$$\{I_0, I_1, I_2, I_3, I_4, I_6\} = \int_{-h-h_p}^{+h+h_p} \{1, z, z^2, z^3, z^4, z^6\}\, \rho(z)\, dz$$

$$\{J_1, J_4\} = \{I_1, I_4\} - \alpha\{I_3, I_6\}, \quad K_1 = I_2 - 2\alpha I_4 + \alpha^2 I_6 \tag{3.12}$$

Here, the higher-order stress resultants P_{ij} and R_{ij} are observed in Eqs. (3.11c) to (3.11e) since the motion equations of the system are derived based on the model given in Eq. (3.5). However, in the motion equations, the terms including P_{ij} and R_{ij} would vanish for the case of FSDT, as is simply observed by setting $\alpha = 0$.

Substituting the stress fields of both porous and piezoelectric materials (given in Eqs. (3.7) and (3.8)) into Eqs. (3.12), one can simply rewrite the stress resultants in terms of the unknowns of the displacement field (u_0,v_0,ψ_x,ψ_y,w_0) as well as the electric voltage $V(t)$, as:

$$N_{xx} = a_{11}^N u_{0,x} + a_{12}^N v_{0,y} + b_{11}^N \psi_{x,x} + b_{12}^N \psi_{y,y} + f_{11}^N w_{0,xx} + f_{12}^N w_{0,yy} + \alpha_N V(t)[H(x) - H(x-a)][H(y) - H(y-b)]$$

$$N_{yy} = a_{12}^N u_{0,x} + a_{11}^N v_{0,y} + b_{12}^N \psi_{x,x} + b_{11}^N \psi_{y,y} + f_{12}^N w_{0,xx} + f_{11}^N w_{0,yy} + \alpha_N V(t)[H(x) - H(x-a)][H(y) - H(y-b)]$$

$$
\begin{aligned}
N_{xy} &= a_{66}^{N}\left(u_{0,y}+v_{0,x}\right)+b_{66}^{N}\left(\psi_{x,y}+\psi_{y,x}\right)+f_{66}^{N}w_{0,xy}\\
M_{xx} &= a_{11}^{M}u_{0,x}+a_{12}^{M}v_{0,y}+b_{11}^{M}\psi_{x,x}+b_{12}^{M}\psi_{y,y}+f_{11}^{M}w_{0,xx}+f_{12}^{M}w_{0,yy}\\
&\quad+\alpha_{M}V(t)[H(x)-H(x-a)][H(y)-H(y-b)]\\
M_{yy} &= a_{12}^{M}u_{0,x}+a_{11}^{M}v_{0,y}+b_{12}^{M}\psi_{x,x}+b_{11}^{M}\psi_{y,y}+f_{12}^{M}w_{0,xx}+f_{11}^{M}w_{0,yy}\\
&\quad+\alpha_{M}V(t)[H(x)-H(x-a)][H(y)-H(y-b)]\\
M_{xy} &= a_{66}^{M}\left(u_{0,y}+v_{0,x}\right)+b_{66}^{M}\left(\psi_{x,y}+\psi_{y,x}\right)+f_{66}^{M}w_{0,xy}\\
P_{xx} &= a_{11}^{P}u_{0,x}+a_{12}^{P}v_{0,y}+b_{11}^{P}\psi_{x,x}+b_{12}^{P}\psi_{y,y}+f_{11}^{P}w_{0,xx}+f_{12}^{P}w_{0,yy}\\
&\quad+\alpha_{P}V(t)[H(x)-H(x-a)][H(y)-H(y-b)]\\
P_{yy} &= a_{12}^{P}u_{0,x}+a_{11}^{P}v_{0,y}+b_{12}^{P}\psi_{x,x}+b_{11}^{P}\psi_{y,y}+f_{12}^{P}w_{0,xx}+f_{11}^{P}w_{0,yy}\\
&\quad+\alpha_{P}V(t)[H(x)-H(x-a)][H(y)-H(y-b)]\\
P_{xy} &= a_{66}^{P}\left(u_{0,y}+v_{0,x}\right)+b_{66}^{P}\left(\psi_{x,y}+\psi_{y,x}\right)+f_{66}^{P}w_{0,xy}\\
Q_{xz} &= a_{55}^{Q}\left(\psi_{x}+w_{0,x}\right)\\
Q_{yz} &= a_{55}^{Q}\left(\psi_{y}+w_{0,y}\right)\\
R_{xz} &= a_{55}^{R}\left(\psi_{x}+w_{0,x}\right)\\
R_{yz} &= a_{55}^{R}\left(\psi_{y}+w_{0,y}\right)
\end{aligned}
\tag{3.13}
$$

Note that the above expressions will be later substituted into Eq. (3.11) to derive the electromechanical governing equations of the plate harvester, so that the electrical terms in Eq. (3.13) are already multiplied by $\Gamma(x,y)=[H(x)-H(x-a)][H(y)-H(y-b)]$ (where H is the Heaviside step function), to avoid the omission of the electrical terms when substituting the stress resultants into the motion equations. Moreover, the definition of the constant coefficients a_{ij}^{N}, a_{ij}^{M}, a_{ij}^{P}, b_{ij}^{N}, b_{ij}^{M}, b_{ij}^{P}, f_{ij}^{N}, f_{ij}^{M}, f_{ij}^{P}, a_{55}^{Q}, a_{55}^{R}, α_{N}, α_{M} and α_{P} are given in Relations (B.1) to (B.3) of Appendix B, for both parallel and series connections.

Substituting the stress resultants of Eq. (3.13) into Eq. (3.11) gives us the following governing equations:

$$a_{11}^N u_{0,xx} + a_{66}^N u_{0,yy} + (a_{12}^N + a_{66}^N) v_{0,yx} + b_{11}^N \psi_{x,xx} + b_{66}^N \psi_{x,yy} + (b_{12}^N + b_{66}^N) \psi_{y,yx} + f_{11}^N w_{0,xxx} + (f_{12}^N + f_{66}^N) w_{0,xyy} - I_0 \ddot{u}_0 - J_1 \ddot{\psi}_x + \alpha I_3 \ddot{w}_{0,x} = -\alpha_N V(t) \Gamma_{,x} \quad (3.14a)$$

$$(a_{66}^N + a_{12}^N) u_{0,xy} + a_{66}^N v_{0,xx} + a_{11}^N v_{0,yy} + (b_{66}^N + b_{12}^N) \psi_{x,xy} + b_{66}^N \psi_{y,xx} + b_{11}^N \psi_{y,yy} + (f_{66}^N + f_{12}^N) w_{0,yxx} + f_{11}^N w_{0,yyy} - I_0 \ddot{v}_0 - J_1 \ddot{\psi}_y + \alpha I_3 \ddot{w}_{0,y} = -\alpha_N V(t) \Gamma_{,y} \quad (3.14b)$$

$$(a_{11}^M - \alpha a_{11}^P) u_{0,xx} + (a_{66}^M - \alpha a_{66}^P) u_{0,yy} + (a_{12}^M + a_{66}^M - \alpha a_{12}^P - \alpha a_{66}^P) v_{0,xy} + \left(-a_{55}^Q + 3\alpha a_{55}^R\right) \psi_x + (b_{11}^M - \alpha b_{11}^P) \psi_{x,xx} + (b_{66}^M - \alpha b_{66}^P) \psi_{x,yy} + (b_{12}^M + b_{66}^M - \alpha b_{12}^P - \alpha b_{66}^P) \psi_{y,xy} + \left(-a_{55}^Q + 3\alpha a_{55}^R\right) w_{0,x} + (f_{11}^M - \alpha f_{11}^P) w_{0,xxx} + (f_{12}^M + f_{66}^M - \alpha f_{12}^P - \alpha f_{66}^P) w_{0,xyy} - J_1 \ddot{u}_0 - K_1 \ddot{\psi}_x + \alpha J_4 \ddot{w}_{0,x} = -(\alpha_M - \alpha \alpha_P) V(t) \Gamma_{,x} \quad (3.14c)$$

$$(a_{66}^M + a_{12}^M - \alpha a_{66}^P - \alpha a_{12}^P) u_{0,xy} + (a_{66}^M - \alpha a_{66}^P) v_{0,xx} + (a_{11}^M - \alpha a_{11}^P) v_{0,yy} + (b_{66}^M + b_{12}^M - \alpha b_{66}^P - \alpha b_{12}^P) \psi_{x,xy} + \left(-a_{55}^Q + 3\alpha a_{55}^R\right) \psi_y + (b_{66}^M - \alpha b_{66}^P) \psi_{y,xx} + (b_{11}^M - \alpha b_{11}^P) \psi_{y,yy} + \left(-a_{55}^Q + 3\alpha a_{55}^R\right) w_{0,y} + (f_{66}^M + f_{12}^M - \alpha f_{66}^P - \alpha f_{12}^P) w_{0,xxy} + (f_{11}^M - \alpha f_{11}^P) w_{0,yyy} - J_1 \ddot{v}_0 - K_1 \ddot{\psi}_y + \alpha J_4 \ddot{w}_{0,y} = -(\alpha_M - \alpha \alpha_P) V(t) \Gamma_{,y} \quad (3.14d)$$

$$\begin{aligned}
&\alpha a_{11}^{P} u_{0,xxx} + (2\alpha a_{66}^{P} + \alpha a_{12}^{P}) u_{0,xyy} + \alpha a_{11}^{P} v_{0,yyy} \\
&\quad + (\alpha a_{12}^{P} + 2\alpha a_{66}^{P}) v_{0,yxx} + \left(a_{55}^{Q} - 3\alpha a_{55}^{R}\right)\psi_{x,x} \\
&\quad + \alpha b_{11}^{P} \psi_{x,xxx} + (2\alpha b_{66}^{P} + \alpha b_{12}^{P})\psi_{x,xyy} \\
&\quad + \left(a_{55}^{Q} - 3\alpha a_{55}^{R}\right)\psi_{y,y} + (\alpha b_{12}^{P} + 2\alpha b_{66}^{P})\psi_{y,yxx} \\
&\quad + \alpha b_{11}^{P} \psi_{y,yyy} + \left(a_{55}^{Q} - 3\alpha a_{55}^{R}\right) w_{0,xx} \\
&\quad + \left(a_{55}^{Q} - 3\alpha a_{55}^{R}\right) w_{0,yy} + \alpha f_{11}^{P} w_{0,xxxx} \\
&\quad + (\alpha f_{12}^{P} + 2\alpha f_{66}^{P} + \alpha f_{12}^{P}) w_{0,yyxx} + \alpha f_{11}^{P} w_{0,yyyy} \\
&\quad - I_0 \ddot{w}_0 + \alpha^2 I_6 \left(\ddot{w}_{0,xx} + \ddot{w}_{0,yy}\right) - \alpha I_3 \left(\ddot{u}_{0,x} + \ddot{v}_{0,y}\right) \\
&\quad - \alpha J_4 \left(\ddot{\psi}_{x,x} + \ddot{\psi}_{y,y}\right) = -\alpha \alpha_P V(t) \left(\Gamma_{,xx} + \Gamma_{,yy}\right) - F_z(t)
\end{aligned} \tag{3.14e}$$

After deriving the set of equations (3.14) as the governing equations of the bimorph plate harvester, the last equation which should be determined is the electrical displacement equation.

3.4.1.3 Gauss's Law

The electric displacement equation coupled with the induced mechanical strain throughout the bimorph plate can be derived with the help of Gauss's law in integral form. Therefore, the generated charge $q(t)$ due to the induced deformation in the plate can be expressed as [29]:

$$\begin{aligned}
q(t) &= \iint_A \vec{D}.\vec{n}\, dA = \int_0^a \int_0^b D_z \, dxdy \\
&= \int_0^a \int_0^b \left(\bar{e}_{31}\varepsilon_{xx} + \bar{e}_{31}\varepsilon_{yy} + \bar{\Xi}_{33} E_z\right) dxdy
\end{aligned} \tag{3.15}$$

in which, $\vec{n}$ is the unit outward normal and A is the electrode surface area. One can simply obtain the electric current $I(t)$ delivered to the resistive load R_L as:

$$I(t) = \dot{q}(t) = \int_0^a \int_0^b \left(\bar{e}_{31}\dot{\varepsilon}_{xx} + \bar{e}_{31}\dot{\varepsilon}_{yy} + \bar{\Xi}_{33}\dot{E}_z\right) dxdy \tag{3.16}$$

Substituting the definition of the electric filed $E_z(t)$ for both parallel and series electrical configurations (given in Eq. (3.3)) and the expressions of ε_{xx} and ε_{yy} into Eq. (3.16), and finally using the Ohm's law yield the harvester circuit equation as follows:

$$\begin{aligned} C_0\dot{V}(t) + \frac{1}{\hat{R}_L}V(t) - \bar{e}_{31}\int_0^a\int_0^b \left(\dot{u}_{0,x} + \dot{v}_{0,y}\right) dxdy \\ - \bar{e}_{31}\hat{h}\int_0^a\int_0^b \left(\dot{\psi}_{x,x} + \dot{\psi}_{y,y}\right) dxdy \\ + \bar{e}_{31}\alpha\tilde{h}\int_0^a\int_0^b \left(\dot{\psi}_{x,x} + \dot{\psi}_{y,y} + \dot{w}_{0,xx} + \dot{w}_{0,yy}\right) dxdy \\ = 0 \end{aligned} \tag{3.17}$$

In Eq. (3.17), $\hat{R}_L$ denotes the equivalent resistance equal to $\hat{R}_L = R_L$ and $\hat{R}_L = 2R_L$ for series and parallel connections, respectively. Moreover, C_0 represents the equivalent capacitance, and is equal to $C_0 = \bar{\bar{\Xi}}_{33}ab/h_p$ and $C_0 = \bar{\bar{\Xi}}_{33}ab/2h_p$ for parallel and series connections, respectively. Note that $\hat{h}$ (which is equal to $\hat{h} = h + 0.5h_p$) and $\tilde{h}$ (which is equal to $\tilde{h} = \left[\left(h + h_p\right)^4 - h^4\right]/4h_p$) in Eq. (3.20) are generated due to averaging in the thickness direction [29].

3.4.2 Governing Equations in Modal Coordinates

Based on the standard modal analysis procedure, the vibration response of the rectangular plate harvester with simply-supported boundary conditions on its four edges can be represented as:

$$\begin{aligned} u_0(x,y,t) &= \frac{2}{\sqrt{ab}}\sum_{m=1}^{\infty}\sum_{n=1}^{\infty}\cos(\beta_m x)\sin(\beta_n y)\,\eta_{mn}^{u_0}(t) \\ v_0(x,y,t) &= \frac{2}{\sqrt{ab}}\sum_{m=1}^{\infty}\sum_{n=1}^{\infty}\sin(\beta_m x)\cos(\beta_n y)\,\eta_{mn}^{v_0}(t) \\ \psi_x(x,y,t) &= \frac{2}{\sqrt{ab}}\sum_{m=1}^{\infty}\sum_{n=1}^{\infty}\cos(\beta_m x)\sin(\beta_n y)\,\eta_{mn}^{\psi_x}(t) \end{aligned} \tag{3.18}$$

$$\psi_y(x,y,t) = \frac{2}{\sqrt{ab}} \sum_{m=1}^{\infty} \sum_{n=1}^{\infty} \sin(\beta_m x) \cos(\beta_n y)\, \eta_{mn}^{\psi_y}(t)$$

$$w_0(x,y,t) = \frac{2}{\sqrt{ab}} \sum_{m=1}^{\infty} \sum_{n=1}^{\infty} \sin(\beta_m x) \sin(\beta_n y)\, \eta_{mn}^{w_0}(t)$$

where m and n are the number of half-waves along x and y directions, respectively, and $\beta_m = m\pi/a$ and $\beta_n = n\pi/b$. Also, the functions η_{mn}^{i}'s ($i = u_0, v_0, \psi_x, \psi_y, w_0$) are the modal mechanical coordinate expressions. It can be simply verified that the set of series expansions for the displacement components (proposed in Eq. (3.18)) satisfy the boundary conditions on the simply supported edges, which are:

$$\begin{aligned} &v_0 = \psi_y = w = N_{xx} = M_{xx} = 0 && \text{at } x = 0, a \\ &u_0 = \psi_x = w = N_{yy} = M_{yy} = 0 && \text{at } y = 0, b \end{aligned} \tag{3.19}$$

Following the procedure of modal analysis for two-dimensional structures, one can derive the governing equations of the plate harvester in modal coordinates by introducing Eq. (3.18) into Eqs. (3.14) and (3.17) yields, as:

$$\begin{bmatrix} K_{11} & \cdots & K_{15} \\ \vdots & \ddots & \vdots \\ K_{51} & \cdots & K_{55} \end{bmatrix} \begin{Bmatrix} \eta_{mn}^{u_0} \\ \eta_{mn}^{v_0} \\ \eta_{mn}^{\psi_x} \\ \eta_{mn}^{\psi_y} \\ \eta_{mn}^{w_0} \end{Bmatrix} + \begin{bmatrix} M_{11} & \cdots & M_{15} \\ \vdots & \ddots & \vdots \\ M_{51} & \cdots & M_{55} \end{bmatrix} \begin{Bmatrix} \ddot{\eta}_{mn}^{u_0} \\ \ddot{\eta}_{mn}^{v_0} \\ \ddot{\eta}_{mn}^{\psi_x} \\ \ddot{\eta}_{mn}^{\psi_y} \\ \ddot{\eta}_{mn}^{w_0} \end{Bmatrix} = - \begin{Bmatrix} V(t) X_{mn}^{u_0} \\ V(t) X_{mn}^{v_0} \\ V(t) X_{mn}^{\psi_x} \\ V(t) X_{mn}^{\psi_y} \\ V(t) X_{mn}^{w_0} + F_{mn}(t) \end{Bmatrix} \tag{3.20a}$$

$$C_0\dot{V}(t)+\frac{1}{\hat{R}_L}V(t)-\sum_{m=1}^{\infty}\sum_{n=1}^{\infty}s_{mn}^{u_0}\dot{\eta}_{mn}^{u_0}-\sum_{m=1}^{\infty}\sum_{n=1}^{\infty}s_{mn}^{v_0}\dot{\eta}_{mn}^{v_0}$$
$$-\sum_{m=1}^{\infty}\sum_{n=1}^{\infty}s_{mn}^{\psi_x}\dot{\eta}_{mn}^{\psi_x}-\sum_{m=1}^{\infty}\sum_{n=1}^{\infty}s_{mn}^{\psi_y}\dot{\eta}_{mn}^{\psi_y} \tag{3.20b}$$
$$-\sum_{m=1}^{\infty}\sum_{n=1}^{\infty}s_{mn}^{w_0}\dot{\eta}_{mn}^{w_0}=0$$

In Eq. (3.20a), $F_{mn}(t)=F_0e^{j\omega t}C_{mn}/\beta_m\beta_n$ where F_0 is the amplitude of the applied force (considered real), ω is the deriving frequency, $j=\sqrt{-1}$ and $C_{mn}=2(1-\cos(\beta_m a))(1-\cos(\beta_n b))/\sqrt{ab}$. Moreover, the expressions corresponding to the components of the stiffness matrix $[K]$, mass matrix $[M]$, and X_{mn}^{i}'s and s_{mn}^{i}'s ($i=u_0,v_0,\psi_x,\psi_y,w_0$) are given in Relations (B.4) to (B.8) of Appendix B, for both FSDT and TSDT. Note that Eqs. (3.20a) and (3.20b) are the electromechanically coupled ordinary differential equations for the modal time response as well as the electrical circuit equation in modal coordinate, respectively, which are further discussed in the next section for the plate harvester under harmonic excitation.

3.5 Steady-State Response to Harmonic Excitation

The electromechanical equations for the piezoelectric bimorph harvester were derived and presented in Eqs. (3.14) and (3.17) in physical coordinates, as well as in Eq. (3.20) in modal coordinates. Since the acting force $F_z(t)$ is assumed to be harmonic (i.e., $F_z(t)=F_0e^{j\omega t}$), and the system of governing equations is linear, the output voltage and the modal response are therefore harmonic at the deriving frequency (for all (m,n)), and can be expressed as:

$$\begin{Bmatrix}\eta_{mn}^{u_0}\\ \eta_{mn}^{v_0}\\ \eta_{mn}^{\psi_x}\\ \eta_{mn}^{\psi_y}\\ \eta_{mn}^{w_0}\end{Bmatrix}=\begin{Bmatrix}H_{mn}^{u_0}\\ H_{mn}^{v_0}\\ H_{mn}^{\psi_x}\\ H_{mn}^{\psi_y}\\ H_{mn}^{w_0}\end{Bmatrix}e^{j\omega t},\quad V(t)=V_0e^{j\omega t} \tag{3.21}$$

in which H_{mn} and V_0 are complex. Introducing Eq. (3.21) into Eq. (3.20) results in:

$$([K]-\omega^2[M])\begin{Bmatrix} H_{mn}^{u_0} \\ H_{mn}^{v_0} \\ H_{mn}^{\psi_x} \\ H_{mn}^{\psi_y} \\ H_{mn}^{w_0} \end{Bmatrix} = -\begin{Bmatrix} V_0 X_{mn}^{u_0} \\ V_0 X_{mn}^{v_0} \\ V_0 X_{mn}^{\psi_x} \\ V_0 X_{mn}^{\psi_y} \\ V_0 X_{mn}^{w_0} + F_0 C_{mn}/\beta_m\beta_n \end{Bmatrix} \tag{3.22a}$$

$$\begin{aligned} V_0 = \frac{j\omega}{\left(\frac{1}{R_L}+j\omega C_0\right)}\Bigg(&\sum_{m=1}^{\infty}\sum_{n=1}^{\infty} s_{mn}^{u_0} H_{mn}^{u_0} + \sum_{m=1}^{\infty}\sum_{n=1}^{\infty} s_{mn}^{v_0} H_{mn}^{v_0} \\ &+ \sum_{m=1}^{\infty}\sum_{n=1}^{\infty} s_{mn}^{\psi_x} H_{mn}^{\psi_x} + \sum_{m=1}^{\infty}\sum_{n=1}^{\infty} s_{mn}^{\psi_y} H_{mn}^{\psi_y} \\ &+ \sum_{m=1}^{\infty}\sum_{n=1}^{\infty} s_{mn}^{w_0} H_{mn}^{w_0}\Bigg) \end{aligned} \tag{3.22b}$$

One can simply observe from Eq. (3.22) that the two responses are coupled. However, setting the determinant of the coefficient matrix in Eq. (3.22a) (i.e., $|[K]-\omega^2[M]|=0$) gives the SC frequencies of the bimorph plate harvester, which corresponds to the free vibration problem of the respective system. To express V_0 explicitly, the modal response expressions have to be omitted from Eq. (3.22b). However, the effect of damping must be first added to the system of Eq. (3.22a) (will be added to the respective coefficient matrix), to avoid instability of responses in resonant frequency excitation. Rayleigh damping is therefore added to the system to include the effect of mechanical damping, as it may be expressed in the following matrix form:

$$[C] = a_M[M] + a_K[K] \tag{3.23}$$

where a_M and a_K are mass and stiffness proportionality constants with units of s^{-1} and s, respectively, and can be simply calculated for a given damping ratio [159]. Based on Eq. (3.23), $[C]$ consists of a mass-proportional term and a stiffness-proportional term. Finally, taking the effect of damping into account, the set of Eq. (3.22a) is altered to:

$$[A]\begin{Bmatrix} H_{mn}^{u_0} \\ H_{mn}^{v_0} \\ H_{mn}^{\psi_x} \\ H_{mn}^{\psi_y} \\ H_{mn}^{w_0} \end{Bmatrix} = -\begin{Bmatrix} V_0 X_{mn}^{u_0} \\ V_0 X_{mn}^{v_0} \\ V_0 X_{mn}^{\psi_x} \\ V_0 X_{mn}^{\psi_y} \\ V_0 X_{mn}^{w_0} + F_0 C_{mn}/\beta_m\beta_n \end{Bmatrix} \tag{3.24}$$

where

$$[A] = [K] - \omega^2[M] + j\omega[C] \tag{3.25}$$

To obtain the closed-form solution of the output voltage V_0, one has to first derive from Eq. (3.24) the vector $\{H_{mn}\}$ in terms of V_0 and other coefficients and then substitutes the resulting expressions into Eq. (3.22b). assuming $[B] = [A]^{-1}$, $\{H_{mn}\}$ may be obtained as:

$$\begin{aligned} \begin{Bmatrix} H_{mn}^{u_0} \\ H_{mn}^{v_0} \\ H_{mn}^{\psi_x} \\ H_{mn}^{\psi_y} \\ H_{mn}^{w_0} \end{Bmatrix} &= -[B]\begin{Bmatrix} V_0 X_{mn}^{u_0} \\ V_0 X_{mn}^{v_0} \\ V_0 X_{mn}^{\psi_x} \\ V_0 X_{mn}^{\psi_y} \\ V_0 X_{mn}^{w_0} + F_0 C_{mn}/\beta_m\beta_n \end{Bmatrix} \\ &= -V_0\begin{Bmatrix} Y_{mn}^1 \\ Y_{mn}^2 \\ Y_{mn}^3 \\ Y_{mn}^4 \\ Y_{mn}^5 \end{Bmatrix} - \frac{F_0 C_{mn}}{\beta_m\beta_n}\begin{Bmatrix} B_{15} \\ B_{25} \\ B_{35} \\ B_{45} \\ B_{55} \end{Bmatrix} \end{aligned} \tag{3.26}$$

in which Y_{mn}^i's ($i = 1,2,3,4,5$) are given in Relation (B.9) of Appendix B, and B_{ij}'s are the components of the fifth column of matrix $[B]$. Substituting the above expressions obtained for H_{mn}^i's ($i = u_0, v_0, \psi_x, \psi_y, w_0$) into Eq. (3.22b) gives the closed-form expression of the output voltage, as:

$$V_0 = \frac{F_0\, S_1/C_0}{j\omega + \dfrac{1}{R_L C_0} + \dfrac{S_2}{C_0}} \tag{3.27}$$

where S_1 and S_2 are obtained as:

$$S_1 = -j\omega\left\{\sum_{m=1}^{\infty}\sum_{n=1}^{\infty}\frac{C_{mn}s_{mn}^{u_0}B_{15}}{\beta_m\beta_n} + \sum_{m=1}^{\infty}\sum_{n=1}^{\infty}\frac{C_{mn}s_{mn}^{v_0}B_{25}}{\beta_m\beta_n} + \sum_{m=1}^{\infty}\sum_{n=1}^{\infty}\frac{C_{mn}s_{mn}^{\psi_x}B_{35}}{\beta_m\beta_n} + \sum_{m=1}^{\infty}\sum_{n=1}^{\infty}\frac{C_{mn}s_{mn}^{\psi_y}B_{45}}{\beta_m\beta_n} + \sum_{m=1}^{\infty}\sum_{n=1}^{\infty}\frac{C_{mn}s_{mn}^{w_0}B_{55}}{\beta_m\beta_n}\right\} \tag{3.28a}$$

$$S_2 = j\omega\left\{\sum_{m=1}^{\infty}\sum_{n=1}^{\infty}Y_{mn}^{1}s_{mn}^{u_0} + \sum_{m=1}^{\infty}\sum_{n=1}^{\infty}Y_{mn}^{2}s_{mn}^{v_0} + \sum_{m=1}^{\infty}\sum_{n=1}^{\infty}Y_{mn}^{3}s_{mn}^{\psi_x} + \sum_{m=1}^{\infty}\sum_{n=1}^{\infty}Y_{mn}^{4}s_{mn}^{\psi_y} + \sum_{m=1}^{\infty}\sum_{n=1}^{\infty}Y_{mn}^{5}s_{mn}^{w_0}\right\} \tag{3.28b}$$

The amplitude of the voltage frequency response function V_{FRF} can be obtained by determining the absolute value of the complex expression of output voltage given in Eq. (3.27), as:

$$V_{\mathrm{FRF}} = \left|\frac{V_0}{F_0}\right| \tag{3.29}$$

It is also very simple to determine the current and the power frequency response functions (I_{FRF} and P_{FRF}, respectively) with the help of Ohm's law and the power equation, as:

$$I = \frac{|V_0|}{R_L}, \qquad P = \frac{|V_0|^2}{R_L}, \qquad I_{\mathrm{FRF}} = \left|\frac{I}{F_0}\right|, \qquad P_{\mathrm{FRF}} = \left|\frac{P}{F_0}\right| \tag{3.30}$$

The obtained output voltage V_0 can also be substituted into the modal response in Eq. (3.26), to calculate the displacements in each vibrational mode, and subsequently the modal response as a function of the excitation frequency ω and the time t.

3.6 Numerical Results

3.6.1 Model Validation

First, the present results are compared with some available in the literature to verify the accuracy of the developed models. Setting the determinant of the coefficient matrix in Eq. (3.22a) to zero gives us the natural frequencies of the smart bimorph plate. However, the first three natural frequencies of a bimorph plate made of a homogeneous substrate and PZT-4 layers are computed and listed in Table 3.1 along with their counterparts reported in Ref. [160]. Comparing these data, one can observe the excellent agreement among the results, which confirms the accuracy of the present model. In all the cases investigated in Table 3.1, the relative differences are less than 1%. Note that these slight differences are due to the employment of different displacement models and electric potential distributions in the present work and Ref. [160].

Table 3.1: Comparison of the first three natural frequencies for the bimorph plates with isotropic substrates

$\frac{2h}{a}$	$\frac{h_p}{2h}$	Source	Natural frequency (Hz)		
			1st mode (1,1)	2nd mode (1,2)	3rd mode (2,2)
0.05	0.1	Ref. [160]	426.818	1050.253	1655.040
		Present (FSDT)	426.685	1049.563	1653.471
		Present (TSDT)	426.884	1050.728	1656.272
		Relative difference FSDT (%)	0.03	0.07	0.09
		Relative difference TSDT (%)	0.03	0.04	0.07
	0.2	Ref. [160]	408.836	1003.195	1576.867
		Present (FSDT)	408.395	1001.108	1572.229
		Present (TSDT)	408.808	1003.490	1577.893
		Relative difference FSDT (%)	0.11	0.21	0.29
		Relative difference TSDT (%)	0.01	0.03	0.07
0.1	0.1	Ref. [160]	827.520	1957.398	2983.884
		Present (FSDT)	826.735	1954.047	2977.766
		Present (TSDT)	828.136	1961.074	2992.752
		Relative difference FSDT (%)	0.09	0.17	0.21
		Relative difference TSDT (%)	0.07	0.19	0.30
	0.2	Ref. [160]	788.433	1849.607	2802.300
		Present (FSDT)	786.115	1839.679	2783.353
		Present (TSDT)	788.947	1853.347	2811.643
		Relative difference FSDT (%)	0.29	0.54	0.68
		Relative difference TSDT (%)	0.00	0.20	0.33

Relative difference = (Present − Ref. [160])×100/ Ref. [160]

3.6.2 Parametric Study and Discussion

Numerical results for the bimorph plate harvesters with piezoelectric layers under both parallel and series configurations are presented in this subsection. The parent material of the substrate layer is assumed to be Aluminum with the following mechanical properties:

$$E_0 = 70 \text{ GPa}, \quad \rho_0 = 2707 \text{ kg/m}^3, \quad \nu = 0.3$$

Note that when the value of the porosity coefficient is set to zero (i.e., setting $e_0 = 0$ in either Eq. (1.17) or Eq. (1.19), which describe the material properties in the porous layer), the substrate layer is assumed to have no porosity (i.e., homogenous substrate), and consequently no variation along any direction is considered for the respective mechanical properties. However, $e_0 \neq 0$ represents a bimorph harvester with a porous Aluminum substrate whose mechanical properties vary along the thickness direction. In the latter case, the effective properties of the core layer are considered based on either Eq. (1.17) or Eq. (1.19), depending on the type of porosity distribution.

The mechanical and electrical properties of some PZT materials used for the piezoelectric layers are also given in Table 3.2.

Table 3.2: Mechanical and electrical properties of some PZT materials [148,161]

Material	Properties							
	Elastic moduli (GPa)						Dielectric moduli (nF/m)	
	C_{11}	C_{12}	C_{33}	C_{13}	C_{55}	C_{66}	Ξ_{11}	Ξ_{33}
PZT-5H	127.2	80.2	117.4	84.7	23.0	23.5	15.1	12.7
PZT-2	134.9	67.9	113.3	68.1	22.2	33.4	4.46	2.4
	Piezoelectric moduli (C/m2)						Mass density (kg/m3)	
	e_{31}	e_{33}	e_{15}				ρ	
PZT-5H	-6.6	23.2	17.0				7500	
PZT-2	-1.82	9.05	9.8				7600	

First, PZT-5H is selected as the material of the piezoelectric layers. Therefore, the following tabulated results are obtained for the bimorph plate harvesters with

homogenous/porous Aluminum substrate and PZT-5H layers. Moreover, the following geometrical dimensions are also considered for the harvester device:

$a = b = 200\ mm, h = 1\ mm, h_p = 0.2\ mm.$

Employing the material and geometrical properties (mentioned above) into the MATLAB codes provided for the present energy harvesting model, the voltage, current, and power FRFs are obtained and plotted in Figs. 3.4 to 3.5. Rather than specifying certain F_0 and ω values for the input, it is preferred to obtain the results in terms of these parameters so that it becomes possible to represent the electromechanical outputs as FRFs. Moreover, since the electrical load resistance is an important parameter that significantly affects the dynamic and electric behavior of the harvester device, the first peak in the output electrical response of the bimorph plate is plotted for different values of R_L ranging from 1Ω to 100MΩ. These plots represent the magnitude of the generated electric voltage, current, and power for the bimorph harvester, for both parallel and series electrical configurations. Due to the electromechanical coupling, each vibration mode has an SC resonance frequency (for $R_L \to 0$) and an OC resonance frequency (for $R_L \to \infty$). Therefore, the resonance frequency of the respective vibration mode takes values between the SC and OC frequencies.

However, one can observe from Fig. 3.3 that, as R_L increases from low values to large values, the amplitude of the output voltage increases monotonically for all the excitation frequencies until it reaches its maximum value at $R_L = 5\text{k}\Omega$ and $R_L = 100\text{k}\Omega$, for parallel and series connections, respectively, and it then remains constant for larger values of R_L. Although the trends for variation of the output voltage against the electrical load are similar for both types of electrical connections, a larger resistance load has to be applied to the harvester under series connection to reach its OC condition, compared to when the parallel connection is used. Moreover, the amount of the OC voltage provided by the harvester with series configuration seems to be much higher than that of the scavenger with parallel configuration. It is also seen from Fig. 3.3 that with increasing the load resistance, the resonance frequency of the plate harvester moves from the SC frequency to the OC frequency, expectedly. These two resonance frequencies are important excitation frequencies in the analysis of energy harvesters, which can be calculated

for the bimorph harvester from either Fig. 3.3(a) or Fig. 3.3(b), since the type of electrical configuration does not affect the resonance frequencies of the SC and OC conditions. Accordingly, they are calculated and found to be 247.4 Hz and 261 Hz for the fundamental vibration mode at SC and OC conditions, respectively.

Fig. 3.4 represents that the amplitude of the electric current goes down monotonically (similar to output voltage) as the value of R_L increases. Unlike the voltage FRFs shown in Fig. 3.3, the amplitude of the current decreases with increasing load resistance. Indeed, this is the opposite of the voltage behavior shown in Fig. 3.3, but the behavior is still monotonic. For every excitation frequency, the maximum value of the current is obtained when the system is close to short circuit conditions.

The power output FRFs for different resistance loads are displayed in Fig. 3.5. Since it is the product of two FRFs that have the opposite behaviors with increasing load resistance, the behavior of the power output FRF with load resistance is more interesting than the previous two electrical outputs and it deserves more discussion. It is obvious from Fig. 3.5 that the output power does not represent a monotonic behavior when the value of R_L increases. As the load resistance gets larger, the power output increases until it reaches its maximum value, at $R_L = 500\Omega$ and $R_L = 1000\Omega$ for parallel and series connections, respectively, then drops for larger values of R_L. What is just realized also shows that the maximum power in series configuration is achieved at a higher resistance load compared to the parallel case. One should note that the values of the load resistance we use in this analysis are taken arbitrarily to observe the general trends. Therefore, the maximum power outputs obtained from each electrical configuration are for these sample values and they are not necessarily the maximum possible (or the optimized) power outputs. Another interesting point to note is the switching between the curves of various values of R_L, which results in intersections between the FRFs. These intersections are seen not only around the resonance frequencies but also they are observed at the off-resonance frequencies. At these intersection frequencies, the two respective load resistance values yield the same power output.

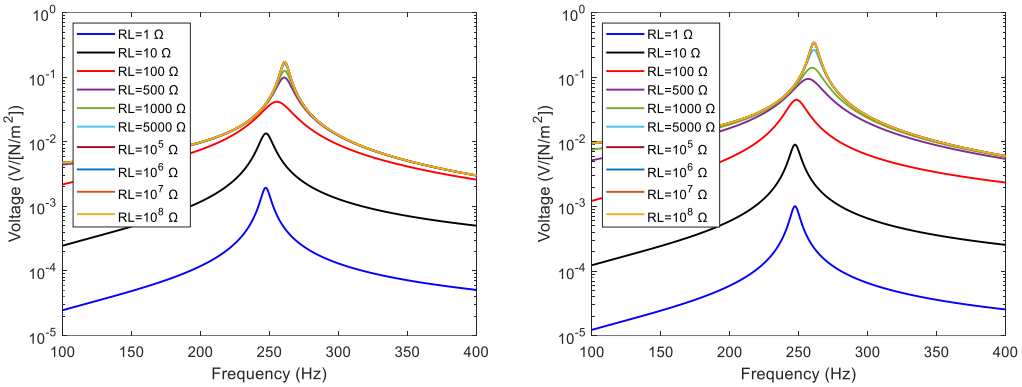

(a) Parallel (b) Series

Fig. 3.3: Voltage FRFs for the bimorph plate harvester under parallel and series electrical connections

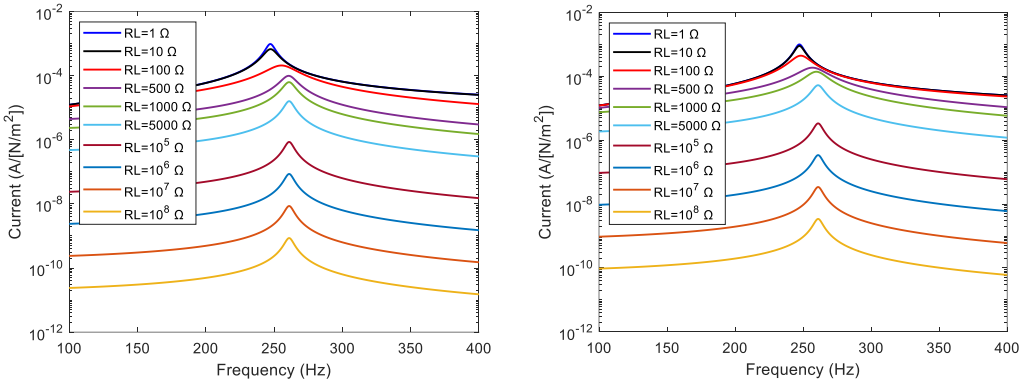

(a) Parallel (b) Series

Fig. 3.4: Current FRFs for the bimorph plate harvester under parallel and series electrical connections

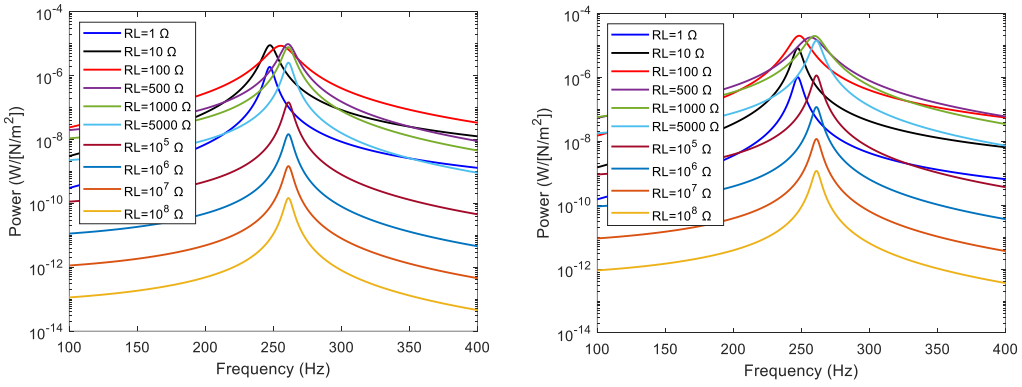

(a) Parallel (b) Series

Fig. 3.5: Power FRFs for the bimorph plate harvester under parallel and series electrical connections

Since the FRF plots for the harvester with porous Aluminum substrate and PZT-5H layers were found to be very similar (in terms of the general trends) to those given in Figs. 3.3 to 3.5, they are not therefore reported here. However, the effects of porosity coefficient and different types of porosity distributions on the dynamic and electric response of the plate harvester are here and hereafter discussed. As a primary examination on the effect of porosity, the SC and OC frequencies of the harvester with a porous Aluminum substrate of $e_0 = 0.4$ are calculated and listed in Table 3.3 along with those of a bimorph harvester with no porosity in its substrate. These results show that the SC and OC frequencies of the energy harvester are significantly affected when the porous substrates are used instead of the homogenous substrate. In particular, the porous bimorph harvester with porosity Pattern I represents the lowest SC and OC frequencies, while the maximum frequencies are obtained when the porosity distribution with Pattern I is adopted.

Table 3.3: Resonance frequency of the bimorph plate harvester with substrate having different porosity patterns

		Porous substrate ($e_0 = 0.4$)		
Variable	Solid Substrate	Pattern I	Pattern II	Pattern III
SC frequency	247.4	247.8	229.6	237.4
OC frequency	261.0	262.2	245.8	252.8

The effect of porosity on the electric response of the plate harvester is investigated and the results are presented in Figs. 3.6 and 3.7. In these figures, the voltage and power FRFs are plotted against the excitation frequency for the homogenous bimorph harvester and the porous bimorph harvester with different porosity distributions and porosity coefficients, namely $e_0 = 0.2$, 0.4, 0.6 and 0.8. The value of the resistance load in this investigation example is assumed to be $R_L = 500\Omega$ and type of electrical connection between the PZT layers is considered to be parallel. Again, it is seen that the harvester resonance frequency is significantly influenced by variation of the porosity parameter as well as the type of porosity distribution. When the porosity Patterns II and III are adopted for the distribution of the internal pores, increasing the value of e_0 decreases the resonance frequency of the harvester, while an increasing trend is seen for porosity Pattern I. The changes

in frequency due to variation of porosity coefficient is attributed to the resulting changes in the effective structural stiffness and mass density of the system, which in turn can lead to higher/lower natural frequencies (depending on the type of porosity distribution) compared to the same system in the absence of porosities. Furthermore, the figures suggest that the sensitivity of the harvester resonance frequency to the porosity is more considerable when the pores are distributed according to the Pattern II with respect to the other profiles. For instance, when the value of e_0 is shifted from zero to 0.8, the reduction in the harvester frequency is 11.5% for the porosity Pattern II and 6.6% for the Pattern III, while it causes an increase of 4% in the scavenger frequency when the porosity Pattern I is adopted. More interesting are the enhancements of both voltage and power generations due to the introduction of porosity to the substrate layer. As is clear from the figures, the higher is the porosity coefficient the greater are the amounts of peak voltage and power, regardless of the type of porosity distribution. In other words, as the value of porosity coefficient changes from 0 to 0.8, an increase of 25.4%, 56.2% and 47.7% in the peak power points are obtained for the harvester with porosity Pattern I, Pattern II and Pattern III, respectively. Again, the harvester with Pattern II is found to be more sensitive to the variation of porosity, in terms of the electric outputs.

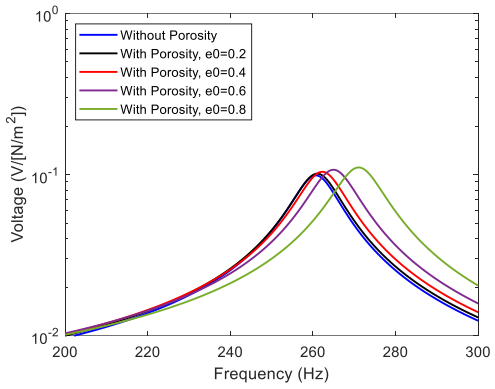

(a) Porosity Pattern I

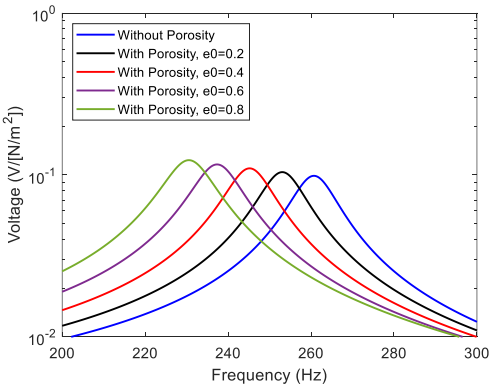

(b) Porosity Pattern II

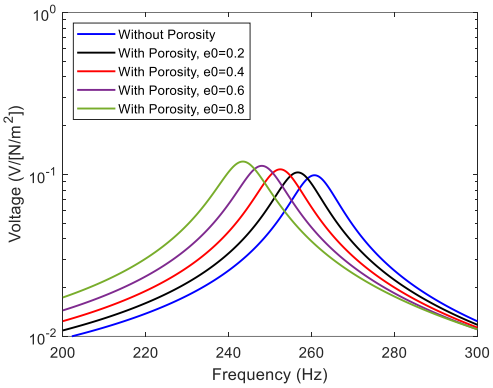

(c) Porosity Pattern III (Uniform)

Fig. 3.6: Voltage FRFs for the bimorph plate harvester under parallel configuration ($R_L = 500\Omega$)

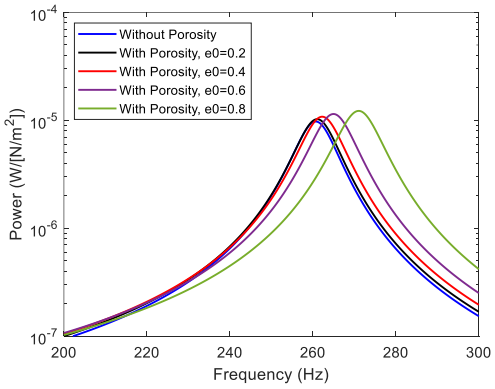

(a) Porosity Pattern I

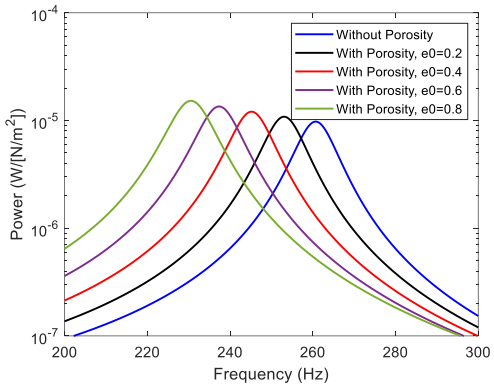

(b) Porosity Pattern II

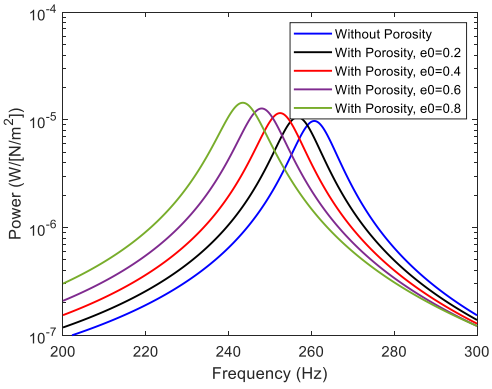

(c) Porosity Pattern III (Uniform)

Fig. 3.7: Power FRFs for the bimorph plate harvester under parallel configuration ($R_L = 500\Omega$)

The effect of load resistance on the current, voltage and power outputs of the bimorph harvester with parallel and series connections is further investigated for excitations at SC and OC frequencies, and the corresponding results are given in Fig. 3.8. The results are presented only for the case of bimorph harvester with the Aluminum substrate having no porosity. Figs. 3.8(a) and 3.8(b) indicate that for low values of load resistance, the voltage outputs at both SC and OC excitation frequencies increase with the same slope (in log-log scale) and the voltage output at the SC resonance frequency is higher because the system is close to SC conditions. However, the SC and OC curves intersect at a certain value of R_L (around 85Ω for parallel, and 339Ω for series connection) and for the values of R_L greater than the value at the intersection point, the voltage output at the OC excitation frequency becomes higher expectedly. Finally, the voltage output remains constant and insensitive to the variations of R_L at OC conditions. Figs. 3.8(c) and 3.8(d) show the current outputs of both parallel and series connections as functions of load resistance for excitations at the SC and the OC resonance frequencies. It is clear from the figures that the current is highly insensitive to the variations of the load resistance at the range of its low values. In this relatively low load resistance region, the current output is higher at the SC resonance frequency, as in the case of voltage (see Figs. 3.8(a) and 3.8(b)), since the system is close to SC conditions. Then, current starts decreasing with further increasing the load resistance, and at a certain value of load resistance (again, around 85Ω for parallel, and 339Ω for series connection), the curves intersect. For the values of load resistance higher than the value at this intersection point, the current output at the OC resonance frequency becomes higher since the system approaches the OC conditions. The variation of power output with load resistance for excitations at the SC and OC resonance frequencies are further investigated through Figs. 3.8(e) and 3.8(f), for the bimorph harvester under both parallel and series electrical connections. It can be remembered from Figs. 3.8(a) to 3.8(d) that the voltage and the current outputs obtained at the SC resonance frequency are higher than those obtained at the OC resonance frequency up to a certain value of R_L (about 85Ω for parallel, and 339Ω for series connection) after which the opposite is valid. Because the power output is simply the product of the voltage and current, this observation is also valid for the power versus load resistance curves. As is evident from Figs. 3.8(e) and 3.8(f), the same intersection points are seen (again, about 85Ω for

parallel, and 339Ω for series connection) and the power output at the SC resonance frequency is higher before this point, whereas the power output at the OC resonance frequency is higher after this point. More importantly, since the variation of power with changing the load resistance is not monotonic, all the power graphs shown in Figs. 3.8(e) and 3.8(f) display peak values, which correspond to the optimum values of load resistance. It must be noted that when the optimum values of resistance load are used for each of the SC and OC excitations, the same values of maximum power are obtained. For instance, from Fig. 3.8(e), the maximum power output generated by the plate harvester is about 10 $\mu W/[N/m^2]$ across the optimum resistance loads of $R_L^{opt} = 19\Omega$ and $R_L^{opt} = 370\Omega$, for excitation at the SC and OC resonance frequencies, respectively. The same amount of peak power is also obtained from Fig. 3.8(f) for the case of series configuration but at higher optimum resistance loads, i.e., $R_L^{opt} = 76\Omega$ and $R_L^{opt} = 1491\Omega$ for the SC and OC excitations, respectively.

For comparison purposes, the optimum resistance loads, and the respective peak powers are calculated for the bimorph harvester with porous substrate having different porosity patterns and porosity coefficients, namely $e_0 = 0.2$ and 0.4. The respective results are listed in Table 3.4 along with those of the same harvester with no porosity. Excitations at both SC and OC frequencies are considered for all the cases. The results listed in Table 3.4 suggest that for a given porosity coefficient, the maximum peak power is generated by the harvester with porosity Pattern II, followed by those with Pattern III and Pattern I, respectively. However, the harvester with non-porous substrate provides the minimum peak power (among all) at its respective optimum resistance load. Such observations can be attributed to the fact that because the effective structural stiffness of the porous substrate is less than that of the non-porous substrate, the former system experiences more bending strain than the latter case, which in turn, leads to more power output generation.

Table 3.4: Optimum load resistance and output power for different porous bimorph harvester excited at the SC and OC resonance frequencies (Parallel configuration).

		Porous substrate		
Parameter	Solid Substrate	Pattern I	Pattern II	Pattern III
		Porosity coefficient ($e_0 = 0.2$)		
SC frequency (Hz)	247.4	247.0	238.6	242.6
Optimum load resistance (Ω)	19	18	17	18
$P_{max}\ \left(\frac{\mu W}{N/m^2}\right)$	10.00	10.39	10.88	10.72
OC frequency (Hz)	261.0	261.4	253.4	257.0
Optimum load resistance (Ω)	370	376	412	384
$P_{max}\ \left(\frac{\mu W}{N/m^2}\right)$	9.95	10.40	10.88	10.66
		Porosity coefficient ($e_0 = 0.4$)		
SC frequency (Hz)	247.4	247.8	229.6	237.4
Optimum load resistance (Ω)	19	17	16	16
$P_{max}\ \left(\frac{\mu W}{N/m^2}\right)$	10.00	11.00	12.06	11.61
OC frequency (Hz)	261.0	262.2	245.8	252.8
Optimum load resistance (Ω)	370	365	474	444
$P_{max}\ \left(\frac{\mu W}{N/m^2}\right)$	9.95	11.02	11.93	11.54

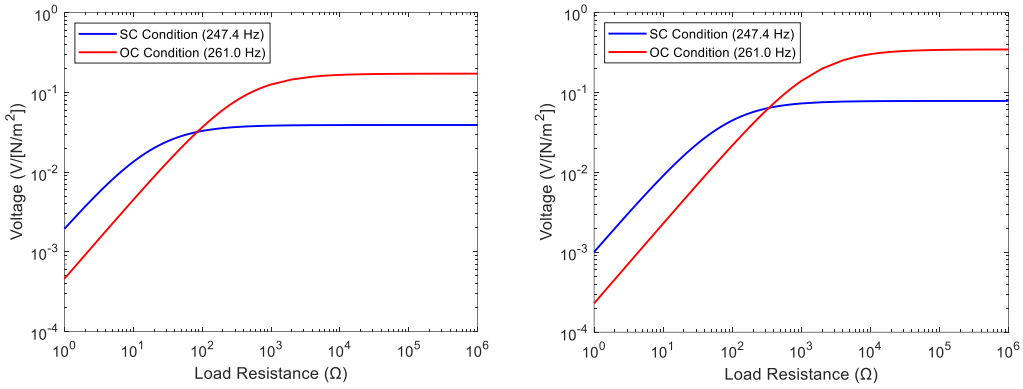

(a) Parallel (b) Series

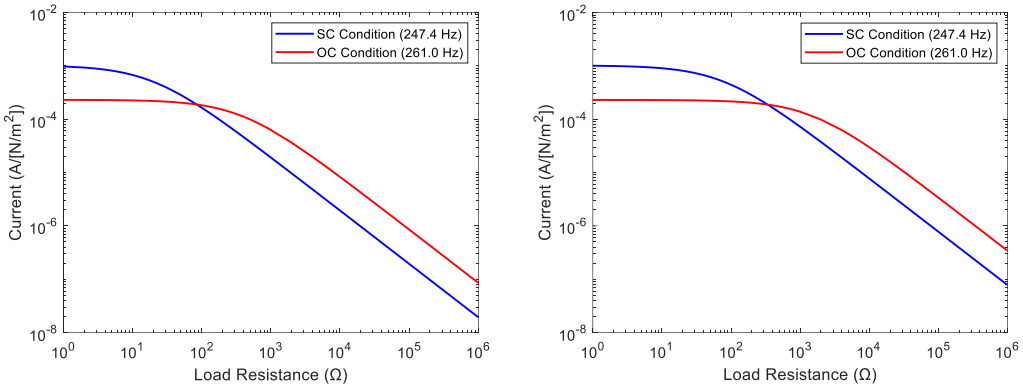

(c) Parallel (d) Series

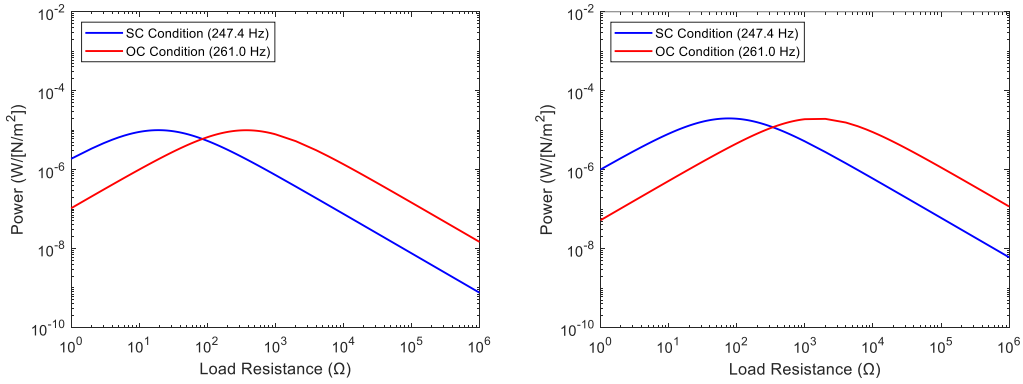

(e) Parallel (f) Series

Fig. 3.8: Variations of the voltage, current and power outputs against the resistance load for the bimorph plate harvester under parallel and series electrical configurations

Keeping the volume of the harvester constant ($ab = 0.04\,m^2$, $h = 1\,mm$, $h_p = 0.2\,mm$), the effects of the aspect ratio a/b on the frequencies and the power outputs of the plate harvester with homogenous and porous substrates are studied. In Table 3.5, the SC frequencies of the bimorph harvester with different values of a/b, namely 0.5, 0.7, 1.5 and 2, are listed. As is evident from the table, irrespective of the type of substrate, the square plate harvester (i.e., with $a/b = 1$) provides the lowest SC resonance frequencies. Similar result is observed for the case of OC condition. On the other hand, in Fig. 3.9, are plotted the output powers versus the electrical load resistance for both homogenous and porous bimorph scavengers with different aspect ratios. For all the cases, the results are obtained for excitation at their respective SC resonance frequencies. As is seen, the maximum peak power is obtained for the square plate scavenger, regardless of the type of substrate. Also, the optimum load resistance (which gives the peak power in each of the plots) is found to be the highest for the case of $a/b = 1$ compared to other cases. For every given value of a/b, the porous bimorph energy harvester with porosity Pattern II exhibits the highest peak power, in comparison with the scavengers with other types of substrates. This last finding is consistent with the conclusions drawn from Table 3.4.

Table 3.5: SC resonance frequencies (Hz) of the porous bimorph harvesters for different aspect ratios ($ab = 0.04\,m^2$)

		Porous substrate ($e_0 = 0.4$)		
a/b	Solid Substrate	Pattern I	Pattern II	Pattern III
0.5	309.1	309.6	287.0	296.6
0.6	280.2	280.7	260.2	268.9
0.7	263.2	263.6	244.3	252.6
0.8	253.5	253.9	235.3	243.2
0.9	248.7	249.1	230.9	238.6
1.0	247.4	247.8	229.6	237.4
1.1	248.4	248.8	230.6	238.4
1.2	251.4	251.8	233.4	241.3
1.3	255.8	256.3	237.5	245.5
1.4	261.4	261.8	242.7	250.9
1.5	267.9	268.3	248.7	257.1
2.0	309.1	309.6	287.0	296.6

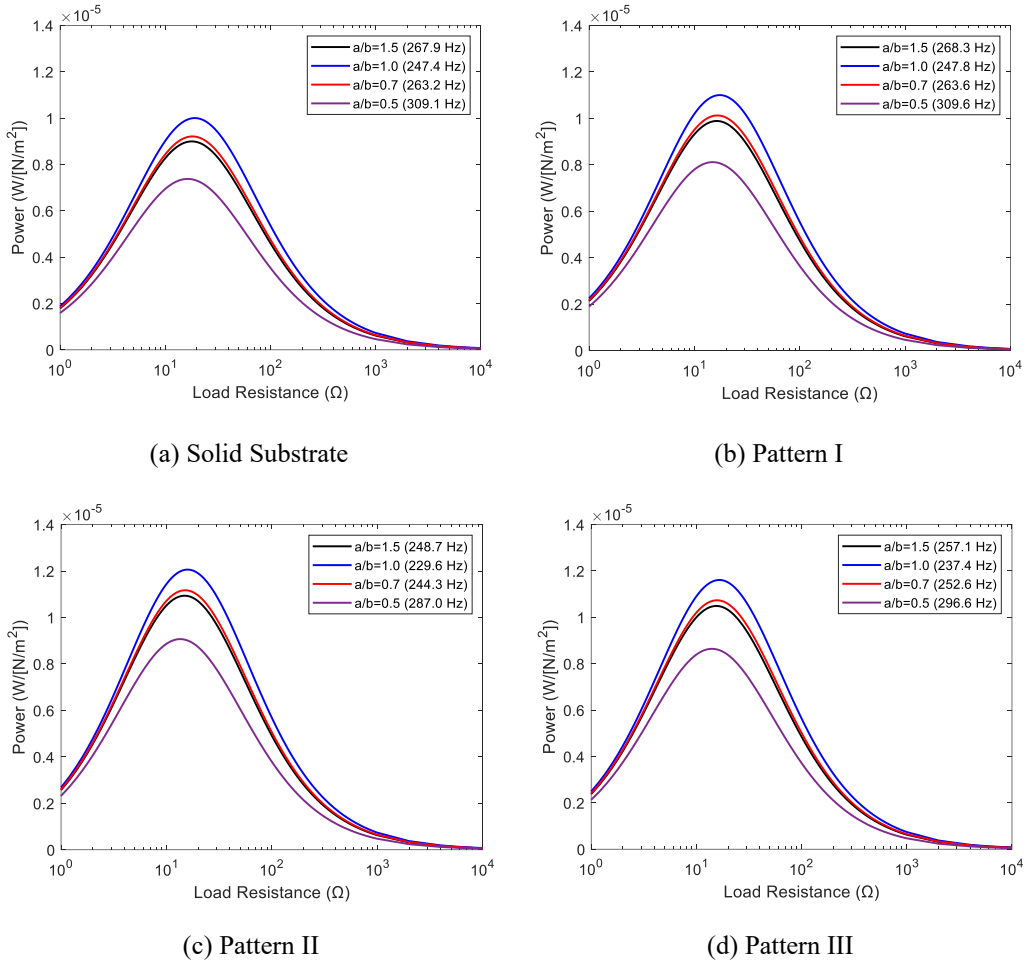

(a) Solid Substrate (b) Pattern I

(c) Pattern II (d) Pattern III

Fig. 3.9: Effect of the aspect ratio on the power output for homogenous and porous bimorph plate harvesters under parallel configuration ($e_0 = 0.4$)

The last investigation example is concerned with the effect of the material of piezoelectric layers on the frequencies and the electric response of the bimorph scavenger. For that purpose, two types of PZT materials, namely PZT-2 and PZT-5H are considered with the Aluminum substrate with/without porosity. The respective optimal resistance loads, and the peak powers are computed for excitations at both SC and OC frequencies, and the obtained results are listed in Table 3.6. The results indicate that in all the cases, the harvester with PZT-5H layers exhibits lower SC and OC frequencies. Furthermore, higher peak powers for excitations at both frequencies are achieved when PZT-5H is used. Compared to the case of PZT-2, lower resistance loads need to be applied to the harvester with

PZT-5H layers to achieve the peak powers. Therefore, PZT-5H provides better properties for energy harvesting applications, and is capable of delivering more output power at lower optimum load resistance.

Table 3.6: Optimum load resistance and output power for different bimorph harvester with three types of piezoelectric layers ($a/b = 1$, $ab = 0.04\ m^2, e_0 = 0.4$)

			Piezoelectric layers	
Substrate	EC	Parameter	PZT-2	PZT-5H
Solid	SC	Resonance frequency (Hz)	265.8	247.4
		Optimum load resistance (Ω)	195	19
		$P_{max}\left(\frac{\mu W}{N/m^2}\right)$	8.64	10.00
	OC	Resonance frequency (Hz)	273.0	261.0
		Optimum load resistance (Ω)	1035	370
		$P_{max}\left(\frac{\mu W}{N/m^2}\right)$	8.64	9.95
Pattern I	SC	Resonance frequency (Hz)	268.0	247.8
		Optimum load resistance (Ω)	183	17
		$P_{max}\left(\frac{\mu W}{N/m^2}\right)$	9.49	11.00
	OC	Resonance frequency (Hz)	275.6	262.2
		Optimum load resistance (Ω)	1055	365
		$P_{max}\left(\frac{\mu W}{N/m^2}\right)$	9.57	11.02
Pattern II	SC	Resonance frequency (Hz)	251.6	229.6
		Optimum load resistance (Ω)	176	16
		$P_{max}\left(\frac{\mu W}{N/m^2}\right)$	10.49	12.06
	OC	Resonance frequency (Hz)	259.6	245.8
		Optimum load resistance (Ω)	1293	474
		$P_{max}\left(\frac{\mu W}{N/m^2}\right)$	10.48	11.93
Pattern III	SC	Resonance frequency (Hz)	258.6	237.4
		Optimum load resistance (Ω)	179	16
		$P_{max}\left(\frac{\mu W}{N/m^2}\right)$	10.07	11.61
	OC	Resonance frequency (Hz)	266.4	252.8
		Optimum load resistance (Ω)	1186	444
		$P_{max}\left(\frac{\mu W}{N/m^2}\right)$	10.07	11.54

3.7 Summary and Conclusions

A comprehensive analytical energy harvesting model based on shear deformation theories is developed for piezoelectric bimorph plate energy harvesters. The model allows to consider both homogenous materials and those containing porosities for the substrate layer. Closed-form expressions are obtained for the electrical outputs, and comprehensive parametric studies are reported to investigate the effect of the system parameters. It is found that the proposed energy harvesting model can accurately predict the electromechanical response of thin, moderately thick, and thick piezoelectric bimorph plate energy harvesters. Moreover, the following conclusions are drawn from the presented numerical results and simulations:

- For the series and parallel configurations, the respective resonance frequencies are identical, the maximum power outputs are close to each other, but the optimum electrical load for the series connection is much higher than that of parallel connection.
- Among the samples studied in the present work, the maximum power output occurs in an excitation frequency between the SC and OC fundamental natural frequencies.
- The presence of porosities in the substrate layer helps enhancing the voltage/power generation of the harvester as compared to its counterpart with no porosity.
- Both free vibration and electric response of the porous bimorph harvester with Pattern II are more sensitive to the porosity variation in comparison with the other porosity distributions.
- The highest power output is provided by the porous bimorph scavenger with porosity Pattern II, followed by its counterparts with porosity Pattern III and Pattern I, respectively.
- The trends for variation of the harvester resonance frequency versus the porosity parameter is highly dependent on the type of porosity distribution. Increasing the porosity coefficient results in a drop in the resonance frequency of the harvester with porosity Pattern II and Pattern III, while an ascending trend is observed for Pattern I.

- Keeping the harvester volume constant, the plate harvester with $a/b = 1$ provides the highest power output and the lowest resonance frequency as compared to the cases with $a/b \neq 1$.
- PZT-5H provides better properties than PZT-2, for energy harvesting applications.

Chapter 4

Free Vibration Analysis of Piezoelectric Bimorph Beams

4.1 Overview

Starting from this chapter, exact electromechanically-coupled models are herein and hereafter presented for dynamic and static problems of 1D (beam) and 2D (shell) structures. There are a number of theories that are used to represent the kinematics of deformation. Presented in this chapter is an analytical model based on the classical, the first-order and the higher-order shear deformation beam theories, for the problem of free vibration of bimorph beams (or 1D structures) with transverse (d_{31}) and shear (d_{15}) piezoelectric layers. The latter two beam theories allow for the effect of transverse shear deformation which is neglected in the classical beam theory. Using the principle of minimum potential energy, the governing equation of motion and boundary conditions are derived for the bimorph beam on the basis of the kinematic assumptions of the aforementioned beam theories. Although the proposed model allows to consider different materials for the substrate layer (with varying properties along the beam thickness), this layer is herein assumed to be made of perfect and porous FGMs. Due to the existence of

internal pores in FGMs, their mechanical properties are considered according to the modified rule of mixture previously discussed in Chapter 1. The distribution of electric potential within the d_{31} and d_{15} piezoelectric layers is modeled based on nonlinear variations for both SC and OC conditions. The governing equations are finally solved analytically for simply supported boundary condition, and parametric studies are presented. After validating the model, a wide range of results covering the effects of porosity volume fraction, porosity distribution, various piezoelectricity modes, power-law index, and the beam theories on free vibration response of the beam are presented. The presented numerical results can be used as benchmarks to check the accuracy of the numerical models.

The results of the research work presented in this chapter was published in *The Journal of Strain Analysis for Engineering Design* [161].

4.2 Problem Modelling

The layouts of the considered FGM beam surrounded by d_{31} and d_{15} piezoelectric layers are shown in Fig. 4.1. The origin of the Cartesian reference system is located in the mid-plane of the FGM core layer. The geometrical properties L, $2h$ and h_p represent the length of the beam, and the thicknesses of the core layer and each piezoelectric layer, respectively. The composite beam consists of an FGM substrate containing porosities, and two integrated piezoelectric layers. The piezoelectric layers, which are polarized either through the thickness or the length direction, are symmetrically bonded on the top and bottom faces of the FGM substrate. Obviously, to each piezoelectric layer are attached two electrodes, one on its top surface and another on its bottom, but they are not shown in Fig. 4.1 due to their very small thicknesses that are negligible compared to the beam thickness.

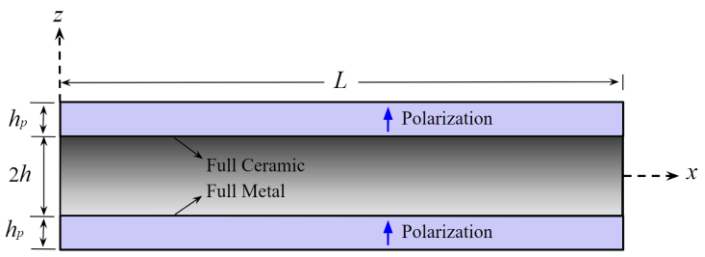

(a)

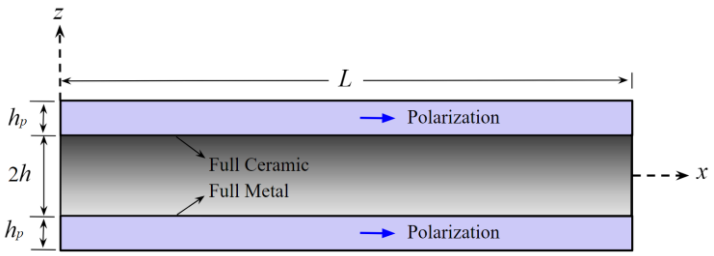

(b)

Fig. 4.1: Layouts of the FGM beam surrounded by piezoelectric layers in (a) d_{31} and (b) d_{15} modes

Mechanical properties of FGMs including porosities vary smoothly along the beam thickness, as were earlier described in Section 1.3 (Chapter 1). Both even and uneven porosity patterns, are here considered to describe the distribution of the internal pores in the substrate layer. Thus, the effective mechanical properties such as Young's modulus $E(z)$ and mass density $\rho(z)$ are modeled based on the modified rule of mixture, as its mathematical expressions were given in Eqs. (1.9) and (1.10). It is reminded that, in those equations, the positive real number N ($0 \leq N < \infty$) and the parameter e_0 ($0 \leq e_0 < 1$) represent the power-law index and the porosity volume fraction of FGMs, respectively. Setting the value of N to zero in Eqs. (1.9) and (1.10), gives a fully ceramic structure while considering large values for N presents the properties of a pure metal structure. However, the material properties of a homogenous beam with no porosity can be obtained by setting $N = e_0 = 0$ in the aforementioned equations. In Fig. 4.2, the cross section of the smart sandwich beam with both perfect and porous FGM substrates are schematically shown. It seems from Fig. 4.2(c) that in uneven pattern, the internal pores are mostly distributed in the middle area of the beam cross-section and the amount of porosity tends to linearly drop to zero at the top and bottom areas of the beam cross-section. According to the fundamental of multi-step infiltration process, which can be employed to fabricate FGM samples, most of the internal pores occur in the middle region. This is due to the reason that it is not easy to totally infiltrate the materials in this area, whilst at the top and bottom zones, the infiltration process of material can be carried out easier, which results in less porosities in these zones.

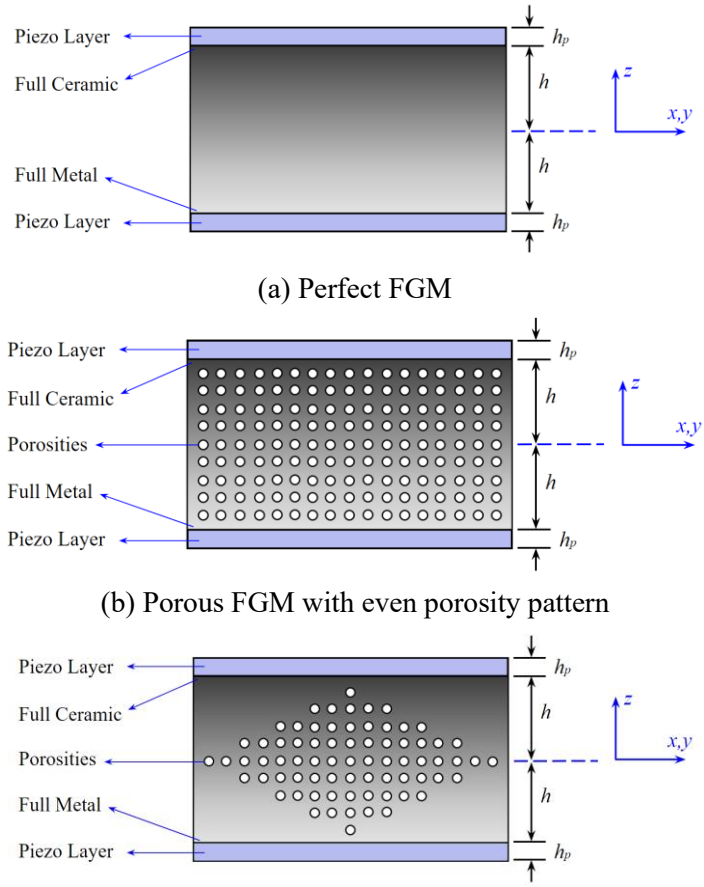

(a) Perfect FGM

(b) Porous FGM with even porosity pattern

(c) Porous FGM with uneven porosity pattern

Fig. 4.2: Patterns of porosity distribution over the cross section of the sandwich beam

Using piezoelectric materials in various operation modes leads to different electromechanical behaviors due to their different piezoelectric coupling coefficients. The shear mode is actually corresponded with the shear deformation of the piezoelectric layers when they are polarized in the axial direction of the beam. Therefore, to provide an accurate prediction, the effects of transverse shear deformation on the system behavior must be considered when analyzing piezoelectrics in shear mode.

Here, the mechanical displacement field is modeled according to Eq. (4.1) in order to consider the shear deformation effects based on various higher-order beam theories:

$$\begin{aligned} U_x(x,z,t) &= u_0 - zw_{0,x} + f(z)\psi \\ U_y(x,z,t) &= 0 \\ U_z(x,z,t) &= w_0 \end{aligned} \tag{4.1}$$

where U_x, U_y and $U_z(x,y,z,t)$ are the components of total displacement at any point of the smart beam along x-, y- and z-direction, respectively. Moreover, $u_0(x,t)$ and $w_0(x,t)$ are the axial and transverse displacement components of the mid-plane of the beam along x- and z-axes, respectively. The rotation function of transverse normal of the mid-plane (at $z = 0$) is also represented by $\psi(x,t)$. Moreover, t is the time, and $f(z)$ is the shape function representing the effect of the transverse shear strain and stress along the thickness of the beam. For comparative purposes, various applicable shape functions corresponded to different beam displacement models and theories are employed in this study as listed in Table 4.1. Note that, in the expressions given in Table 4.1, H is the total thickness of the sandwich beam that is equal to $H = 2h + 2h_p$.

Table 4.1: Various shape functions for different beam theories

Theory	Shape Function
Classical Beam Theory (CBT)	$f(z) = 0$
First-order Shear Deformation Beam Theory (FBT)	$f(z) = z$
Parabolic Shear Deformation Beam Theory (PBT)	$f(z) = z\left[1 - \frac{4}{3}\left(\frac{z}{H}\right)^2\right]$
Sinusoidal Shear Deformation Beam Theory (SBT)	$f(z) = \frac{H}{\pi}\sin\left(\frac{\pi z}{H}\right)$
Exponential Shear Deformation Beam Theory (EBT)	$f(z) = z\exp\left[-2\left(\frac{z}{H}\right)^2\right]$

Using the linear strain-displacement relationship, the components of the strain field for the sandwich beam can be derived from Eq. (4.1), as:

$$\begin{aligned} \varepsilon_{xx} &= u_{0,x} - zw_{0,xx} + f(z)\psi_{,x} \\ \gamma_{xz} &= f'(z)\psi \\ \varepsilon_{yy} &= \varepsilon_{zz} = \gamma_{xy} = \gamma_{yz} = 0 \end{aligned} \tag{4.2}$$

In CBT (see Table 4.1), since $f(z) = 0$, the value of γ_{xz} equals to zero at any point of the beam, meaning that the transverse shear deformation is neglected in this theory. This leads to make this theory not suitable for analyzing moderately-thick and thick beams, unlike the higher-order shear deformation theories.

In the current study, the piezoelectric materials are assumed to be homogenous and transversely isotropic, with the z and x axes as the axes of isotropy in d_{31} and d_{15} operation modes, respectively. The general constitutive equations for both transverse and shear modes are already given in Eq. (1.4) and Eq. (1.5) (Chapter 1).

It should be mentioned that here and hereafter, the superscripts 31 and 15 denote the corresponding variables for the transverse and shear modes of piezoelectric layers, respectively. From Eq. (1.4) and Eq. (1.5), it can be easily seen that the electromechanical relationships between stress and strain components as well as mechanical and electrical properties of piezoelectric materials are dependent on the polarization direction. Thus, these differences in the constitutive equations result in different electromechanical behaviors when using piezoelectric materials in transverse and shear modes.

Approximation of the electric potential variation ϕ through the piezoelectric layers is an important issue. In this study, the electric potential is assumed to have a nonlinear variation [96,167] along the thickness of piezoelectric layers for both transverse and shear modes as well as SC and OC conditions. In the SC condition, both inner and outer surfaces of each piezoelectric layer are held at zero electric voltage, i.e., $\phi(x,\pm h,t) = \phi\left(x,\pm\left(h + h_p\right),t\right) = 0$. On the other hand, applying these conditions only on the outer surfaces and electrically insulating the inner surfaces of each piezoelectric layer result in the OC electrical condition, $\phi(x,\pm h,t) = D_z\left(x,\pm\left(h + h_p\right),t\right) = 0$. Therefore, the electric potential function is first assumed to have the following form with respect to z-coordinate:

$$\phi(x,z,t) = \begin{cases} \phi_0(x,t)\left[1-\left(\dfrac{+2z-2h-h_p}{h_p}\right)^2\right] + Az + B, & h \le z \le h+h_p \\ \phi_0(x,t)\left[1-\left(\dfrac{-2z-2h-h_p}{h_p}\right)^2\right] + Cz + D, & -h-h_p \le z \le -h \end{cases} \tag{4.3}$$

In Eq. (4.3), $\phi_0(x,t)$ denotes the electric potential distribution at the mid-plane of each piezoelectric layer. Also, A, B, C and D are four unknowns, which are functions of the x-coordinate and time, and will be determined satisfying the electrical conditions. Therefore, for each of SC and OC conditions, different expressions will be obtained for A, B, C and D. Applying the respective conditions of both SC and OC cases to Eq. (4.3), the final form of the electric potential function can be obtained for both top and bottom piezoelectric layers, as:

For the *top* piezoelectric layer ($h \le z \le h+h_p$):

$$\begin{aligned} \phi(x,z,t) = \phi_0(x,t)&\left[1-\left(\frac{+2z-2h-h_p}{h_p}\right)^2\right] \\ &+ (z-h)\left[\alpha_1\left(\frac{4}{h_p}\phi_0(x,t) + \frac{e_{15}\zeta_1}{\Xi_{11}}\psi(x,t)\right)\right. \\ &+ \alpha_2\left(\frac{4}{h_p}\phi_0(x,t) + \frac{e_{31}}{\Xi_{33}}\frac{\partial u_0}{\partial x} - \frac{e_{31}(h+h_p)}{\Xi_{33}}\frac{\partial^2 w_0}{\partial x^2}\right. \\ &\left.\left. + \frac{e_{31}\eta_1}{\Xi_{33}}\frac{\partial \psi}{\partial x}\right)\right] \end{aligned} \tag{4.4}$$

For the *bottom* piezoelectric layer ($-h-h_p \le z \le -h$):

$$\begin{aligned}\phi(x,z,t) = \phi_0(x,t)\left[1-\left(\frac{-2z-2h-h_p}{h_p}\right)^2\right] \\ +(z+h)\left[\alpha_3\left(\frac{-4}{h_p}\phi_0(x,t)+\frac{e_{15}\zeta_2}{\Xi_{11}}\psi(x,t)\right)\right. \\ +\alpha_4\left(\frac{-4}{h_p}\phi_0(x,t)+\frac{e_{31}}{\Xi_{33}}\frac{\partial u_0}{\partial x}+\frac{e_{31}(h+h_p)}{\Xi_{33}}\frac{\partial^2 w_0}{\partial x^2}\right. \\ \left.\left.+\frac{e_{31}\eta_2}{\Xi_{33}}\frac{\partial \psi}{\partial x}\right)\right]\end{aligned} \tag{4.5}$$

where the coefficients α_i $(i = 1,2,3,4)$ can be either $\alpha_i = 0$ or $\alpha_i = 1$, for the studied piezoelectric modes and electrical circuit conditions (see Table 4.2). Furthermore, the coefficients $\zeta_1 = f'(z = h + h_p)$, $\zeta_2 = f'(z = -h - h_p)$, $\eta_1 = f(z = h + h_p)$ and $\eta_2 = f(z = -h - h_p)$ have different values depending on the shape function $f(z)$, which is different for each theory (see Table 4.1).

Table 4.2: Values of the parameters α_i $(i = 1,2,3,4)$ for various piezoelectric modes and electrical boundary conditions

Piezoelectric layers (Electrical Circuit Condition)	α_1	α_2	α_3	α_4
d_{31} Mode (SC condition)	0	0	0	0
d_{31} Mode (OC condition)	0	1	0	1
d_{15} Mode (SC condition)	0	0	0	0
d_{15} Mode (OC condition)	1	0	1	0

Using the electric potential functions given in Eqs. (4.4) and (4.5), the components of the electric field in piezoelectric layers can be simply obtained from following relation:

$$(E_x, E_y, E_z) = -(\phi_{,x}, \phi_{,y}, \phi_{,z}) \tag{4.6}$$

On the other hand, since FGMs are isotropic materials, they simply obey the Hooke's law, and their constitutive equations are of the form already given in Eq. (1.12) in Chapter 1.

4.3 Governing Equations

Employing the variational principle, the electromechanical equations of motion for the hybrid beam can be derived as:

$$\begin{aligned}
&\frac{\partial N_{xx}^{pq}}{\partial x} - I_0\frac{\partial^2 u_0}{\partial t^2} - I_{01}\frac{\partial^2 \psi}{\partial t^2} + I_1\frac{\partial^3 w_0}{\partial x \partial t^2} = 0\\
&\frac{\partial^2 M_{xx}^{pq}}{\partial x^2} - I_1\frac{\partial^3 u_0}{\partial x \partial t^2} - I_{11}\frac{\partial^3 \psi}{\partial x \partial t^2} - I_0\frac{\partial^2 w_0}{\partial t^2} + I_2\frac{\partial^4 w_0}{\partial x^2 \partial t^2} = 0\\
&\frac{\partial \widehat{M}_{xx}^{pq}}{\partial x} - \hat{Q}_{xz}^{pq} - I_{01}\frac{\partial^2 u_0}{\partial t^2} - I_{02}\frac{\partial^2 \psi}{\partial t^2} + I_{11}\frac{\partial^3 w_0}{\partial x \partial t^2} = 0
\end{aligned} \tag{4.7}$$

where N_{xx}, M_{xx}, $\widehat{M}_{xx}$ and $\hat{Q}_{xz}$ are the stress resultants. It should be noted that here and hereafter, the superscript *pq* represents the associated variables and coefficients for the transverse and shear modes of piezoelectric materials so that it can be either 31 or 15. For instance, when *pq* is equal to 31, it means that the respective constitutive equations of d_{31} mode (given in Eq. (1.4) in Chapter 1) must be used to determine the related coefficients and variables such as the stress resultants. Moreover, the appearance of the terms $\widehat{M}_{xx}^{pq}$ and $\hat{Q}_{xz}^{pq}$ in Eq. (4.7) is due to the particular form of the mechanical displacement field and they are not appeared in the equations of motion, when using the classical beam theory (or CBT). The terms I_i and I_{ij} which represent the mass inertias of the sandwich beam are also defined as:

$$I_i = \int_{-h-h_p}^{-h} \rho\, z^i\, dz + \int_{-h}^{h} \rho(z)\, z^i\, dz + \int_{h}^{h+h_p} \rho\, z^i\, dz, \quad (i = 0, 1, 2) \tag{4.8a}$$

$$\begin{aligned}
I_{ij} = &\int_{-h-h_p}^{-h} \rho\, z^i\, [f(z)]^j\, dz + \int_{-h}^{h} \rho\, z^i\, [f(z)]^j\, dz\\
&+ \int_{h}^{h+h_p} \rho\, z^i\, [f(z)]^j\, dz, \quad (i = 0, 1 \text{ and } j = 1, 2)
\end{aligned} \tag{4.8b}$$

And similarly, the stress resultants are defined in terms of stress components in the following forms:

$$\left(N_{xx}^{pq}, M_{xx}^{pq}\right) = \int_{-h-h_p}^{-h} \sigma_{xx}^{pq}\,(1, z)\,dz + \int_{-h}^{h} \sigma_{xx}^{c}\,(1, z)\,dz + \int_{h}^{h+h_p} \sigma_{xx}^{pq}\,(1, z)\,dz \tag{4.9a}$$

$$\widehat{M}_{xx}^{pq} = \int_{-h-h_p}^{-h} \sigma_{xx}^{pq}\, f(z)\,dz + \int_{-h}^{h} \sigma_{xx}^{c}\, f(z)\,dz + \int_{+h}^{h+h_p} \sigma_{xx}^{pq}\, f(z)\,dz \tag{4.9b}$$

$$\widehat{Q}_{xz}^{pq} = \int_{-h-h_p}^{-h} \sigma_{xz}^{pq}\, f'(z)\,dz + \int_{-h}^{h} \sigma_{xz}^{c}\, f'(z)\,dz + \int_{h}^{h+h_p} \sigma_{xz}^{pq}\, f'(z)\,dz \tag{4.9c}$$

Moreover, from the Hamilton's principle, the following mechanical boundary conditions at the edges $x = 0$ and $x = L$ can be obtained:

$$\begin{array}{lll} u_0 = 0 & \text{or} & N_{xx}^{pq} = 0 \\ w_{0,x} = 0 & \text{or} & M_{xx}^{pq} = 0 \\ w_0 = 0 & \text{or} & M_{xx,x}^{pq} = 0 \\ \psi = 0 & \text{or} & \widehat{M}_{xx}^{pq} = 0 \end{array} \tag{4.10}$$

Generally, the left-hand side boundary conditions in Eq. (4.10) are called essential or geometric conditions, because they correspond to prescribe displacements and rotations, and must be rigorously imposed according to the beam boundaries. Besides, the right-hand side ones are called natural boundary conditions, which are associated with the loads and moment resultants acting on each end of the beam, and they are implicitly contained in the Hamilton's principle. In the next section, the expressions given in Eq. (4.10) will be summarized for a particular type of mechanical boundary condition at the beam boundaries.

Using the mechanical displacement field and strain-displacement relations given in Eqs. (4.1) and (4.2), as well as with the help of constitutive equations of both piezoelectrics and FGMs, the stress resultants of Eq. (4.9) can be rewritten in terms of displacement components and electric potential function, as:

$$N_{xx}^{pq} = a_1^{pq}\frac{\partial u_0}{\partial x} + a_2^{pq}\frac{\partial^2 w_0}{\partial x^2} + a_3^{pq}\frac{\partial \psi}{\partial x} + \mu_1^{pq}\phi_0 + \beta_1^{pq}\frac{\partial \phi_0}{\partial x} \tag{4.11a}$$

$$M_{xx}^{pq} = a_4^{pq}\frac{\partial u_0}{\partial x} + a_5^{pq}\frac{\partial^2 w_0}{\partial x^2} + a_6^{pq}\frac{\partial \psi}{\partial x} + \mu_2^{pq}\phi_0 + \beta_2^{pq}\frac{\partial \phi_0}{\partial x} \tag{4.11b}$$

$$\widehat{M}_{xx}^{pq} = a_7^{pq}\frac{\partial u_0}{\partial x} + a_8^{pq}\frac{\partial^2 w_0}{\partial x^2} + a_9^{pq}\frac{\partial \psi}{\partial x} + \mu_3^{pq}\phi_0 + \beta_3^{pq}\frac{\partial \phi_0}{\partial x} \tag{4.11c}$$

$$\widehat{Q}_{xz}^{pq} = a_{10}^{pq}\psi + a_{11}^{pq}\frac{\partial^2 \psi}{\partial x^2} + a_{12}^{pq}\frac{\partial^2 \psi}{\partial x^2} + a_{13}^{pq}\frac{\partial^3 w_0}{\partial x^3} + \mu_4^{pq}\phi_0 + \beta_4^{pq}\frac{\partial \phi_0}{\partial x} \tag{4.11d}$$

where the coefficients a_i^{pq} $(i = 1, 2, \dots, 13)$, β_i^{pq} $(i = 1, 2, \dots, 4)$, and μ_i^{pq} $(i = 1, 2, \dots, 4)$ are functions of the geometry parameters, as well as mechanical and electrical properties of both FGM core and piezoelectric layers. The respective expressions of such coefficients are given in Relations (C.1-C.4) of the Appendix C. note that those coefficients have different values for transverse and shear modes, as well as for SC and OC electrical conditions, as are given separately the Appendix C.

Substituting Eq. (4.11) into Eq. (4.7) leads to the beam equations of motion in terms of displacement field components and the electric potential function, as:

$$a_1^{pq}\frac{\partial^2 u_0}{\partial x^2} + a_2^{pq}\frac{\partial^3 w_0}{\partial x^3} + a_3^{pq}\frac{\partial^2 \psi}{\partial x^2} + \mu_1^{pq}\frac{\partial \phi_0}{\partial x} + \beta_1^{pq}\frac{\partial^2 \phi_0}{\partial x^2} - I_0\frac{\partial^2 u_0}{\partial t^2} - I_{01}\frac{\partial^2 \psi}{\partial t^2} + I_1\frac{\partial^3 w_0}{\partial x \partial t^2} = 0 \tag{4.12a}$$

$$a_4^{pq}\frac{\partial^3 u_0}{\partial x^3} + a_5^{pq}\frac{\partial^4 w_0}{\partial x^4} + a_6^{pq}\frac{\partial^3 \psi}{\partial x^3} + \mu_2^{pq}\frac{\partial^2 \phi_0}{\partial x^2} + \beta_2^{pq}\frac{\partial^3 \phi_0}{\partial x^3} - I_1\frac{\partial^3 u_0}{\partial x \partial t^2} - I_{11}\frac{\partial^3 \psi}{\partial x \partial t^2} - I_0\frac{\partial^2 w_0}{\partial t^2} + I_2\frac{\partial^4 w_0}{\partial x^2 \partial t^2} = 0 \tag{4.12b}$$

$$\left(a_7^{pq} - a_{12}^{pq}\right)\frac{\partial^2 u_0}{\partial x^2} + \left(a_8^{pq} - a_{13}^{pq}\right)\frac{\partial^3 w_0}{\partial x^3} + \left(a_9^{pq} - a_{11}^{pq}\right)\frac{\partial^2 \psi}{\partial x^2} - a_{10}^{pq}\psi + \left(\mu_3^{pq} - \beta_4^{pq}\right)\frac{\partial \phi_0}{\partial x} + \beta_3^{pq}\frac{\partial^2 \phi_0}{\partial x^2} - \mu_4^{pq}\phi_0 - I_{01}\frac{\partial^2 u_0}{\partial t^2} - I_{02}\frac{\partial^2 \psi}{\partial t^2} + I_{11}\frac{\partial^3 w_0}{\partial x \partial t^2} = 0 \tag{4.12c}$$

The last equation, which is the electric displacement equation coupled with the induced mechanical displacements, can be determined according to the Maxwell's electrostatic equation:

$$\int_{-t_c-t_p}^{-t_c} \left(D_{x,x}^{pq} + D_{z,z}^{pq}\right) dz + \int_{+t_c}^{+t_c+t_p} \left(D_{x,x}^{pq} + D_{z,z}^{pq}\right) dz = 0 \tag{4.13}$$

Substituting the expressions of electric displacement field components in Eq. (4.13), the last electromechanical governing equation can be derived for both transverse and shear modes as:

$$\begin{aligned} b_1^{pq}\psi + b_2^{pq}\frac{\partial \psi}{\partial x} + b_3^{pq}\frac{\partial^2 \psi}{\partial x^2} + b_4^{pq}\frac{\partial^3 \psi}{\partial x^3} + b_5^{pq}\frac{\partial^2 u_0}{\partial x^2} + b_6^{pq}\frac{\partial^3 u_0}{\partial x^3} \\ + b_7^{pq}\frac{\partial^2 w_0}{\partial x^2} + b_8^{pq}\frac{\partial^3 w_0}{\partial x^3} + b_9^{pq}\frac{\partial^4 w_0}{\partial x^4} + \mu_5^{pq}\phi_0 \\ + \beta_5^{pq}\frac{\partial^2 \phi_0}{\partial x^2} = 0 \end{aligned} \tag{4.14}$$

The coefficients b_i^{pq} $(i = 1, \dots, 9)$, μ_5^{pq} and β_5^{pq} are defined in Relation (C.1-C.4) of Appendix C, for both piezoelectric modes, as well as the electrical boundary conditions.

4.4 Solution Procedure

In the previous section, the four electromechanical governing equations of motion (4.12) and (4.14) were derived according to the considered mechanical displacement field. Here, it is assumed that the edges $x = 0$ and $x = L$ of the sandwich beam are mechanically simply supported and electrically grounded to zero potential in both transverse and shear modes. Therefore, the essential and natural boundary conditions (i.e., Eq. (4.10)) can be expressed for beams with simply supported edges, as:

$$N_{xx}^{pq} = w_0 = M_{xx}^{pq} = \widehat{M}_{xx}^{pq} = \phi_0 = 0 \tag{4.15}$$

The Navier-type procedure is indeed employed to analytically solve the beam governing equations (4.12) and (4.14) for calculating the exact resonance frequencies. According to Navier's technique, the unknown components of the

mechanical displacement field, as well as the electric potential function may be of the form:

$$\begin{Bmatrix} u_0 \\ \psi \\ w_0 \\ \phi_0 \end{Bmatrix} = \sum_{m=1}^{\infty} \begin{Bmatrix} X_m^{u_0} \cos(\beta_m x) \\ X_m^{\psi} \cos(\beta_m x) \\ X_m^{w_0} \sin(\beta_m x) \\ X_m^{\phi_0} \sin(\beta_m x) \end{Bmatrix} T(t) \tag{4.16}$$

where m denotes the number of half-waves in the axial direction, and $\beta_m = m\pi/L$. Also, $X_m^{u_0}$, X_m^{ψ}, $X_m^{w_0}$ and $X_m^{\phi_0}$ are the unknown coefficients, and $T(t) = e^{i\omega t}$ in which $i = \sqrt{-1}$, and ω is the natural frequency of the coupled beam. It can be verified that such set of series-type solution can satisfy the boundary conditions of simply supported beam given in Eq. (4.15).

Substituting the expansions of u_0, ψ, w_0 and ϕ_0 from Eq. (4.16) into the governing equations (4.12) and (4.14) results in the following eigenvalue problem:

$$([K]_{4\times4} - \omega^2[M]_{4\times4}) \begin{Bmatrix} X_m^{u_0} \\ X_m^{\psi} \\ X_m^{w_0} \\ X_m^{\phi_0} \end{Bmatrix} = \{0\} \tag{4.17}$$

in which $[K]$, $[M]$ and $\left\{X_m^{u_0}, X_m^{\psi}, X_m^{w_0}, X_m^{\phi_0}\right\}^T$ denote the stiffness matrix, mass matrix and the vector of unknown coefficients, respectively. Eq. (4.17) represents a system of four algebraic homogenous equations in terms of the unknown coefficients. For a nontrivial solution of the vector of coefficients, the determinant of the coefficient matrix must be set to zero (i.e., $|[K] - \omega^2[M]| = 0$), which yields a characteristic equation in terms of ω. Positive real roots of that equation are the natural free vibration frequencies of the piezoelectric bimorph beam.

4.5 Numerical Results

4.5.1 Model Validation

To ensure the accuracy of the present models and formulations, the present numerical results are first compared with some available in the literature. It must be mentioned that due to slight variation of the Poisson's ratio ν through the thickness direction, its value is assumed to be constant [8]. In Table 4.3, the present results are compared with those reported by Pradhan et al. [168], for a sandwich beam composed of an isotropic core and d_{31} piezoelectric layers. It is obvious that as the value of the thickness ration $h_p/2h$ goes to zero, the natural frequencies of the sandwich beam approach those of the homogenous beam. The numerical results reported by Pradhan et al. [168] are numerically calculated based on Bernoulli-Euler's and Timoshenko's beam theories (called CBT and TBT, respectively, in [168]), for the following material properties of an FGM beam:

Alumina: E_c=380 GPa, ρ_c=3800 kg/m^3, ν_c=0.3

Aluminum: E_m=70 GPa, ρ_m=2700 kg/m^3, ν_m=0.3

Table 4.3: Comparison of the first five dimensionless frequencies, $[\omega L^2/2h]\sqrt{\rho_m/E_m}$, with those reported in [168] ($e_0 = 0, N = 0$)

$h_p/2h$	Source	1st mode	2nd mode	3rd mode	4th mode	5th mode
$L/2h = 20$						
10^{-1}	CBT (Present)	6.1549	24.4738	54.5326	95.6643	126.7363
10^{-2}	CBT (Present)	6.8282	27.2202	60.9025	107.4347	149.8236
10^{-3}	CBT (Present)	6.9386	27.6686	61.9359	109.3302	153.0845
10^{-4}	CBT (Present)	6.9503	27.7160	62.0450	109.5302	153.4245
10^{-5}	CBT (Present)	6.9515	27.7207	62.0560	109.5503	153.4586
0	CBT (Present)	6.9516	27.7212	62.0572	109.5525	153.4624
0	CBT [168]	6.9516	27.7212	62.0573	109.5542	153.4624
$L/2h = 5$						
10^{-1}	CBT (Present)	5.9790	22.0144	31.6841	44.2232	63.3681
10^{-2}	CBT (Present)	6.7147	25.5444	37.4559	53.3843	74.9118
10^{-3}	CBT (Present)	6.8331	26.1012	38.2711	54.8405	76.5422
10^{-4}	CBT (Present)	6.8456	26.1599	38.3561	54.9946	76.7122
10^{-5}	CBT (Present)	6.8469	26.1658	38.3646	55.0102	76.7293
0	CBT (Present)	6.8470	26.1665	38.3656	55.0119	76.7312
0	CBT [168]	6.8470	26.1665	38.3655	55.0119	76.7312

The results of the second comparison study are presented in Table 4.4, where the fundamental frequencies of a simply supported beam made of FGMs are computed for different power-law indices (ranging from 0 to 10), and compared with those of Pradhan et al. [168], and Aydogdu and Taskin [169].

As one can see from Table 4.3 and the second column of Table 4.4, when $N = 0$, the present results correspond closely to those of Ref. [168] and Ref. [169]. For $N \neq 0$, again, excellent agreement is clearly seen when compared with the analytically computed results of Ref. [169]. However, in some cases, the differences between the results of the present analytical models and the Rayleigh-Ritz's method (utilized in [168]) are greater than those with the frequency values predicted in [169]. It is possible that the numerical approach used in [168] did not give fully converged values of the frequencies.

Table 4.4. Comparison of the dimensionless fundamental frequency, $[\omega L^2/2h]\sqrt{\rho_m/E_m}$, for an FGM beam with those of Refs. [168,169] ($L/2h = 20$, $e_0 = 0$)

Source	$N = 0$	$N = 0.5$	$N = 0.5$	$N = 2$	$N = 5$	$N = 10$
CBT [168]	6.9516	5.7627	5.2563	4.8259	4.3803	4.0208
CBT [169]	6.9510	-	4.9070	4.3340	-	3.8040
CBT (Present)	6.9516	5.5942	4.9039	4.3305	3.9814	3.7998
FBT [168]	6.9317	5.7471	5.2417	4.8112	4.3647	4.0059
FBT [169]	6.9310	-	4.8950	4.3230	-	3.7910
FBT (Present)	6.9314	5.5797	4.8919	4.3197	3.9695	3.7870
PBT (Present)	6.9273	5.5770	4.8895	4.3168	3.9643	3.7815
SBT (Present)	6.9274	5.5771	4.8895	4.3168	3.9641	3.7814
EBT (Present)	6.9275	5.5771	4.8895	4.3168	3.9641	3.7814

In the last comparison example, the fundamental resonant frequencies of an FGM beam with $N = 1$ are calculated for different values of $L/2h$, and the respective dimensionless results along with those of Su et al. [170] are listed in Table 4.5. Note that in Ref. [170], Bernoulli-Euler's beam theory is used in conjunction with the Wittrick-Williams's algorithm to extract the natural frequencies of the FGM beam. A maximum difference of 3% is seen among the results, which may be appeared due to employing the different numerical and analytical solution approaches developed in the two studies. It is also interesting to

note that with increasing the thickness-to-length ratio ($2h/L$), the difference between the frequencies calculated by the classical (CBT) and the higher-order theories (e.g., FBT) increases. This is due to the fact that in classical theories, the transverse shear deformation effect is neglected so that the results predicted by such theories are not accurate for relatively-thick and thick structures.

Table 4.5: Comparison of the dimensionless fundamental frequency of an FGM beam, $[100\omega(2h)]\sqrt{\rho_m/E_m}$, with those of Ref. [170]

	$L/2h$		
Source	5	10	100
CBT [170]	15.436	3.9059	0.039218
CBT (Present)	15.912	4.0312	0.040492
FBT (Present)	15.275	3.9868	0.040487
PBT (Present)	15.157	3.9781	0.040486
SBT (Present)	15.158	3.9782	0.040486
EBT (Present)	15.162	3.9784	0.040486

Having completed the above verification examples which confirm the accuracy of the present model, a parametric study covering the effects of various beam parameters and piezoelectric characteristics is presented in the next subsection.

4.5.2 Parametric Study and Discussion

In this section, new results are presented in both tabular and graphical forms, for the free vibration of FGM beams integrated with d_{31} and d_{15} piezoelectric layers. Aluminum (Al) and Alumina (Al_2O_3) are considered as the metal and ceramic constituents of the FGM core, respectively; and the piezoelectric layers are also assumed to be made of PZT-5H.

In Tables 4.6 to 4.9, based on the presented CBT, FBT, PBT, SBT and EBT, the effects of porosity volume fraction e_0, porosity distribution, power-law index N and electrical circuit condition on the resonance frequencies of both d_{31} and d_{15} piezoelectric bimorph FGM beams are investigated. In those tables are listed the

first three SC and OC eigenfrequencies of smart FGM beams for different values of power-law index and porosity parameter. The tables imply that FGM beams sandwiched between d_{15} piezoelectric layers provide lower frequencies than those of FGM beams with d_{31} piezoelectric layers. In addition, when the bonded piezoelectric layers are polarized through their thickness, the OC natural frequencies are considerably larger than those of the similar beams with SC condition, whereas there is minimal differences between the SC and OC resonant frequencies when the beams are surrounded by d_{15} piezoelectric layers. The power-law index also plays an important role on the frequency behavior of the piezoelectric coupled FGM beam. As seen in the tables, for both even and uneven porosity distributions, increasing the power-law index significantly decreases the first three natural frequencies of the smart sandwich beam irrespective of the value of e_0, piezoelectricity mode and electrical boundary condition. This is due to the fact that an increase in the value of N leads to a decrease in the effective modulus of elasticity, and consequently the beam becomes less rigid. Thus, as it is well-known from mechanical vibration, resonance frequencies reduce as the structure stiffness decreases. It is obvious that the beam resonant frequencies are the same for both even and uneven porosity distribution, when $e_0 = 0$. This is due to the considered functions for the mechanical properties of FGMs with porosities. For the studied power-law indices and porosity parameters, the bimorph FGM beams with uneven porosity pattern exhibit higher frequencies than those of the beams with evenly distributed pores. Inspection of these tables reveals that the natural frequencies predicted by CBT are comparatively greater than those forecasted by higher deformation beam theories, regardless of the considered electrical and material parameters of the hybrid beams. It is also observed that the results of the higher-order theories (i.e. PBT, SBT and EBT) are close to each other for all the considered beam parameters.

Table 4.6: First three SC resonance frequencies (Hz) of piezoelectric bimorph FGM beams with even porosity distribution ($L/2h = 10,\ h_p/2h = 0.2$)

Source	Mode 1 ($m = 1$)		Mode 2 ($m = 2$)		Mode 3 ($m = 3$)	
	$N = 0$	$N = 10$	$N = 0$	$N = 10$	$N = 0$	$N = 10$
$e_0 = 0$						
FGM beam with d_{31} piezoelectric layers						
CBT	435.309	349.683	1691.218	1353.334	3637.466	2894.397
FBT	428.399	339.793	1600.435	1230.287	3286.992	2444.241
PBT	427.996	337.747	1594.783	1207.247	3263.123	2367.621
SBT	427.979	337.624	1594.517	1205.928	3261.883	2363.508
EBT	427.974	337.529	1594.398	1204.915	3261.190	2360.444
FGM beam with d_{15} piezoelectric layers						
CBT	429.433	340.917	1668.391	1319.352	3588.370	2821.552
FBT	422.792	331.726	1581.021	1204.554	3250.641	2400.152
PBT	422.360	329.753	1574.984	1182.130	3225.237	2324.884
SBT	422.339	329.631	1574.662	1180.794	3223.773	2320.650
EBT	422.329	329.533	1574.480	1179.743	3222.836	2317.404
$e_0 = 0.15$						
FGM beam with d_{31} piezoelectric layers						
CBT	438.306	343.240	1700.688	1325.258	3651.151	2824.439
FBT	431.172	331.531	1607.609	1183.332	3294.759	2318.360
PBT	430.770	327.491	1602.029	1140.739	3271.113	2184.861
SBT	430.763	327.167	1601.815	1137.516	3270.049	2175.412
EBT	430.763	326.872	1601.754	1134.621	3269.554	2167.085
FGM beam with d_{15} piezoelectric layers						
CBT	432.023	333.362	1676.310	1286.971	3598.814	2742.457
FBT	425.183	322.589	1586.941	1155.814	3256.171	2272.850
PBT	424.756	318.791	1580.953	1115.291	3230.911	2144.459
SBT	424.739	318.483	1580.677	1112.175	3229.607	2135.195
EBT	424.733	318.201	1580.548	1109.361	3228.849	2126.979
$e_0 = 0.3$						
FGM beam with d_{31} piezoelectric layers						
CBT	441.771	333.189	1711.595	1281.583	3666.819	2715.761
FBT	434.368	317.771	1615.777	1103.598	3303.404	2108.475
PBT	433.977	303.600	1610.253	975.9310	3279.916	1755.067
SBT	433.970	301.470	1610.100	959.1190	3279.057	1713.398
EBT	433.976	299.089	1610.108	940.9700	3278.793	1669.579
FGM beam with d_{15} piezoelectric layers						
CBT	435.020	321.571	1685.438	1236.523	3610.783	2619.086
FBT	427.942	307.633	1593.686	1074.488	3262.293	2063.365
PBT	427.518	294.665	1587.728	955.2960	3237.110	1728.135
SBT	427.506	292.705	1587.508	939.4290	3235.992	1688.057
EBT	427.505	290.511	1587.441	922.2590	3235.443	1645.799

Table 4.7: First three OC resonance frequencies (Hz) of piezoelectric bimorph FGM beams with even porosity distribution ($L/2h = 10,\ h_p/2h = 0.2$)

Source	Mode 1 ($m = 1$)		Mode 2 ($m = 2$)		Mode 3 ($m = 3$)	
	$N = 0$	$N = 10$	$N = 0$	$N = 10$	$N = 0$	$N = 10$
$e_0 = 0$						
FGM beam with d_{31} piezoelectric layers						
CBT	437.319	352.659	1699.004	1364.830	3654.124	2918.911
FBT	430.260	342.382	1606.324	1237.283	3296.560	2453.361
PBT	429.908	340.405	1601.322	1215.129	3275.147	2379.920
SBT	429.895	340.288	1601.100	1213.873	3274.074	2376.040
EBT	429.893	340.198	1601.024	1212.928	3273.551	2373.227
FGM beam with d_{15} piezoelectric layers						
CBT	429.433	340.917	1668.391	1319.362	3588.370	2821.608
FBT	423.017	332.786	1583.783	1216.734	3260.564	2441.427
PBT	422.360	329.753	1574.984	1182.137	3225.237	2324.910
SBT	422.339	329.631	1574.662	1180.801	3223.773	2320.676
EBT	422.329	329.534	1574.480	1179.750	3222.836	2317.429
$e_0 = 0.15$						
FGM beam with d_{31} piezoelectric layers						
CBT	440.454	346.592	1708.998	1338.171	3668.898	2851.946
FBT	433.157	334.357	1613.855	1190.439	3304.845	2326.738
PBT	432.816	330.351	1608.978	1148.459	3283.841	2195.712
SBT	432.807	330.029	1608.812	1145.272	3282.957	2186.432
EBT	432.811	329.736	1608.799	1142.420	3282.646	2178.294
FGM beam with d_{15} piezoelectric layers						
CBT	432.023	333.363	1676.310	1286.991	3598.814	2742.571
FBT	425.437	324.260	1590.035	1174.401	3267.203	2334.091
PBT	424.756	318.792	1580.953	1115.303	3230.911	2144.497
SBT	424.739	318.484	1580.677	1112.186	3229.607	2135.233
EBT	424.733	318.202	1580.548	1109.372	3228.849	2127.015
$e_0 = 0.3$						
FGM beam with d_{31} piezoelectric layers						
CBT	444.079	337.096	1720.506	1296.685	3685.808	2748.004
FBT	436.494	320.876	1622.424	1110.363	3314.058	2114.974
PBT	436.164	306.425	1617.666	981.4270	3293.427	1760.467
SBT	436.161	304.244	1617.565	964.3930	3292.765	1718.554
EBT	436.171	301.807	1617.626	946.0130	3292.702	1674.495
FGM beam with d_{15} piezoelectric layers						
CBT	435.020	321.574	1685.438	1236.574	3610.783	2619.379
FBT	428.232	310.864	1597.194	1108.407	3274.695	2169.794
PBT	427.518	294.668	1587.728	955.3130	3237.110	1728.172
SBT	427.506	292.707	1587.508	939.4440	3235.992	1688.087
EBT	427.505	290.513	1587.441	922.2730	3235.443	1645.823

Table 4.8: First three SC resonance frequencies (Hz) of piezoelectric bimorph FGM beams with uneven porosity distribution ($L/2h = 10,\ h_p/2h = 0.2$)

Source	Mode 1 ($m = 1$)		Mode 2 ($m = 2$)		Mode 3 ($m = 3$)	
	$N = 0$	$N = 10$	$N = 0$	$N = 10$	$N = 0$	$N = 10$
$e_0 = 0$						
FGM beam with d_{31} piezoelectric layers						
CBT	435.309	349.683	1691.218	1353.334	3637.466	2894.397
FBT	428.399	339.793	1600.435	1230.287	3286.992	2444.241
PBT	427.996	337.747	1594.783	1207.247	3263.123	2367.621
SBT	427.979	337.624	1594.517	1205.928	3261.883	2363.508
EBT	427.974	337.529	1594.398	1204.915	3261.190	2360.444
FGM beam with d_{15} piezoelectric layers						
CBT	429.433	340.917	1668.391	1319.352	3588.370	2821.552
FBT	422.792	331.726	1581.021	1204.554	3250.641	2400.152
PBT	422.360	329.753	1574.984	1182.130	3225.237	2324.884
SBT	422.339	329.631	1574.662	1180.794	3223.773	2320.650
EBT	422.329	329.533	1574.480	1179.743	3222.836	2317.404
$e_0 = 0.15$						
FGM beam with d_{31} piezoelectric layers						
CBT	439.971	351.524	1707.924	1358.639	3669.067	2900.099
FBT	432.801	340.421	1614.195	1222.581	3309.303	2409.524
PBT	432.322	336.877	1607.598	1184.239	3281.976	2286.552
SBT	432.297	336.543	1607.223	1180.804	3280.334	2276.160
EBT	432.283	336.225	1606.996	1177.559	3279.244	2266.487
FGM beam with d_{15} piezoelectric layers						
CBT	433.944	342.375	1684.530	1323.200	3618.811	2824.199
FBT	427.057	332.084	1594.373	1196.535	3272.307	2365.818
PBT	426.551	328.713	1587.402	1159.683	3243.480	2246.465
SBT	426.521	328.393	1586.971	1156.340	3241.617	2236.224
EBT	426.502	328.085	1586.682	1153.169	3240.285	2226.649
$e_0 = 0.3$						
FGM beam with d_{31} piezoelectric layers						
CBT	444.932	353.235	1725.657	1363.125	3702.488	2903.019
FBT	437.477	340.506	1628.719	1210.070	3332.682	2360.871
PBT	436.907	333.870	1621.001	1142.228	3301.309	2153.628
SBT	436.871	332.968	1620.492	1133.638	3299.182	2129.197
EBT	436.846	331.997	1620.133	1124.572	3297.609	2103.865
FGM beam with d_{15} piezoelectric layers						
CBT	438.746	343.640	1701.665	1325.973	3651.012	2823.493
FBT	431.589	331.878	1608.471	1183.837	3295.021	2318.004
PBT	430.993	325.630	1600.396	1119.174	3262.199	2118.325
SBT	430.952	324.777	1599.832	1110.937	3259.855	2094.601
EBT	430.923	323.859	1599.412	1102.234	3258.042	2069.968

Table 4.9: First three OC resonance frequencies (Hz) of piezoelectric bimorph FGM beams with uneven porosity distribution ($L/2h = 10,\ h_p/2h = 0.2$)

Source	Mode 1 ($m = 1$)		Mode 2 ($m = 2$)		Mode 3 ($m = 3$)	
	$N = 0$	$N = 10$	$N = 0$	$N = 10$	$N = 0$	$N = 10$
$e_0 = 0$						
FGM beam with d_{31} piezoelectric layers						
CBT	437.319	352.659	1699.004	1364.830	3654.124	2918.911
FBT	430.260	342.382	1606.324	1237.283	3296.560	2453.361
PBT	429.908	340.405	1601.322	1215.129	3275.147	2379.920
SBT	429.895	340.288	1601.100	1213.873	3274.074	2376.040
EBT	429.893	340.198	1601.024	1212.928	3273.551	2373.227
FGM beam with d_{15} piezoelectric layers						
CBT	429.433	340.917	1668.391	1319.362	3588.370	2821.608
FBT	423.017	332.786	1583.783	1216.734	3260.564	2441.427
PBT	422.360	329.753	1574.984	1182.137	3225.237	2324.910
SBT	422.339	329.631	1574.662	1180.801	3223.773	2320.676
EBT	422.329	329.534	1574.480	1179.750	3222.836	2317.429
$e_0 = 0.15$						
FGM beam with d_{31} piezoelectric layers						
CBT	442.033	354.626	1715.902	1370.618	3686.116	2925.620
FBT	434.706	343.076	1620.188	1229.467	3318.972	2417.995
PBT	434.279	339.576	1614.259	1191.799	3294.162	2297.641
SBT	434.257	339.244	1613.928	1188.396	3292.690	2287.402
EBT	434.247	338.927	1613.747	1185.187	3291.774	2277.899
FGM beam with d_{15} piezoelectric layers						
CBT	433.944	342.376	1684.530	1323.214	3618.811	2824.277
FBT	427.302	333.452	1597.366	1211.953	3283.004	2417.196
PBT	426.551	328.714	1587.402	1159.691	3243.480	2246.495
SBT	426.521	328.393	1586.971	1156.348	3241.617	2236.253
EBT	426.502	328.086	1586.682	1153.177	3240.285	2226.677
$e_0 = 0.3$						
FGM beam with d_{31} piezoelectric layers						
CBT	447.048	356.485	1733.838	1375.669	3719.949	2929.730
FBT	439.427	343.226	1634.818	1216.747	3342.450	2368.464
PBT	438.911	336.568	1627.787	1149.089	3313.654	2162.713
SBT	438.879	335.654	1627.323	1140.446	3311.700	2138.260
EBT	438.858	334.672	1627.010	1131.324	3310.303	2112.907
FGM beam with d_{15} piezoelectric layers						
CBT	438.746	343.641	1701.665	1325.993	3651.012	2823.606
FBT	431.857	333.713	1611.727	1204.022	3306.591	2383.878
PBT	430.993	325.631	1600.396	1119.185	3262.199	2118.356
SBT	430.952	324.778	1599.832	1110.947	3259.855	2094.631
EBT	430.923	323.860	1599.412	1102.243	3258.042	2069.995

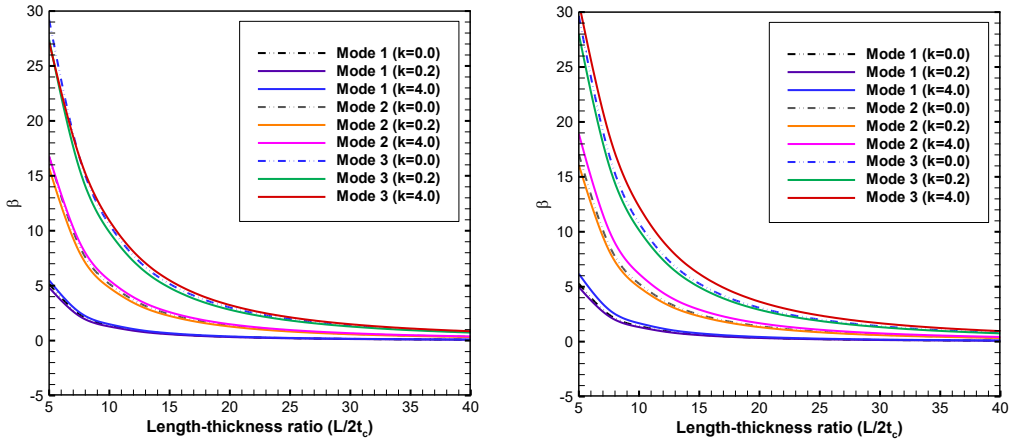

(a) Even (b) Uneven

Fig. 4.3: Variation of β versus the length-thickness ratio ($L/2h$) for an FGM beam without piezoelectric layers (e_0=0.3, $h_p = 0$, k is power-law index)

To gain a deeper insight into the effect of various beam theories on the eigenfrequency response, the variation of percentage difference in frequency β (defined by Eq. (4.18)) versus the length-to-thickness ratio $L/2h$ is plotted in Fig. 4.3 for an FGM beam with different patterns of porosity distribution.

$$\beta = \frac{\omega|_{\text{Predicted by CBT}} - \omega|_{\text{Predicted by PBT}}}{\omega|_{\text{Predicted by PBT}}} \times 100 \tag{4.18}$$

Since the frequencies predicted by higher-order beam theories are very close to each other, only PBT is used in Eq. (4.18). Figs. (4.3a) and (4.3b) show the variation of β for the first three natural frequencies of the FGM beam with different values of power-law index, namely 0, 0.2 and 4. As expected, positive values are obtained for β in all the vibration modes, which show that CBT predicts higher frequencies with respect to those calculated by PBT. As obvious in the figures, at a fixed value of length-to-thickness ratio, the amplitude of β is the most for the frequency of the third vibrational mode, and the least value is determined for the fundamental frequency. This means that there is a considerable difference between the results of CBT and higher-order theories, when calculating the frequencies of higher vibrational modes, especially for thicker beams (i.e. $L/2h < 15$). In other words, the influence of shear transverse deformation becomes more significant for

thick beams, and affects the respective results remarkably. Similar trends have been seen for FGM beams surrounded by surface-bonded piezoelectric layers.

Hereafter, in order to increase the accuracy of the presented numerical simulations, all the figures are plotted based on the results of PBT, which virtually predicts the same frequencies as other higher-order theories presented in this study (i.e., SBT and EBT).

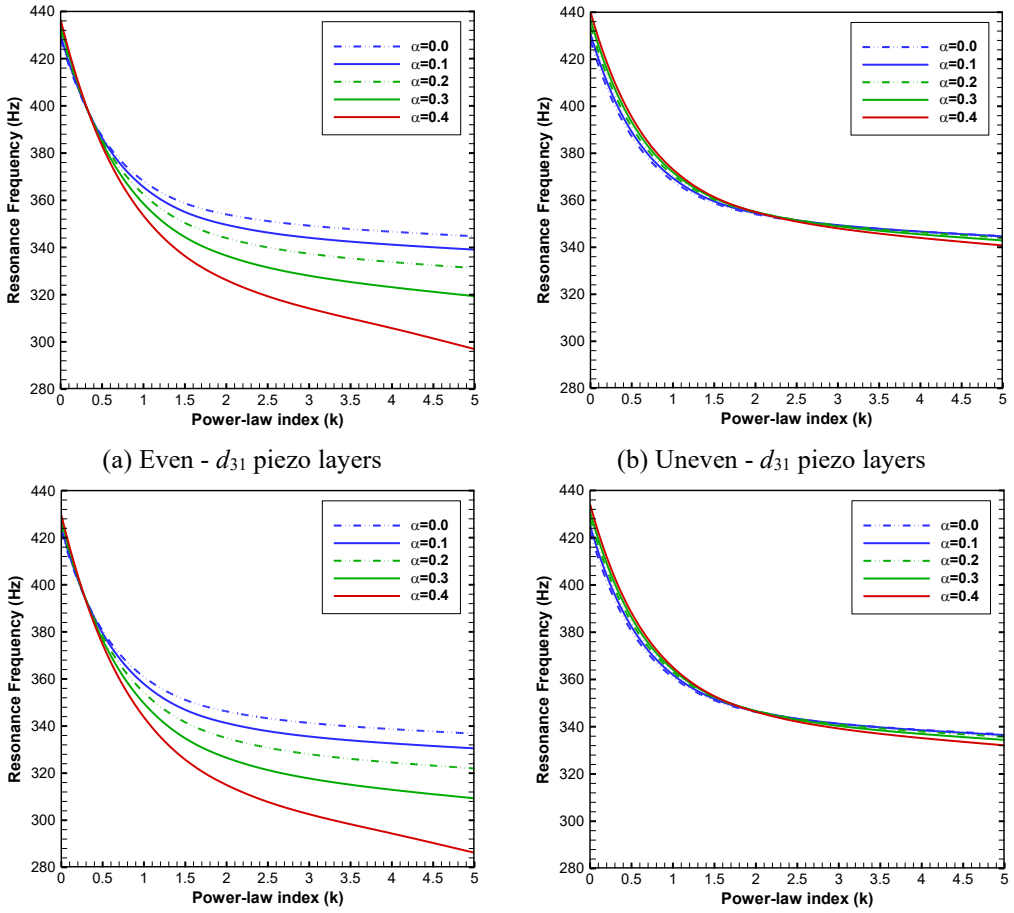

(a) Even - d_{31} piezo layers

(b) Uneven - d_{31} piezo layers

(c) Even - d_{15} piezo layers

(d) Uneven - d_{15} piezo layers

Fig. 4.4: Variation of the fundamental natural frequency versus the power-law index for FGM beam with integrated piezoelectric layers in SC condition ($L/2h = 10, h_p/2h = 0.2$, α is the porosity volume fraction)

One may see a specific upward or downward trend in Tables 4.6 to 4.9 for the eigenfrequency behavior of the coupled FGM beam versus the porosity volume fraction for any given N, regardless of the pattern of porosity distribution. For

example, by carrying out a careful inspection of those tables, it can be ascertained that for $N = 0$, the first three natural frequencies increase as the value of porosity parameter increases for both porosity distribution, whereas opposite trend is seen for frequencies of the beams with evenly distributed pores when the power-law index increases up to 1. To further investigate this matter, the effects of changes in the value of porosity parameter and the type of porosity distribution on variation of the SC fundamental frequency versus the power-law index are shown in Fig. 4.4 for FGP beams with d_{31} and d_{15} piezoelectric layers. It can be observed that the free vibration behavior of the beam with even porosity distribution is influenced remarkably by changing the power-law index as well as the porosity parameter in comparison with the beam with uneven porosity distribution. Furthermore, it can be inferred from the figures that before the crossing point, the natural frequency increases as the value of porosity parameter rises, while the opposite trend is seen after the mentioned point, regardless of the porosity distribution pattern and the type of piezoelectric layers. Moreover, the value of the power-law index at the point of intersection is much higher for the hybrid FGM beam with unevenly distributed pores (around $N = 2.5$) than that of the beam with even distribution (about $N = 0.3$). Therefore, the trends for variation of the resonance frequencies versus porosity volume fraction depend on the value of power-law index for the beams with both even and uneven distribution.

Fig. (4.5) shows the combined effects of changes in power-law index and porosity distribution on variation of the first three eigenfrequencies of smart FGM beam with respect to the porosity volume fraction. Inspection of the figures reveals that the curves corresponded to even porosity distribution tend to incrementally lie below those related to beam with unevenly distributed pores, as N increases. Besides, for the small values of N, by increasing the porosity parameter, the SC and OC resonant frequencies of the first three vibrational modes increase, for both even and uneven porosity distribution. Nevertheless, the frequencies become lower as N is increased up to a prescribed value, for FGM beams with even porosity distribution. This behavior can finally be seen for beams with unevenly distributed pores as the power-law index gets greater. These trends are seen mainly because the influence of dropping effective stiffness of the smart hybrid beam (due to increasing the value of N) overcomes its decreasing inertia at this point, which results in a downward

trend for resonance frequencies. Similar trends are also observed for the FGM beams with d_{15} piezoelectric layers.

In the following, the influence of the piezoelectric layer thickness on the resonant frequencies of FGM beams are quantified for different power-law indices and porosity volume fractions. To this end, the new parameter θ, which represents the relative difference in natural frequency of the beams with and without piezoelectric layers is defined as follows

$$\theta = \frac{\omega|_{\text{With Piezo Layers}} - \omega|_{\text{Without Piezo Layers}}}{\omega|_{\text{Without Piezo Layers}}} \times 100 \tag{4.19}$$

For the coupled FGM beams with $L/2h = 15$ and $e_0 = 0.2$, the variation of θ versus $h_p/2h$ is plotted in Fig. 4.6. The figure reveals that, at a fixed value of the thickness ratio, the value of θ is more sensitive to N for the beams with evenly distributed pores than that of the ones with uneven distribution. When N is small, the values of θ are negative regardless of the type of piezoelectric layers and porosity distribution, meaning that the coupled FGM beams have lower frequencies than the corresponding core beams. This behavior is due to the fact that the mass density of the material of piezoelectric layers (here PZT-5H) is greater than that of the considered material for the core layer, and consequently the effective mass density of the hybrid beam increases. Furthermore, the elastic modulus of the material of the core layer is higher than that of piezoelectric material, resulting in a decrease in the effective structural stiffness of the sandwich beam. On the other hand, when coupling piezoelectric layers with the core layer, the electromechanical coupling effect of piezoelectrics tends to increase the natural frequency of the hybrid structure. Thus, negative values of θ show that the electromechanical coupling effect of piezoelectric layers is less than that of the combined effects coming from the reduction in overall mass density and the growth in the effective stiffness. In addition, when the power-law index gets larger, the addition of piezoelectric layers results in opposite changes in the effective mass density and stiffness of the hybrid structure which finally leads to increase the natural frequencies, as seen from the curves corresponded to $N = 0.5$, 1 and 5.

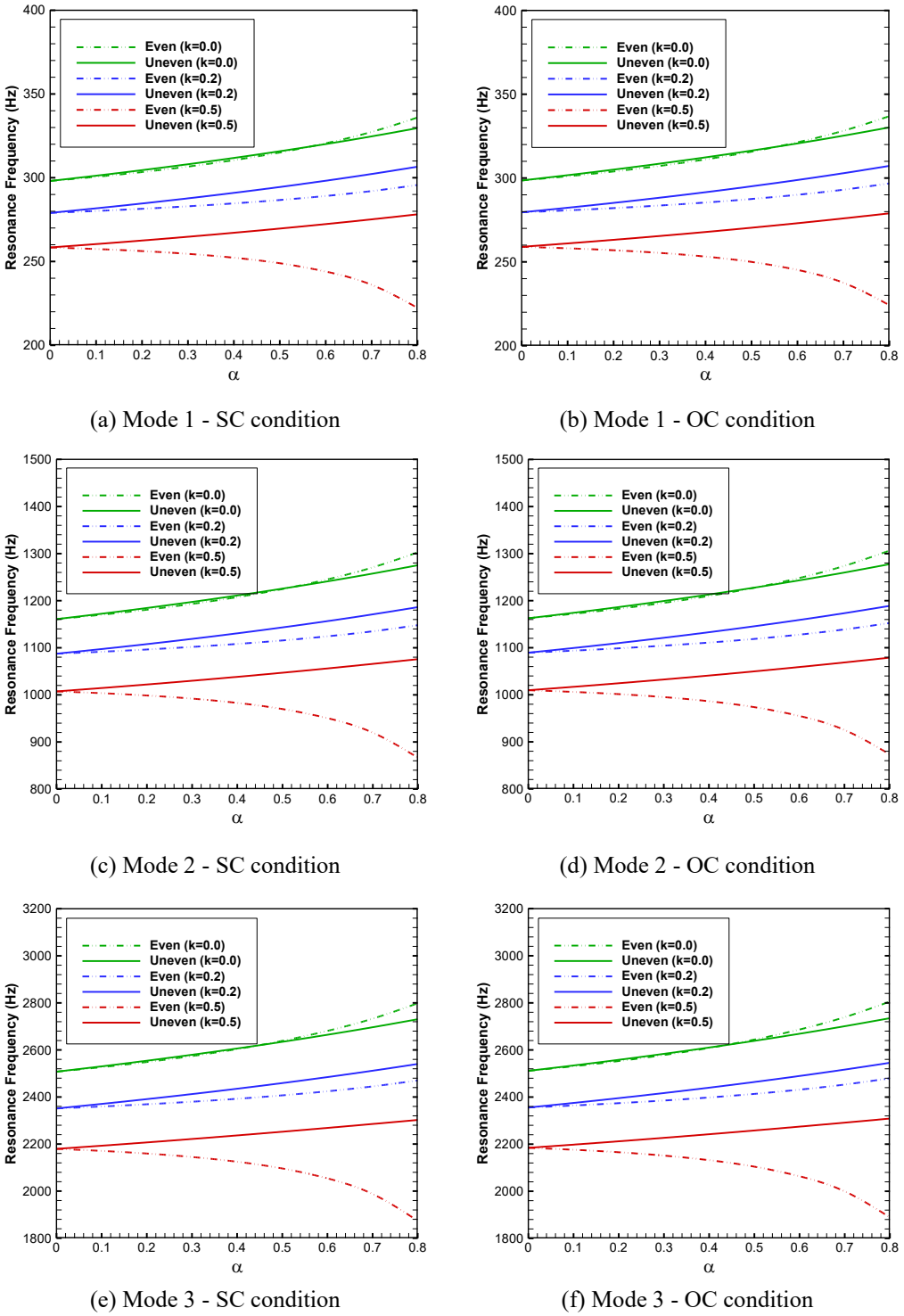

(a) Mode 1 - SC condition

(b) Mode 1 - OC condition

(c) Mode 2 - SC condition

(d) Mode 2 - OC condition

(e) Mode 3 - SC condition

(f) Mode 3 - OC condition

Fig. 4.5: Variation of the first three natural frequencies of the coupled FGM beam versus porosity volume fraction ($L/2h = 15$, $2h/h_p = 15$, d_{31} mode)

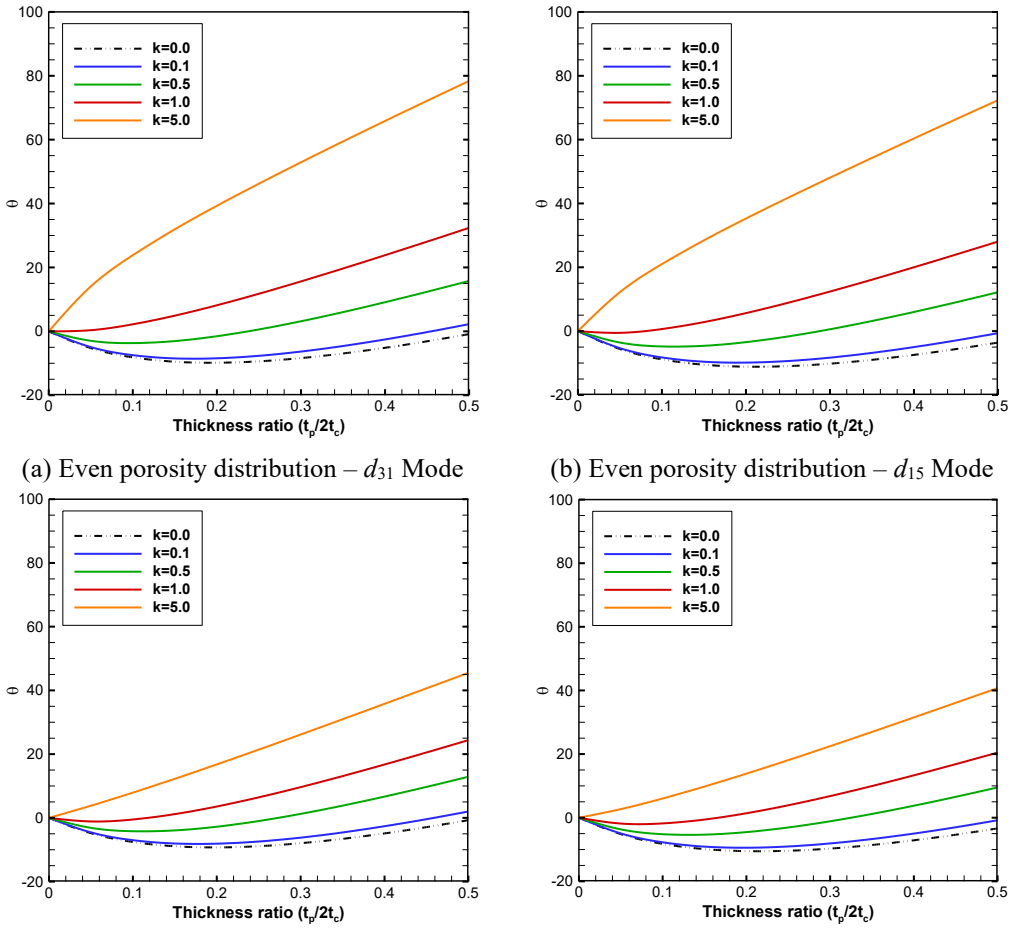

(a) Even porosity distribution – d_{31} Mode

(b) Even porosity distribution – d_{15} Mode

(c) Uneven porosity distribution – d_{31} Mode

(d) Uneven porosity distribution – d_{15} Mode

Fig. 4.6: Variation of θ versus the thickness ratio for the FGM beam coupled with d_{31} and d_{15} piezoelectric layers in SC condition ($L/2h = 15$, $e_0 = 0.2$, k is the power-law index)

In Fig. 4.7, for different values of the porosity parameter 0, 0.15 and 0.3, and the power-law index 0.1 and 2, variation of θ versus the thickness ratio is plotted for the FGM beam with integrated d_{31} and d_{15} piezoelectric layers in OC electrical condition. Again, it is seen that the addition of both transverse and shear piezoelectric layers to FGM core beam has a greater effect on the natural frequencies when the internal pores are evenly distributed with respect to uneven distribution, regardless of the value of N. Moreover, by increasing the porosity volume fraction, the magnitude of θ increases for both even and uneven porosity distribution in such a way that this growth is more significant for the beam with even distribution and $N = 2$ (see Fig. 4.7(c)). It is also observed that when $N =$

0.1, the magnitude of θ raises with an increase in the thickness of piezoelectric layers till $h_p/2h = 0.25$; subsequently, the magnitude of θ drops as the value of $h_p/2h$ increases. It is due to the reason that when $h_p/2h$ is less than 0.25, the combined effects of the rise in the effective mass density and the fall in the structural stiffness are more than the increasing electromechanical effect due to increasing the piezoelectric layers' thickness. However, from $h_p/2h = 0.25$ to 0.5, the trend of θ changes reversely, as the thickness ratio increases, meaning that the electromechanical effect overcomes the other two mentioned effects, which leads to the increasing trend of θ, as shown in Fig. 4.7(a) and 4.7(b). By examining the numerical results, it is simple to acquire the similar conclusions for SC condition.

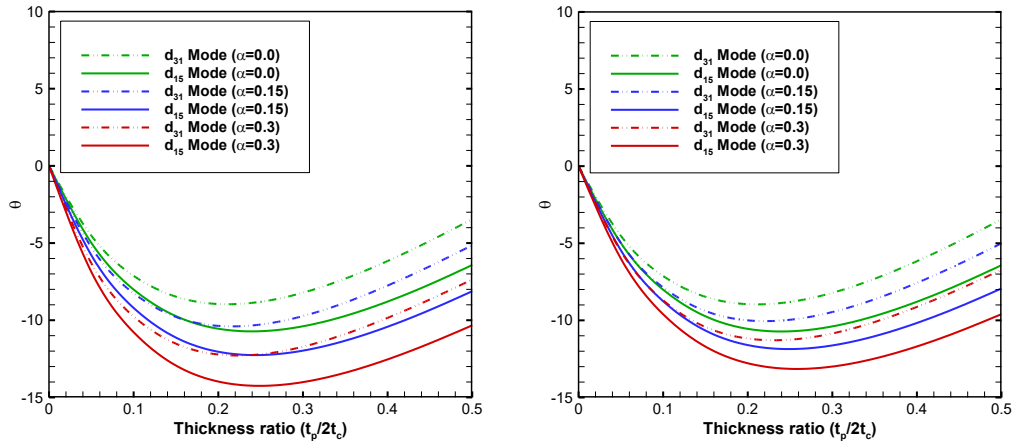

(a) Even porosity distribution ($N = 0.1$) (b) Uneven porosity distribution ($N = 0.1$)

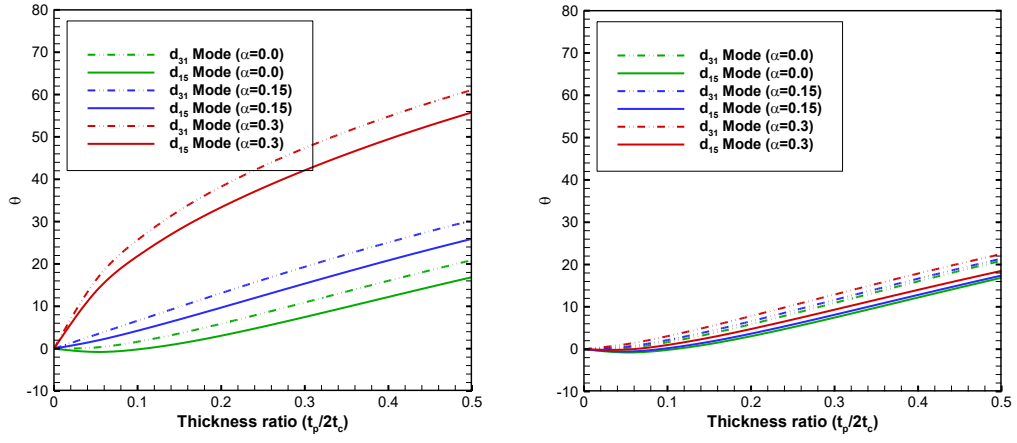

(c) Even porosity distribution ($N = 2$) (d) Uneven porosity distribution ($N = 2$)

Fig. 4.7. Variation of θ versus the thickness ratio for an FGM beam integrated with d_{31} and d_{15} piezoelectric layers in OC condition ($L/2h = 5$)

The last numerical example is provided in Figure (8) to show the effect of the piezoelectric layers' thickness on the SC fundamental frequency of FGP beams having $2t_c/L$=0.05, 0.1 and 0.2. As obvious, the value of θ decreases with an increase in the value of the core thickness for both d_{31} and d_{15} modes. It does mean that adding piezoelectric layers to FGP beams has a greater effect on the eigenfrequencies of the beams with lower core thickness.

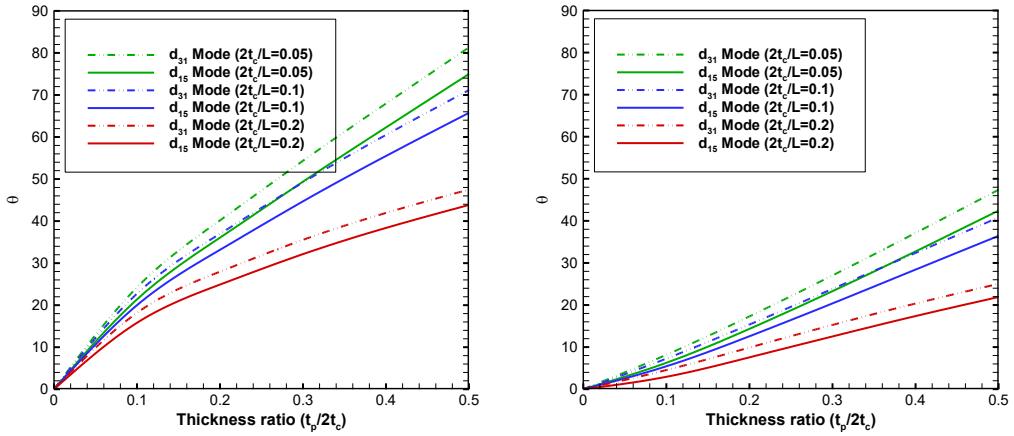

(c) Even porosity distribution (d) Uneven porosity distribution

Fig. 4.8: Variation of θ versus the thickness ratio for smart FGP beams in SC condition with different values of $L/2h$ ($N = 5$, $e_0 = 0.2$)

4.6 Summary and Conclusions

In this chapter, an exact electromechanical model was presented to study the eigenfrequency behavior of d_{31} and d_{15} piezoelectric bimorph beams with FGM substrate containing porosities. The effects of material variation, porosity, beam dimensions, beam theories and piezoelectric characteristics on the resonance frequencies were investigated in detail. By analyzing the numerical simulations, the following conclusions are reached:

- FGM beams coupled with d_{15} piezoelectric layers provide lower resonant frequencies than their counterparts with d_{31} piezoelectric layers.

- In d_{31} mode, the OC natural frequencies are greater than those of the SC condition, while there are slight differences between SC and OC frequencies when the FGM beam is surrounded by d_{15} piezoelectric layers.
- Adding piezoelectric layers has more effects on the eigenfrequencies when the internal pores are evenly distributed, and the changes in natural frequency due to adding piezoelectric layers is highly dependent upon the value of N.
- Variation of the eigenfrequencies versus porosity depends on the value of power-law index and the type of porosity distribution regardless of the piezoelectric characteristics.
- The bimorph FGM beam with unevenly distributed pores usually provide higher resonant frequencies than those of the beams with even porosity pattern.
- Increasing the power-law index remarkably decrease the eigenfrequencies irrespective of the type of porosity pattern.
- The beam natural frequencies are more sensitive when the internal pores are evenly distributed.

Chapter 5

On Wave Propagation and Free Vibration Analysis of Piezoelectric Bimorph Plates

5.1 Overview

This chapter provides a comprehensive 2D model based on an efficient four-variable higher-order shear deformation theory for analysis of piezoelectric bimorph plate structures. The problems of plane wave propagation and free vibration are herein addressed. As is well-known, higher-order theories often require solutions of more complicated governing equations. Based on the literature, closed-form solutions for the plate problems have been derived for some simple cases. Where these exact solutions cannot be obtained, the analysts can draw on very general finite element software, to solve the problems. Nevertheless, it is desirable to present exact models for such 2D structures based on higher-order theories, which allow for the effect of transverse shear deformation. The refined model employed here drops the need of any shear correction factor, and results in fewer governing equations compared to the conventional higher-order theories. The

exact model of the coupled plate structure is established through the use of Hamilton's principle, and Maxwell's equation. Analytical solutions are finally proposed to extract the results for two investigations: (I) the plane wave propagation of infinite smart plates and (II) the free vibration of smart rectangular plates considering different combinations of classical boundary conditions. After verifying the model, extensive numerical results are presented for the plate structure with perfect and porous FGM substrates, demonstrating the capability of the present model to provide accurate results with a strong reduction in the computational cost compared to the numerical approaches.

The results of the research work presented in this chapter was published in the *Journal of Intelligent Material Systems and Structures* [171].

5.2 State of the Art

With the development of new materials and structural solutions, a number of new structural models have been introduced in order to perform an accurate design of advanced structures. Classical structural models have been improved introducing more refined kinematics formulation. One- and two- dimensional models are widely used in aerospace structure design, and the limitations introduced by the classical models have been overcome by introducing refined kinematic formulations able to deal with the complexities of the problems. Regarding the analysis of travelling plane waves across piezoelectric and functionally graded structures, few studies are presented in the literature. For instance, phase velocity and attenuation quality factor of the waves travelling in porous piezoelectric materials was studied by Vashishth and Gupta [172], and the dependence of these parameters on phase direction was demonstrated. For a functionally graded piezoelectric substrate under SC and OC conditions, the existence and propagation behavior of transverse surface waves was examined by Qian et al. [173] through an analytical technique. Sun and Luo [174–176] analyzed the wave propagation in functionally grade plates in presence/absence of thermal environments and investigated the effect of material parameters on the dispersion behavior and the associated phase velocity. Ebrahimi et al. [177] analyzed wave dispersion behavior of size-dependent rotating inhomogeneous nanobeams according to nonlocal elasticity theory. Using a general

nonlocal higher-order beam model, wave propagation in two-dimensional rotating nano-beams made of FGMs was studied by Faroughi et al. [178]. Ebrahimi and Seyfi [179] investigated propagation of wave in metal foam cylindrical shells rested on variable elastic substrates. In the framework of classical and shear deformation plate theories, Gao et al. [180] dealt with wave propagation of porous plates reinforced with graphene platelets using Halpin-Tsai model for expressing the corresponding material properties. The study examines the effect of different material and geometrical parameters on the dispersion characteristics of the system. A semi-analytical approach was presented by Li et al. [181] to investigate wave propagation characteristics in functionally graded piezoelectric composite plates reinforced with graphene platelets. Most recently, other types of geometries, such as shells were also considered in this regard. For instance, Aminpour et al. [182] investigated the propagation of waves in functionally graded doubly curved shells via higher-order shear deformation theory by adopting different types of FGMs including FG porous ceramic-metal and FG carbon nanotubes-reinforced composites.

On the other hand, numerous contributions have discussed the dynamic response including vibration of thin-walled structures with a core composed of functionally graded materials as well as piezoelectric sandwich structures with FGM substrate [84,100,165,183–188]. For instance, the classical plate theory was adopted by He et al. [100] for active control of FGM plates with integrated piezoelectric sensors and actuators, and the effect of volume fraction index and feedback control gain was studied of the static and dynamic response of the system. Vel and Batra [189] investigated the vibration of simply supported FGM rectangular plates by providing a three-dimensional exact solution. The approach, which takes the advantage of power series method is capable of extracting valid results for both thin and thick plates. Askari et al. [190] developed an analytical work to study the free vibration problem of simply supported porous FGM beams integrated with thickness-poled and length-poled piezoelectric layers, in both SC and OC electrical conditions. Besides, many research works have been presented to study the response of functionally graded porous materials due to growing interest in lightweight structures. In this context, Rezaei et al. [191] presented an analytical solution based on a simple shear deformation theory containing four unknowns for rectangular plates with Levy boundary conditions. Highly accurate natural

frequencies of thick functionally graded porous rectangular plates with arbitrary boundary conditions were extracted by Zhao et al. [192] using Rayleigh-Ritz procedure.

Due to the complexity of the governing equations based on shear deformation theories, most published papers studied the free vibration of piezoelectric bimorph plates with FGM substrates through numerical techniques. Moreover, the existing analytical approaches for such problems are either limited to Navier-type and Levy-type boundary conditions or are proposed for analyses based on classical plate theories. Therefore, an exact solution for the free vibration of thick rectangular FGM plates integrated with piezoelectric layers under various boundary conditions can be helpful to check the accuracy of numerical analysis in this field. On the other hand, no studies can be found for the analysis of plane wave propagation in infinite sandwich plates composed of either perfect or porous FGM substrates with integrated piezoelectric layers. Therefore, the gaps just mentioned have motivated us to develop analytical solutions in the present work for the problems of plane wave propagation and free vibration of perfect and porous FGM plate structures coupled with piezoelectric sensors/actuators.

5.3 Problem Modelling

Consider a piezoelectric bimorph plate structure with schematic representation the same as what is already given in Fig. 3.1. It is reminded that the thicknesses of the substrate and each piezoelectric layer of the plate are defined by the symbols $2h$ and h_p, respectively. Although the smart composite plate is represented as a finite rectangular plate with length a and width b, it will be assumed as an unbonded plate structure (with infinite in-plane dimensions) in subsection 5.5.1, where the bulk wave propagation of this system is investigated. The core layer of the coupled plate is assumed to be made of FGMs (both perfect and porous FGMs) with metal and ceramic constituents, and the piezoelectric layers are polarized though the thickness direction (with constitutive relations given in Eq. (3.8), and $K_s^2 = 1$). The effective mechanical properties of perfect and porous FGMs were earlier given in Eqs. (1.8) to (1.10) (see Chapter 1) so that it avoided to re-express those equations here. In

those equations, the parameter N was used to indicate the power-law index, and the porosity volume fraction was also represented by e_0.

Based on the four-variable higher-order shear deformation theory, the three components of the displacement field at any point of the smart plate can be expressed as:

$$\begin{aligned} U_x(x,y,z,t) &= u_0 - zw_{b,x} - f(z)w_{s,x} \\ U_y(x,y,z,t) &= v_0 - zw_{b,y} - f(z)w_{s,y} \\ U_z(x,y,z,t) &= w_b + w_s \end{aligned} \tag{5.1}$$

where U_x, U_y and $U_z(x,y,z,t)$ are the components of total displacement along x, y, and z directions, respectively. Moreover, $u_0(x,y,t)$ and $v_0(x,y,t)$ represent the in-plane displacements of the mid-surface of the plate (at $z=0$) through x and y directions, respectively. The transverse displacement U_z includes two components of bending $w_b(x,y,t)$ and shear $w_s(x,y,t)$. Both of these components are functions of the coordinates x and y. The function $f(z)$ is the shape function, representing the effect of the transverse shear strain and stress along the thickness of the plate. Various applicable shape functions have been derived and presented in the literature by different researchers. For instance, the shape functions presented by Shimpi [193] and Touratier [194] are listed in Table 5.1. Note that, in the expressions given in Table 1, H is the total thickness of the sandwich plate that is equal to $H = 2h + 2h_p$.

Table 5.1: Different shape functions for the proposed displacement model

Model	Shape function	Source
Sinusoidal shear plate theory (SSPT)	$f(z) = z - \frac{H}{\pi}\sin\left(\frac{\pi z}{H}\right)$	Touratier [194]
Polynomial shear plate theory (PSPT)	$f(z) = -\frac{z}{4} + \frac{5}{3}\frac{z^3}{H^2}$	Shimpi [193]

Unlike the first-order shear deformation theory, the higher-order refined theory does not require any shear correction factor to vanish the shear stresses σ_{xz} and σ_{yz} at the top and bottom faces of the plate. In the present work, the transverse

normal stress σ_{zz} is assumed to be negligible compared to in-plane normal stresses σ_{xx} and σ_{yy} [195].

Based on the linear strain-displacement assumptions, the components of the strain field can be derived from the displacement field (i.e., Eq. (5.1)), as:

$$\begin{aligned}
\varepsilon_{xx} &= u_{0,x} - zw_{b,xx} - f(z)w_{s,xx} \\
\varepsilon_{yy} &= v_{0,y} - zw_{b,yy} - f(z)w_{s,yy} \\
\gamma_{xy} &= 2\varepsilon_{xy} = u_{0,y} + v_{0,x} - 2zw_{b,xy} - 2f(z)w_{s,xy} \\
\gamma_{xz} &= 2\varepsilon_{xz} = g(z)w_{s,x} \\
\gamma_{yz} &= 2\varepsilon_{yz} = g(z)w_{s,y}
\end{aligned} \tag{5.2}$$

Here and hereafter, comma stands for partial differentiation with respect to the corresponding coordinate. The function $g(z)$ in Eq. (5.2) is given as:

$$g(z) = \begin{cases} 1 - f'(z), & f(z) \neq 0 \\ k^2, & f(z) = 0 \end{cases} \tag{5.3}$$

with k^2 being a shear correction factor. Also, $f'(z)$ is the first derivative of the shape function with respect to z-coordinate. Obviously, for $f(z) \neq 0$, no shear correction factor needs to be included in the strain-displacement relations, while it is compulsory to consider a shear correction factor for the case of $f(z) = 0$ [191], to satisfy the condition of zero shear stresses on the outer surfaces of the composite plate.

Approximation of the electric potential variation within the piezoelectric layers is an important issue. Here, the sinusoidal profile presented in [196] is used for the distribution of electric potential ϕ through the top and bottom piezoelectric layers of the bimorph plate, as:

$$\begin{aligned}
\phi_t(x, y, z, t) = {} & \phi_0(x, y, t) \sin\left(\frac{\pi(+z - h)}{h_p}\right) + A_t(x, y, t) \\
& + zB_t(x, y, t)
\end{aligned} \tag{5.4a}$$

$$\begin{aligned}
\phi_b(x, y, z, t) = {} & \phi_0(x, y, t) \sin\left(\frac{\pi(-z - h)}{h_p}\right) + A_b(x, y, t) \\
& + zB_b(x, y, t)
\end{aligned} \tag{5.4b}$$

in which subscript's "t" and "b" are associated with the top and bottom piezoelectric layers, respectively. The function $\phi_0(x, y, t)$ denotes the electric potential at the mid-plane of the piezoelectric layers. Moreover, $A(x, y, t)$ and $B(x, y, t)$ are two unknown functions to be obtained later by considering the electrical circuit conditions applied to the piezoelectric layers. Both SC and OC circuit conditions are herein considered, as are shown in Fig. 5.1.

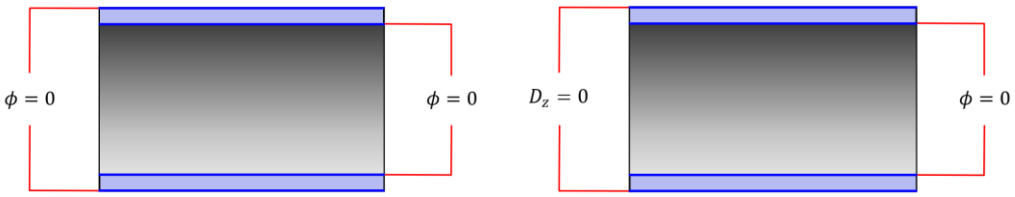

(a) SC condition (b) OC condition

Fig. 5.1: Electrical circuit conditions applied to piezoelectric layers

***SC Condition*:** Both inner and outer surfaces of each piezoelectric layer are kept at zero voltage (see Fig. 5.1(a)). The SC condition is usually used when employing piezoelectric patches/layers for sensing applications. This case can be mathematically described as

$$\begin{aligned}\phi_b(x, y, -h, t) = \phi_b\big(x, y, -h - h_p, t\big) = \phi_t(x, y, +h, t)\\ = \phi_t\big(x, y, +h + h_p, t\big) = 0\end{aligned} \tag{5.5}$$

Substituting Eq. (5.5) into Eq. (5.4), the form of electric potential functions in SC condition can be obtained as

$$\phi_t(x, y, z, t) = \phi_0(x, y, t) \sin\left(\frac{\pi(+z - h)}{h_p}\right) \tag{5.6a}$$

$$\phi_b(x, y, z, t) = \phi_0(x, y, t) \sin\left(\frac{\pi(-z - h)}{h_p}\right) \tag{5.6b}$$

***OC Condition*:** In this case, the inner surfaces of both top and bottom piezoelectric layers are held at zero voltage, while outer surfaces are electrically insulated (see Fig. 5.1(b)), thus:

$$\begin{aligned}\phi_b(x,y,-h,t) &= D_z\big(x,y,-h-h_p,t\big) = \phi_t(x,y,+h,t)\\ &= D_z\big(x,y,+h+h_p,t\big) = 0\end{aligned} \tag{5.7}$$

Similar to the previous case, the functions of electric potential in OC condition can be simply obtained by employing Eq. (5.7) into Eq. (5.4), as:

$$\begin{aligned}\phi_t(x,y,z) = \phi_0(x,y)&\left\{\sin\left(\frac{\pi(z-h)}{h_p}\right)+\frac{\pi(z-h)}{h_p}\right\}\\ &+\frac{\bar{e}_{31}(z-h)}{\bar{\bar{\Xi}}_{33}}\big\{u_{0,x}+v_{0,y}-\big(h+h_p\big)\big(w_{b,xx}+w_{b,yy}\big)\\ &-\alpha_t\big(w_{s,xx}+w_{s,yy}\big)\big\}\end{aligned} \tag{5.8a}$$

$$\begin{aligned}\phi_b(x,y,z) = \phi_0(x,y)&\left\{\sin\left(\frac{\pi(-z-h)}{h_p}\right)-\frac{\pi(z+h)}{h_p}\right\}\\ &+\frac{\bar{e}_{31}(z+h)}{\bar{\bar{\Xi}}_{33}}\big\{u_{0,x}+v_{0,y}+\big(h+h_p\big)\big(w_{b,xx}+w_{b,yy}\big)\\ &-\alpha_b\big(w_{s,xx}+w_{s,yy}\big)\big\}\end{aligned} \tag{5.8b}$$

In Eq. (5.8), $\alpha_t = f\big(h+h_p\big)$ and $\alpha_b = f\big(-h-h_p\big)$ where f is the shape function of the displacement model presented by Eq. (5.1).

Considering Eqs. (5.6) and (5.8), and the relation between electric potential and electric field (i.e., $\vec{E} = \vec{\nabla}\phi$), the components of the electric field in piezoelectric domains can be simply obtained.

5.4 Governing Equations

Based on the higher-order refined theory given in Eq. (5.1), the following four governing equations are derived through the use of Hamilton's principle:

$$N_{xx,x} + N_{xy,y} = I_0\ddot{u}_0 - I_1\ddot{w}_{b,x} - J_1\ddot{w}_{s,x} \tag{5.9a}$$

$$N_{xy,x} + N_{yy,y} = I_0\ddot{v}_0 - I_1\ddot{w}_{b,y} - J_1\ddot{w}_{s,y} \tag{5.9b}$$

$$M^b_{xx,xx} + 2M^b_{xy,xy} + M^b_{yy,yy} = I_0(\ddot{w}_b + \ddot{w}_s) + I_1\left(\ddot{u}_{0,x} + \ddot{v}_{0,y}\right) - I_2\left(\ddot{w}_{b,xx} + \ddot{w}_{b,yy}\right) - J_2\left(\ddot{w}_{s,xx} + \ddot{w}_{s,yy}\right) \quad (5.9c)$$

$$M^s_{xx,xx} + 2M^s_{xy,xy} + M^s_{yy,yy} + Q_{xz,x} + Q_{yz,y} = I_0(\ddot{w}_b + \ddot{w}_s) + J_1\left(\ddot{u}_{0,x} + \ddot{v}_{0,y}\right) - J_2\left(\ddot{w}_{b,xx} + \ddot{w}_{b,yy}\right) - K_2\left(\ddot{w}_{s,xx} + \ddot{w}_{s,yy}\right) \quad (5.9d)$$

in which dot-superscript denotes the differentiation with respect to the time t. The stress resultants N_i, M_i and Q_j ($i = xx, yy, xy$ and $j = xz, yz$) and the mass inertias I_i ($i = 0,1,2$), J_i ($i = 1,2$) and K_2 are defined as:

$$\left\{N_i, M^b_i, M^s_i\right\} = \int_{-h-h_p}^{+h+h_p} \{1, z, f(z)\}\, \sigma_i\, dz, \quad (i = xx, yy, xy)$$

$$Q_j = \int_{-h-h_p}^{+h+h_p} g(z)\, \sigma_j\, dz, \quad (j = xz, yz) \quad (5.10)$$

$$\{I_0, I_1, I_2, J_1, J_2, K_2\} = \int_{-h-h_p}^{+h+h_p} \{1, z, z^2, f, zf, f^2\}\, \rho(z)\, dz$$

The above stress resultants can be expressed in terms of the displacement field unknowns, as:

$$\begin{aligned}
N_{xx} &= (a_{11} + \lambda_1)u_{0,x} + (a_{12} + \lambda_1)v_{0,y} - (b_{11} + \lambda_2)w_{b,xx} \\
&\quad - (b_{12} + \lambda_2)w_{b,yy} - (d_{11} + \lambda_3)w_{s,xx} \\
&\quad - (d_{12} + \lambda_3)w_{s,yy} + \mu_1\phi_0 \\
N_{yy} &= (a_{12} + \lambda_1)u_{0,x} + (a_{11} + \lambda_1)v_{0,y} - (b_{12} + \lambda_2)w_{b,xx} \\
&\quad - (b_{11} + \lambda_2)w_{b,yy} - (d_{12} + \lambda_3)w_{s,xx} \\
&\quad - (d_{11} + \lambda_3)w_{s,yy} + \mu_1\phi_0 \\
N_{xy} &= a_{66}\left(u_{0,y} + v_{0,x}\right) - 2b_{66}w_{b,xy} - 2d_{66}w_{s,xy} \\
M^b_{xx} &= \left(b_{11} + \hat{\lambda}_1\right)u_{0,x} + \left(b_{12} + \hat{\lambda}_1\right)v_{0,y} - \left(f_{11} + \hat{\lambda}_2\right)w_{b,xx} \\
&\quad - \left(f_{12} + \hat{\lambda}_2\right)w_{b,yy} - \left(g_{11} + \hat{\lambda}_3\right)w_{s,xx} \\
&\quad - \left(g_{12} + \hat{\lambda}_3\right)w_{s,yy} + \hat{\mu}_1\phi_0
\end{aligned} \quad (5.11)$$

$$M_{yy}^{b} = \left(b_{12} + \hat{\lambda}_1\right)u_{0,x} + \left(b_{11} + \hat{\lambda}_1\right)v_{0,y} - \left(f_{12} + \hat{\lambda}_2\right)w_{b,xx} - \left(f_{11} + \hat{\lambda}_2\right)w_{b,yy} - \left(g_{12} + \hat{\lambda}_3\right)w_{s,xx} - \left(g_{11} + \hat{\lambda}_3\right)w_{s,yy} + \hat{\mu}_1\phi_0$$

$$M_{xy}^{b} = b_{66}\left(u_{0,y} + v_{0,x}\right) - 2f_{66}w_{b,xy} - 2g_{66}w_{s,xy}$$

$$M_{xx}^{s} = \left(d_{11} + \tilde{\lambda}_1\right)u_{0,x} + \left(d_{12} + \tilde{\lambda}_1\right)v_{0,y} - \left(g_{11} + \tilde{\lambda}_2\right)w_{b,xx} - \left(g_{12} + \tilde{\lambda}_2\right)w_{b,yy} - \left(h_{11} + \tilde{\lambda}_3\right)w_{s,xx} - \left(h_{12} + \tilde{\lambda}_3\right)w_{s,yy} + \tilde{\mu}_1\phi_0$$

$$M_{yy}^{s} = \left(d_{12} + \tilde{\lambda}_1\right)u_{0,x} + \left(d_{11} + \tilde{\lambda}_1\right)v_{0,y} - \left(g_{12} + \tilde{\lambda}_2\right)w_{b,xx} - \left(g_{11} + \tilde{\lambda}_2\right)w_{b,yy} - \left(h_{12} + \tilde{\lambda}_3\right)w_{s,xx} - \left(h_{11} + \tilde{\lambda}_3\right)w_{s,yy} + \tilde{\mu}_1\phi_0$$

$$M_{xy}^{s} = d_{66}\left(u_{0,y} + v_{0,x}\right) - 2g_{66}w_{b,xy} - 2h_{66}w_{s,xy}$$

$$Q_{xz} = a_{55}w_{s,x} + \lambda_4\left[u_{0,xx} + v_{0,yx}\right] + \lambda_5\left[w_{b,xxx} + w_{b,yyx}\right] + \lambda_6\left[w_{s,xxx} + w_{s,yyx}\right] + \mu_2\phi_{0,x}$$

$$Q_{yz} = a_{55}w_{s,y} + \lambda_4\left[u_{0,xy} + v_{0,yy}\right] + \lambda_5\left[w_{b,xxy} + w_{b,yyy}\right] + \lambda_6\left[w_{s,xxy} + w_{s,yyy}\right] + \mu_2\phi_{0,y}$$

The constant coefficients in Eq. (5.11), i.e., a_i, b_i, d_i, f_i, g_i, h_i ($i = 11,12,66$), a_{55}, λ_j, $\hat{\lambda}_j$, $\tilde{\lambda}_j$ ($j = 1,2,3$), μ_1, μ_2, $\hat{\mu}_1$, $\tilde{\mu}_1$ and λ_k ($k = 4,5,6$) are given in Relations (D.1) to (D.3) of Appendix D, for both SC and OC electrical conditions.

One can simply obtain the governing equations of motion in terms of the displacement field unknowns and the electric potential function by substituting Eq. (5.11) into Eq. (5.9), as:

$$(a_{11} + \lambda_1)u_{0,xx} + a_{66}u_{0,yy} + (a_{12} + a_{66} + \lambda_1)v_{0,yx} - (b_{11} + \lambda_2)w_{b,xxx} - (b_{12} + 2b_{66} + \lambda_2)w_{b,yyx} - (d_{11} + \lambda_3)w_{s,xxx} - (d_{12} + 2d_{66} + \lambda_3)w_{s,yyx} + \mu_1\phi_{0,x} = I_0\ddot{u}_0 - I_1\ddot{w}_{b,x} - J_1\ddot{w}_{s,x} \quad (5.12a)$$

$$a_{66}v_{0,xx} + (a_{11} + \lambda_1)v_{0,yy} + (a_{12} + a_{66} + \lambda_1)u_{0,yx} - (b_{11} + \lambda_2)w_{b,yyy} - (b_{12} + 2b_{66} + \lambda_2)w_{b,xxy} - (d_{11} + \lambda_3)w_{s,yyy} - (d_{12} + 2d_{66} + \lambda_3)w_{s,xxy} + \mu_1\phi_{0,y} = I_0\ddot{v}_0 - I_1\ddot{w}_{b,y} - J_1\ddot{w}_{s,y} \quad (5.12b)$$

$$\begin{aligned}
&\left(b_{11}+\hat{\lambda}_1\right)u_{0,xxx}+\left(b_{12}+2b_{66}+\hat{\lambda}_1\right)u_{0,yyx}\\
&\quad+\left(b_{12}+2b_{66}+\hat{\lambda}_1\right)v_{0,yxx}+\left(b_{11}+\hat{\lambda}_1\right)v_{0,yyy}\\
&\quad-\left(f_{11}+\hat{\lambda}_2\right)w_{b,xxxx}-2\left(f_{12}+2f_{66}+\hat{\lambda}_2\right)w_{b,yyxx}\\
&\quad-\left(f_{11}+\hat{\lambda}_2\right)w_{b,yyyy}-\left(g_{11}+\hat{\lambda}_3\right)w_{s,xxxx}\\
&\quad-2\left(g_{12}+2g_{66}+\hat{\lambda}_3\right)w_{s,yyxx}-\left(g_{11}+\hat{\lambda}_3\right)w_{s,yyyy}\\
&\quad+\hat{\mu}_1\phi_{0,xx}+\hat{\mu}_1\phi_{0,yy}\\
&\quad=I_0(\ddot{w}_b+\ddot{w}_s)+I_1\left(\ddot{u}_{0,x}+\ddot{v}_{0,y}\right)-I_2\left(\ddot{w}_{b,xx}+\ddot{w}_{b,yy}\right)\\
&\quad-J_2\left(\ddot{w}_{s,xx}+\ddot{w}_{s,yy}\right)
\end{aligned}\tag{5.12c}$$

$$\begin{aligned}
&\left(d_{11}+\tilde{\lambda}_1+\lambda_4\right)u_{0,xxx}+\left(d_{12}+2d_{66}+\tilde{\lambda}_1+\lambda_4\right)u_{0,xyy}\\
&\quad+\left(d_{12}+2d_{66}+\tilde{\lambda}_1+\lambda_4\right)v_{0,yxx}\\
&\quad+\left(d_{11}+\tilde{\lambda}_1+\lambda_4\right)v_{0,yyy}-\left(g_{11}+\tilde{\lambda}_2+\lambda_5\right)w_{b,xxxx}\\
&\quad+2\left(-g_{12}-2g_{66}-\tilde{\lambda}_2+\lambda_5\right)w_{b,yyxx}\\
&\quad-\left(g_{11}+\tilde{\lambda}_2-\lambda_5\right)w_{b,yyyy}-\left(h_{11}+\tilde{\lambda}_3-\lambda_6\right)w_{s,xxxx}\\
&\quad+2\left(-h_{12}-2h_{66}-\tilde{\lambda}_3+\lambda_6\right)w_{s,yyxx}\\
&\quad-\left(h_{11}+\tilde{\lambda}_3-\lambda_6\right)w_{s,yyyy}+a_{55}\left(w_{s,xx}+w_{s,yy}\right)\\
&\quad+\left(\tilde{\mu}_1+\mu_2\right)\phi_{0,xx}+\left(\tilde{\mu}_1+\mu_2\right)\phi_{0,yy}\\
&\quad=I_0(\ddot{w}_b+\ddot{w}_s)+J_1\left(\ddot{u}_{0,x}+\ddot{v}_{0,y}\right)-J_2\left(\ddot{w}_{b,xx}+\ddot{w}_{b,yy}\right)\\
&\quad-K_2\left(\ddot{w}_{s,xx}+\ddot{w}_{s,yy}\right)
\end{aligned}\tag{5.12d}$$

The last governing equation of the smart composite plate can be derived from the integral form of Maxwell's equation, as:

$$\int_{-h-h_p}^{-h}\left(D_{x,x}+D_{y,y}+D_{z,z}\right)+\int_{+h}^{+h+h_p}\left(D_{x,x}+D_{y,y}+D_{z,z}\right)=0 \tag{5.13}$$

Substituting the definitions of D_i's ($i=x,y,z$) from Eq. (5.4(b)) into Eq. (5.13), and taking into account Eqs. (5.6) and (5.8), yield:

$$\begin{aligned}
&\lambda_7\left(w_{s,xx}+w_{s,yy}\right)+\lambda_8\left(w_{b,xx}+w_{b,yy}\right)+\lambda_9\phi_0+\lambda_{10}\left(\phi_{0,xx}+\phi_{0,yy}\right)\\
&\quad+\lambda_{11}\left(u_{0,xxx}+v_{0,yxx}+u_{0,xyy}+v_{0,yyy}\right)\\
&\quad+\lambda_{12}\left(w_{b,xxxx}+2w_{b,xxyy}+w_{b,yyyy}\right)\\
&\quad+\lambda_{13}\left(w_{s,xxxx}+2w_{s,xxyy}+w_{s,yyyy}\right)=0
\end{aligned}\tag{5.14}$$

The constant coefficients λ_i $(i = 7,8,..,13)$ are given in Relations (D.4) and (D.5) of Appendix D, for both SC and OC conditions.

5.5 Solution Procedure

Five coupled electromechanical governing equations of motion (i.e., Eqs. (5.12) and (5.14)) have been derived for the smart plate. In the following subsections, analytical solutions are presented for two problems of plane wave propagation and free vibration of the smart plate structures.

5.5.1 Wave Propagation Analysis

The analytical solution of governing equations for the bulk wave dispersion in an unbonded smart plate structure is proposed in this subsection. Bulk waves exist in infinite domains and propagate indefinitely without being interrupted by boundaries or interfaces. Thus, to investigate the bulk wave propagation in the unbonded smart plate, one must consider that the plate has to be expanded from all sides to infinite (except its thickness). The generalized displacements can then be expressed as:

$$\begin{Bmatrix} u_0(x,y,t) \\ v_0(x,y,t) \\ w_b(x,y,t) \\ w_s(x,y,t) \\ \phi_0(x,y,t) \end{Bmatrix} = \begin{Bmatrix} u_0^* \\ v_0^* \\ w_b^* \\ w_s^* \\ \phi_0^* \end{Bmatrix} e^{-j(\omega t-\beta_1 x-\beta_2 y)} \tag{5.15}$$

where β_1 and β_2 indicate the wavenumbers along x-axis and y-axis directions, respectively, ω is the angular frequency, and j is the imaginary unit. The vector $\{u_0^*, v_0^*, w_b^*, w_s^*, \phi_0^*\}^T$ represents the amplitude of the generalized displacements, namely physical field including the displacement and the electric potential. It is, again, noted that because the current study considers wave propagation in unbounded elastic domains, it is not necessary to consider the boundary conditions in this subsection [197,198].

By substituting Eq. (5.15) and its derivatives into the governing Eqs. (5.12) and (5.14), such set of equations is simplified as:

$$\begin{bmatrix} K_{11} & K_{12} & K_{13} & K_{14} & K_{15} \\ K_{21} & K_{22} & K_{23} & K_{24} & K_{25} \\ K_{31} & K_{32} & K_{33} & K_{34} & K_{35} \\ K_{41} & K_{42} & K_{43} & K_{44} & K_{45} \\ K_{51} & K_{52} & K_{53} & K_{54} & K_{55} \end{bmatrix} \begin{Bmatrix} u_0^* \\ v_0^* \\ w_b^* \\ w_s^* \\ \phi_0^* \end{Bmatrix} = 0 \tag{5.16}$$

where the components of the matrix $[K]$ are given in Relation (D.6) of Appendix D.

The dispersion relation that relates the wavenumber of the wave propagation in the infinite plate to its frequency is given by

$$|K| = 0 \tag{5.17}$$

Assuming $\beta_1 = \beta_2 = \beta$, Eq. (5.17) can be rewritten as:

$$\omega^8 + \alpha_1\omega^6 + \alpha_2\omega^4 + \alpha_3\omega^2 + \alpha_4 = 0 \tag{5.18}$$

where α_i's are functions of β. For a given β, the dispersion relation provides four positive eigenvalues for ω^2 or eight real solutions for the frequency ω, once it is solved. When β varies continuously, each pair of the solution represents a wave propagation mode. The roots of Eq. (5.18) can be expressed as:

$$\omega_1 = W_1(\beta),\ \ \omega_2 = W_2(\beta),\ \ \omega_3 = W_3(\beta),\ \ \omega_4 = W_4(\beta) \tag{5.19}$$

in which the frequencies ω_1, ω_2, ω_3 and ω_4 correspond to the wave modes M_0, M_1, M_2 and M_3, respectively.

Additionally, the phase velocity of wave propagation in the unbonded smart plate can be expressed as:

$$C_i = \frac{W_i(\beta)}{\beta} \qquad (i = 1, 2, 3, 4) \tag{5.20}$$

5.5.2 Free Vibration Analysis

In this subsection, an analytical solution is proposed to study the free vibration of the smart coupled FG plate having various boundary conditions. According to

Hamilton's principle, for the plate with clamped, simply-supported, and free edges, the mechanical boundary conditions can be expressed as:

Simply-Supported (S):

at edges $x = 0, a$:

$$v_0 = w_b = w_s = N_{xx} = M_{xx}^b = M_{xx}^S = 0 \tag{5.21}$$

at edges $y = 0, b$:

$$u_0 = w_b = w_s = N_{yy} = M_{yy}^b = M_{yy}^S = 0 \tag{5.22}$$

Clamped (C):

at edges $x = 0, a$:

$$u_0 = v_0 = w_b = w_s = w_{b,x} = w_{s,x} = 0 \tag{5.23}$$

at edges $y = 0, b$:

$$u_0 = v_0 = w_b = w_s = w_{b,y} = w_{s,y} = 0 \tag{5.24}$$

Free (F):

at edges $x = 0, a$:

$$N_{xx} = N_{xy} = M_{xx}^b = M_{xx}^s = Q_{xz} = 0 \tag{5.25}$$

at edges $y = 0, b$:

$$N_{yy} = N_{xy} = M_{yy}^b = M_{yy}^s = Q_{yz} = 0 \tag{5.26}$$

To satisfy different types of boundary conditions, the following expressions of the displacement components and the electric potential function are considered:

$$\begin{Bmatrix} u_0(x,y,t) \\ v_0(x,y,t) \\ w_b(x,y,t) \\ w_s(x,y,t) \\ \phi_0(x,y,t) \end{Bmatrix} = \sum_{m=1}^{\infty}\sum_{n=1}^{\infty} \begin{Bmatrix} A_{mn}F_m'(x)F_n(y) \\ B_{mn}F_m(x)F_n'(y) \\ C_{mn}F_m(x)F_n(y) \\ D_{mn}F_m(x)F_n(y) \\ E_{mn}F_m(x)F_n(y) \end{Bmatrix} e^{j\omega t} \tag{5.27}$$

where $\omega = \omega_{mn}$ is the eigenfrequency associated with (mth, nth) eigenmode, and $(A_{mn},\ B_{mn}, C_{mn}, D_{mn}, E_{mn})$ are the unknown coefficients. The functions $F_m(x)$ and $F_n(y)$ are the admissible functions that are given in Table 5.2 for various types of boundary conditions [199]. Note that, in Table 5.2, the parameters $\beta_m = m\pi/a$ and $\beta_n = n\pi b$ are the wave numbers along x-axis and y-axis directions, respectively.

Table 5.2: Admissible functions $F_m(x)$ and $F_n(y)$ for various boundary conditions

	Boundary conditions		Admissible functions
	At edges: $x = 0, a$	At edges: $y = 0, b$	
SSSS	$F_m(0) = F_m''(0) = 0$	$F_n(0) = F_n''(0) = 0$	$F_m(x) = \sin(\beta_m x)$
	$F_m(a) = F_m''(a) = 0$	$F_n(b) = F_n''(b) = 0$	$F_n(y) = \sin(\beta_n y)$
CSCS	$F_m(0) = F_m'(0) = 0$	$F_n(0) = F_n'(0) = 0$	$F_m(x) = \sin(\beta_m x)\,[\cos(\beta_m x) - 1]$
	$F_m(a) = F_m''(a) = 0$	$F_n(b) = F_n''(b) = 0$	$F_n(y) = \sin(\beta_n y)\,[\cos(\beta_n y) - 1]$
CCCS	$F_m(0) = F_m'(0) = 0$	$F_n(0) = F_n'(0) = 0$	$F_m(x) = \sin^2(\beta_m x)$
	$F_m(a) = F_m'(a) = 0$	$F_n(b) = F_n''(b) = 0$	$F_n(y) = \sin(\beta_n y)\,[\cos(\beta_n y) - 1]$
CCCC	$F_m(0) = F_m'(0) = 0$	$F_n(0) = F_n'(0) = 0$	$F_m(x) = \sin^2(\beta_m x)$
	$F_m(a) = F_m'(a) = 0$	$F_n(b) = F_n'(b) = 0$	$F_n(y) = \sin^2(\beta_n y)$
CCFF	$F_m(0) = F_m'(0) = 0$	$F_n''(0) = F_n'''(0) = 0$	$F_m(x) = \sin^2(\beta_m x)$
	$F_m(a) = F_m'(a) = 0$	$F_n''(b) = F_n'''(b) = 0$	$F_n(y) = \cos^2(\beta_n y)\,[\sin^2(\beta_n y) + 1]$
WXYZ means W, X, Y and Z boundary conditions on the edges $x = 0$, $x = a$, $y = 0$ and $y = b$, respectively.			
$(\ldots)'$ shows the derivative with respect to the corresponding coordinates, i.e., x or y.			

Substituting the proposed solution (i.e., Eq. (5.27)) into the electromechanical governing Eqs. (5.12) and (5.14), multiplying each equation by the corresponding eigenfunction then integrating over the domain of solution ($0 \le x \le a$, $0 \le y \le$

b), and finally doing some mathematical simplification result in the following equation:

$$\begin{bmatrix} K'_{11} & K'_{12} & K'_{13} & K'_{14} & K'_{15} \\ K'_{21} & K'_{22} & K'_{23} & K'_{24} & K'_{25} \\ K'_{31} & K'_{32} & K'_{33} & K'_{34} & K'_{35} \\ K'_{41} & K'_{42} & K'_{43} & K'_{44} & K'_{45} \\ K'_{51} & K'_{52} & K'_{53} & K'_{54} & K'_{55} \end{bmatrix} \begin{Bmatrix} A_{mn} \\ B_{mn} \\ C_{mn} \\ D_{mn} \\ E_{mn} \end{Bmatrix} = 0 \tag{5.28}$$

in which the components of the matrix $[K']$ are given in Relation (D.7) of Appendix D. Setting the determinant of matrix $[K']$ in Eq. (5.28) to zero (i.e., $|K'| = 0$), one can obtain the natural frequency ω_{mn} of the (mth, nth) eigenmode. The fundamental natural frequency of the smart plate is obviously the smallest value of ω_{mn} that is obtained for $m = n = 1$.

5.6 Numerical Results

5.6.1 Model Validation

First, to confirm the reliability of the proposed solutions and the mathematical formulations developed in the previous sections, comparative examples are provided here. To that end, the present natural frequencies are compared with some available in the literature. In Table 5.3, eigenfrequencies of a thin smart sandwich plate have been calculated and compared with those reported in Askari Farsangi et al. [165] and He et al. [100]. In the works presented by He et al. [100] and Askari Farsangi et al. [165], the classical plate theory and the first-order shear deformation theory were employed, respectively, for the free vibration of coupled plates with Navier-type and Levy-type boundary conditions.

Table 5.3: Comparison of the first eight natural frequencies (Hz) for an isotropic plate integrated with piezoelectric layers

Mode	Source					
	Present (SSPT)	Present (PSPT)	He et al. [100]	Difference (%)	Askari Farsangi et al. [165]	Difference (%)
1	144.94	144.94	144.25	0.48	145.35	0.28
2	362.01	362.01	359.00	0.84	363.05	0.29
3	362.01	362.01	359.00	0.84	363.05	0.29
4	578.70	578.70	564.10	2.59	580.35	0.28
5	722.95	722.95	717.80	0.72	725.00	0.28
6	722.95	722.95	717.80	0.72	725.00	0.28
7	938.98	938.98	908.25	3.38	941.64	0.28
8	938.98	938.98	908.25	3.38	941.64	0.28

In a second validation example, the natural frequencies of an isotropic plate coupled with piezoelectric layers are extracted from the present study are listed in Table 5.4 alongside their counterparts reported in [200].

Table 5.4: Comparison of the fundamental frequency (Hz) of an isotropic plate integrated with piezoelectric layers

$\frac{a}{b}$	$\frac{2h_p}{2h}$	Source			
		Present (SSPT)	Present (PSPT)	Ref. [200]	Difference (%)
1	0.5	875	875	873	0.23
	1.0	797	797	791	0.76
2	0.5	1093	1093	1091	0.18
	1.0	996	996	988	0.81
3	0.5	1457	1457	1454	0.21
	1.0	1328	1328	1317	0.84

Tables 5.3 and 5.4 show good agreements between the results of the present study and those available in the literature, confirming reliability and accuracy of the present models and numerical results. Note that minor differences among the results originate from employing various electric potential distributions and plate theories in the current work and the mentioned papers. For instance, the electric potential

function considered in Ref. [200] is a linear function of z-coordinate only, while in the present study, the electric potential distribution is assumed to be a function of all three coordinates.

5.6.2 Parametric Study and Discussion

In this section, the numerical results of both wave propagation and free vibration of the smart composite plate are presented for a wide range of design parameters such as power-law index, porosity volume fraction, porosity distribution boundary conditions, as well as piezoelectric characteristics. Note that the FG core layer is assumed to be made of Aluminum and Alumina with the following material properties [161]:

Aluminum: $E = 70$ GPa, $\rho = 2700$ kg/m^3, $\nu = 0.3$
Alumina: $E = 380$ GPa, $\rho = 3800$ kg/m^3, $\nu = 0.3$

The electrical and mechanical properties of several common piezoelectric materials such as PZT-4, PZT-5H, and PZT-5A are listed in Table 5.5. In the present work, PZT-4 is considered as the material of piezoelectric layers to extract all the numerical results in all the following tabulated results.

Table 5.5: Mechanical and electrical properties of PZT materials

Material	Properties							
	Elastic moduli (GPa)						Dielectric moduli (nF/m)	
	C_{11}	C_{12}	C_{33}	C_{13}	C_{55}	C_{66}	Ξ_{11}	Ξ_{33}
PZT-4	139.0	77.8	115.0	74.3	25.6	30.6	6.75	5.90
PZT-5H	127.2	80.2	117.4	84.7	23.0	23.5	15.1	12.7
PZT-5A	99.2	54.0	86.9	50.8	21.1	22.6	15.3	15.0
	Piezoelectric moduli (C/m^2)						Mass density (kg/m^3)	
	e_{31}	e_{33}	e_{15}				ρ	
PZT-4	-5.2	15.1	12.7				7500	
PZT-5H	-6.6	23.2	17.0				7500	
PZT-5A	-7.2	15.1	12.3				7750	

5.6.2.1 Numerical Results of Wave Propagation Analysis

The dispersion relation (i.e., Eq. (5.18)) provides the chance to study the dispersion behavior and the corresponding phase velocity for various smart FG plates. Three different cases are here taken into account: i) smart plates with the core layer made of perfect FGM, ii) smart plates with the core made of porous FGM having even porosity distribution, and iii) smart plates with the core made of porous FGM having uneven porosity distribution. To examine the wave characteristics of these cases, the corresponding dispersion curves are plotted in Fig. 5.2 for a plate under SC condition. It is seen from Fig. 5.2 that, in all cases, the wave frequencies corresponded to all wave modes, namely M_0, M_1, M_2 and M_3 increase with an increase of the wavenumber β. Based on the figure, one can observe that the smart plate with perfect FG substrate provides the highest wave frequencies followed by porous FGM plates with uneven and even porosity distribution, respectively.

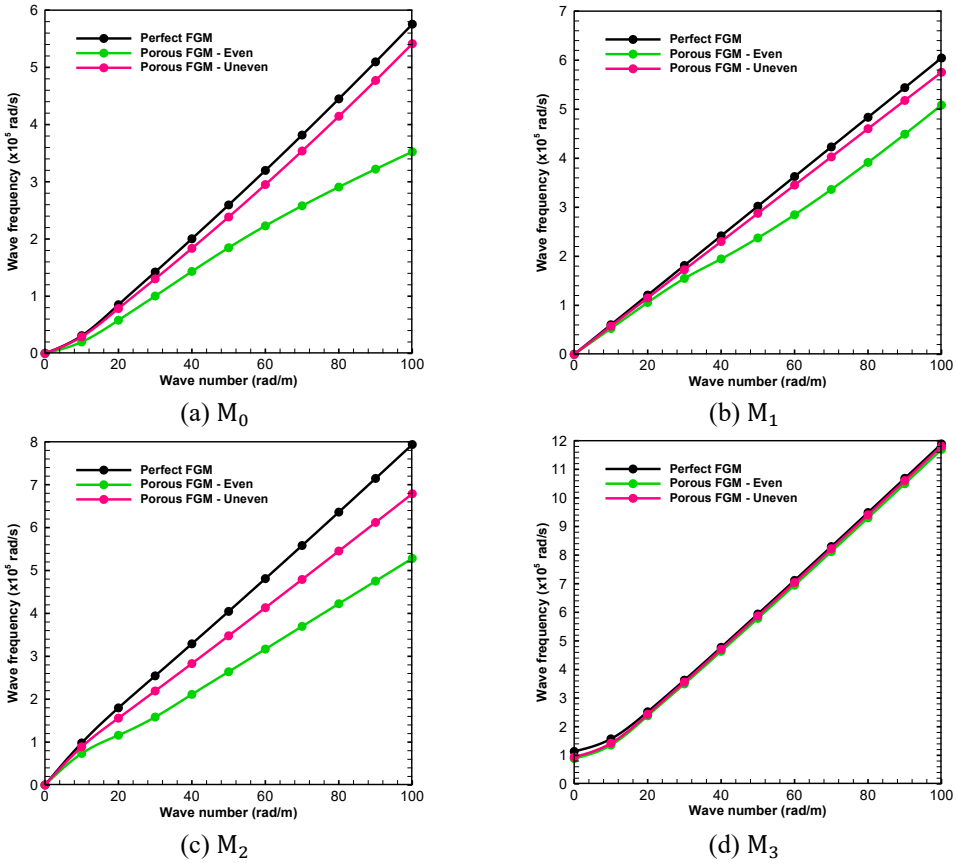

(a) M_0 (b) M_1

(c) M_2 (d) M_3

Fig. 5.2: Variation of wave frequency versus wave number for smart sandwich plates in SC condition ($2h = 0.1m, h_p/2h = 0.05, N = 2, e_0 = 0.4$)

The phase velocity response of the system is shown in Fig. 5.3 for all four wave modes. The trend of phase velocity curves is highly dependent on the wave mode and the porosity distribution profile. Fig. 5.3a exhibits an increasing trend of phase velocity for the mode M_0, when β is rising, regardless of the type of material selected for the core layer. Regarding the second mode, Fig. 5.3b suggests a constant phase velocity for the smart plates with the core layer made of perfect FGM and uneven FGM while a non-flat curve is associated with even porosity distribution. The phase velocity corresponding to the third and fourth modes decreases and then gradually tends to a constant value as the wavenumber increases. However, the drop in the value of curves associated with the fourth mode in the low wavenumber band is considerably sharper with respect to the third mode.

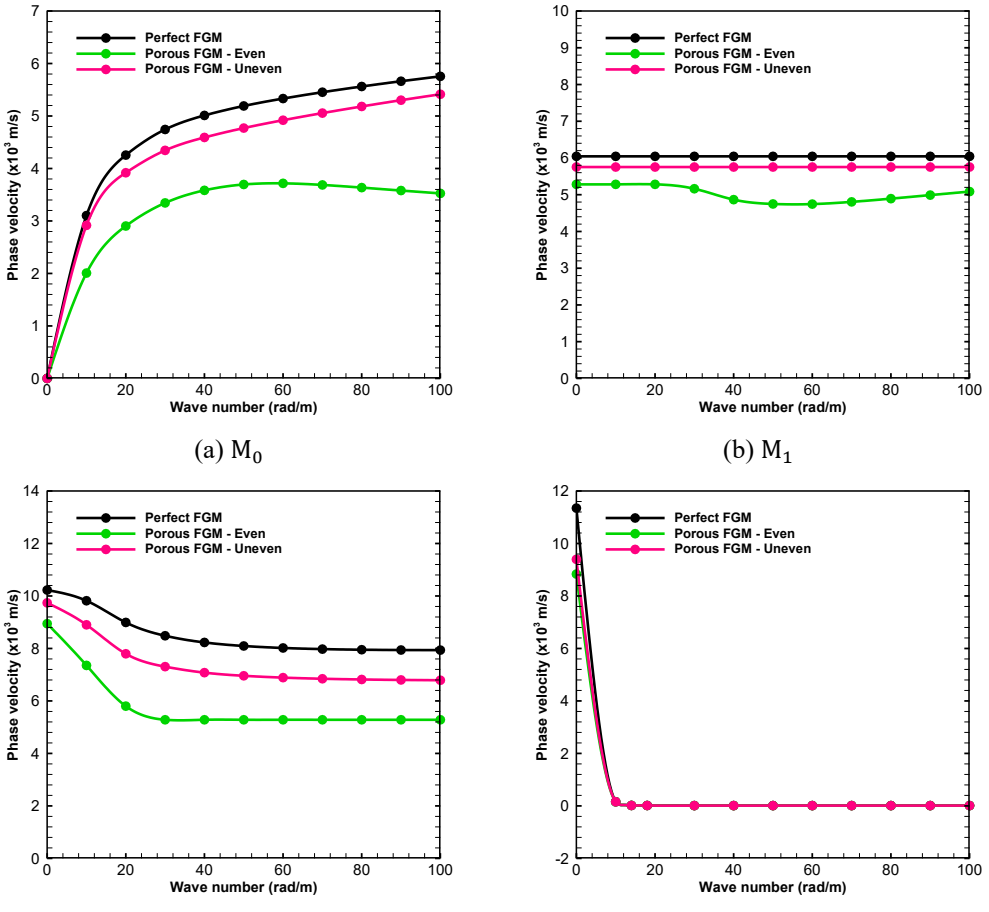

(a) M_0 (b) M_1

(c) M_2 (d) M_3

Fig. 5.3: Variation of wave velocity versus wave number for SC smart plates with four different porosity distributions ($2h = 0.1m, h_p/2h = 0.05, N = 2, e_0 = 0.4$)

To indicate the influences of the electrical and mechanical properties of the piezoelectric layers on dispersion characteristics of the systems under investigation, Fig. 5.4 and Fig. 5.5 present the dispersion and phase velocity curves of the first mode, respectively, when the core plate is made of perfect and porous FG materials. As demonstrated in these figures, the electrical effect in the SC condition is negligibly higher than a case in which only the mechanical effect of the piezoelectric layers (stiffness) is taken into account. However, the electrical effect in the OC condition causes a rather significant increase in the value of frequency. Consequently, the curve associated with the OC condition lies above the other two cases, regardless of the adopted porosity distribution and the power-law index N. Regarding the overall trend of the dispersion and phase velocity curves, it is observed that they follow a similar path in comparison to what is already portrayed in Fig. 5.2a and Fig. 5.3a.

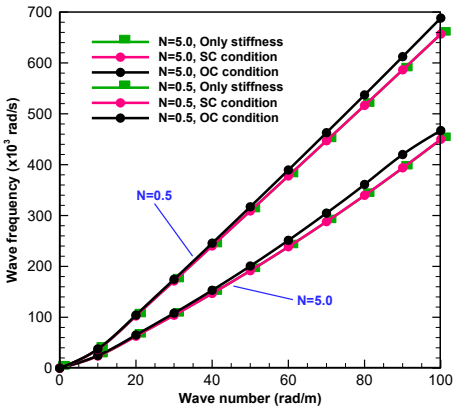

(a) Porous FGM - Even

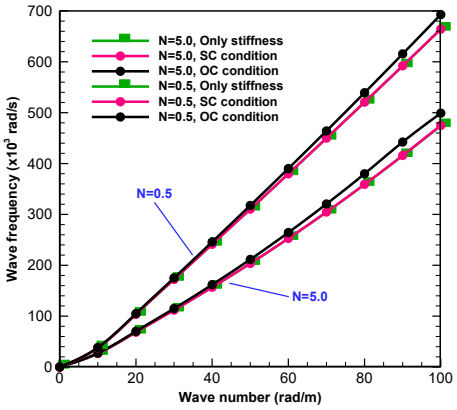

(b) Porous FGM - Uneven

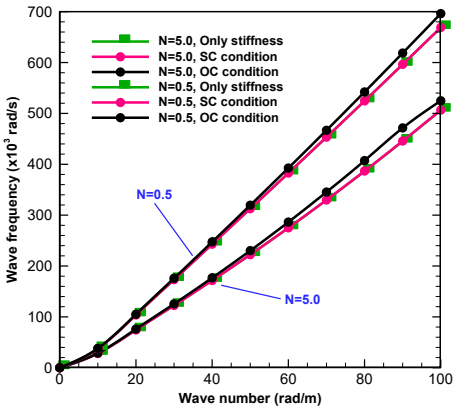

(c) Perfect FGM

Fig. 5.4: Electrical and mechanical effects of piezoelectric layers on wave frequency $(M_0, 2h = 0.1m, h_p/2h = 0.05, e_0 = 0.2)$

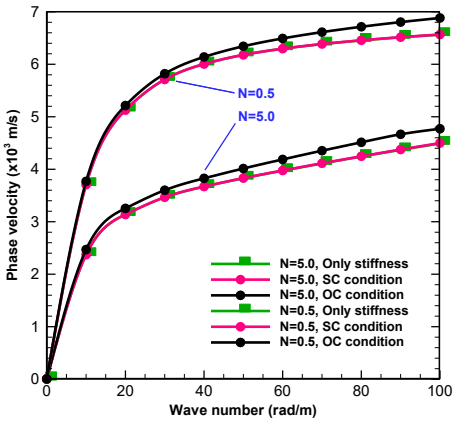

(a) Porous FGM - Even

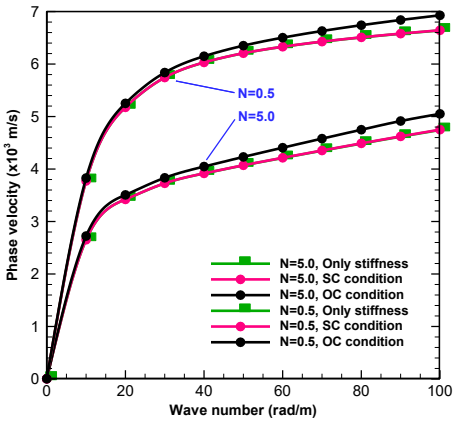

(b) Porous FGM - Uneven

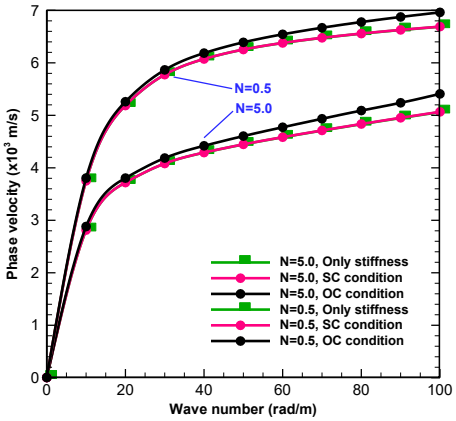

(c) Perfect FGM

Fig. 5.5: Electrical and mechanical effects of piezoelectric layers on phase velocity $(M_0, 2h = 0.1m, h_p/2h = 0.05, e_0 = 0.2)$

The variation of wave frequency associated with the first mode against the power-law index is plotted in Fig. 5.6, for different values of porosity volume fraction e_0, porosity distribution and electrical circuit conditions. According to the figures, the wave frequencies are significantly influenced by the variation of the power-law index. Regardless of the type of porosity distribution, the wave frequencies decrease with increasing the value of N, although a sharper decline in the value of frequencies is observed for the system with even porosity distribution compared to the case with uneven porosity distribution. Besides, the existence of a switching power-law index is identified, before which the wave frequencies increase by a drop in e_0 (for a fixed value of N) while the opposite behavior is seen after the switching point for both even and uneven porosity distributions. This value depends on the adopted porosity distribution and electrical boundary conditions. For instance, the switch power-law index for the hybrid plate with a core characterized by the even porosity profile is around 0.3, whereas this point appears around 0.8 for the system with uneven porosity distribution. Furthermore, the figure suggests that the sensitivity of the system to the porosity is more considerable when the pores are evenly distributed inside the core layer with respect to the uneven distribution profile.

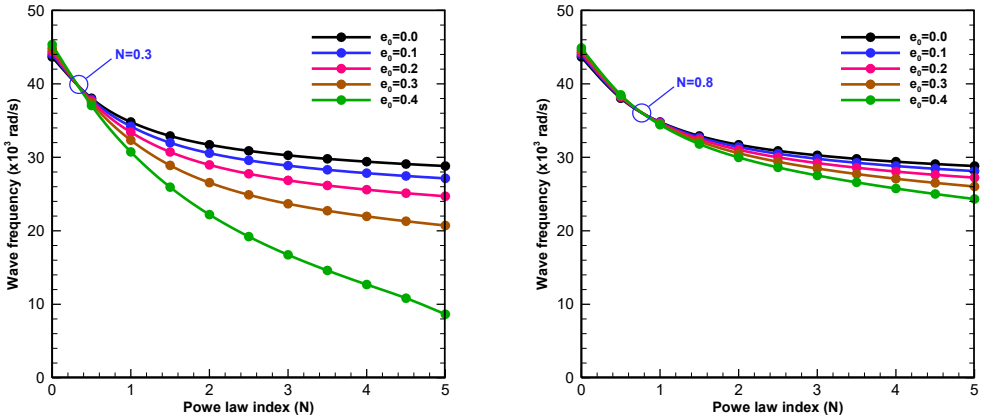

(a) OC Porous FGM - Even (b) OC Porous FGM - Uneven

Fig. 5.6: Variation of wave frequency versus power-law index for OC smart plates $(M_0, K = 10, 2h = 0.1m, h_p/2h = 0.05)$

The combined effects of the power-law index and porosity volume fraction are further investigated in Fig. 5.7, where the variation of wave frequency of all four modes is plotted versus the porosity parameter for both even and uneven porosity profiles. The curves shown in this figure confirm the decreasing trend for wave frequency due to the increase in value of e_0 for the adopted N, a conclusion drawn from the previous figure (i.e., Fig. 5.6).

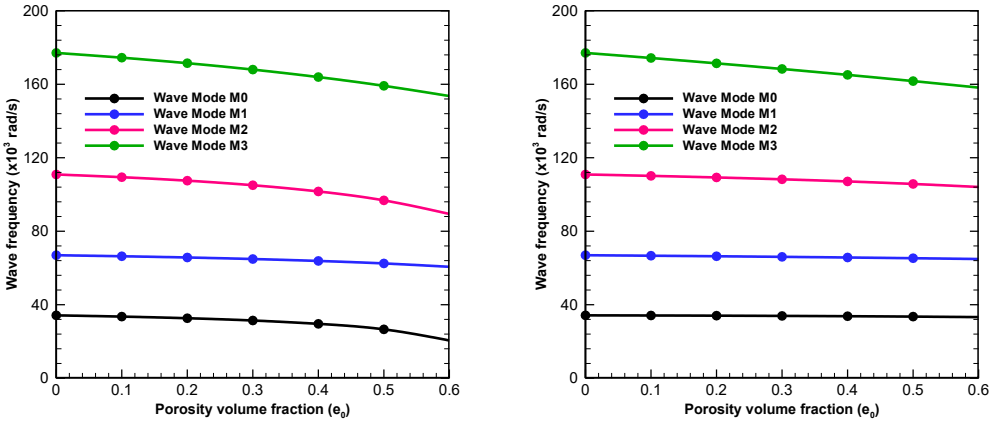

(a) Even porosity distribution (b) Uneven porosity distribution

Fig. 5.7. Variation of wave velocity versus porosity volume fraction for smart plates under SC condition $(N = 1, 2h = 0.1m, h_p/2h = 0.05, K = 10)$

5.6.2.2 Numerical Results of Free Vibration Analysis

The results obtained from the mathematical formulation presented in subsection 5.5.2 will be discussed here for smart square plates. For that matter, Table 5.6 provides a comprehensive parametric study to realize the effect of electrical and mechanical boundary conditions, porosity volume fraction, type of porosity distribution, and the adopted plate theory on the natural frequencies of the hybrid plate. As the primary observation, the table suggests that the PSPT yields higher frequencies with respect to SSPT, which can be attributed to the definition of the shape function $f(z)$ for each theory. Besides, similar to what is found in the previous subsection (i.e., subsection 5.6.2.1.), the plates under OC condition deliver higher frequencies compared to their counterpart under SC condition. This fact can be attributed to the various electric potential distributions in the thickness direction of the piezoelectric layers in these two cases. It is worth noticing that in the case of SC condition, a large amount of electrical energy is released through the outer electrodes connected to each piezoelectric layer; therefore, the significant drop in the effectiveness of the piezoelectric effect causes the smart hybrid plate stiffness to increase slightly. Conversely, the electrical energy of the bonded piezoelectric layers cannot be released whilst the hybrid plate is vibrating freely in the OC mode, which ultimately results in considerable growth in effective stiffness of the coupled piezoelectric FG plate and its natural frequencies as well. Furthermore, according to the table, the plate under CCFF boundary conditions provides the highest frequencies with respect to other cases, followed by CCCC, CCCS, CCSS, and SSSS boundary conditions, irrespective of other considered parameters. As expected, it appears that the coupled plate with a perfect FGM core owns the highest frequencies. Comparing the frequencies of plates with the substrate made of porous FGM characterized by uneven and even distribution profiles, the former yields higher frequencies, which is in agreement with the results portrayed in Fig. 5.4. Eventually, higher sensitivity of natural frequency to porosity for the case of even distribution compared to the uneven porosity profile can also be perceived from the table, compliant with what is demonstrated in Fig. 5.6.

In this subsection, the graphical presentation of results is given in terms of natural frequency relative difference θ, defined as:

$$\theta = \frac{\omega_{HP} - \omega_P}{\omega_P} \times 100 \tag{31}$$

where ω_{HP} and ω_P are the natural frequency of the hybrid plate and that of the same plate in absence of piezoelectric layers, respectively. Fig. 5.8 surveys the impact of the thickness ratio $h_p/2h$ and power-law index N on the value of θ, for a simply supported square plate. The figure reveals that the trend of curves is alike when the core plate is either made of perfect FGM or porous FGM with uneven profile though curve path can differ for the coupled plates with substrates composed of porous FGM with even profile depending on N. In the former case, θ initially decreases as the piezoelectric thickness ratio rises and then adopts an increasing trend owing to further growth of $h_p/2h$, and the porosity distribution profile. A similar trend can also be observed for the curves corresponding to the latter case as long as the power-law index does not exceed a certain threshold. Outside that threshold, the relative difference θ follows an ever-increasing trend. It is worth mentioning that the higher the N, the greater the θ is, irrespective of the distribution in the core plate.

Table 5.6: Eigenfrequencies (Hz) of perfect and porous FG plates integrated with piezoelectric layers ($a = b = 1m$, $2h/a = 0.1$, $h_p/2h = 0.05$, $N = 5$).

BC's	e_0	EC's	Model	Substrate material		
				Perfect FGM	Porous FGM-Even	Porous FGM-Uneven
SSSS	0.1	SC	SSPT	589.651	555.624	583.768
			PSPT	589.935	555.966	584.219
		OC	SSPT	605.946	574.973	600.948
			PSPT	606.474	575.620	601.692
	0.3	SC	SSPT	589.651	402.639	563.213
			PSPT	589.935	403.099	564.456
		OC	SSPT	605.946	440.236	582.583
			PSPT	606.474	441.346	584.320
CCCC	0.1	SC	SSPT	1048.481	986.515	1032.877
			PSPT	1049.648	987.916	1034.713
		OC	SSPT	1075.877	1018.777	1061.361
			PSPT	1078.075	1021.453	1064.414
	0.3	SC	SSPT	1048.481	718.610	980.443
			PSPT	1049.648	720.536	985.316
		OC	SSPT	1075.877	780.088	1011.097
			PSPT	1078.075	784.696	1017.889
CSCS	0.1	SC	SSPT	1024.159	963.833	1010.537
			PSPT	1025.070	964.924	1011.971
		OC	SSPT	1051.371	995.984	1038.972
			PSPT	1053.082	998.067	1041.357
	0.3	SC	SSPT	1024.159	699.612	964.378
			PSPT	1025.070	701.073	968.223
		OC	SSPT	1051.371	761.418	995.493
			PSPT	1053.082	764.962	1000.869
CCCS	0.1	SC	SSPT	1035.236	974.181	1020.747
			PSPT	1036.261	975.409	1022.359
		OC	SSPT	1062.569	1006.426	1049.243
			PSPT	1064.495	1008.772	1051.925
	0.3	SC	SSPT	1035.236	708.291	971.818
			PSPT	1036.261	709.956	976.122
		OC	SSPT	1062.569	770.033	1002.767
			PSPT	1064.495	774.048	1008.777
CCFF	0.1	SC	SSPT	1100.263	1034.939	1082.453
			PSPT	1101.677	1036.638	1084.674
		OC	SSPT	1128.482	1068.090	1111.681
			PSPT	1131.153	1071.340	1115.379
	0.3	SC	SSPT	1100.263	755.505	1023.104
			PSPT	1101.677	757.873	1028.946
		OC	SSPT	1128.482	818.263	1054.167
			PSPT	1131.153	823.889	1062.299

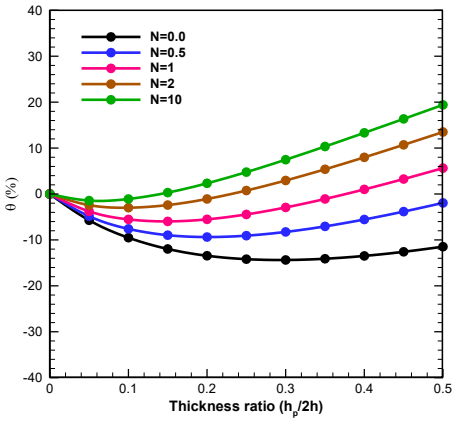

(a) Perfect FGM

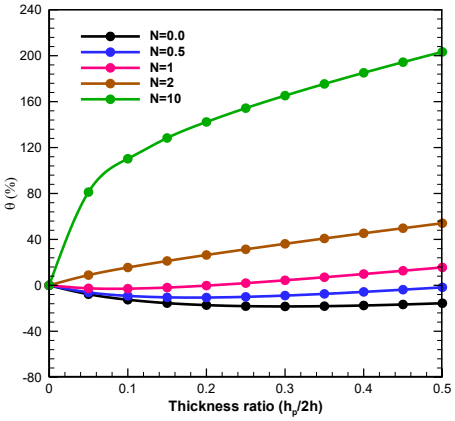

(b) Porous FGM - Even

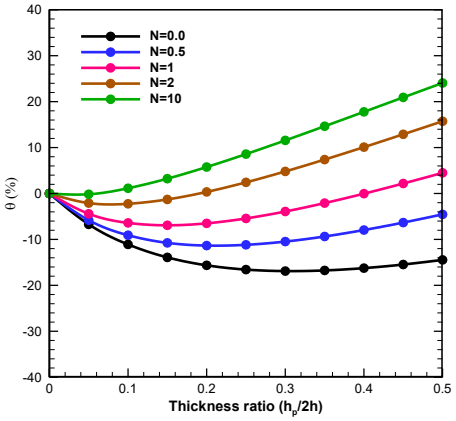

(c) Porous FGM - Uneven

Fig. 5.8: Effect of piezoelectric layers on the fundamental frequency of the smart FGM plates in SC condition ($a = b = 1m$, $2h/a = 0.1$, $e_0 = 0.3$, S-S-S-S)

The effect of boundary conditions, namely SSSS, CSCS, CCCS, CCCC and CCFF on the relative difference θ versus the piezoelectric thickness ratio $h_p/2h$ is highlighted in Figure 5.9, for both SC and OC conditions. From the figure, it is perceived that the integration of piezoelectric layers with the core plate is more influential for the simply supported plate, followed by CSCS, CCCS, CCCC, and CCFF boundary conditions. For instance, the natural frequency of the simply-supported hybrid plate with $h_p/2h = 0.5$ under OC condition increases by 16% due to the introduction of piezoelectric layers while this value is around 11% for its clamped counterpart. It is worth mentioning that the aforementioned increase is more considerable for plates under OC condition compared to those under SC condition.

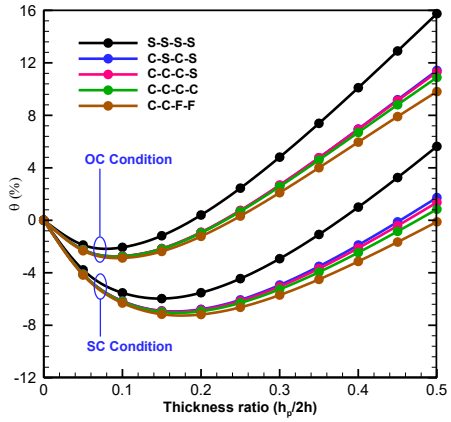

Fig. 5.9: Effect of piezoelectric layers on the fundamental frequency of the perfect FGM plate having different boundary conditions ($a = b = 1m$, $2h/a = 0.1$, $N = 1$)

The variation of natural frequency with piezoelectric thickness ratio $h_p/2h$ is plotted in Fig. 5.10, for different values of porosity volume fraction e_0 considering both OC and SC conditions. It is observed that by increasing the value of e_0, the effect of piezoelectric layers on the response becomes more dominant. This is due to the fact that these three curves approach each other at the termination point ($h_p/2h = 0.5$) though their starting points are widely separated. In fact, the share of piezoelectric layers in the effective stiffness of the system rises while the share of the substrate is dropping. Another crucial point is related to the impact of porosity on the trend of curves. For instance, in both Fig. 5.10(a) and Fig. 5.10(b), by increasing the value of $h_p/2h$, the curves corresponding to "Perfect FGM" experience a drop initially and then start growing after touching the local minimum of the curves at a particular piezoelectric thickness ratio. However, natural frequencies of systems associated with "Porous FGM - Even ($e_0 = 0.4$)" follow a constantly growing path, unlike those of "Perfect FGM".

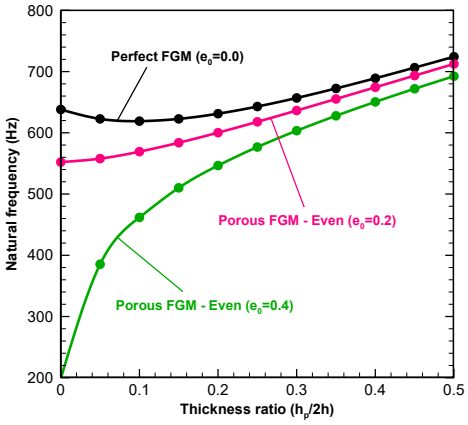

(a) SC condition

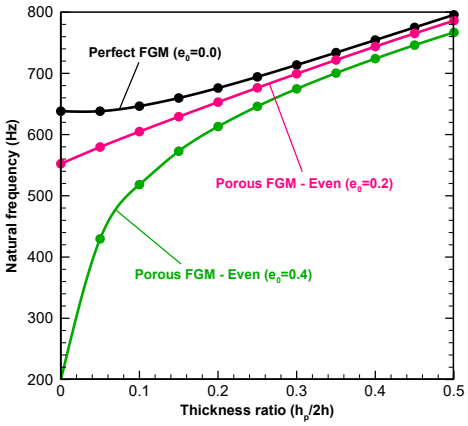

(b) OC condition

Fig. 5.10: Effect of piezoelectric layers on the fundamental frequency of the smart porous FGM plate ($a = b = 1m$, $2h/a = 0.1$, $N = 2$, S-S-S-S)

The combined effects of the power-law index, porosity distribution, and mechanical and electrical boundary conditions are demonstrated in Fig. 5.11 by plotting the variation of natural frequency against the porosity volume fraction. Regarding the case of smart porous FGM plate with uneven porosity profile, the natural frequency increases as e_0 grows in the range plotted, regardless of other considered factors, including boundary conditions and power-law index. On the other hand, the curves associated with the core composed of porous FGM with the even porosity profile can either have an ascending or descending trend depending upon the value of N. Furthermore, choosing a higher power-law index results in lower frequencies due to the drop in the effective stiffness of the plate, which is

consistent with the results of Fig. 5.8. Note that the figure also confirms the previous findings concerning the relation of frequencies with electrical and mechanical boundary conditions.

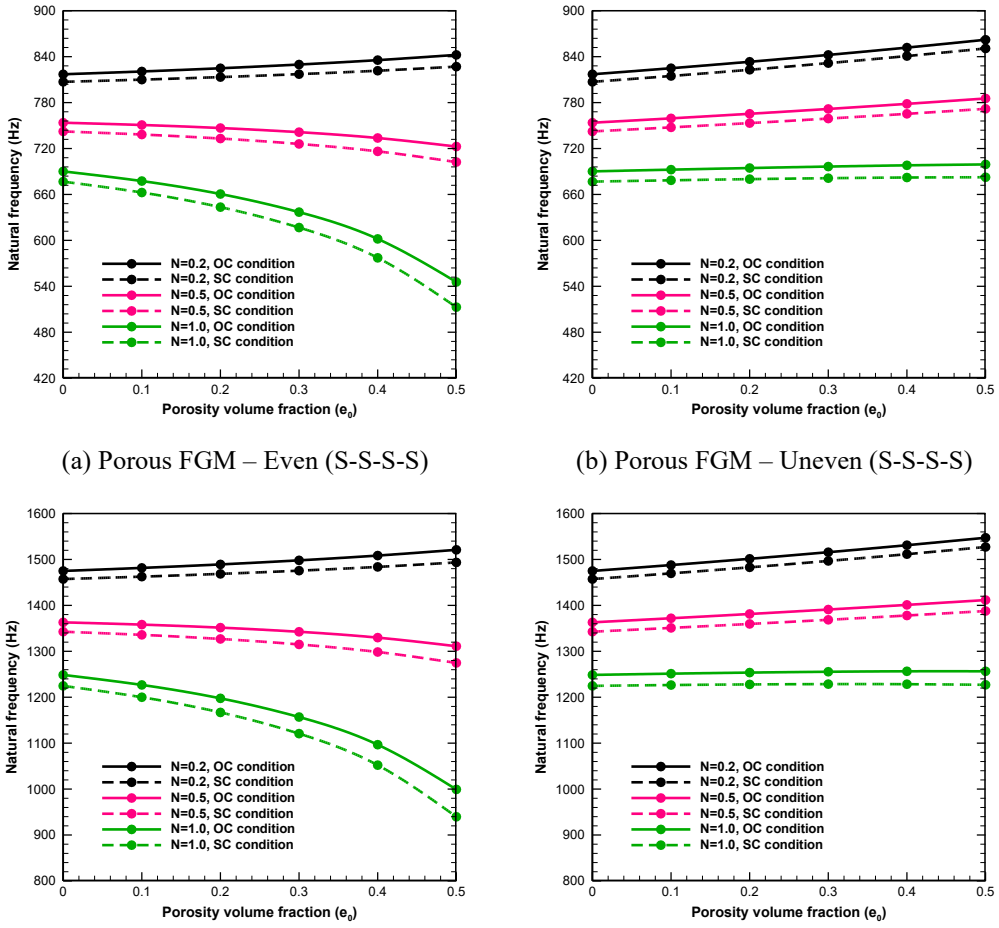

(a) Porous FGM – Even (S-S-S-S)

(b) Porous FGM – Uneven (S-S-S-S)

(c) Porous FGM – Even (C-C-C-C)

(d) Porous FGM – Uneven (C-C-C-C)

Fig. 5.11: Effect of piezoelectric layers on the fundamental frequency of FG porous smart plate in SC condition ($a = b = 1m$, $2h/a = 0.1$, $h_p/2h = 0.05$)

5.7 Summary and Conclusions

In this chapter, an efficient and simple four-variable shear deformation theory is used to establish a 2D model for the wave propagation and free vibration analysis of perfect and porous FGM plates integrated with piezoelectric layers. The respective governing equations are derived using Hamilton's principle and

Maxwell's equation. The plane wave solution is considered to address the problem of wave propagation in infinite smart coupled plates. Regarding the exact solution for the free vibration analysis, general boundary conditions are satisfied by assigning particular admissible functions to each type. It is concluded that the adopted theory is not only accurate but also efficient in prediction of the wave propagation and free vibration characteristics of the smart plates compared to other shear deformation theories. The existence of porosities in the FGM core leads to hybrid plates with lower wave frequency and phase velocity (in the context of wave propagation) and natural frequencies (in the context of free vibration), compared to the smart plates with perfect FGM substrate. Moreover, some other important conclusions are drawn from the parametric studies, as:

- Higher frequencies (in both contexts) and higher wave velocities are obtained for the smart porous FGM plates with uneven porosity distribution compared to their counterparts with even distribution.
- Depending on the value of the power-law index, an increase in the porosity volume fraction can lead to either an increase or decrease in the wave/natural frequencies of the smart porous FGM plates.
- In the context of wave propagation, wave frequency always grows while the phase velocity can adopt both uptrend and downtrend, as the wavenumber increases.
- In both context, higher sensitivity of the response (wave/natural frequency) to the porosity is demonstrated for the case of even porosity distribution as compared to the uneven one.
- In both contexts, the changes in frequencies (due to adding piezoelectric layers) of the plates with porous FGM substrates is more significant as compared with the corresponding results for the plates without porosities.
- In the context of free vibration, significant effect of boundary conditions on the respective response is realized. The hybrid plate under CCFF boundary condition owns the highest natural frequencies, followed by its counterparts with CCCC, CCCS, CSCS and SSSS edge conditions, respectively.

Chapter 6

Buckling Analysis of Piezoelectric Bimorph Plates

6.1 Overview

Based on the higher-order displacement model employed in the previous chapter, an exact solution with the help of *state space approach* is herein presented to study the buckling behavior of the composite bimorph plate. The smart plate is assumed to be subjected to different in-plane mechanical loadings so that it buckles and undergoes a deviation from the flat state when the applied loads are increased up to a certain value, which is called critical buckling load. Since the developed model allows to consider the substrate layer made of materials with varying properties along the thickness, it is assumed (in this analysis) to be made of saturated porous materials, in which the internal pore pressure is included in the stress-strain relationships. Accordingly, the constitutive equations of porous materials are considered based on Biot's poroelasticity theory, which takes into account the effect of pore fluid compressibility. For comparison, different symmetric and asymmetric patterns are considered for the distribution of porosities within the porous substrate. A generalized *Levy-type* solution in conjunction with the *State Space* concept is

used to solve the respective equations for the smart coupled plate. Exact buckling loads of the system are obtained for the system under different loading conditions, and arbitrary boundary conditions. It is finally shown that the magnitude of the buckling load depends on geometry, material properties, piezoelectric characteristics, and the buckling mode shape, i.e., geometric configuration of the plate at buckling.

6.2 Problem Modelling

When a plate is subjected to uniform compressive forces applied in the middle plane of the plate, and if the forces are sufficiently small, the force-displacement response is linear. The linear relationship holds until a certain load is reached. At that load, called the *buckling load*, the stable state of the plate is disturbed, and the plate seeks an alternative equilibrium configuration accompanied by a change in the load deflection behavior. The phenomenon of changing the equilibrium configuration at the same load and without drastic changes in deformation is termed *bifurcation*.

It is assumed here that the piezoelectric bimorph plate (which is schematically shown in Fig. 1.3) undergoes three different loading condition, as presented in Fig. 6.1. Note that the in-plane loads are acting at the middle plane of the plate.

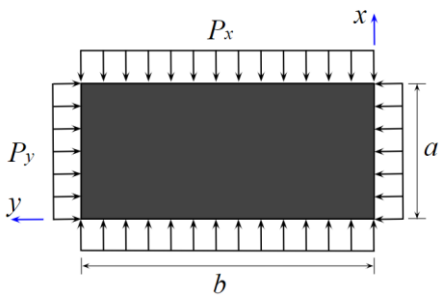

(a) Biaxial compressive loading

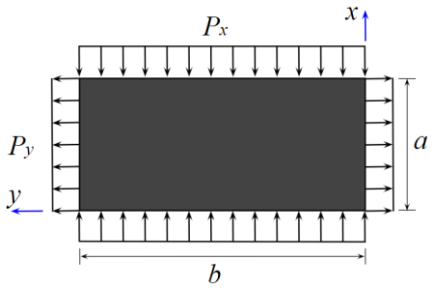

(b) Biaxial compressive and tension loading

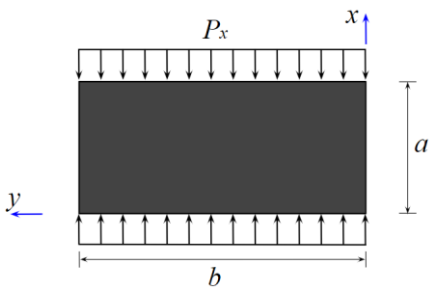

(c) Uniaxial compressive loading

Fig. 6.1: Cross-section of the porous bimorph plate with various porosity distributions

As mentioned earlier, the substrate layer is considered to be made of saturated porous materials (here, *Tennessee marble*), which means the material properties in the core layer vary from one point to another within the thickness direction (due to the presence of porosities). In the analysis performed in this chapter, all the porosity profiles presented in Fig. 1.10 of Chapter 1 are considered as the patterns of porosity distribution within the porous substrate, in which the related formulations (corresponding to the effective material properties) are given in Eqs. (1.17) to (1.20).

According to the Biot's poroelasticity theory, the linear constitutive equations describing stress-strain relationships for a fluid-filled porous material can be expressed as [16]:

$$\sigma_{ij} = 2G(z)\varepsilon_{ij} + \frac{2G(z)\nu_u}{1-2\nu_u}\varepsilon\delta_{ij} - \alpha M\zeta\delta_{ij} \tag{6.1}$$

It is reminded that the parameter M represents the Biot modulus, defined as the rise in the amount of fluid, ν_u is the undrained Poisson ratio, and ε denotes the volumetric strain. δ_{ij} is the Kronecker delta function, ζ is the variation of fluid volume content inside the pores, and α denotes the Biot coefficient of effective stress which is defined as $\alpha = \alpha(z) = 1 - G(z)/G_t$ $(0 < \alpha < 1)$. The parameters M and ν_u are defined in terms of other material properties as follows:

$$M = \frac{2G(z)(\nu_u - \nu)}{\alpha^2(1-2\nu_u)(1-2\nu)} \tag{6.2a}$$

$$\nu_u = \frac{3\nu + \alpha B(1-2\nu)}{3 - \alpha B(1-2\nu)} \tag{6.2b}$$

$$\alpha = 1 - \frac{G(z)}{G_t} = e_1 \cos\left(\frac{\pi z}{2h} + \frac{\pi}{4}\right) \tag{6.2c}$$

Here, B and ν represent the Skempton pore pressure coefficient and the drained Poisson's ratio ($\nu \leq \nu_u \leq 0.5$), respectively. It should be noted that the Skempton coefficient B is a measure, determining the degree of saturation in the porous body. In particular, when the value of B equals zero, it refers to nearly absent pore fluid, thus estimating the porous solid as a dry porous medium. In this study, the porous media is considered to operate under undrained condition, implying the entrapment of fluid in the porous solid accompanied by no variation in the fluid volume content in the internal pores, i.e. $\zeta = 0$. Therefore, the constitutive Eq. (6.1) for plane-stress condition take the form [16]:

$$\begin{Bmatrix} \sigma_{xx} \\ \sigma_{yy} \\ \sigma_{xy} \\ \sigma_{xz} \\ \sigma_{yz} \end{Bmatrix} = \begin{bmatrix} Q_{11} & Q_{12} & 0 & 0 & 0 \\ Q_{12} & Q_{11} & 0 & 0 & 0 \\ 0 & 0 & Q_{22} & 0 & 0 \\ 0 & 0 & 0 & Q_{22} & 0 \\ 0 & 0 & 0 & 0 & Q_{22} \end{bmatrix} \begin{Bmatrix} \varepsilon_{xx} \\ \varepsilon_{yy} \\ \varepsilon_{xy} \\ \varepsilon_{xz} \\ \varepsilon_{yz} \end{Bmatrix} \tag{6.3}$$

where Q_{11}, Q_{12} and Q_{22} are the material stiffness coefficients as:

$$Q_{11} = \frac{2G(z)}{1-\nu_u}, \qquad Q_{12} = \frac{2G(z)\nu_u}{1-\nu_u}, \qquad Q_{22} = G(z) \tag{6.4}$$

in which ν_u is defined in Eq. (6.2b).

6.3 Governing Equations

The displacement field at any point of the smart plate is considered based on the four-variable higher-order shear deformation theory given in Eq. (5.1) of Chapter 5. Based on such displacement model, the stability equations of the plate can be derived by means of principle of minimum total potential energy, as:

$$\delta(U + V) = 0 \tag{6.5}$$

where δ denotes a variation with respect to x and y; U and V are the strain energy of the coupled plate and potential energy of external loads, respectively. Performing the mathematical calculations for δU and δV, the stability equations can be obtained as follows:

$$N_{xx,x} + N_{xy,y} = 0 \tag{6.6a}$$

$$N_{xy,x} + N_{yy,y} = 0 \tag{6.6b}$$

$$M^b_{xx,xx} + 2M^b_{xy,xy} + M^b_{yy,yy} + N(w) = 0 \tag{6.6c}$$

$$M^s_{xx,xx} + 2M^s_{xy,xy} + M^s_{yy,yy} + Q_{xz,x} + Q_{yz,y} + N(w) = 0 \tag{6.6d}$$

The term $N(w)$ in Eq. (6.6), is appeared due to the loads applied to the bimorph plate, and is given in the following expression for the in-plane loading condition:

$$\begin{aligned} N(w) = N^0_{xx}\left(w_{b,xx} + w_{s,xx}\right) + N^0_{yy}\left(w_{b,yy} + w_{s,yy}\right) \\ + 2N^0_{xy}\left(w_{b,xy} + w_{s,xy}\right) \end{aligned} \tag{6.7}$$

in which N^0_{xx}, N^0_{yy} and N^0_{xy} are the in-plane pre-buckling forces. In case the in-plane forces are assumed to be acting only in two-direction (i.e., x and y, see Fig. 6.1), we may have:

$$N^0_{xx} = r_x N_{cr},\ N^0_{yy} = r_y N_{cr},\ N^0_{xy} = 0 \tag{6.8}$$

where $r_x = r_y = -1$ for the biaxial compressive uniform loading (see Fig. 6.1(a)), $r_x = -1$ and $r_y = +1$ for the compressive-tension uniform loading (see Fig. 6.1(b)), and finally $r_x = -1$ and $r_y = 0$ when there is only compressive loading applied in the x-direction (see Fig. 6.1(c)). However, considering Eq. (6.8), Eq. (6.7) can be rewritten as:

$$N(w) = r_x N_{cr}\left(w_{b,xx} + w_{s,xx}\right) + r_y N_{cr}\left(w_{b,yy} + w_{s,yy}\right) \tag{6.9}$$

The stress resultants in Eq. (6.6) (i.e., N_{ij}, M^b_{ij}, M^s_{ij} and Q_{ij}) can be expressed in terms of the displacement field unknowns, and the electric potential function (see Eq. 5.13 in Chapter 5). One can simply obtain the stability equations in terms of the displacement field unknowns and the electric potential function by substituting the stress resultants (which are derived in terms of the unknowns) into Eq. (6.6), as:

$$(a_{11}+\lambda_1)u_{0,xx}+a_{66}u_{0,yy}+(a_{12}+a_{66}+\lambda_1)v_{0,yx} - (b_{11}+\lambda_2)w_{b,xxx}-(b_{12}+2b_{66}+\lambda_2)w_{b,yyx} - (d_{11}+\lambda_3)w_{s,xxx}-(d_{12}+2d_{66}+\lambda_3)w_{s,yyx} + \mu_1\phi_{0,x}=0 \tag{6.10a}$$

$$a_{66}v_{0,xx}+(a_{11}+\lambda_1)v_{0,yy}+(a_{12}+a_{66}+\lambda_1)u_{0,yx} - (b_{11}+\lambda_2)w_{b,yyy}-(b_{12}+2b_{66}+\lambda_2)w_{b,xxy} - (d_{11}+\lambda_3)w_{s,yyy}-(d_{12}+2d_{66}+\lambda_3)w_{s,xxy} + \mu_1\phi_{0,y}=0 \tag{6.10b}$$

$$\left(b_{11}+\hat{\lambda}_1\right)u_{0,xxx}+\left(b_{12}+2b_{66}+\hat{\lambda}_1\right)u_{0,yyx} + \left(b_{12}+2b_{66}+\hat{\lambda}_1\right)v_{0,yxx}+\left(b_{11}+\hat{\lambda}_1\right)v_{0,yyy} - \left(f_{11}+\hat{\lambda}_2\right)w_{b,xxxx}-2\left(f_{12}+2f_{66}+\hat{\lambda}_2\right)w_{b,yyxx} - \left(f_{11}+\hat{\lambda}_2\right)w_{b,yyyy}-\left(g_{11}+\hat{\lambda}_3\right)w_{s,xxxx} - 2\left(g_{12}+2g_{66}+\hat{\lambda}_3\right)w_{s,yyxx}-\left(g_{11}+\hat{\lambda}_3\right)w_{s,yyyy} + \hat{\mu}_1\phi_{0,xx}+\hat{\mu}_1\phi_{0,yy}+r_xN_{cr}\left(w_{b,xx}+w_{s,xx}\right) + r_yN_{cr}\left(w_{b,yy}+w_{s,yy}\right)=0 \tag{6.10c}$$

$$\left(d_{11}+\tilde{\lambda}_1+\lambda_4\right)u_{0,xxx}+\left(d_{12}+2d_{66}+\tilde{\lambda}_1+\lambda_4\right)u_{0,xyy} + \left(d_{12}+2d_{66}+\tilde{\lambda}_1+\lambda_4\right)v_{0,yxx} + \left(d_{11}+\tilde{\lambda}_1+\lambda_4\right)v_{0,yyy}-\left(g_{11}+\tilde{\lambda}_2+\lambda_5\right)w_{b,xxxx} + 2\left(-g_{12}-2g_{66}-\tilde{\lambda}_2+\lambda_5\right)w_{b,yyxx} - \left(g_{11}+\tilde{\lambda}_2-\lambda_5\right)w_{b,yyyy}-\left(h_{11}+\tilde{\lambda}_3-\lambda_6\right)w_{s,xxxx} + 2\left(-h_{12}-2h_{66}-\tilde{\lambda}_3+\lambda_6\right)w_{s,yyxx} - \left(h_{11}+\tilde{\lambda}_3-\lambda_6\right)w_{s,yyyy}+a_{55}\left(w_{s,xx}+w_{s,yy}\right) + (\tilde{\mu}_1+\mu_2)\phi_{0,xx}+(\tilde{\mu}_1+\mu_2)\phi_{0,yy} + r_xN_{cr}\left(w_{b,xx}+w_{s,xx}\right)+r_yN_{cr}\left(w_{b,yy}+w_{s,yy}\right)=0 \tag{6.10d}$$

The constant coefficients in Eq. (6.10), i.e., a_i, b_i, d_i, f_i, g_i, h_i ($i=11,12,66$), a_{55}, λ_j, $\hat{\lambda}_j$, $\tilde{\lambda}_j$ ($j=1,2,3$), μ_1, μ_2, $\hat{\mu}_1$, $\tilde{\mu}_1$ and λ_k ($k=4,5,6$) are the same as those given in Relations (D.1) to (D.3) of Appendix D, for both SC and OC electrical conditions.

The last governing equation of the smart composite plate can be derived from the integral form of Maxwell's equation, as:

$$\begin{aligned}\lambda_7\left(w_{s,xx}+w_{s,yy}\right)+\lambda_8\left(w_{b,xx}+w_{b,yy}\right)+\lambda_9\phi_0+\lambda_{10}\left(\phi_{0,xx}+\phi_{0,yy}\right)\\+\lambda_{11}\left(u_{0,xxx}+v_{0,yxx}+u_{0,xyy}+v_{0,yyy}\right)\\+\lambda_{12}\left(w_{b,xxxx}+2w_{b,xxyy}+w_{b,yyyy}\right)\\+\lambda_{13}\left(w_{s,xxxx}+2w_{s,xxyy}+w_{s,yyyy}\right)=0\end{aligned} \tag{6.11}$$

The constant coefficients λ_i $(i = 7,8,..,13)$ are the same as those given in Relations (D.4) and (D.5) of Appendix D, for both SC and OC conditions.

6.4 Solution Procedure

6.4.1 Navier-type Solution

Considering simply supported boundary conditions on all the edges of the piezoelectric bimorph plate structure, we may have:

$$v_0 = w_b = w_s = N_{xx} = M_{xx}^b = M_{xx}^s = \phi_0 = 0 \qquad \text{on edges } x = 0, a \tag{6.12a}$$

$$u_0 = w_b = w_s = N_{yy} = M_{yy}^b = M_{yy}^s = \phi_0 = 0 \qquad \text{on edges } y = 0, b \tag{6.12b}$$

Based on the Navier method, the following expansions of displacements (u_0, v_0, w_b, w_s), and electric potential function ϕ_0 are chosen to automatically satisfy the boundary conditions in Eq. (6.12):

$$\begin{aligned}u_0(x,y)&=\sum_{m=1}^{\infty}U_{0mn}\cos(\eta_m x)\sin(\eta_n y)\\v_0(x,y)&=\sum_{m=1}^{\infty}V_{0mn}\sin(\eta_m x)\cos(\eta_n y)\\w_b(x,y)&=\sum_{m=1}^{\infty}W_{bmn}\sin(\eta_m x)\sin(\eta_n y)\\w_s(x,y)&=\sum_{m=1}^{\infty}W_{smn}\sin(\eta_m x)\sin(\eta_n y)\\\phi_0(x,y)&=\sum_{m=1}^{\infty}\phi_{0mn}\sin(\eta_m x)\sin(\eta_n y)\end{aligned} \tag{6.13}$$

where $\eta_m = m\pi/a$, $\eta_n = n\pi/b$, and $(U_{0mn}, V_{0mn}, W_{bmn}, W_{smn}, \phi_{0mn})$ are unknown functions to be determined. Substituting Eq. (6.13) into Eqs. (6.10) and (6.11), the closed-form solution of buckling load N_{cr} can be obtained from:

$$\begin{bmatrix} B_{11} & B_{12} & B_{13} & B_{14} & B_{15} \\ B_{21} & B_{22} & B_{23} & B_{24} & B_{25} \\ B_{31} & B_{32} & B_{33} & B_{34} & B_{35} \\ B_{41} & B_{42} & B_{43} & B_{44} & B_{45} \\ B_{51} & B_{52} & B_{53} & B_{54} & B_{55} \end{bmatrix} \begin{Bmatrix} U_{0mn} \\ V_{0mn} \\ W_{bmn} \\ W_{smn} \\ \phi_{0mn} \end{Bmatrix} = \begin{Bmatrix} 0 \\ 0 \\ 0 \\ 0 \\ 0 \end{Bmatrix} \tag{6.14}$$

The buckling load term N_{cr} is included in the components of the coefficient matrix $[B]$. Therefore, for nontrivial solution, the determinant of the coefficient matrix in Eq. (6.14) must be zero. That solution gives closed-form solution for N_{cr}, in which for each choice of m and n, there is a corresponsive unique value of N_{cr}. The critical buckling load is the smallest value of N_{cr} (m, n).

6.4.2 Levy-type Solution by Means of State Space Concept

In Levy-type solution presented in this subsection, it is assumed that the two opposite edges of the plate that are parallel to the x-axis (i.e., edges $y = 0$ and $y = b$) have simply supported and the other two edges can have any arbitrary conditions such as free, simply supported, or clamped conditions. The simply supported boundary conditions on two opposite edges parallel to the x-axis are given in Eq. (6.12b), and the boundary conditions for the remaining two edges (at $x = 0$ and $x = a$) are:

Simply supported (S):

$$v_0 = w_b = w_s = N_{xx} = M_{xx}^b = M_{xx}^s = 0 \tag{6.15a}$$

Clamped (C):

$$u_0 = v_0 = w_b = w_s = w_{b,x} = w_{s,x} = 0 \tag{6.15b}$$

Free (F):

$$N_{xx} = N_{xy} = M_{xx}^b = M_{xx}^s = 0 \tag{6.15c}$$

$$M^b_{xx,x} + 2M^b_{xy,y} + N^0_{xx}\left(w_{b,x} + w_{s,x}\right) = 0$$
$$M^s_{xx,x} + 2M^s_{xy,y} + Q_{xz} + N^0_{xx}\left(w_{b,x} + w_{s,x}\right) = 0$$

Moreover, the edges $x = 0$ and $x = a$ are considered to be electrically isolated, so that the respective electrical boundary conditions can be obtained from the following equation:

$$\int_{-h-h_p}^{-h} D_x(x,y,z)\,dz + \int_{+h}^{+h+h_p} D_x(x,y,z) = 0 \tag{6.16}$$

Substituting the electrical displacement field into the above equation gives us:

$$T_1 w_{s,x} + T_2 \phi_{0,x} = 0$$
$$T_1 W'_{sm} + T_2 \phi'_{0m} = 0 \tag{6.17}$$

In order to solve the stability equations (6.10) and (6.11) with the prescribed boundary conditions, a generalized Levy-type approach in conjunction with state space concept is employed to obtain the closed-form solutions. Assuming simply supported boundary conditions on $y = 0$ and $y = b$, the following solutions for the transverse displacement unknowns as well as the electric potential are chosen to automatically satisfy the boundary conditions:

$$u_0(x,y) = \sum_{n=1}^{\infty} U_{0m}(x)\sin(\eta_n y)$$
$$v_0(x,y) = \sum_{n=1}^{\infty} V_{0m}(x)\cos(\eta_n y)$$
$$w_b(x,y) = \sum_{n=1}^{\infty} W_{bm}(x)\sin(\eta_n y) \tag{6.18}$$
$$w_s(x,y) = \sum_{n=1}^{\infty} W_{sm}(x)\sin(\eta_n y)$$
$$\phi_0(x,y) = \sum_{n=1}^{\infty} \phi_{0m}(x)\sin(\eta_n y)$$

Substituting Eq. (6.18) into Eqs. (6.10) and (6.11), a system of ordinary differential equations along the x-axis is obtained. In the following, the resulting equations of the case of bimorph plate under SC condition is given:

$$U_{0m}'' = Z_1 U_{0m} + Z_2 V_{0m}' + Z_3 W_{bm}' + Z_4 W_{bm}''' + Z_5 W_{sm}' + Z_6 W_{sm}''' \tag{6.19a}$$

$$V_{0m}'' = \tilde{Z}_1 U_{0m}' + \tilde{Z}_2 V_{0m} + \tilde{Z}_3 W_{bm} + \tilde{Z}_4 W_{bm}'' + \tilde{Z}_5 W_{sm} + \tilde{Z}_6 W_{sm}'' \tag{6.19b}$$

$$\phi_{0m}'' = \beta_1 \phi_{0m} + \beta_2 W_{bm}'' + \beta_3 W_{bm} + \beta_4 W_{sm}'' + \beta_5 W_{sm} \tag{6.19c}$$

$$\begin{aligned} &\xi_1 U_{0m}''' + \xi_2 U_{0m}' + \xi_3 V_{0m}'' + \xi_4 V_{0m} + \xi_5 W_{bm}'''' + \xi_6 W_{bm}'' + \xi_7 W_{bm} \\ &\quad + \xi_8 W_{sm}'''' + \xi_9 W_{sm}'' + \xi_{10} W_{sm} + \xi_{11} \phi_{0m}'' + \xi_{12} \phi_{0m} \\ &\quad = 0 \end{aligned} \tag{6.19d}$$

$$\begin{aligned} &\tilde{\xi}_1 U_{0m}''' + \tilde{\xi}_2 U_{0m}' + \tilde{\xi}_3 V_{0m}'' + \tilde{\xi}_4 V_{0m} + \tilde{\xi}_5 W_{bm}'''' + \tilde{\xi}_6 W_{bm}'' + \tilde{\xi}_7 W_{bm} \\ &\quad + \tilde{\xi}_8 W_{sm}'''' + \tilde{\xi}_9 W_{sm}'' + \tilde{\xi}_{10} W_{sm} + \tilde{\xi}_{11} \phi_{0m}'' + \tilde{\xi}_{12} \phi_{0m} \\ &\quad = 0 \end{aligned} \tag{6.19e}$$

The coefficients Z_i and $\tilde{Z}_i$ ($i = 1,2,\dots,6$), β_i ($i = 1,2,\dots,5$), as well as ζ_i and $\tilde{\zeta}_i$ ($i = 1,2,\dots,12$) in Eq. (6.19) are given in Relation (E.1) of Appendix E.

Substituting Eqs. (6.19a), (6.19b) and (6.19c) into Eq. (6.19d) yields:

$$\begin{aligned} &\alpha_1 W_{bm}'''' + \alpha_2 W_{sm}'''' + \alpha_3 U_{0m}' + \alpha_4 V_{0m} + \alpha_5 W_{bm} + \alpha_6 W_{bm}'' + \alpha_7 W_{sm} \\ &\quad + \alpha_8 W_{sm}'' + \alpha_9 \phi_{0m} = 0 \end{aligned} \tag{6.20}$$

Similarly, substituting Eqs. (6.19a), (6.19b) and (6.19c) into Eq. (6.19e) yields:

$$\begin{aligned} &\tilde{\alpha}_1 W_{bm}'''' + \tilde{\alpha}_2 W_{sm}'''' + \tilde{\alpha}_3 U_{0m}' + \tilde{\alpha}_4 V_{0m} + \tilde{\alpha}_5 W_{bm} + \tilde{\alpha}_6 W_{bm}'' + \tilde{\alpha}_7 W_{sm} \\ &\quad + \tilde{\alpha}_8 W_{sm}'' + \tilde{\alpha}_9 \phi_{0m} = 0 \end{aligned} \tag{6.21}$$

One can simply derive the following expression for the term W_{bm}'''' by multiplying Eq. (6.20) by $1/\alpha_2$ and Eq. (6.21) by $1/\tilde{\alpha}_2$, and performing some simple mathematical operations between the resulting equations, as:

$$\begin{aligned} W_{bm}'''' = {} & Z_8 U_{0m}' + Z_9 V_{0m} + Z_{10} W_{bm} + Z_{11} W_{bm}'' + Z_{12} W_{sm} + Z_{13} W_{sm}'' \\ & + Z_{14} \phi_{0m} \end{aligned} \tag{6.22}$$

Similarly, the following expression can be obtained for the term W_{sm}'''', as:

$$W_{sm}'''' = \tilde{Z}_8 U_{0m}' + \tilde{Z}_9 V_{0m} + \tilde{Z}_{10} W_{bm} + \tilde{Z}_{11} W_{bm}'' + \tilde{Z}_{12} W_{sm} + \tilde{Z}_{13} W_{sm}'' + \tilde{Z}_{14} \phi_{0m} \tag{6.23}$$

The coefficients α_i and $\tilde{\alpha}_i$ ($i = 1,2, \ldots ,9$), as well as Z_i and $\tilde{Z}_i$ ($i = 8,9 \ldots ,14$) in Eqs. (6.20) to (6.23) are given in Relation (E.2) of Appendix E.

Now, one can observe that substituting the Levy-type solution into the stability equations, as well as performing some mathematical operations, have led to the following set of ordinary equations to be solved through the use of the state space concept:

$$U_{0m}'' = Z_1 U_{0m} + Z_2 V_{0m}' + Z_3 W_{bm}' + Z_4 W_{bm}''' + Z_5 W_{sm}' + Z_6 W_{sm}''' \tag{6.24a}$$

$$V_{0m}'' = \tilde{Z}_1 U_{0m}' + \tilde{Z}_2 V_{0m} + \tilde{Z}_3 W_{bm} + \tilde{Z}_4 W_{bm}'' + \tilde{Z}_5 W_{sm} + \tilde{Z}_6 W_{sm}'' \tag{6.24b}$$

$$\phi_{0m}'' = \beta_1 \phi_{0m} + \beta_2 W_{bm}'' + \beta_3 W_{bm} + \beta_4 W_{sm}'' + \beta_5 W_{sm} \tag{6.24c}$$

$$W_{bm}'''' = Z_8 U_{0m}' + Z_9 V_{0m} + Z_{10} W_{bm} + Z_{11} W_{bm}'' + Z_{12} W_{sm} + Z_{13} W_{sm}'' + Z_{14} \phi_{0m} \tag{6.24d}$$

$$W_{sm}'''' = \tilde{Z}_8 U_{0m}' + \tilde{Z}_9 V_{0m} + \tilde{Z}_{10} W_{bm} + \tilde{Z}_{11} W_{bm}'' + \tilde{Z}_{12} W_{sm} + \tilde{Z}_{13} W_{sm}'' + \tilde{Z}_{14} \phi_{0m} \tag{6.24e}$$

Such equations can be rewritten in the following matrix form:

$$\{Z'(x)\} = [T]\{Z(x)\} \tag{6.25}$$

in which:

$$\{Z(x)\} = \begin{Bmatrix} U_{0m} \\ U'_{0m} \\ V_{0m} \\ V'_{0m} \\ W_{bm} \\ W'_{bm} \\ W''_{bm} \\ W'''_{bm} \\ W_{sm} \\ W'_{sm} \\ W''_{sm} \\ W'''_{sm} \\ \phi_{0m} \\ \phi'_{0m} \end{Bmatrix} \tag{6.26}$$

and:

$$[T] = \begin{bmatrix} 0 & 1 & 0 & 0 & 0 & 0 & 0 & 0 & 0 & 0 & 0 & 0 & 0 & 0 \\ Z_1 & 0 & 0 & Z_2 & 0 & Z_3 & 0 & Z_4 & 0 & Z_5 & 0 & Z_6 & 0 & 0 \\ 0 & 0 & 0 & 1 & 0 & 0 & 0 & 0 & 0 & 0 & 0 & 0 & 0 & 0 \\ 0 & \tilde{Z}_1 & \tilde{Z}_2 & 0 & \tilde{Z}_3 & 0 & \tilde{Z}_4 & 0 & \tilde{Z}_5 & 0 & \tilde{Z}_6 & 0 & 0 & 0 \\ 0 & 0 & 0 & 0 & 0 & 1 & 0 & 0 & 0 & 0 & 0 & 0 & 0 & 0 \\ 0 & 0 & 0 & 0 & 0 & 0 & 1 & 0 & 0 & 0 & 0 & 0 & 0 & 0 \\ 0 & 0 & 0 & 0 & 0 & 0 & 0 & 1 & 0 & 0 & 0 & 0 & 0 & 0 \\ 0 & Z_8 & Z_9 & 0 & Z_{10} & 0 & Z_{11} & 0 & Z_{12} & 0 & Z_{13} & 0 & Z_{14} & 0 \\ 0 & 0 & 0 & 0 & 0 & 0 & 0 & 0 & 0 & 1 & 0 & 0 & 0 & 0 \\ 0 & 0 & 0 & 0 & 0 & 0 & 0 & 0 & 0 & 0 & 1 & 0 & 0 & 0 \\ 0 & 0 & 0 & 0 & 0 & 0 & 0 & 0 & 0 & 0 & 0 & 1 & 0 & 0 \\ 0 & \tilde{Z}_8 & \tilde{Z}_9 & 0 & \tilde{Z}_{10} & 0 & \tilde{Z}_{11} & 0 & \tilde{Z}_{12} & 0 & \tilde{Z}_{13} & 0 & \tilde{Z}_{14} & 0 \\ 0 & 0 & 0 & 0 & 0 & 0 & 0 & 0 & 0 & 0 & 0 & 0 & 0 & 1 \\ 0 & 0 & 0 & 0 & \beta_3 & 0 & \beta_2 & 0 & \beta_5 & 0 & \beta_4 & 0 & \beta_1 & 0 \end{bmatrix} \tag{6.27}$$

A formal solution of Eq. (6.25) is given by:

$$\{Z(x)\} = e^{Tx}\{K\}_{14\times 1} \tag{6.28}$$

where $\{K\}$ is a constant column vector determined from the boundary conditions of the two edges parallel to the y-axis ($x = 0$ and $x = a$), and e^{Tx} is the general matrix solution of Eq. (6.25), which can be expressed by:

$$e^{Tx} = [E]\begin{bmatrix} e^{\lambda_1 x} & & 0 \\ & \ddots & \\ 0 & & e^{\lambda_{14} x} \end{bmatrix}[E]^{-1} \tag{6.29}$$

where λ_i $(i = 1,2, \ldots 14)$ and $[E]$ are distinct eigenvalues and the corresponding matrix of eigenvectors, respectively, associated with the matrix $[T]$. Substituting Eq. (6.28) into the appropriate fourteen boundary conditions of the two edges along the y-axis ($x = 0$ and $x = a$), a homogeneous system of equations is obtained, as:

$$[M]_{14\times14}\{K\}_{14\times1} = 0 \tag{6.30}$$

The buckling load $N_{cr}(n)$ associated with the nth mode can be obtained by setting the determinant of matrix $[M]$ equal to zero. The critical buckling load is the smallest value of $N_{cr}(n)$. It should be noted that this solution procedure cannot provide buckling load directly because the undetermined buckling load N_{cr} is included in matrix $[T]$. Hence, a trial and error procedure needs to be used to obtain the buckling results. The following iteration procedure has been used in the present study to calculate the critical bucking load:

Step 1. Assign a small initial value to N_{cr}.
Step 2. Form matrix T and compute the eigenvalues λ_i and eigenvectors $[E]$ of $[T]$.
Step 3. Form matrix $[M]$ on the basis of appropriate boundary conditions given in Eqs. (6.15) and (6.17).
Step 4. Check if the determinant of matrix $[M]$ changes sign.
(a) If no, increase the buckling load and go back to Step 2.
(b) If yes, decrease the buckling load by a small amount and go to next step.
Step 5. Check if the relative error between two successive iterations is within a given tolerance, stop the iteration. Otherwise, return to Step 2.

6.5 Numerical Results

6.5.1 Model Validation

For the sake of verification of the presented formulation, the numerical results are first compared with those of some studies available in the literature. Table 2 compares the extracted results with the spline strip solution of Shufrin and Eisenberger [201] for the buckling response of a simply supported isotropic rectangular plate. The results are given for rectangular plates with three different thickness-length ratios, namely 0.1, 0.2 and 0.3, subjected to both biaxial and uniaxial compressive in-plane loading conditions.

Table 6.1: Comparison of the buckling loads obtained from the present model with those of Ref. [201], for a simply supported plate

$\frac{a}{b}$	$\frac{2h}{a}$	Source	Loading Type		
			$r_x = -1, r_y = 0$	$r_x = 0, r_y = -1$	$r_x = -1, r_y = -1$
1	0.1	FSDT [201]	3.7865	3.7865	1.8932
		TSDT [201]	3.7866	3.7866	1.8933
		Present	3.7854	3.7854	1.8920
	0.2	FSDT [38]	3.2637	3.2637	1.6327
		Present	3.2652	3.2652	1.6325
	0.3	FSDT [201]	2.6586	2.6586	1.3293
		TSDT [201]	2.6586	2.6586	1.3293
		Present	2.6586	2.6586	1.3292
2	0.1	FSDT [201]	3.7865	1.5093	1.2074
		TSDT [201]	3.7866	1.5093	1.2075
		Present	3.7862	1.5075	1.2074
	0.2	FSDT [201]	3.2637	1.3694	1.0955
		TSDT [201]	3.2653	1.3697	1.0958
		Present	3.2653	1.3696	1.0956
	0.3	FSDT [201]	2.5726	1.1862	0.9498
		TSDT [201]	2.5839	1.1873	0.9498
		Present	2.5839	1.1872	0.9498

One can observe the excellent agreement between the results, confirming reliability and accuracy of the analytical model presented in this chapter.

6.5.2 Parametric Study and Discussion

In this section, a piezoelectric bimorph rectangular plate with two opposite edges simply supported, and the other two edges having arbitrary boundary conditions is considered. The core layer of the coupled plate is assumed to be made of saturated porous materials, that is, *Tennessee marble*, here. For convenience, a two letter notation is used to describe the boundary conditions of the remaining edges. For instance, FC indicates that one edge is free (F) and the other is clamped (C). Three different in-plane loading conditions are used in this study: (i) biaxial compression along the x- and y-axis; (ii) compression along the x-axis, while tension along y-axis; and (iii) uniaxial compression along x-axis (see Fig. 6.3). The following material properties are used for the substrate layers, and piezoelectric layers:

Substrate layer [16]:

Tennessee marble: $G_0 = 24$ GPa, $\nu = 0.25$, $B = 0.51$

Piezoelectric layers:

PZT-5H: *Electrical and mechanical properties are given in Table 1.2 in Chapter 1*.

As a primary observation, the electromechanical effect of piezoelectric layers on the buckling behavior of the smart plate is investigated in Fig. 6.2. In general, regardless of the electrical condition, the figure demonstrate that N_{cr} of the coupled piezoelectric system is considerably higher with respect to that of the core porous plate without embedded piezoelectric layers. When the system is in OC mode, the critical buckling load is higher with respect to its counterpart in SC mode, i.e., zero electric potential on the top and bottom surfaces of the piezoelectric layers. This could be attributed to the prominence of electrical effects in the OC case with respect to the SC one, indeed, the effect induced by piezoelectric layers in the SC mode is majorly concerned with their mechanical characteristics and the corresponding electrical effects are negligible. This point is clear in the figure, where the curves associated to the SC and OC smart plates alongside that of a plate, when the electrical effects are absent, i.e. $e_{ij} = 0$ [34]. As observed, the plot of the SC case lies almost perfectly on the top of the curve corresponding to the plate with missing electrical effects.

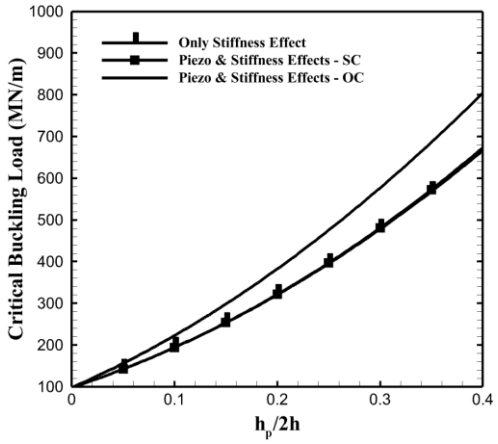

Fig. 6.2: The electromechanical effect of piezoelectric layers on critical buckling load (SS)

One of the main focuses of this present work concerns with the effect of porosity on the buckling response of the bimorph plate under investigation. In Fig. 6.3 are plotted variation of the critical buckling load with respect to the porosity parameter for the smart porous plate having different porosity distribution profiles. It must be mentioned that higher porosity coefficient induces larger occupying pore volume at the initial step and hence higher population of pores at the substrate layer, leading to overall decrease in the effective rigidity of the plate. The effect promoted by the decrease in rigidity is shown in the figure, where the N_{cr} drops substantially as e_0 grows. It is clear from the figure that the drop in the buckling load (as e_0 increases) is the most for the Pattern I (or symmetric 2), followed by the Pattern III (asymmetric), Pattern IV (uniform), and Patterns II (symmetric 1), respectively. Note that the recognized trends remains true regardless of the adopted electrical and mechanical boundary conditions and geometrical parameters. Furthermore, it is realized that the corresponding decrease for plates with piezoelectric layers is smaller with respect to that without the layers.

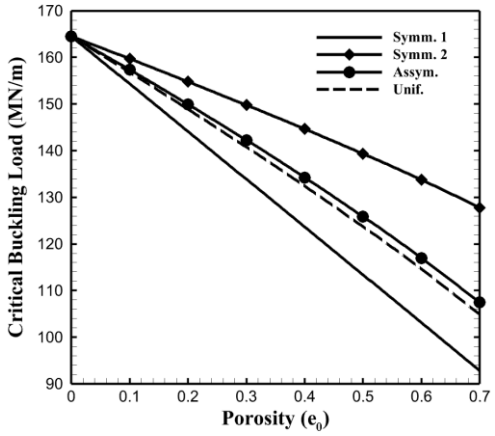

Fig. 6.3: The combined effect of porosity parameter and porosity distribution on the critical buckling load (SS)

Are presented in Fig. 6.4 variation of the buckling load versus the porosity parameter, for the three different loading conditions, as are: i) biaxial compressive loading of the same magnitude acting on all the plate edges, ii) biaxial compressive (on edges parallel to x-axis) and tension loading (on edges parallel to y-axis) of the same magnitude, and iii) uniaxial compressive loading acting on edges parallel to x-axis. As expected, the first type of loading drives the system towards buckling failure earlier with respect to other two cases, followed by the third and the second type, in the order given. In fact, exceeding from the safety threshold in terms of stress, when tensile loading act on horizontal edges, occurs the latest due to the induction of higher equivalent rigidity. Moreover, it is observed from the figure, in case of biaxial compressive loading, that the buckling phenomenon occurs in a higher mode (here, mode (2,1)), meaning that the first mode extracted from the mathematical framework is not essentially the fundamental buckling mode, and the phenomenon may take place by exerting even a smaller N_{cr}, in terms of magnitude, which is produced by higher modes. In a general sense, the buckling mode transition is seen for the plates with stiffer edge conditions, especially when the plates undergo dissimilar loading types on it corresponding horizonal and vertical edges.

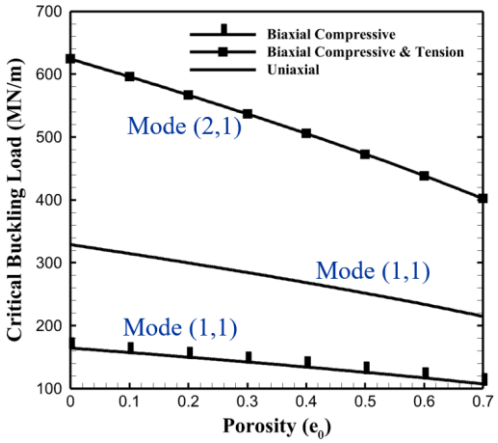

Fig. 6.4: The effect of porosity parameter on the critical buckling load for the bimorph plate under different loading conditions (SS)

In Fig. 6.5, variation of the critical buckling load against the pore pressure coefficient B is plotted for the bimorph plate with various porosity distributions. Form the figure, an increment in N_{cr} is observed for all the porosity profiles, when the pore fluid compressibility, i.e., B, increases. This indeed refers to the increasing equivalent stiffness of the plate as the result of increase in pore pressure. As the matter of fact, the entrapment of fluid in the interconnected network of pores causes the solid and fluid to behave as an integrated body, sustaining the forces the applied to the boundaries in a more productive way with respect to the case in which the pores are free of fluid. For this reason, the buckling load of a fluid-saturated plate is higher comparing with the corresponding fluid-free plate.

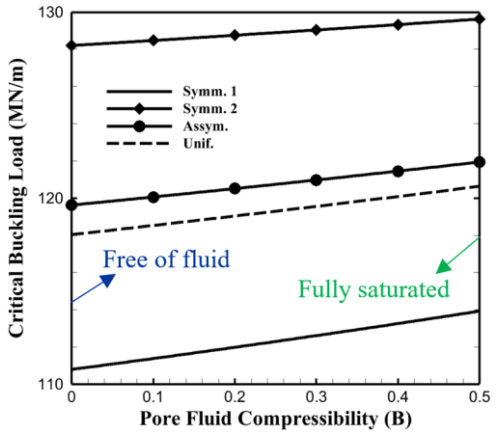

Fig. 6.5: The effect of porosity parameter on the critical buckling load for the bimorph plate under different loading conditions (SS)

In Tables 6.2 to 6.4, the buckling load is calculated for rectangular porous plates of different aspect ratio and thickness-length ratio for several porosity coefficients under various saturation and loading conditions. Each table is devoted to presenting the data for two of the six possible Levy-type boundary conditions. Note that only the principal buckling mode is given in the tables. Several point can be realized from the tables including the effect of geometrical parameters, loading and saturation on the critical buckling load of the plate. As can be seen, the magnitude of force required for reaching the unstable phase, is related to the type of constraints applied on edges. For instance, if an edge is clamped, higher loads are requited for buckling as compared to the similar system with this edge adopting free and simply support boundary conditions. This indeed is concerned with degrees of freedom being divested by the boundary condition of the edge. Some of the buckling loads N_{cr} shown in the tables are accompanied by the "*" symbol, implying the occurrence of buckling in a higher mode, meaning that the first mode extracted from the mathematical framework presented above is not essentially the fundamental buckling mode, and the phenomenon may take place by exerting even a smaller N_{cr}, in terms of magnitude, which is produced by higher modes. In a general sense, the buckling mode transition is seen for the plates with stiffer edge conditions including CC, SC, and SS, especially when the plates undergo dissimilar loading types on it corresponding horizonal and vertical edges. The effect of geometrical parameters on the critical buckling load of the plates under studying is also demonstrated in tables. Tables imply that an increase in the value of thickness-length ratio, when all other parameters are fixed, leads to higher buckling loads. The underlying reason may be realized intuitively since higher $2h/a$ is in direct correspondence to the equivalent rigidity of the plate. Based on the tables, doubling the value of $2h/a$ is accompanied by a few hundred percent increase in N_{cr}. Thus, higher thicknesses may be considered as a qualified solution for avoiding low N_{cr} in systems; however, the geometrical and weight constraints of the desired component are of importance as well. Regarding the effect of aspect ratio on the output, one observes that N_{cr} rises as the aspect ratio increases for all boundary conditions expect for the plate with vertical edges free. In fact, the plate under FF boundary condition behaves like a beam which becomes slenderer by increase in a/b, and thereby a decrease in N_{cr}.

Table 6.2: The critical buckling load (MN/m) for a rectangular plate with FF and SS boundary conditions ($h_p/2h = 0$)

e_0		$a/b = 0.5$		$a/b = 1$	
		$2h/a = 0.1$	$2h/a = 0.2$	$2h/a = 0.1$	$2h/a = 0.2$
($r_x = -1, r_y = +1$), FF boundary condition					
0	Homogenous	50.544	375.313	49.874	370.233
0.3	Fluid-free	41.203	305.562	40.6580	301.426
	Fluid-saturated	42.161	312.045	41.514	307.901
0.5	Fluid-free	34.167	253.489	33.714	250.058
	Fluid-saturated	35.578	262.983	34.974	258.502
($r_x = -1, r_y = 0$), FF boundary condition					
0	Homogenous	50.289	373.339	49.500	367.390
0.3	Fluid-free	40.996	303.955	40.350	299.150
	Fluid-saturated	41.906	310.093	41.144	304.409
0.5	Fluid-free	33.995	252.156	33.460	248.140
	Fluid-saturated	35.331	261.159	34.633	255.958
($r_x = r_y = -1$), FF boundary condition					
0	Homogenous	49.434	365.310	48.641	359.865
0.3	Fluid-free	40.432	297.323	39.650	292.972
	Fluid-saturated	41.036	302.050	40.304	297.096
0.5	Fluid-free	33.416	247.600	32.880	243.050
	Fluid-saturated	34.506	253.442	33.853	249.220
($r_x = -1, r_y = +1$), SS boundary condition					
0	Homogenous	106.170	775.416	387.708(*)	2303.979(*)
0.3	Fluid-free	86.541	631.062	315.531(*)	1867.216(*)
	Fluid-saturated	88.752	645.681	322.840(*)	1898.756(*)
0.5	Fluid-free	71.765	523.586	261.793(*)	1551.427(*)
	Fluid-saturated	74.992	544.897	272.448(*)	1597.169(*)
($r_x = -1, r_y = 0$), SS boundary condition					
0	Homogenous	79.628	581.562	200.029	1392.047
0.3	Fluid-free	64.906	473.297	162.992	1131.690
	Fluid-saturated	66.564	484.261	167.072	1156.091
0.5	Fluid-free	53.824	392.689	135.178	939.285
	Fluid-saturated	56.244	408.673	141.132	974.816
($r_x = r_y = -1$), SS boundary condition					
0	Homogenous	63.702	465.250	100.014	696.023
0.3	Fluid-free	51.925	378.637	81.496	565.845
	Fluid-saturated	53.251	387.409	83.535	578.045
0.5	Fluid-free	43.059	314.151	67.588	469.642
	Fluid-saturated	44.995	326.938	70.566	487.407

Table 6.3: The critical buckling load (MN/m) for a rectangular plate with CC and SC boundary conditions ($h_p/2h = 0$)

e_0		$a/b = 0.5$		$a/b = 1$	
		$2h/a = 0.1$	$2h/a = 0.2$	$2h/a = 0.1$	$2h/a = 0.2$
($r_x = -1, r_y = +1$), CC boundary condition					
0	Homogenous	134.077	933.601	466.800(*)	2573.541(*)
0.3	Fluid-free	109.246	759.137	379.568(*)	2083.840(*)
	Fluid-saturated	111.968	775.639	387.819(*)	2115.674(*)
0.5	Fluid-free	90.607	630.089	315.044(*)	1732.426(*)
	Fluid-saturated	94.580	654.126	327.063(*)	1778.519(*)
($r_x = -1, r_y = 0$), CC boundary condition					
0	Homogenous	96.472	681.242	340.621(*)	1902.521(*)
0.3	Fluid-free	78.615	554.051	277.026(*)	1540.593(*)
	Fluid-saturated	80.591	566.289	283.145(*)	1564.386(*)
0.5	Fluid-free	65.199	459.808	229.904(*)	1280.592(*)
	Fluid-saturated	68.083	477.638	238.819(*)	1315.059(*)
($r_x = r_y = -1$), CC boundary condition					
0	Homogenous	74.608	530.789	179.215	1089.372
0.3	Fluid-free	60.802	431.743	145.871	883.365
	Fluid-saturated	62.336	441.375	149.274	898.880
0.5	Fluid-free	50.424	358.280	121.023	733.8508
	Fluid-saturated	52.664	372.315	125.985	756.3798
($r_x = -1, r_y = +1$), SC boundary condition					
0	Homogenous	118.406	846.9825	423.491(*)	2431.200(*)
0.3	Fluid-free	96.499	689.037	344.518(*)	1969.496(*)
	Fluid-saturated	98.938	704.559	352.279(*)	2001.255(*)
0.5	Fluid-free	80.028	571.783	285.891(*)	1636.854(*)
	Fluid-saturated	83.589	594.403	297.201(*)	1682.881(*)
($r_x = -1, r_y = 0$), SC boundary condition					
0	Homogenous	86.769	625.012	276.889	1791.870
0.3	Fluid-free	70.719	508.516	225.489	1454.766
	Fluid-saturated	72.514	520.067	230.924	1482.983
0.5	Fluid-free	58.647	421.955	187.048	1208.098
	Fluid-saturated	61.267	438.790	194.978	1249.126
($r_x = r_y = -1$), SC boundary condition					
0	Homogenous	68.055	492.070	129.743	854.051
0.3	Fluid-free	55.469	400.381	105.674	693.560
	Fluid-saturated	56.879	409.522	108.247	707.333
0.5	Fluid-free	45.999	332.216	87.654	575.867
	Fluid-saturated	48.058	345.540	91.408	595.899

Table 6.4: The critical buckling load (MN/m) for a rectangular plate with CF and SF boundary conditions ($h_p/2h = 0$)

e_0		$a/b = 0.5$		$a/b = 1$	
		$2h/a = 0.1$	$2h/a = 0.2$	$2h/a = 0.1$	$2h/a = 0.2$
($r_x = -1, r_y = +1$), CF boundary condition					
0	Homogenous	62.469	458.846	124.922	869.720
0.3	Fluid-free	50.866	373.642	101.913	707.216
	Fluid-saturated	52.019	381.149	103.736	718.919
0.5	Fluid-free	42.199	309.868	84.389	586.985
	Fluid-saturated	43.872	321.091	88.765	604.147
($r_x = -1, r_y = 0$), CF boundary condition					
0	Homogenous	57.569	423.879	84.606	601.172
0.3	Fluid-free	46.928	345.043	68.975	489.029
	Fluid-saturated	47.917	351.728	69.992	495.339
0.5	Fluid-free	38.915	286.261	57.180	406.110
	Fluid-saturated	40.369	295.876	58.997	415.405
($r_x = r_y = -1$), CF boundary condition					
0	Homogenous	51.991	381.311	58.869	418.053
0.3	Fluid-free	42.377	310.366	47.971	340.086
	Fluid-saturated	43.037	316.666	48.391	342.362
0.5	Fluid-free	35.145	257.500	39.785	282.212
	Fluid-saturated	36.241	264.074	40.458	285.959
($r_x = -1, r_y = +1$), SF boundary condition					
0	Homogenous	60.462	446.954	99.810	728.642
0.3	Fluid-free	49.320	363.852	81.369	591.968
	Fluid-saturated	50.419	371.450	83.013	602.454
0.5	Fluid-free	40.871	301.875	67.468	491.975
	Fluid-saturated	42.530	312.972	71.234	506.656
($r_x = -1, r_y = 0$), SF boundary condition					
0	Homogenous	56.224	415.510	72.526	528.882
0.3	Fluid-free	45.832	338.255	59.115	430.437
	Fluid-saturated	46.821	344.840	60.116	436.789
0.5	Fluid-free	38.006	280.620	49.023	357.127
	Fluid-saturated	39.459	290.370	50.516	366.634
($r_x = r_y = -1$), SF boundary condition					
0	Homogenous	51.512	378.024	54.704	395.036
0.3	Fluid-free	41.968	310.229	44.938	321.460
	Fluid-saturated	42.883	311.479	45.085	324.336
0.5	Fluid-free	34.803	255.308	36.974	266.724
	Fluid-saturated	36.241	261.130	37.749	271.196

6.6 Summary and Conclusions

The numerical results presented in the previous section enable one to draw the following conclusions:

- Generalized Levy-type solutions are obtained for the linear buckling problem of porous piezoelectric bimorph thick plates using the four-variable higher-order theory. It is shown that the state space concept can be used to obtain exact solutions of the critical buckling loads for thin, moderately thick, and thick piezoelectric bimorph plates.
- It is revealed that the increase in pore volume fraction is accompanied by a decrease in the critical buckling load.
- Increasing pore pressure coefficient leads to higher critical buckling loads.
- Sensitivity of the buckling load growth, as the consequence of increasing pore fluid compressibility, to various parameters including the loading and boundary conditions is demonstrated.
- The inclusion of piezoelectric layers to the core porous plate causes a substantial rise in the associated buckling load.
- Higher buckling loads are met, when the piezoelectric layers are in open-circuit mode with respect to short-circuit case due to the prominence of electrical effects.

Chapter 7

Free Vibration Analysis of Piezoelectric Bimorph/Unimorph Doubly-Curved Shells

7.1 Overview

For relatively complicated structural configurations, i.e., piezoelectric bimorph/unimorph doubly-curved panels, which are usually studied through numerical solutions, an analytical solution using Navier's method is provided in this chapter. The problem of free vibration of such structures with porous substrate is considered here, and the respective governing equations are derived based on the first-order shear deformation theory (FSDT). The formulation given here should be preferred for thin, and moderately-thick shells, due to the assumptions of the adopted theory concerning the effect of transverse shear deformations. Applying Navier's technique to the governing equations, a closed-form expression is obtained for the free vibration response of the smart panel. After conducting several comparison examples for the validation of the model, extensive numerical results are presented for the smart bimorph/unimorph panel having different geometries

such as spherical, cylindrical, hyperbolic paraboloidal, and plate shapes. The presented results cover the effect of a wide range of parameters such as piezoelectric characteristics, porosity, and other design parameters. The analysis confirms that the mentioned parameters play major roles on the natural frequency response of the smart system and must be carefully considered in the mechatronic design of this smart structure, although they allow to tailor the system behavior to the selected application. Moreover, It is shown that the model developed in this chapter can be used as a benchmark solution, and the obtained results are found suitable for validating the accuracy and reliability of numerical approaches.

The results of the research work presented in this chapter was published in the journal *Actuators* [202].

7.2 Problem Modelling

The layouts of the bimorph and unimorph doubly-curved panels made of porous media and piezoelectric materials are presented in Fig. 7.1. As is shown, the bimorph structure is composed of a porous core integrated with two identical thickness-poled piezoelectric layers ($h_{pt} = h_{pb}$), while the unimorph panel has only one piezoelectric layer ($h_{pb} = 0$) mounted on the top surface of its substrate. Both the panels have arc lengths L_1 and L_2, and R_x and R_y are the curvature radii of the mid-surface of the substrate layer. Also, $2h$ is the thickness of the substrate and h_{pt} and h_{pb} are corresponded to the thicknesses of the top and bottom piezoelectric layers, respectively. To extract the mathematical formulations, the origin of the coordinate system is located on the middle-surface of the substrate layer.

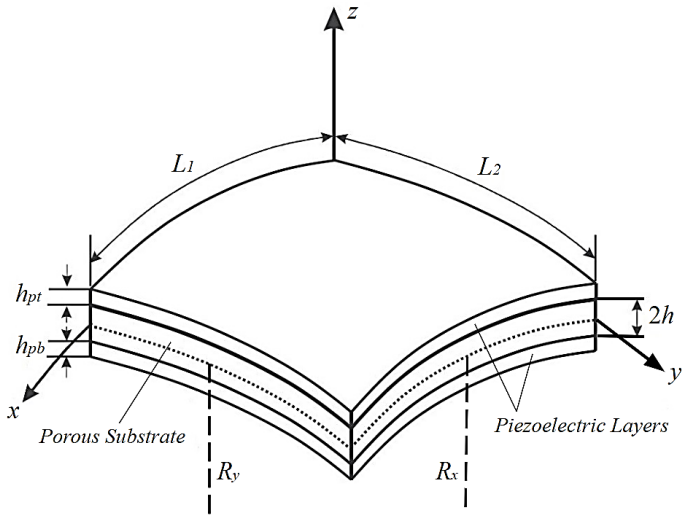

(a) Bimorph panel

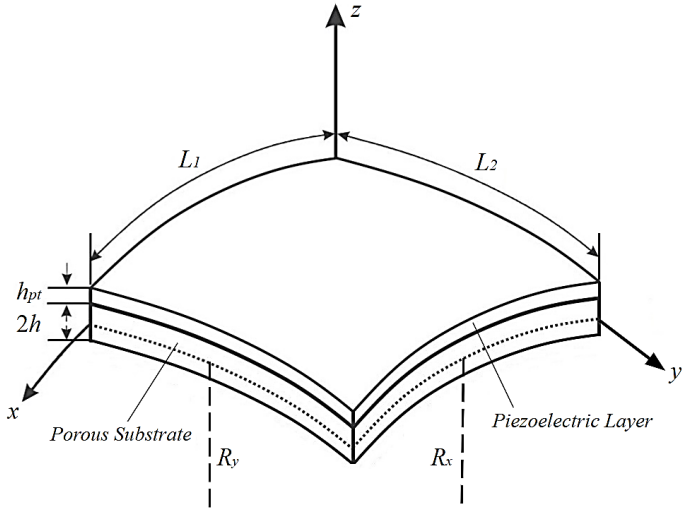

(b) Unimorph panel

Fig. 7.1: Sketch of porous bimorph and unimorph doubly curved panels

In the coupled structures given in Fig. 7.1, it is assumed that the piezoelectric layers are perfectly bonded on the substrate layer with an adhesive layer of negligible thickness, therefore there is no relative displacement between the layers of the sandwich panel. For the variation of porosities within the porous substrate, only the case of asymmetric profile is considered in this work (see Fig. 6.2(c)). Therefore, the respective mechanical properties are (referred to Eqs. (6.1) and (6.2)):

$$
\begin{aligned}
E(z) &= E_0\left(1 - e_0 \cos\left(\frac{\pi z}{4h} + \frac{\pi}{4}\right)\right) \\
G(z) &= G_0\left(1 - e_0\, cos\left(\frac{\pi z}{4h} + \frac{\pi}{4}\right)\right) \\
\rho(z) &= \rho_0\left(1 - e_m \cos\left(\frac{\pi z}{4h} + \frac{\pi}{4}\right)\right) \\
e_m &= 1 - \sqrt{1 - e_0}
\end{aligned}
\tag{7.1}
$$

Note that the definition of the parameters of Eq. (7.1) are already given the preceding chapters. The constitutive equations of both porous media and piezoelectric materials were also given in the preceding chapters, therefore, it is avoided to repeat those equations here.

In this present analysis, the first-order shear deformation theory is employed, in which the effects of the transverse shear deformations are taken into account. Based on this theory, the components of mechanical displacement filed can be expressed as:

$$
\begin{aligned}
U_x(x, y, z, t) &= u_0(x, y, t) + z\psi_x(x, y, t) \\
U_y(x, y, z, t) &= v_0(x, y, t) + z\psi_y(x, y, t) \\
U_z(x, y, z, t) &= w_0(x, y, t)
\end{aligned}
\tag{7.2}
$$

where u_0, v_0 and w_0 are the mechanical displacements of any point of the shell mid-surface along the orthogonal curvilinear coordinates. The functions ψ_x and ψ_y represent the rotations of normal to mid-plane about y and x axes, respectively, and t is the time variable. One can simply derive the strain field using Eq. (7.2), as:

$$
\begin{aligned}
\varepsilon_{xx} &= u_{0,x} + z\psi_{x,x} + \frac{w_0}{R_x} \\
\varepsilon_{yy} &= v_{0,y} + z\psi_{y,y} + \frac{w_0}{R_y} \\
\varepsilon_{zz} &= 0 \\
\gamma_{xy} &= u_{0,y} + v_{0,x} + z\left(\psi_{x,y} + \psi_{y,x}\right) \\
\gamma_{xz} &= \psi_x + w_{0,x} - \frac{u_0}{R_x}
\end{aligned}
\tag{7.3}
$$

$$\gamma_{yz} = \psi_y + w_{0,y} - \frac{v_0}{R_y}$$

Moreover, it is assumed that the electric potential has nonlinear variations with respect to the z-coordinate. In the following relations, the electric potential functions are given for the top and bottom piezoelectric layers, respectively:

$$\begin{aligned}\phi(x,y,z,t) &= Az + B + \left(1 - \left(\frac{2z - 2h - h_{pt}}{h_{pt}}\right)^2\right)\phi_0(x,y,t)\\ \phi(x,y,z,t) &= Cz + D + \left(1 - \left(\frac{-2z - 2h - h_{pb}}{h_{pb}}\right)^2\right)\phi_0(x,y,t)\end{aligned} \tag{7.4}$$

where the function ϕ_0 is the electric potential function in the mid-surface of piezoelectric layers; A, B, C and $D(x,y,t)$ are four unknown functions, which equal to zero for the case of short circuit (SC) condition, while they are obtained for the open circuit (OC) as follows:

$$\begin{aligned}A &= \frac{e_{31}}{\Xi_{33}}\left(u_{0,x} + v_{0,y} + (h + h_{pt})\left[\psi_{x,x} + \psi_{y,y}\right] + \left(\frac{1}{R_x} + \frac{1}{R_y}\right)w_0\right)\\ &\quad + \frac{4\phi_0}{h_{pt}}\\ C &= \frac{e_{31}}{\Xi_{33}}\left(u_{0,x} + v_{0,y} - (h + h_{pb})\left[\psi_{x,x} + \psi_{y,y}\right] + \left(\frac{1}{R_x} + \frac{1}{R_y}\right)w_0\right)\\ &\quad - \frac{4\phi_0}{h_{pb}}\\ B &= -Ah\\ D &= +Ch\end{aligned} \tag{7.5}$$

7.3 Governing Equations

Employing Hamilton's principle, the following five equations of motion are obtained for doubly-curved shells based on the first-order shear deformation theory:

$$
\begin{aligned}
&N_{xx,x} + N_{xy,y} + \frac{Q_{xz}}{R_x} = I_0\ddot{u}_0 + I_1\ddot{\psi}_x \\
&N_{xy,x} + N_{yy,y} + \frac{Q_{yz}}{R_y} = I_0\ddot{v}_0 + I_1\ddot{\psi}_y \\
&M_{xx,x} + M_{xy,y} - Q_{xz} = I_1\ddot{u}_0 + I_2\ddot{\psi}_x \\
&M_{xy,x} + M_{yy,y} - Q_{yz} = I_1\ddot{v}_0 + I_2\ddot{\psi}_y \\
&Q_{xz,x} + Q_{yz,y} - \frac{N_{xx}}{R_x} - \frac{N_{yy}}{R_y} = I_0\ddot{w}_0
\end{aligned}
\tag{7.6}
$$

where the stress resultants N_{ij}, M_{ij} and Q_{ij}, and the mass inertias I_i are defined as follows:

$$
\begin{aligned}
&\left(N_{xx}, N_{xy}, N_{yy}\right) = \int_{-h-h_{pb}}^{+h+h_{pt}} \left(\sigma_{xx}, \sigma_{xy}, \sigma_{yy}\right) dz \\
&\left(M_{xx}, M_{xy}, M_{yy}\right) = \int_{-h-h_{pb}}^{+h+h_{pt}} \left(\sigma_{xx}, \sigma_{xy}, \sigma_{yy}\right) z dz \\
&\left(Q_{xz}, Q_{yz}\right) = \int_{-h-h_{pb}}^{+h+h_{pt}} \left(\sigma_{xz}, \sigma_{yz}\right) dz \\
&(I_0, I_1, I_2) = \int_{-h-h_{pb}}^{+h+h_{pt}} \rho(z)(1, z, z^2)\, dz
\end{aligned}
\tag{7.7}
$$

To derive the electromechanical governing equations, the stress resultants must be obtained in terms of mechanical displacement components (u_0, v_0, w_0) and electric potential (ϕ_0), through substitution of the constitutive equation of both porous substrate and piezoelectric layers into Eq. (7.7). The resulting equation are:

$$
\begin{aligned}
&N_{xx} = a_{11}u_{0,x} + a_{12}v_{0,y} + b_{11}\psi_{x,x} + b_{12}\psi_{y,y} + p_{11}w_0 + \beta_5\phi_0 \\
&N_{yy} = a_{12}u_{0,x} + a_{11}v_{0,y} + b_{12}\psi_{x,x} + b_{11}\psi_{y,y} + p_{11}^{'}w_0 + \beta_5\phi_0 \\
&N_{xy} = a_{66}\left(u_{0,y} + v_{0,x}\right) + b_{66}\left(\psi_{x,y} + \psi_{y,x}\right) \\
&M_{xx} = b_{11}u_{0,x} + b_{12}v_{0,y} + d_{11}\psi_{x,x} + d_{12}\psi_{y,y} + q_{11}w_0 + \beta_6\phi_0 \\
&M_{yy} = b_{12}u_{0,x} + b_{11}v_{0,y} + d_{12}\psi_{x,x} + d_{11}\psi_{y,y} + q_{11}^{'}w_0 + \beta_6\phi_0 \\
&M_{xy} = b_{66}\left(u_{0,y} + v_{0,x}\right) + d_{66}\left(\psi_{x,y} + \psi_{y,x}\right)
\end{aligned}
\tag{7.8}
$$

$$Q_{xz} = a_{55}\left(\psi_x + w_{0,x} - \frac{u_0}{R_x}\right) + \beta_7\phi_{0,x} + \beta_8\left(u_{0,xx} + v_{0,yx} + \frac{w_{0,x}}{R_x} + \frac{w_{0,x}}{R_y}\right) + \beta_9\left(\psi_{x,xx} + \psi_{y,yx}\right)$$

$$Q_{yz} = a_{55}\left(\psi_y + w_{0,y} - \frac{v_0}{R_y}\right) + \beta_7\phi_{0,y} + \beta_8\left(u_{0,xy} + v_{0,yy} + \frac{w_{0,y}}{R_x} + \frac{w_{0,y}}{R_y}\right) + \beta_9\left(\psi_{x,xy} + \psi_{y,yy}\right)$$

where the constant coefficients a_{ij}, b_{ij}, d_{ij}, p_{ij}, q_{ij} and β_i (i =5, 6, 7, 8, 9) are given in Appendix F.

Introducing Eq. (7.8) into Eq. (7.6) leads to the following coupled partial differential governing equations:

$$\begin{aligned}&\left(a_{11} + \frac{\beta_8}{R_x}\right)u_{0,xx} + a_{66}u_{0,yy} + \left(a_{12} + a_{66} + \frac{\beta_8}{R_x}\right)v_{0,xy} \\ &\quad + \left(b_{11} + \frac{\beta_9}{R_x}\right)\psi_{x,xx} + b_{66}\psi_{x,yy} \\ &\quad + \left(b_{12} + b_{66} + + \frac{\beta_9}{R_x}\right)\psi_{y,xy} - \frac{a_{55}}{{R_x}^2}u_0 + \frac{a_{55}}{R_x}\psi_x \\ &\quad + \left(p_{11} + \frac{a_{55}}{R_x} + \frac{\beta_8}{{R_x}^2} + \frac{\beta_8}{R_xR_y}\right)w_{0,x} + \left(\beta_5 + \frac{\beta_7}{R_x}\right)\phi_{0,x} \\ &\quad = I_0\ddot{u}_0 + I_1\ddot{\psi}_x\end{aligned} \tag{7.9a}$$

$$\begin{aligned}&\left(a_{12} + a_{66} + \frac{\beta_8}{R_y}\right)u_{0,xy} + \left(a_{11} + \frac{\beta_8}{R_y}\right)v_{0,yy} + a_{66}v_{0,xx} \\ &\quad + \left(b_{12} + b_{66} + \frac{\beta_9}{R_y}\right)\psi_{x,xy} + \left(b_{11} + \frac{\beta_9}{R_y}\right)\psi_{y,yy} \\ &\quad + b_{66}\psi_{y,xx} - \frac{a_{55}}{{R_y}^2}v_0 + \frac{a_{55}}{R_y}\psi_y \\ &\quad + \left(p_{11}^{'} + \frac{a_{55}}{R_y} + \frac{\beta_8}{R_y} + \frac{\beta_8}{R_xR_y}\right)w_{0,y} + \left(\beta_5 + \frac{\beta_7}{R_y}\right)\phi_{0,y} \\ &\quad = I_0\ddot{v}_0 + I_1\ddot{\psi}_y\end{aligned} \tag{7.9b}$$

$$(b_{11}-\beta_8)u_{0,xx}+b_{66}u_{0,yy}+(b_{12}+b_{66}-\beta_8)v_{0,xy}+(d_{11}-\beta_9)\psi_{x,xx}+d_{66}\psi_{x,yy}+(d_{12}+d_{66}-\beta_9)\psi_{y,xy}+\frac{a_{55}}{R_x}u_0-a_{55}\psi_x+\left(q_{11}-a_{55}-\frac{\beta_8}{R_x}-\frac{\beta_8}{R_y}\right)w_{0,x}+(\beta_6-\beta_7)\phi_{0,x}=I_1\ddot{u}_0+I_2\ddot{\psi}_x \tag{7.9c}$$

$$(b_{12}+b_{66}-\beta_8)u_{0,xy}+(b_{11}-\beta_8)v_{0,yy}+b_{66}v_{0,xx}+(d_{12}+d_{66}-\beta_9)\psi_{x,xy}+(d_{11}-\beta_9)\psi_{y,yy}+d_{66}\psi_{y,xx}+\frac{a_{55}}{R_y}v_0-a_{55}\psi_y+\left(q_{11}^{'}-a_{55}-\frac{\beta_8}{R_x}-\frac{\beta_8}{R_y}\right)w_{0,y}+(\beta_6-\beta_7)\phi_{0,y}=I_1\ddot{v}_0+I_2\ddot{\psi}_y \tag{7.9d}$$

$$\left(a_{55}+\frac{\beta_8}{R_x}+\frac{\beta_8}{R_y}\right)\nabla^2 w_0+\beta_7\nabla^2\phi_0-\left(\frac{a_{11}}{R_x}+\frac{a_{12}}{R_y}+\frac{a_{55}}{R_x}\right)u_{0,x}-\left(\frac{a_{12}}{R_x}+\frac{a_{11}}{R_y}+\frac{a_{55}}{R_y}\right)v_{0,y}-\left(\frac{b_{11}}{R_x}+\frac{b_{12}}{R_y}\right)\psi_{x,x}-\left(\frac{b_{12}}{R_x}+\frac{b_{11}}{R_y}\right)\psi_{y,y}+a_{55}\psi_{x,x}+a_{55}\psi_{y,y}-\left(\frac{p_{11}}{R_x}+\frac{p_{11}^{'}}{R_y}\right)w_0-\left(\frac{\beta_5}{R_x}+\frac{\beta_5}{R_y}\right)\phi_0+\beta_8\nabla^2 u_{0,x}+\beta_8\nabla^2 v_{0,x}+\beta_9\nabla^2\psi_{x,x}+\beta_9\nabla^2\psi_{y,y}=I_0\ddot{w}_0 \tag{7.9e}$$

With the help of the electrostatic Maxwell's equation, the last equation of motion can be derived as:

$$\beta_1\left(\psi_{x,x}+\psi_{y,y}+\nabla^2 w_0-\frac{u_{0,x}}{R_x}-\frac{v_{0,y}}{R_y}\right)+\beta_2\left(\psi_{x,x}+\psi_{y,y}\right)+\beta_3\varphi_0+\beta_4\nabla^2\varphi_0+\eta_1\left(\nabla^2\left(u_{0,x}\right)+\nabla^2\left(v_{0,y}\right)+\left(\frac{1}{R_x}+\frac{1}{R_y}\right)\nabla^2 w_0\right)+\eta_2\left(\nabla^2\left(\psi_{x,x}\right)+\nabla^2\left(\psi_{y,y}\right)\right)=0 \tag{7.10}$$

where $\nabla^2(\ldots)$ is Laplace operator, and the coefficients β_i (i =1, 2, 3, 4) and η_j (j =1, 2) are defined for both the SC and OC electrical conditions, in Appendix F.

7.4 Solution Procedure

To solve the dynamic equations (7.9), and the electrostatic Maxwell's equation (7.10), mechanical and electrical boundary conditions must be applied to the plate edges. In this study, simply supported mechanical boundary conditions are assumed for all the four edges of the doubly-curved panel. Also, it is considered that all the edges are electrically grounded to zero potential for both bimorph and unimorph structures. With the help of the variational method and divergence theorem, these conditions can be mathematically expressed as:

$$\begin{aligned} &v_0 = \psi_y = w_0 = N_{xx} = M_{xx} = \phi_0 = 0 && \text{at } x = 0 \text{ and } x = L_1 \\ &u_0 = \psi_x = w_0 = N_{yy} = M_{yy} = \phi_0 = 0 && \text{at } y = 0 \text{ and } y = L_2 \end{aligned} \tag{7.11}$$

Here, Navier's method is employed to solve the governing equations. Based on this approach, the unknown mechanical displacement components u_0, v_0, w_0, ψ_x and ψ_x, as well as the electric potential ϕ_0 are assumed to have the following trigonometric expansions:

$$\begin{aligned} u_0(x,y,t) &= \sum_{m=1}^{\infty}\sum_{n=1}^{\infty} \cos(\mu_m x)\sin(\mu_n y)\,\eta_{mn}^{u_0}(t) \\ v_0(x,y,t) &= \sum_{m=1}^{\infty}\sum_{n=1}^{\infty} \sin(\mu_m x)\cos(\mu_n y)\,\eta_{mn}^{v_0}(t) \\ w_0(x,y,t) &= \sum_{m=1}^{\infty}\sum_{n=1}^{\infty} \sin(\mu_m x)\sin(\mu_n y)\,\eta_{mn}^{w_0}(t) \\ \psi_x(x,y,t) &= \sum_{m=1}^{\infty}\sum_{n=1}^{\infty} \cos(\mu_m x)\sin(\mu_n y)\,\eta_{mn}^{\psi_x}(t) \\ \psi_y(x,y,t) &= \sum_{m=1}^{\infty}\sum_{n=1}^{\infty} \sin(\mu_m x)\cos(\mu_n y)\,\eta_{mn}^{\psi_y}(t) \end{aligned} \tag{7.12}$$

$$\phi_0(x,y,t) = \sum_{m=1}^{\infty}\sum_{n=1}^{\infty} \sin(\mu_m x)\sin(\mu_n y)\,\eta_{mn}^{\phi_0}(t)$$

The solution given in Eq. (7.12) satisfy the boundary conditions (7.11). In Eq. (7.12), the parameters μ_m and μ_n are equal to $m\pi/L_1$ and $n\pi/L_2$, respectively, where m and n are number of half-waves through x and y directions, respectively.

By assuming the harmonic motion for the system, the functions $\eta_{mn}(t)$ can be defined as:

$$\begin{Bmatrix} \eta_{mn}^{u_0} \\ \eta_{mn}^{v_0} \\ \eta_{mn}^{w_0} \\ \eta_{mn}^{\psi_x} \\ \eta_{mn}^{\psi_y} \\ \eta_{mn}^{\phi_0} \end{Bmatrix} = \begin{Bmatrix} S_{mn}^{u_0} \\ S_{mn}^{v_0} \\ S_{mn}^{w_0} \\ S_{mn}^{\psi_x} \\ S_{mn}^{\psi_y} \\ S_{mn}^{\phi_0} \end{Bmatrix} e^{i\omega t} \tag{7.13}$$

In which $i = \sqrt{-1}$ and ω is the natural frequency of the smart doubly-curved panel.

Substitution of Eqs. (7.12) and (7.13) into Eqs. (7.9) and (7.10) results in the following eigenproblem:

$$([K] - \omega^2[M]) \begin{Bmatrix} S_{mn}^{u_0} \\ S_{mn}^{v_0} \\ S_{mn}^{w_0} \\ S_{mn}^{\psi_x} \\ S_{mn}^{\psi_y} \\ S_{mn}^{\phi_0} \end{Bmatrix} = \begin{Bmatrix} 0 \\ 0 \\ 0 \\ 0 \\ 0 \\ 0 \end{Bmatrix} \tag{7.14}$$

where $[K]$ and $[M]$ are the stiffness and inertia matrices, respectively.

The solution of the eigenproblem (7.14) allows to extract the eigenfrequencies of the smart shell. In the next section, the natural frequencies are presented for bimorphs and unimorphs, a wide range of parameters, as well as various geometries.

7.5 Numerical Results

7.5.1 Model Validation

Comparison examples are first presented to verify the accuracy of the presented model. Due to slight variation of Poisson's ratio along the thickness of the substrate layer, its value is considered to be constant, and equal to 0.3. The parameter H_p in the following tables and figures represents the total thickness of piezoelectric layers, which is equal to $H_p = h_{pt} + h_{pb}$ and $H_p = h_{pt}$ for bimorph and unimorph structures, respectively (see Fig. 7.1). In Table 7.11, the SC and OC fundamental frequencies are compared with their counterparts in Ref. [203], for a bimorph doubly curved shell, consisted of a homogenous core surrounded by two identical PZT-4 layers. In Ref. [203], the authors considered shell through-thickness kinematics based on the higher-order shear deformation theory, and used a quadratic variation for the electric potential distribution in piezoelectric layers.

Table 7.1: Comparison of the fundamental eigenfrequency (Hz) of a bimorph isotropic shell.

Electrical boundary condition (EBC)	L_1/R_x	$H_p/2h$	Ref. [203]	Present
SC	0.0	0.1	839.368	838.273
		0.2	801.794	799.360
	0.1	0.1	853.147	852.075
		0.2	813.413	811.024
OC	0.0	0.1	856.455	854.844
		0.2	833.781	829.958
	0.1	0.1	870.057	868.476
		0.2	845.108	841.347

In Table 7.2, the first ten SC natural frequencies of an isotropic plate with piezoelectric layers are listed along with their counterparts reported in [100,105,160], to check the accuracy of this study to predict natural frequencies of higher vibrational modes.

The last comparative study is presented in Table 7.3 for the SC fundamental frequencies of the present formulations and those reported in [200], for bimorph and unimorph structures having different geometries. In [200], the electric potential distribution within piezoelectric layers is considered as function of z coordinate

only, whereas in the current study it is modeled by a function of all three coordinates.

However, since various mechanical displacement models and electric potential distributions are employed in the current study and the above-mentioned references, some slight differences are observed among the results. Nevertheless, it is evident from Tables 7.1 to 7.3 that the results of the present exact solution based on the first-order shear deformation theory are in close agreement with those reported in the literature.

Table 7.2: Comparison of the first ten eigenfrequencies (Hz) of a bimorph isotropic plate in SC condition.

Mode (m,n)	Ref. [100]	Ref. [105]	Ref. [161]	Present
1st (1,1)	144.25	145.35	145.35	144.49
2nd (1,2)	359.00	363.05	363.06	360.89
3rd (2,1)	359.00	363.05	363.06	360.89
4th (2,2)	564.10	580.35	580.37	576.90
5th (1,3)	717.80	725.00	725.03	720.70
6th (3,1)	717.80	725.00	725.03	720.70
7th (2,3)	908.25	941.64	941.69	936.06
8th (3,2)	908.25	941.64	941.69	936.06
9th (1,4)	1223.14	1229.88	1229.96	1222.61
10th (4,1)	1223.14	1229.88	1229.96	1222.61

Table 7.3. Comparison of the fundamental eigenfrequencies (Hz) for piezoelectric bimorphs and unimorphs with isotropic substrate.

Geometry	$H_p/2h$	Bimorph		Unimorph	
		Ref. [200]	Present	Ref. [200]	Present
Spherical	0.5	2652	2653	2654	2654
	1.0	2405	2408	2411	2411
	2.0	2211	2215	2217	2217
Cylindrical	0.5	1526	1527	1531	1531
	1.0	1383	1387	1393	1393
	2.0	1273	1280	1285	1285
Plate	0.5	873	875	887	887
	1.0	791	797	813	813
	2.0	730	743	755	755

7.5.2 Parametric Study and Discussion

In the following, new results are presented for SC and OC eigenfrequencies of porous bimorph and unimorph panels having spherical (R_x, $R_y > 0$), hyperbolic paraboloidal ($R_x > 0$, $R_y < 0$), cylindrical ($R_x \neq 0$, $R_y \approx \infty$) and plate ($R_x \approx \infty$), $R_y \approx \infty$)) geometries. Aluminum ($E_0 = 70$ GPa, $\rho_0 = 2700$ kg/m^3), and PZT-5H (properties are given in Table 1.2, Chapter 1) are assumed as the materials of the substrate and piezoelectric layers, respectively. To be able of making comparisons among various geometries of bimorph and unimorph panels, the same volume of materials is considered for all the considered cases.

In Table 7.4, for length ratio $L_1/L_2 = 1$, thickness-length ratio $2h/L_1 = 0.05$, and thickness ratio $H_p/2h = 0.2$, the SC and OC resonance frequencies are listed for porous bimorph and unimorph panels having different geometries with identical volumes. The results show that increasing the porosity parameter causes a decrease in the value of natural frequency regardless of the type of smart panel (i.e. bimorph or unimorph), as well as the electrical condition. This behavior is observed for all the panel geometries and structures studied here. In fact, it is due to the fact that when the porosity increases, the structural stiffness drops, which leads to reduction in eigenfrequencies. Furthermore, it is seen that for the same materials composition and the constant volume, various geometries exhibit different natural frequencies in such a way that the highest values are related to spherical shells followed by cylindrical, plate and hyperbolic paraboloidal panels. Also, the table illustrates that both bimorph and unimorph structures have higher frequencies in OC condition in comparison with when the piezoelectric layers are kept at SC condition.

Fundamental natural frequencies of different bimorphs and unimorphs in SC condition are depicted in Tables 7.5 and 7.6 for wide range of parameters including $2h/L_1$, $H_p/2h$ and R_x/L_1. These tables indicate that by increasing the shell curvature, the eigenfrequencies decrease for all the studied curved panels (i.e. spherical and cylindrical shells) except for hyperbolic paraboloidal shell in which the natural frequency significantly rises, as the radius increases. In addition, it seems that increasing the thickness of the substrate layer raises the natural frequency in such a manner that this growth is more remarkable for hybrid shells

with higher values of R_x/L_1. For example, when $R_x/L_1 = 1$, the natural frequency of bimorph spherical shell has a growth of 11.5 % due to increasing the thickness-length ratio ($2h/L_1$) from 0.1 to 0.15, while the value of this growth is about 42.5 % when $R_x/L_1 = 10$, as seen in Table 7.5. Similar behaviors can be observed for other geometries. Moreover, the tables reveal that the natural frequencies for bimorph panels are usually greater than those of unimorphs in same composition of materials, owing to asymmetry of unimorph structures.

Table 7.4: Fundamental eigenfrequencies (Hz) of smart porous panels having various geometries ($L_1/L_2 = 1$, $R_x/L_1 = 5$, $2h/L_1 = 0.05$, $H_p/2h = 0.2$).

EBC	e_0	Spherical (R_y/L_1=R_x/L_1)	Cylindrical (R_y/L_1=∞)	Plate (R_y/L_1=R_x/L_1=∞)	Hyperbolic Paraboloidal (R_y/L_1=-R_x/L_1)
Bimorph					
SC	0.0	280.488	253.228	244.123	242.135
	0.1	277.570	251.004	242.163	240.189
	0.2	274.537	248.677	240.104	238.147
	0.3	271.374	246.232	237.931	235.992
	0.4	268.070	243.653	235.627	233.706
	0.5	264.614	240.924	233.173	231.271
OC	0.0	299.762	273.571	264.980	262.815
	0.1	297.286	271.846	263.589	261.434
	0.2	294.738	270.074	262.168	260.023
	0.3	292.116	268.254	260.720	258.586
	0.4	289.423	266.391	259.252	257.129
	0.5	286.673	264.500	257.784	255.672
Unimorph					
SC	0.0	281.395	254.198	245.202	243.203
	0.1	276.825	250.150	241.350	239.382
	0.2	271.804	245.632	237.019	235.086
	0.3	266.223	240.522	232.082	230.189
	0.4	259.937	234.655	226.365	224.520
	0.5	252.739	227.794	219.620	217.829
OC	0.0	308.683	278.646	265.389	263.218
	0.1	303.993	274.389	261.260	259.123
	0.2	298.796	269.602	256.590	254.491
	0.3	292.975	264.155	251.242	249.186
	0.4	286.368	257.868	245.028	243.023
	0.5	278.758	250.492	237.683	235.739

Table 7.5: Fundamental SC eigenfrequencies (Hz) of porous bimorph panels ($L_1/L_2 = 1$, $e_0 = 0.2$).

Geometry of the Smart Panel	R_x/L_1=1	R_x/L_1=2	R_x/L_1=5	R_x/L_1=10
$2h/L_1$=0.1, $H_p/2h$=0.05				
Spherical (R_y/L_1=R_x/L_1)	817.439	572.816	474.190	458.105
Cylindrical (R_y/L_1=∞)	549.656	480.008	457.156	453.776
Plate (R_y/L_1=R_x/L_1=∞)	452.686	452.686	452.686	452.686
Hyperbolic Paraboloidal (R_y/L_1=-R_x/L_1)	369.247	429.736	448.902	451.736
$2h/L_1$=0.1, $H_p/2h$=0.1				
Spherical (R_y/L_1=R_x/L_1)	794.466	564.937	473.786	459.051
Cylindrical (R_y/L_1=∞)	541.781	478.626	458.098	455.074
Plate (R_y/L_1=R_x/L_1=∞)	454.102	454.102	454.102	454.102
Hyperbolic Paraboloidal (R_y/L_1=-R_x/L_1)	370.360	431.054	450.301	453.147
$2h/L_1$=0.15, $H_p/2h$=0.05				
Spherical (R_y/L_1=R_x/L_1)	911.460	727.852	662.487	652.559
Cylindrical (R_y/L_1=∞)	694.283	661.115	651.139	649.757
Plate (R_y/L_1=R_x/L_1=∞)	649.386	649.386	649.386	649.386
Hyperbolic Paraboloidal (R_y/L_1=-R_x/L_1)	526.775	615.218	643.723	647.963
$2h/L_1$=0.15, $H_p/2h$=0.1				
Spherical (R_y/L_1=R_x/L_1)	889.776	720.098	660.438	651.429
Cylindrical (R_y/L_1=∞)	686.543	658.381	650.006	648.858
Plate (R_y/L_1=R_x/L_1=∞)	648.562	648.562	648.562	648.562
Hyperbolic Paraboloidal (R_y/L_1=-R_x/L_1)	525.963	614.352	642.888	647.136

Table 7.6: Fundamental SC eigenfrequencies (Hz) of porous unimorph panels ($L_1/L_2 = 1, e_0 = 0.2$).

Geometry of the Smart Panel	R_x/L_1=1	R_x/L_1=2	R_x/L_1=5	R_x/L_1=10
$2h/L_1$=0.1, $H_p/2h$=0.05				
Spherical (R_y/L_1=R_x/L_1)	819.827	572.226	472.471	456.188
Cylindrical (R_y/L_1=∞)	548.928	478.424	455.241	451.794
Plate (R_y/L_1=R_x/L_1=∞)	450.657	450.657	450.657	450.657
Hyperbolic Paraboloidal (R_y/L_1=-R_x/L_1)	367.585	427.808	446.890	449.711
$2h/L_1$=0.1, $H_p/2h$=0.1				
Spherical (R_y/L_1=R_x/L_1)	798.410	563.822	470.813	455.765
Cylindrical (R_y/L_1=∞)	540.425	475.869	454.816	451.688
Plate (R_y/L_1=R_x/L_1=∞)	450.646	450.646	450.646	450.646
Hyperbolic Paraboloidal (R_y/L_1=-R_x/L_1)	367.510	427.764	446.872	449.698
$2h/L_1$=0.15, $H_p/2h$=0.05				
Spherical (R_y/L_1=R_x/L_1)	914.868	727.352	660.50	650.254
Cylindrical (R_y/L_1=∞)	693.449	659.300	648.835	647.317
Plate (R_y/L_1=R_x/L_1=∞)	646.825	646.825	646.825	646.825
Hyperbolic Paraboloidal (R_y/L_1=-R_x/L_1)	524.677	612.786	641.183	645.407
$2h/L_1$=0.15, $H_p/2h$=0.1				
Spherical (R_y/L_1=R_x/L_1)	895.375	719.168	657.105	647.585
Cylindrical (R_y/L_1=∞)	685.017	655.306	646.164	644.804
Plate (R_y/L_1=R_x/L_1=∞)	644.319	644.319	644.319	644.319
Hyperbolic Paraboloidal (R_y/L_1=-R_x/L_1)	522.440	610.305	638.677	642.901

To discuss the observed behaviors of resonance frequencies for the SC and OC electrical conditions, the fundamental frequencies of various porous hybrid structures are listed in Tables 7.7 and 7.8, for different values of $h_p/2h$. In the second and fifth columns of this table, the listed frequencies are quantified by eliminating the electrical effect of piezoelectric layers, to show only the mechanical effect of piezoelectric layers on the results. By inspecting the values in the table, one can realize that the electrical effect in SC condition is negligible, whilst it plays a key role in the OC condition to increase the value of eigenfrequencies. It does mean that the observed changes in natural frequency, due to mounting the SC piezoelectric layers on the substrate, are associated with the stiffening effect of piezoelectric layers only, whereas the frequencies are significantly influenced by the electrical part (in addition to mechanical part), when keeping piezoelectric layers in OC condition. This behavior could be ascribed to various electric potential distributions in SC and OC conditions. Furthermore, both the SC and OC natural frequencies increase by raising the thickness ratio, regardless of the type of structure. It is also observed that in case of spherical porous smart panel, the electrical effect associated with OC piezoelectric layer is more remarkable for unimorphs compared to that of bimorphs, while the opposite result is seen for other geometries.

Table 7.7: Fundamental eigenfrequencies (Hz) of smart porous bimorph panels (L_1/L_2=1, R_x/L_1=5, $2h/L_1$=0.1, e_0=0.3).

$H_p/2h$	(e_{ij}=0[1])	SC (Ω(%)[2])	OC (Ω(%)[2])
Spherical (R_y/L_1=R_x/L_1)			
0.0	468.898	468.898 (0.00)	468.898 (0.00)
0.1	467.185	467.205 (0.00)	490.957 (5.09)
0.2	473.266	473.395 (0.03)	512.563 (8.30)
0.3	483.409	483.762 (0.07)	533.559 (10.4)
0.4	495.832	496.527 (0.14)	553.864 (11.7)
Cylindrical (R_y/L_1=∞)			
0.0	450.644	450.644 (0.00)	450.644 (0.00)
0.1	451.961	451.982 (0.00)	476.423 (5.41)
0.2	460.132	460.265 (0.03)	500.343 (8.74)
0.3	471.819	472.182 (0.08)	522.934 (10.8)
0.4	485.438	486.150 (0.15)	544.411 (12.1)
Plate (R_y/L_1=R_x/L_1=∞)			
0.0	445.780	445.780 (0.00)	445.780 (0.00)
0.1	448.158	448.180 (0.00)	473.069 (5.56)
0.2	457.080	457.215 (0.03)	497.912 (8.93)
0.3	469.339	469.707 (0.08)	521.138 (11.0)
0.4	483.415	484.136 (0.15)	543.091 (12.3)
Hyperbolic Paraboloidal (R_y/L_1=-R_x/L_1)			
0.0	442.057	442.057 (0.00)	442.057 (0.00)
0.1	444.406	444.427 (0.00)	469.070 (5.55)
0.2	453.234	453.368 (0.03)	493.662 (8.92)
0.3	465.365	465.730 (0.08)	516.631 (11.0)
0.4	479.293	480.006 (0.15)	538.329 (12.3)

[1]Natural frequency without piezo effect, [2] $\Omega = \left(\left(\omega_{(\mathrm{sc/oc})} - \omega_{(e_{ij}=0)}\right)/\omega_{(e_{ij}=0)}\right)$*100

Table 7.8: Fundamental eigenfrequencies (Hz) of smart porous unimorph panels (L_1/L_2=1, R_x/L_1=5, $2h/L_1$=0.1, e_0=0.3).

$H_p/2h$	(e_{ij}=0[1])	SC (Ω(%)[2])	OC (Ω(%)[2])
Spherical ($R_y/L_1=R_x/L_1$)			
0.0	468.898	468.898 (0.00)	468.898 (0.00)
0.1	461.490	461.490 (0.00)	488.044 (5.75)
0.2	464.088	464.088 (0.00)	506.619 (9.16)
0.3	472.066	472.066 (0.00)	524.660 (11.1)
0.4	483.163	483.163 (0.00)	542.115 (12.2)
Cylindrical ($R_y/L_1=\infty$)			
0.0	450.644	450.644 (0.00)	450.644 (0.00)
0.1	445.870	445.870 (0.00)	470.093 (5.43)
0.2	450.444	450.444 (0.00)	489.287 (8.62)
0.3	459.984	459.984 (0.00)	508.060 (10.5)
0.4	472.363	472.363 (0.00)	526.285 (11.4)
Plate ($R_y/L_1=R_x/L_1=\infty$)			
0.0	445.780	445.780 (0.00)	445.780 (0.00)
0.1	441.867	441.867 (0.00)	463.333 (4.86)
0.2	447.164	447.164 (0.00)	481.775 (7.74)
0.3	457.328	457.328 (0.00)	500.345 (9.41)
0.4	470.262	470.262 (0.00)	518.664 (10.3)
Hyperbolic Paraboloidal ($R_y/L_1=-R_x/L_1$)			
0.0	442.057	442.057 (0.00)	442.057 (0.00)
0.1	438.167	438.167 (0.00)	459.427 (4.85)
0.2	443.398	443.398 (0.00)	477.665 (7.73)
0.3	453.449	453.449 (0.00)	496.020 (9.93)
0.4	466.240	466.240 (0.00)	514.118 (10.3)

[1]Natural frequency without piezo effect, [2] $\Omega = \left(\left(\omega_{(\mathrm{sc/oc})} - \omega_{(e_{ij}=0)}\right)/\omega_{(e_{ij}=0)}\right)*100$

In Fig. 7.2, for different values of porosity parameter namely 0.2 and 0.5, variations of the SC fundamental frequency with respect to $H_p/2h$ are plotted. Regardless of the panel geometry, it seems that by increasing the value of $H_p/2h$, the shell natural frequencies considerably increase, in such a way that this growth is more remarkable for bimorph structures. As obvious, at any fixed value of

$H_p/2h$, the frequencies of bimorphs are higher than those of unimorphs and this difference increases by raising the porosity parameter. In addition, for the bimorph panels, the curves corresponded to $e_0 = 0.5$ have greater slopes in comparison with the ones associated with $e_0 = 0.2$, which means that the natural frequency of bimorph panels with higher coefficient of porosity are more influenced by changing the thickness ratio $H_p/2h$, whereas the curves related to unimorph structures seem to be parallel for the studied values of e_0. By investigating the numerical results, similar trends can be observed for the OC electrical condition.

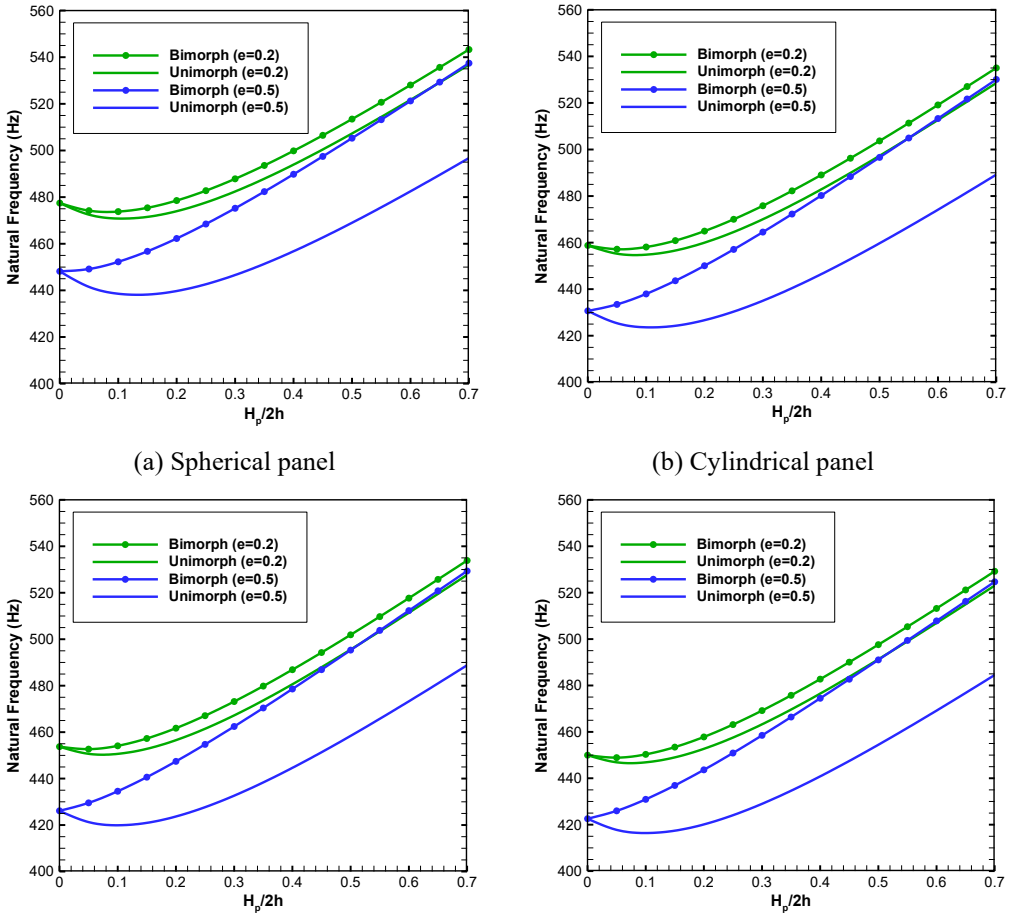

(a) Spherical panel (b) Cylindrical panel

(c) Plate panel (d) Hyperbolic paraboloidal panel

Fig. 7.2: Variation of the fundamental eigenfrequency versus the thickness ratio for coupled smart panels under SC condition.

Fig. 7.3 shows the effect of changes in the shell curvature on variation of the SC natural frequencies of smart doubly curved panels, with respect to the porosity

parameter. As observed, changing the shell radius significantly affects the natural frequency. It is seen that by increasing the value of curvature, the fundamental frequency of spherical shells decreases, while opposite trend is seen for hyperbolic paraboloidal shells. Moreover, those figures reveal that changing the porosity parameter has greater effect on the natural frequencies of unimorph panels with respect to bimorphs.

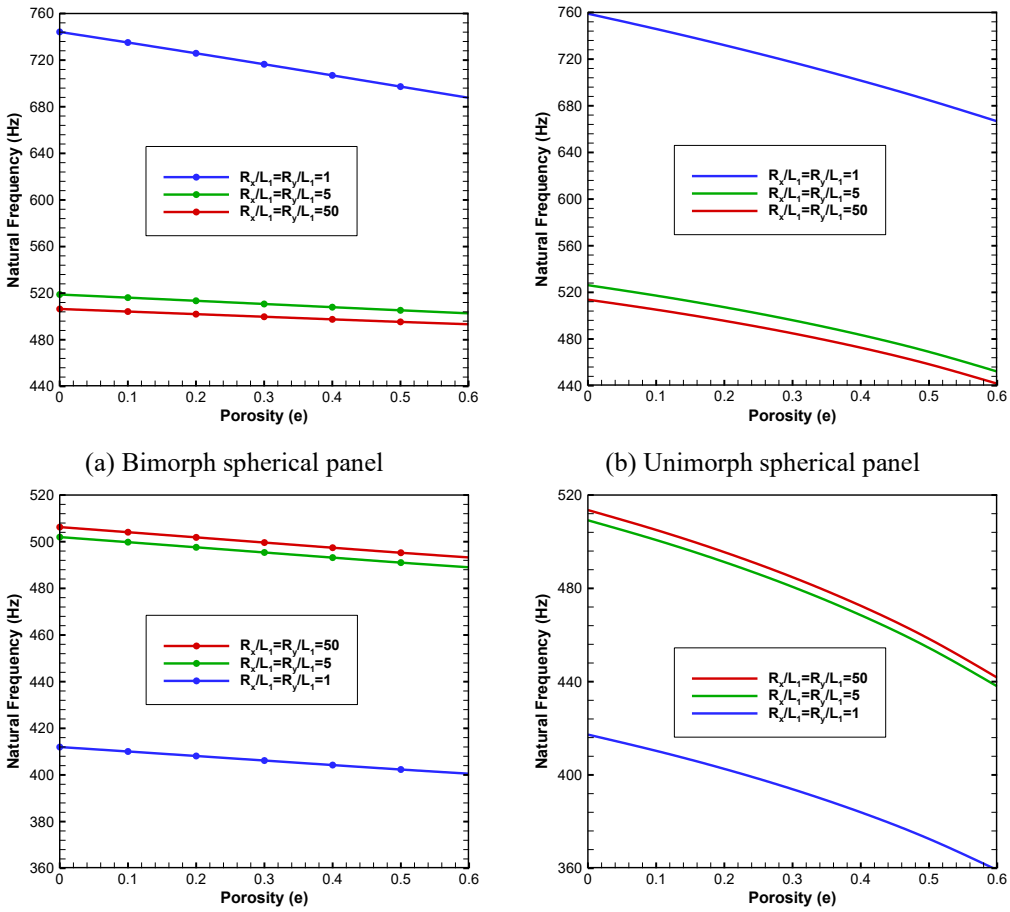

(a) Bimorph spherical panel (b) Unimorph spherical panel

(c) Bimorph hyperbolic paraboloidal panel (d) Unimorph hyperbolic paraboloidal panel

Fig. 7.3: Variation of the fundamental eigenfrequency with respect to porosity coefficient.

In Fig. 7.4, variations of the first two resonance frequencies of spherical smart shells with respect to R_x/L_1 are plotted for the SC and OC electrical conditions. Again, it is seen that by increasing the shell curvature, the frequencies of both vibrational modes decrease. When the value of R_x/L_1 increases from 1 to around

3, the frequencies greatly reduce, while by further increasing the curvature, very smooth decreasing trends are observed for both Mode 1 and Mode 2.

Parameters L_1 and L_2 have direct influence on the eigenfrequencies. By changing the length ratio in constant surface area, the variation of resonance frequency versus L_2/L_1 is shown in Fig. 7.5 for spherical porous bimorphs and unimorphs in SC electrical condition. The value of L_2/L_1 is considered to change from 1/5 to 5, while the surface area is kept constant (equal to $L_2 \times L_1 = 1m^2$). It is observed that for any considered value of the substrate thickness, the minimum frequency is achieved at $L_2/L_1 = 1$, and the frequency response has symmetric behavior around $L_2/L_1 = 1$. This behavior originates from the induced increase in the panel stiffness due to declining/raising the length ratio. For other geometries and electrical condition, similar results can be obtained.

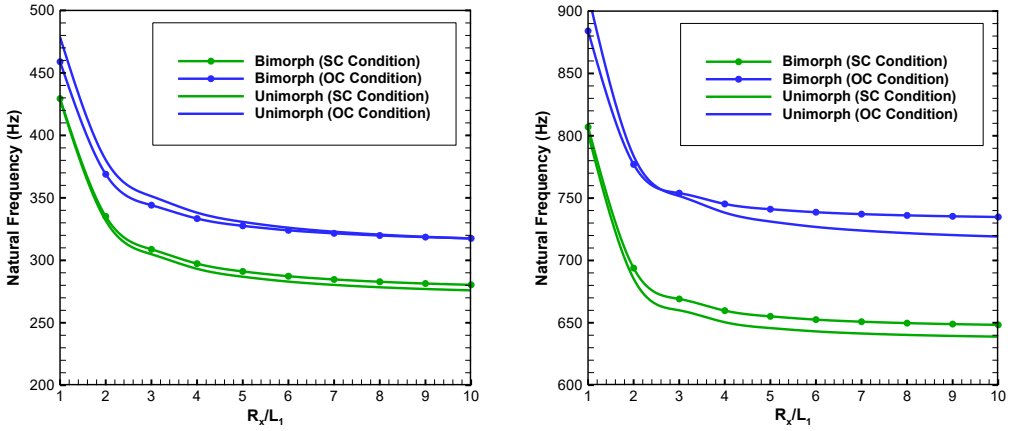

(a) Mode 1 (b) Mode 2

Fig. 7.4: Variations of the first two frequencies of spherical porous bimorph and unimorph shells with respect to R_x/L_1 ($L_1/L_2 = 1$, $R_y/L_1 = 5$, $2h/L_1 = 0.05$, $H_p/2h = 0.5$, $e_0 = 0.2$).

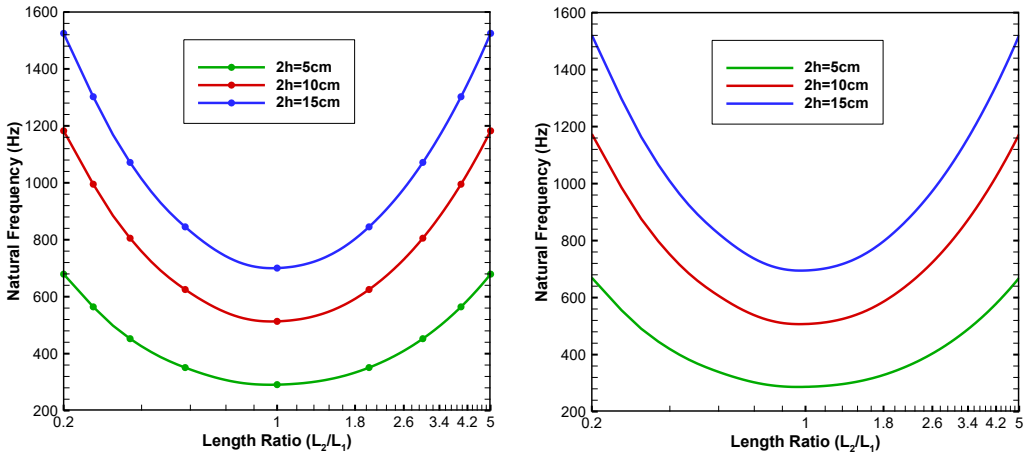

(a) Bimorph spherical panel (b) Unimorph spherical panel

Fig. 7.5: Variation of the fundamental frequency versus the length ratio ($H_p/2h = 0.5$, $e_0 = 0.2$).

To gain a deeper insight into the effect of piezoelectric layers on the frequency response of the system, the parameter θ, representing the relative difference in frequency is defined as follows:

$$\theta = \frac{\omega|_{\text{With Piezoelectric Layers}} - \omega|_{\text{Without Piezoelectric Layers}}}{\omega|_{\text{Without Piezoelectric Layers}}} \times 100 \qquad (7.15)$$

For smart panels with $L_1/L_2 = 1$, $2h/L_2 = 0.1$, $R_x/L_1 = R_y/L_1 = 5$ and $e_0 = 0.3$, the variation of θ with respect to $H_p/2h$ is plotted in Fig. 7.6. Those figures show that at a fixed value of the thickness ratio, the magnitude of θ is the most for both plate and hyperbolic paraboloidal panels and the least for spherical shells irrespective of the electrical condition. It does mean that the addition of piezoelectric layers to the porous substrate has quantitatively different effects on the frequencies of panels with various geometries. Moreover, it seems that in the SC condition, by adding piezoelectric layers, the natural frequencies of coupled panels initially decrease till $H_p/2h = 0.15$, and subsequently increase as the value of Hp/2h rises. This descending/ascending trend is regarded to the changes in the effective mass density and structural stiffness of the coupled smart panels due to increasing the thickness ratio. Differently, since the electrical effect of piezoelectric layers plays a significant role in the growth of OC frequencies, only ascending trends are seen for the variation of eigenfrequencies from $H_p/2h = 0$ to $H_p/2h =$

0.5 in OC condition. In addition, it is clear that for the same thickness of piezoelectric layers, the value of θ for bimorphs is greater than that of unimorph panels, in both SC and OC conditions.

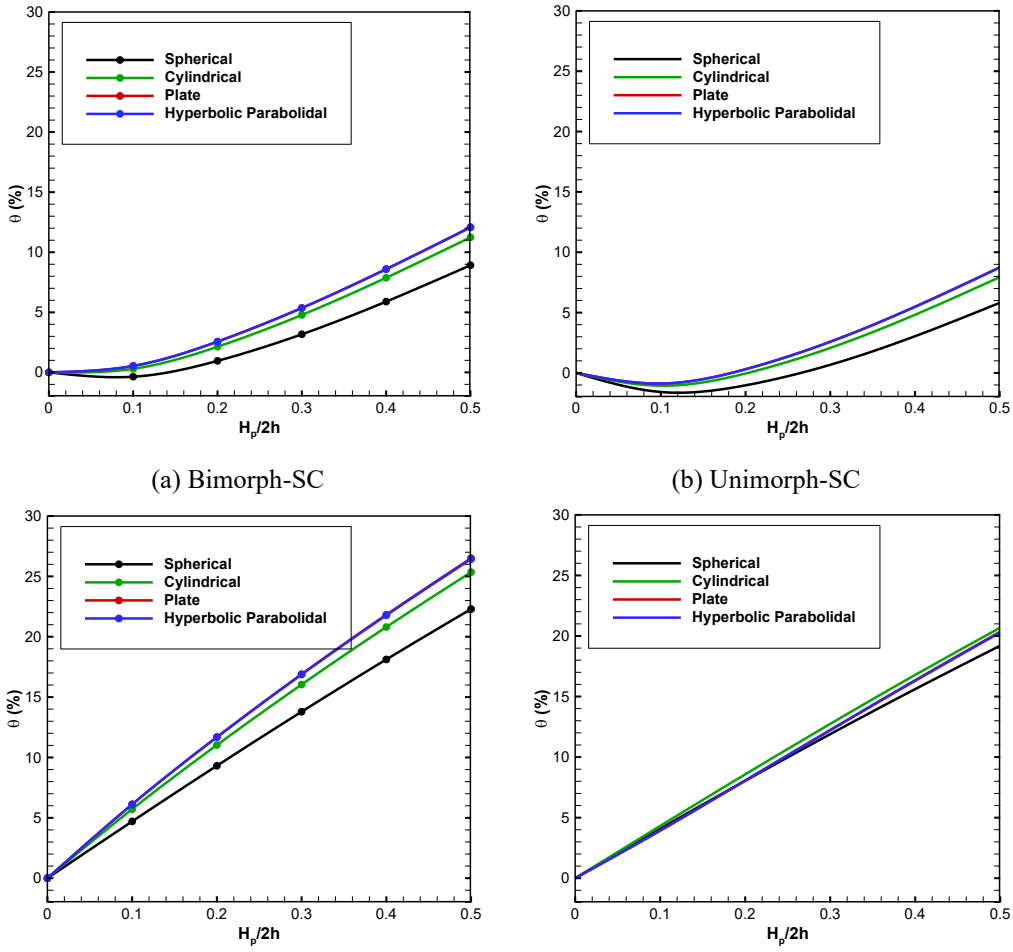

(a) Bimorph-SC (b) Unimorph-SC

(c) Bimorph-OC (d) Unimorph-OC

Fig. 7.6: The effect of piezoelectric layers' thickness on the fundamental frequency of bimorphs and unimorphs.

To investigate the influence of electrical circuits (i.e. SC and OC), thickness ratio $H_p/2h$ and electrical and mechanical effects of piezoelectric layers on frequencies of various vibration modes, Figs. 7.7 and 7.8 are plotted for spherical shells with $2h/L_1 = 0.1$, $L_1/L_2 = 1$, and $R_x/L_1 = R_y/L1 = 5$. Particularly in Fig. 7.7, the variation of θ with respect to $H_p/2h$ is presented for both spherical bimorphs and unimorphs under SC and OC conditions. In addition, by setting $e_{ij} =$

0, the stiffness effect of piezoelectric layers on the first three frequencies is examined in Fig. 7.8(a), while Figs. 7.8(b) and 7.8(c) show the variation of Ω versus thickness ratio $H_p/2h$, in which the parameter Ω (defined in Table 7.7) is related to electrical effect of piezoelectric layers. From Fig. 7.8, it can be simply observed that the natural frequencies associated with higher vibration modes are less influenced by changing the value of $H_p/2h$ in comparison with the fundamental frequency. Moreover, the change in the value of natural frequency due to the effects of both electrical and mechanical parts of piezoelectric layers is the most for Mode 1 and the least for Mode 3, as obvious in Fig. 7.8.

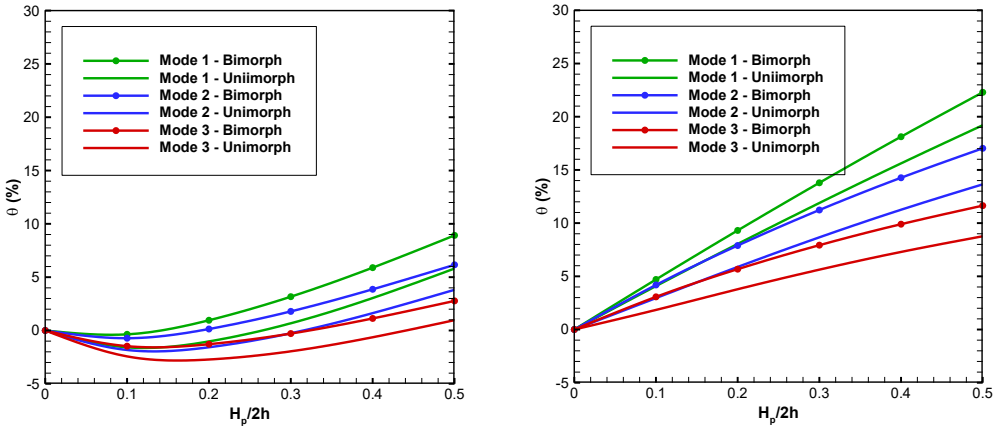

(a) SC condition (b) OC condition

Fig. 7.7: The effect of the thickness ratio on the first three resonance frequencies of porous bimorph and unimorph spherical shells ($e_0 = 0.3$).

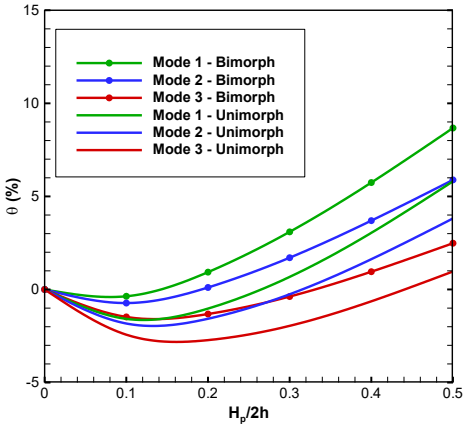

(a) Stiffness effect

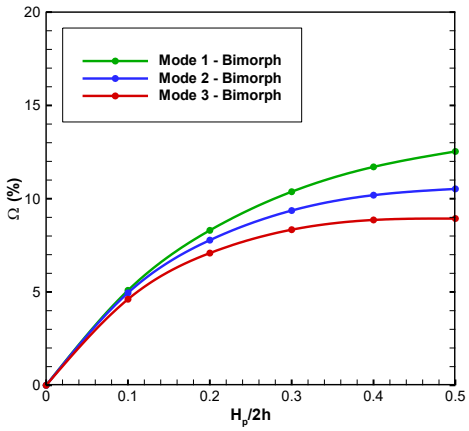

(b) Electrical effect-bimorph shell

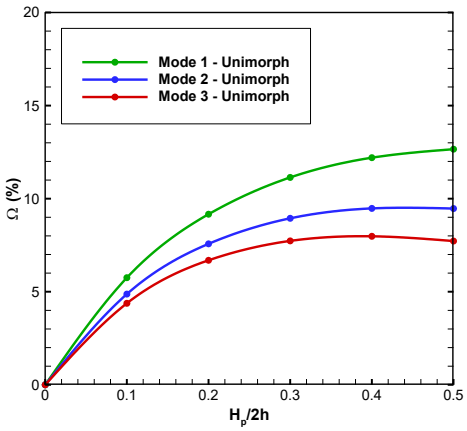

(c) Electrical effect-unimorph shell

Fig. 7.8: The mechanical and electrical effects of piezoelectric layers on the first three natural frequencies of spherical bimorphs and unimorph

In the following, the parameter Γ is defined to investigate the sensitivity of various vibration modes to the variation of porosity:

$$\Gamma = \frac{\omega|_{\text{Shell with Porosity}} - \omega|_{\text{Shell without Porosity}}}{\omega|_{\text{Shell without Porosity}}} \times 100 \tag{7.16}$$

Fig. 7.9 represents the variation of Γ with respect to e for the first three resonance frequencies of spherical bimorph shells under SC and OC conditions.

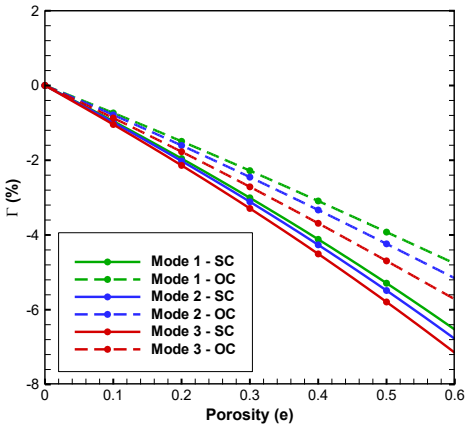

Fig. 7.9: The effect of porosity parameter on the first three resonance frequencies of porous bimorph spherical shells ($L_1/L_2 = 1, R_x/L_1 = R_y/L_1 = 5, 2h/L_1 = 0.1, H_p/2h = 0.2$).

It is seen that in both SC and OC conditions, all the three eigenfrequencies of Mode 1, Mode 2 and Mode 3 are linearly reduced by increasing the value of porosity in such a way that the frequencies of higher modes are more sensitive to the porosity parameter. In addition, it seems that changing the value of porosity has more effect on SC frequencies compared to OC ones.

7.6 Summary and Conclusions

The electromechanical free vibration of porous piezoelectric bimorph and unimorph doubly curved panels has been studied via FSDT. Employing the variational principle and the Maxwell's equation, the governing equations have been derived in terms of mechanical displacement variables and electric function. Assuming simply supported mechanical boundary condition on all the four edges of the panel, the exact eigenfrequencies are extracted analytically. Finally, the influence of various parameters such as porosity, electrical condition, thickness ratio and electrical and mechanical effects of piezoelectric layers on natural frequencies are studied in detail. By investigating the presented numerical simulations, the following conclusions may be drawn:

- It is necessary to consider the electrical effects for the smart panels under OC condition unlike the SC one.
- Bimorph structures usually exhibit higher frequencies compared to the unimorph ones.
- Increasing the porosity parameter reduces the natural frequencies, having greater effect on the frequencies of unimorphs compared to those of bimorph panels.
- By increasing the curvature, the resonant frequencies of spherical and cylindrical shells remarkably decline, while ascending trend is seen for hyperbolic paraboloidal panels.
- Keeping the volume constant, spherical shells exhibit the highest frequencies followed by cylindrical, plate and hyperbolic paraboloidal panels, in descending order of frequency.

- Keeping the surface area $L_1 \times L_2$ constant, the least value of natural frequency is achieved when $L_2/L_1 = 1$, irrespective of the value of curvature.
- Frequencies of higher vibration modes are more influenced by variation of porosity and thickness ratio, compared to the fundamental frequency.

The existence of internal pores within the substrate significantly affects the frequency response of smart structures so that introducing porosity makes it possible to modify the resonance frequency in a desired manner.

Chapter 8

Summary and Conclusions

8.1 Summary and Conclusions

In the first chapter, an introduction to the smart piezoelectric structures, that are widely used for different applications such as vibration and shape control, energy harvesting, etc., is first given. In addition to describe great properties of piezoelectric materials and their broad applications, two particular types of engineering materials, namely FGMs and porous materials, are also introduced, and the motivation behind their use in piezoelectric coupled structures is presented, and finally possible applications are discussed. A comprehensive literature survey is conducted in not only the growing area of vibration-to-electricity energy conversion via piezoelectric materials, but also in the research field related to the smart structures (such as beams, plates, and shells) including piezoelectric elements. The gaps and the shortcomings of available studies in the above research fields are realized, and highlighted. It is shown that, if not all, most of the commonly used designs for piezoelectric vibration energy harvesting, which employ cantilevered beam geometries, suffer from higher-than-expected natural frequencies (compared to those of ambient vibrations), which require further tuning. Thus, design of flexible energy harvesters having low resonance frequencies and higher power

densities is of particular importance. Furthermore, the conducted literature survey reveals that most of the existing models for studying electromechanical behavior of various piezoelectric coupled structures (e.g., beams, plates, and shells) have been developed either based on classical theories or for simply supported boundary conditions. Classical theories ignore the effect of shear deformations, which are of high importance when analyzing moderately-thick or thick structures. On the other hand, the models based on higher-order theories are mostly limited to either simply supported boundary conditions or coupled structures consisting of homogenous substrates (e.g., made of metals) and PZT layers. Therefore, there seemed to be an urgent need to develop reliable electromechanical models based on higher-order shear deformation theories, which can be used for analysis of thin, moderately-thick, and thick piezoelectric coupled structures with different boundary conditions.

In the second chapter is first presented analytical and numerical modeling of unimorph piezoelectric energy harvesters, which are subjected to harmonic base excitation. The analytical model is established based on the Euler-Bernoulli beam assumptions, and closed-form solutions are obtained as the harvester response to the harmonic base excitation. Next, the FE numerical model of the unimorph harvester is created in COMSOL Multiphysics® software. Verification studies are first conducted by comparing the results of both analytical and numerical models to each other, then by updating the present COMSOL model, and comparing the respective results with experimental and numerical works presented in the literature. More importantly, as an attempt to fill the existing gaps in the literature, is proposed in this chapter a novel multi-beam piezoelectric smart structure of disc-like geometry for harvesting vibration from low frequency applications. Using the model developed for the former case, the 3D model of the novel system is created in COMSOL). Different case studies of the novel multi-beam structure are parametrically studied, where the simulations are given for the series and parallel connection cases, to investigate the performance of the harvester device in terms of voltage and power generation, as well as mechanical response. From the simulations, the existence of strain nodes is identified in the fundamental mode of the novel structure; therefore, preliminary optimization studies are first performed to efficiently equip the system with the PZT patches, and consequently, to avoid any voltage cancellation. The results demonstrated that this new multi-beam harvester offers high flexibility in matching its resonance frequency to that of a

target application, simply by either changing the number/shape of the smart beams or altering the proof masses used to design the structure. It is also found that increasing the number of the smart beams significantly improves the electric outputs and reduces the resonance frequency of the scavenger. Under the same base excitation, the novel harvester exhibits a power density of up to six times greater than that of the simple unimorph. Among the considered cases, the 8-beam structure provides the lowest resonance frequency, and can generate several milliwatts of power across its optimum load resistance, when a harmonic base acceleration of 0.4g as applied.

The third chapter is concerned with developing a reliable electromechanical energy harvesting model for 2D piezoelectric bimorph plate structures with substrate made of materials containing porosities. Three different porosity patterns are herein considered for the distribution of internal pores within the porous substrate. The energy harvesting model of the plate scavenger is established based on the conventional shear deformation plate theories, and through the use of Hamilton's principle and Gauss's law. Such theories allow for consideration of transverse shear deformations, therefore, deriving a highly accurate model that can be used for analysis of relatively-thick and thick plate-like piezoelectric harvesters. An analytical solution is then applied to the governing equations, and closed-form expressions are obtained for the voltage, current and power outputs as the scavenger response to harmonic excitation. Comparing the present results with some available in the literature, the proposed model is validated, and extensive electromechanical analysis is presented. It is shown that introducing porosities to the substrate of the bimorph harvester allows tailoring the resonance frequencies of the scavenger, which is highly beneficial for matching the harvester frequency with that of a target application. More interestingly, the presence of porosities helps enhancing the voltage/power generation of the plate harvester, compared to its counterpart with no porosity. Although the trends for variation of the harvester resonance frequency versus the porosity parameter is highly dependent on the type of porosity distribution, it is seen that higher power output is generated by the harvesters with higher porosity parameter, regardless of the type of porosity profile.

In Chapters 4 to 7, the focus is placed on proposing comprehensive analytical solutions for the problems of free vibration, wave propagation and buckling

analysis of beam-, plate-, and shell-like smart sandwich structures consisting of functionally graded or porous substrates, and integrated piezoelectric layer(s). To study the above-mentioned problems analytically, the governing equations of each system are first derived based on higher-order shear deformation theories, and through the use of Hamilton's principle and Maxwell's equation. Depending on the type of boundary conditions, the respective governing equations, that are highly coupled, are solved using Navier's approach, state space approach and Galerkin method. As the systems response, closed-form expressions have been extracted for the wave characteristics, free vibration, and buckling problems of the systems of interest, providing the chance to study the effects of the systems parameters explicitly, and understand the physics of the problem clearly. Moreover, the analytical models provided in Chapters 4 to 7 enable one to extract the exact numerical results for the systems response much faster, when comparing to numerical approaches. Such exact models not only furnish benchmark solutions of shear deformation theories for the piezoelectric coupled structures but also provide insight into the significance of shear deformations on the systems response.

8.2 Research Impact

Each PhD dissertation produced in the Department of Mechanical and Aerospace Engineering (DIMEAS) at Politecnico di Torino must address the social impact. While harvesting energy at the level discussed here does not have a significant impact on reducing the world's energy demands (compared to the well-known forms of green energy, e.g., solar energy and wind energy) it does have the potential to considerably decreasing the world's dependency on chemical batteries, so that reducing the amount of chemical waste created by conventional batteries. Future applications of vibration energy harvesting, that eliminate the need for battery replacement and related maintenance efforts, can lead to long-lasting wireless sensor networks and autonomous low-power electronic components. It is worth noting that the energy required to keep such low-power wireless systems running includes the maintenance costs as well, which can be significant in applications such as wireless damage monitoring systems in critical civil engineering structures at remote locations. Additionally, even if the power outputs are not comparable,

vibration energy is frequently available when/where wind energy and solar energy are not available.

In particular, the linear multi-beam piezoelectric scavenger proposed in Chapter 2 can be of high interest for applications where low frequency vibration is available for energy conversion. The proposed structure can be adjusted depending on the vibration characteristics and other design constraints of a desired application while offering a suitable power density as compared to the piezoelectric scavengers presented in the literature. Moreover, in Chapter 3, a comprehensive 2D analytical model was proposed for the first time for simulation of plate harvesters based on the shear deformation theories. Even though piezoelectric energy harvesters are usually designed and manufactured as thin structures for larger flexibility and higher power generation, there might be need to use configurations where the structure might have moderate thickness (e.g., due to the limitations in the active material dimensions) where the shear deformation and the rotary inertia effects are pronounced. The analytical models presented in Chapters 4 to 7 provide the chance to extract closed-form expressions for static and dynamic response of electromechanically coupled structures (1D and 2D elements), which allows calculating the results of the systems with much lower computational efforts in comparison with numerical methods. Such models can be considered as benchmark solutions for verification of numerical techniques developed by researchers of the field. Moreover, it was also aimed in this dissertation to compare the performances of different materials in order to provide the materials scientists a physical understanding of how different properties of materials affect the resulting response of electromechanically coupled systems (such as power generation of piezoelectric harvesters) so that the composition of the materials can be optimized using the models developed here. Therefore, the models given here are for designing and optimizing not only the mechanical structure of piezoelectric devices (e.g., energy harvesters) but also the materials aspects.

8.3 Publications

The outcomes of the research activities presented in this PhD dissertation have been published in peer-reviewed journals and conferences of Mechanical Engineering. In the following, the *Published* articles extracted from this thesis are listed:

1. Askari, M., Brusa, E. and Delprete, C., 2022. On wave propagation and free vibration of piezoelectric sandwich plates with perfect and porous functionally graded substrates. *Journal of Intelligent Material Systems and Structures*, p.1045389X211072195.

Doi: https://doi.org/10.1177/1045389X211072195

2. Askari, M., Brusa, E. and Delprete, C., 2021. Design and modeling of a novel multi-beam piezoelectric smart structure for vibration energy harvesting. *Mechanics of Advanced Materials and Structures*, pp.1-23.

Doi: https://doi.org/10.1080/15376494.2021.2001122

3. Askari, M., Brusa, E. and Delprete, C., 2021. On the vibration analysis of coupled transverse and shear piezoelectric functionally graded porous beams with higher-order theories. *The Journal of Strain Analysis for Engineering Design*, 56(1), pp.29-49.

Doi: https://doi.org/10.1177/0309324720922085

4. Askari, M., Brusa, E. and Delprete, C., 2020. Electromechanical vibration characteristics of porous bimorph and unimorph doubly curved panels. In *Actuators* (Vol. 9, No. 1, p. 7). Multidisciplinary Digital Publishing Institute.

Doi: https://doi.org/10.3390/act9010007

5. Askari, M., Brusa, E. and Delprete, C., 2019. Vibration analysis of porous bimorph doubly-curved shells for energy harvesting applications. In *International Conference on Mechanics and Materials in Design (M2D)*, 4-6 September 2019, Bologna, Italy.

References

[1] Janocha H. Adaptronics and smart structures: Basics, materials, design and applications. Springer, Berlin, Heidelberg; 2007. https://doi.org/10.1007/978-3-540-71967-0.

[2] Jalili N. Piezoelectric-based vibration control: From macro to micro/nano scale systems. Springer US; 2009. https://doi.org/10.1007/978-1-4419-0070-8.

[3] Lane R, Craig B. Materials that sense and respond- An introduction to smart materials. The AMPTIAC Quarterly 2003;7:9–14.

[4] Berlincourt D. Piezoelectric ceramics: Characteristics and applications. The Journal of the Acoustical Society of America 1998;70:1586. https://doi.org/10.1121/1.387224.

[5] Yang Z, Zhou S, Zu J, Inman D. High-Performance Piezoelectric Energy Harvesters and Their Applications. Joule 2018;2:642–97. https://doi.org/10.1016/j.joule.2018.03.011.

[6] Naebe M, Shirvanimoghaddam K. Functionally graded materials: A review of fabrication and properties. Applied Materials Today 2016;5:223–45. https://doi.org/10.1016/J.APMT.2016.10.001.

[7] Suresh S, Mortensen A. Fundamentals of Functionally Graded Materials. The Institute of Materials; 1998.

[8] Reddy JN. Analysis of functionally graded plates. International Journal for Numerical Methods in Engineering 2000;47:663–84. https://doi.org/10.1002/(SICI)1097-0207(20000110/30)47:1/3<663::AID-NME787>3.0.CO;2-8.

[9] Miyamoto Y, Kaysser WA, Rabin BH, Kawasaki A, Ford RG. Functionally graded materials: design, processing and applications. Berlin: Springer; 2013. https://doi.org/10.1007/978-1-4615-5301-4.

[10] Birman V, Byrd LW. Modeling and Analysis of Functionally Graded Materials and Structures. Applied Mechanics Reviews 2007;60:195–216. https://doi.org/10.1115/1.2777164.

[11] Jha DK, Kant T, Singh RK. A critical review of recent research on functionally graded plates. Composite Structures 2013;96:833–49. https://doi.org/10.1016/J.COMPSTRUCT.2012.09.001.

[12] Zhu J, Lai Z, Yin Z, Jeon J, Lee S. Fabrication of ZrO2-NiCr functionally graded material by powder metallurgy. Materials Chemistry and Physics 2001;68:130–5. https://doi.org/10.1016/S0254-0584(00)00355-2.

[13] Wolfgang E, Joachim B. Porous Media: Theory, Experiments and Numerical Applications. Springer Berlin Heidelberg; 2002. https://doi.org/10.1007/978-3-662-04999-0.

[14] Banhart J. Manufacture, characterisation and application of cellular metals and metal foams. Progress in Materials Science 2001;46:559–632. https://doi.org/10.1016/S0079-6425(00)00002-5.

[15] Goodall R, Mortensen A. Porous Metals. Physical Metallurgy: Fifth Edition 2014;1:2399–595. https://doi.org/10.1016/B978-0-444-53770-6.00024-1.

[16] Detournay E, Cheng AHD. Fundamentals of Poroelasticity. Comprehensive Rock Engineering Vol 2 1993:113–71. https://doi.org/10.1016/B978-0-08-040615-2.50011-3.

[17] Baz A, Ro J. Vibration control of plates with active constrained layer damping. Smart Materials and Structures 1996;5:272. https://doi.org/10.1088/0964-1726/5/3/005.

[18] Pukada E. History and recent progress in piezoelectric polymers. IEEE Transactions on Ultrasonics, Ferroelectrics, and Frequency Control 2000;47:1277–90. https://doi.org/10.1109/58.883516.

[19] Sullivan JL, Gaines L. A review of battery life-cycle analysis : state of knowledge and critical needs. Argonne, IL (United States): 2010. https://doi.org/10.2172/1000659.

[20] Rafique S. Piezoelectric Vibration Energy Harvesting: Modeling & Experiments. Berlin: Springer International Publishing; 2018. https://doi.org/10.1007/978-3-319-69442-9.

[21] Chalasani S, Conrad JM. A survey of energy harvesting sources for embedded systems. Conference Proceedings - IEEE SOUTHEASTCON, 2008, p. 442–7. https://doi.org/10.1109/SECON.2008.4494336.

[22] Roundy S, Wright PK, Rabaey J. A study of low level vibrations as a power source for wireless sensor nodes. Computer Communications 2003;26:1131–44. https://doi.org/10.1016/S0140-3664(02)00248-7.

[23] Jeon YB, Sood R, Jeong JH, Kim SG. MEMS power generator with transverse mode thin film PZT. Sensors and Actuators A: Physical 2005;122:16–22. https://doi.org/10.1016/J.SNA.2004.12.032.

[24] Williams CB, Yates RB. Analysis of a micro-electric generator for microsystems. Sensors and Actuators, A: Physical 1996;52:8–11. https://doi.org/10.1016/0924-4247(96)80118-X.

[25] Glynne-Jones P, Tudor MJ, Beeby SP, White NM. An electromagnetic, vibration-powered generator for intelligent sensor systems. Sensors and Actuators A: Physical 2004;110:344–9. https://doi.org/10.1016/J.SNA.2003.09.045.

[26] Arnold DP. Review of microscale magnetic power generation. IEEE Transactions on Magnetics 2007;43:3940–51. https://doi.org/10.1109/TMAG.2007.906150.

[27] Roundy S, Wright PK, Rabaey JM. Energy Scavenging for Wireless Sensor Networks. Boston: Kluwer Academic Publishers; 2003. https://doi.org/10.1007/978-1-4615-0485-6.

[28] Mitcheson PD, Miao P, Stark BH, Yeatman EM, Holmes AS, Green TC. MEMS electrostatic micropower generator for low frequency operation. Sensors and Actuators A: Physical 2004;115:523–9. https://doi.org/10.1016/J.SNA.2004.04.026.

[29] Alper Erturk, Daniel J. Inman. Piezoelectric Energy Harvesting. John Wiley & Sons; 2011.

[30] Ahmed R, Mir F, Banerjee S, Safaei M, Sodano HA, Anton SR. Powering MEMS portable devices—a review of non-regenerative and regenerative power supply systems with special emphasis on piezoelectric energy harvesting systems. Smart Materials and Structures 2008;17:043001. https://doi.org/10.1088/0964-1726/17/4/043001.

[31] Tianchen Y, Jian Y, Ruigang S, - al, Yoon S, Cho Y-H. Energy harvesting vibration sources for microsystems applications. Measurement Science and Technology 2006;17:R175. https://doi.org/10.1088/0957-0233/17/12/R01.

[32] Safaei M, Sodano HA, Anton SR. A review of energy harvesting using piezoelectric materials: state-of-the-art a decade later (2008-2018). Smart Materials and Structures 2019;28:113001. https://doi.org/10.1088/1361-665X/ab36e4.

[33] Anton SR, Sodano HA. A review of power harvesting using piezoelectric materials (2003-2006). Smart Materials and Structures 2007;16:R1. https://doi.org/10.1088/0964-1726/16/3/R01.

[34] Priya S. Advances in energy harvesting using low profile piezoelectric transducers. Journal of Electroceramics 2007;19:165–82. https://doi.org/10.1007/S10832-007-9043-4/FIGURES/22.

[35] Saadon S, Sidek O. A review of vibration-based MEMS piezoelectric energy harvesters. Energy Conversion and Management 2011;52:500–4. https://doi.org/10.1016/J.ENCONMAN.2010.07.024.

[36] Liu H, Zhong J, Lee C, Lee SW, Lin L. A comprehensive review on piezoelectric energy harvesting technology: Materials, mechanisms, and applications. Applied Physics Reviews 2018;5:041306. https://doi.org/10.1063/1.5074184.

[37] Li H, Tian C, Deng ZD. Energy harvesting from low frequency applications using piezoelectric materials. Applied Physics Reviews 2014;1:041301. https://doi.org/10.1063/1.4900845.

[38] Choi WJ, Jeon · Y, Jeong J-H, Sood · R, Kim · S G. Energy harvesting MEMS device based on thin film piezoelectric cantilevers. Journal of Electroceramics 2006;17:543–8. https://doi.org/10.1007/s10832-006-6287-3.

[39] Ali F, Raza W, Li X, Gul H, Kim KH. Piezoelectric energy harvesters for biomedical applications. Nano Energy 2019;57:879–902. https://doi.org/10.1016/J.NANOEN.2019.01.012.

[40] Sodano HA, Inman DJ, Park G. Comparison of Piezoelectric Energy Harvesting Devices for Recharging Batteries: Journal of Intelligent Material Systems and Structures 2005;16:799–807. https://doi.org/10.1177/1045389X05056681.

[41] Derayatifar M, Tahani M, Moeenfard H. Nonlinear analysis of functionally graded piezoelectric energy harvesters. Composite Structures 2017;182:199–208. https://doi.org/10.1016/J.COMPSTRUCT.2017.09.030.

[42] Larkin K, Abdelkefi A. Neutral axis modeling and effectiveness of functionally graded piezoelectric energy harvesters. Composite Structures 2019;213:25–36. https://doi.org/10.1016/J.COMPSTRUCT.2019.01.067.

[43] Amini Y, Emdad H, Farid M. Finite element modeling of functionally graded piezoelectric harvesters. Composite Structures 2015;129:165–76. https://doi.org/10.1016/J.COMPSTRUCT.2015.04.011.

[44] Cao Y, Huang H, Zhu ZH, Su S. Optimized energy harvesting through piezoelectric functionally graded cantilever beams. Smart Materials and Structures 2019;28:025038. https://doi.org/10.1088/1361-665X/AAF761.

[45] Roscow J, Zhang Y, Taylor J, Bowen CR. Porous ferroelectrics for energy harvesting applications. The European Physical Journal Special Topics 2015 224:14 2015;224:2949–66. https://doi.org/10.1140/EPJST/E2015-02600-Y.

[46] Yan M, Liu S, Xiao Z, Yuan X, Zhai D, Zhou K, et al. Evaluation of the pore morphologies for piezoelectric energy harvesting application. Ceramics International 2021. https://doi.org/10.1016/J.CERAMINT.2021.11.039.

[47] Kiran R, Kumar A, Chauhan VS, Kumar R, Vaish R. Finite Element Study on Performance of Piezoelectric Bimorph Cantilevers Using Porous/Ceramic 0–3 Polymer Composites. Journal of Electronic Materials 2017 47:1 2017;47:233–41. https://doi.org/10.1007/S11664-017-5751-Y.

[48] Shin DJ, Lim DH, Koo BK, Kim MS, Kim IS, Jeong SJ. Porous sandwich structures based on BaZrTiO3–BaCaTiO3 ceramics for piezoelectric energy harvesting. Journal of Alloys and Compounds 2020;831:154792. https://doi.org/10.1016/J.JALLCOM.2020.154792.

[49] Roscow JI, Lewis RWC, Taylor J, Bowen CR. Modelling and fabrication of porous sandwich layer barium titanate with improved piezoelectric energy harvesting figures of merit. Acta Materialia 2017;128:207–17. https://doi.org/10.1016/J.ACTAMAT.2017.02.029.

[50] Martínez-Ayuso G, Friswell MI, Adhikari S, Khodaparast HH, Featherston CA. Energy harvesting using porous piezoelectric beam with impacts. Procedia Engineering 2017;199:3468–73. https://doi.org/10.1016/J.PROENG.2017.09.454.

[51] Zhang Y, Bao Y, Zhang D, Bowen CR. Porous PZT Ceramics with Aligned Pore Channels for Energy Harvesting Applications. Journal of the American Ceramic Society 2015;98:2980–3. https://doi.org/10.1111/JACE.13797.

[52] Dong L, Han X, Xu Z, Closson AB, Liu Y, Wen C, et al. Flexible Porous Piezoelectric Cantilever on a Pacemaker Lead for Compact Energy Harvesting. Advanced Materials Technologies 2019;4:1800148. https://doi.org/10.1002/ADMT.201800148.

[53] Mahesh V. Porosity effect on the energy harvesting behaviour of functionally graded magneto-electro-elastic/fibre-reinforced composite beam. The European Physical Journal Plus 2021 137:1 2021;137:1–39. https://doi.org/10.1140/EPJP/S13360-021-02235-9.

[54] Kim SB, Park JH, Kim SH, Ahn H, Wikle HC, Kim DJ. Modeling and evaluation of d33 mode piezoelectric energy harvesters. Journal of Micromechanics and Microengineering 2012;22:105013. https://doi.org/10.1088/0960-1317/22/10/105013.

[55] Kashyap R, Lenka TR, Baishya S. Distributed Parameter Modeling of Cantilevered-d33-Mode Piezoelectric Energy Harvesters. IEEE Transactions on Electron Devices 2016;63:1281–7. https://doi.org/10.1109/TED.2015.2514160.

[56] Malakooti MH, Sodano HA. Piezoelectric energy harvesting through shear mode operation. Smart Materials and Structures 2015;24:055005. https://doi.org/10.1088/0964-1726/24/5/055005.

[57] Zhao J, Zheng X, Zhou L, Zhang Y, Sun J, Dong W, et al. Investigation of a d15 mode PZT-51 piezoelectric energy harvester with a series connection structure. Smart Materials and Structures 2012;21:105006. https://doi.org/10.1088/0964-1726/21/10/105006.

[58] Zhu YK, Yu YG, Li L, Jiang T, Wang XY, Zheng XJ. Modeling and characterization of multilayered d15 mode piezoelectric energy harvesters in series and parallel connections. Smart Materials and Structures 2016;25:075027. https://doi.org/10.1088/0964-1726/25/7/075027.

[59] Guan MJ, Liao WH. On the efficiencies of piezoelectric energy harvesting circuits towards storage device voltages. Smart Materials and Structures 2007;16:498. https://doi.org/10.1088/0964-1726/16/2/031.

[60] Ottman GK, Hofmann HF, Lesieutre GA. Optimized piezoelectric energy harvesting circuit using step-down converter in discontinuous conduction mode. IEEE Transactions on Power Electronics 2003;18:696–703. https://doi.org/10.1109/TPEL.2003.809379.

[61] Ottman GK, Hofmann HF, Bhatt AC, Lesieutre GA. Adaptive piezoelectric energy harvesting circuit for wireless remote power supply. IEEE Transactions on Power Electronics 2002;17:669–76. https://doi.org/10.1109/TPEL.2002.802194.

[62] Roundy S, Wright PK. A piezoelectric vibration based generator for wireless electronics. Smart Materials and Structures 2004;13:1131–42. https://doi.org/10.1088/0964-1726/13/5/018.

[63] DuToit NE, Wardle BL, Kim SG. DESIGN CONSIDERATIONS FOR MEMS-SCALE PIEZOELECTRIC MECHANICAL VIBRATION ENERGY HARVESTERS. Https://DoiOrg/101080/10584580590964574 2006;71:121–60. https://doi.org/10.1080/10584580590964574.

[64] Stephen NG. On energy harvesting from ambient vibration. Journal of Sound and Vibration 2006;293:409–25. https://doi.org/10.1016/J.JSV.2005.10.003.

[65] Daqaq MF, Renno JM, Farmer JR, Inman DJ. Effects of system parameters and damping on an optimal vibration-based energy harvester. Collection of Technical Papers - AIAA/ASME/ASCE/AHS/ASC Structures, Structural Dynamics and Materials Conference 2007;8:7901–11. https://doi.org/10.2514/6.2007-2361.

[66] Sodano HA, Park G, Inman DJ. Estimation of Electric Charge Output for Piezoelectric Energy Harvesting. Strain 2004;40:49–58. https://doi.org/10.1111/J.1475-1305.2004.00120.X.

[67] DuToit NE, Wardle BL. Experimental Verification of Models for Microfabricated Piezoelectric Vibration Energy Harvesters. AIAA Journal 2007;45:1126–37. https://doi.org/10.2514/1.25047.

[68] Hagood NW, Chung WH, von Flotow A. Modelling of Piezoelectric Actuator Dynamics for Active Structural Control: Journal of Intelligent Material Systems and Structures 1990;1:327–54. https://doi.org/10.1177/1045389X9000100305.

[69] Erturk A, Inman DJ. An experimentally validated bimorph cantilever model for piezoelectric energy harvesting from base excitations. Smart Materials and Structures 2009;18:18. https://doi.org/10.1088/0964-1726/18/2/025009.

[70] Lu Q, Liu L, Scarpa F, Leng J, Liu Y. A novel composite multi-layer piezoelectric energy harvester. Composite Structures 2018;201:121–30. https://doi.org/10.1016/J.COMPSTRUCT.2018.06.024.

[71] Benasciutti D, Moro L, Zelenika S, Brusa E. Vibration energy scavenging via piezoelectric bimorphs of optimized shapes. Microsystem Technologies, vol. 16, Springer; 2010, p. 657–68. https://doi.org/10.1007/s00542-009-1000-5.

[72] Mateu L, Moll F. Optimum Piezoelectric Bending Beam Structures for Energy Harvesting using Shoe Inserts. Journal of Intelligent Material Systems and Structures 2005;16:835–45. https://doi.org/10.1177/1045389X05055280.

[73] Goldschmidtboeing F, Woias P. Characterization of different beam shapes for piezoelectric energy harvesting. Journal of Micromechanics and Microengineering 2008;18:7. https://doi.org/10.1088/0960-1317/18/10/104013.

[74] Pradeesh EL, Udhayakumar S. Investigation on the geometry of beams for piezoelectric energy harvester. Microsystem Technologies 2019;25:3463–75. https://doi.org/10.1007/s00542-018-4220-8.

[75] Muthalif AGA, Nordin NHD. Optimal piezoelectric beam shape for single and broadband vibration energy harvesting: Modeling, simulation and experimental results. Mechanical Systems and Signal Processing 2015;54:417–26. https://doi.org/10.1016/j.ymssp.2014.07.014.

[76] Qi L. Energy harvesting properties of the functionally graded flexoelectric microbeam energy harvesters. Energy 2019;171:721–30. https://doi.org/10.1016/J.ENERGY.2019.01.047.

[77] Motlagh PL, Anamagh MR, Bediz B, Basdogan I. Electromechanical analysis of functionally graded panels with surface-integrated piezo-patches for optimal energy harvesting. Composite Structures 2021;263:113714. https://doi.org/10.1016/J.COMPSTRUCT.2021.113714.

[78] Cao Y, Huang H, Ding Y. Isogeometric optimization of piezoelectric functionally graded material for energy harvester. Composite Structures 2021;273:114261. https://doi.org/10.1016/J.COMPSTRUCT.2021.114261.

[79] Heshmati M, Amini Y. A comprehensive study on the functionally graded piezoelectric energy harvesting from vibrations of a graded beam under travelling multi-oscillators. Applied Mathematical Modelling 2019;66:344–61. https://doi.org/10.1016/J.APM.2018.09.002.

[80] Amini Y, Fatehi P, Heshmati M, Parandvar H. Time domain and frequency domain analysis of functionally graded piezoelectric harvesters subjected to random vibration: Finite element modeling. Composite Structures 2016;136:384–93. https://doi.org/10.1016/J.COMPSTRUCT.2015.10.029.

[81] Wu N, Bao B, Wang Q. Review on engineering structural designs for efficient piezoelectric energy harvesting to obtain high power output. Engineering Structures 2021;235:112068. https://doi.org/10.1016/J.ENGSTRUCT.2021.112068.

[82] Saravanos DA, Heyliger PR. Mechanics and Computational Models for Laminated Piezoelectric Beams, Plates, and Shells. Applied Mechanics Reviews 1999;52:305–20. https://doi.org/10.1115/1.3098918.

[83] Ebrahimi F, Hosseini SHS, Singhal A. A comprehensive review on the modeling of smart piezoelectric nanostructures. Structural Engineering and Mechanics 2020;74:611. https://doi.org/10.12989/SEM.2020.74.5.611.

[84] Zhang S-Q, Zhao G-Z, Rao MN, Schmidt R, Yu Y-J. A review on modeling techniques of piezoelectric integrated plates and shells. Journal of Intelligent Material Systems and Structures 2019;30:1133–47. https://doi.org/10.1177/1045389X19836169.

[85] Benjeddou A. Advances in piezoelectric finite element modeling of adaptive structural elements: a survey. Computers & Structures 2000;76:347–63. https://doi.org/10.1016/S0045-7949(99)00151-0.

[86] Bailey T, Ubbard JE. Distributed piezoelectric-polymer active vibration control of a cantilever beam. Journal of Guidance, Control, and Dynamics 1985;8:605–11. https://doi.org/10.2514/3.20029.

[87] Wang BT, Rogers CA. Laminate Plate Theory for Spatially Distributed Induced Strain Actuators: Journal of Composite Materials 1991;25:433–52. https://doi.org/10.1177/002199839102500405.

[88] Ha SK, Keilers C, Chang FK. Finite element analysis of composite structures containing distributed piezoceramic sensors and actuators. AIAA Journal 2012;30:772–80. https://doi.org/10.2514/3.10984.

[89] Wang DQ, Miao Liew K, Wang D, Wang Q, Liew K, Wang D. Issues of control of structures using piezoelectric actuators. International Conference on Experimental Mechanics: Advances and Applications, vol. 2921, SPIE; 1997, p. 425–30. https://doi.org/10.1117/12.269854.

[90] Crawley EF, de Luis J. Use of piezoelectric actuators as elements of intelligent structures. AIAA Journal 2012;25:1373–85. https://doi.org/10.2514/3.9792.

[91] Crawley EF, Anderson EH. Detailed Models of Piezoceramic Actuation of Beams: Journal of Intelligent Material Systems and Structures 1990;1:4–25. https://doi.org/10.1177/1045389X9000100102.

[92] Haojiang D, Chenbuo, Liangjian. General solutions for coupled equations for piezoelectric media. International Journal of Solids and Structures 1996;33:2283–98. https://doi.org/10.1016/0020-7683(95)00152-2.

[93] Man JH, Lee I. Analysis of composite plates with piezoelectric actuators for vibration control using layerwise displacement theory. Composites Part B: Engineering 1998;29:621–32. https://doi.org/10.1016/S1359-8368(98)00027-4.

[94] Na S, Librescu L. Oscillation control of cantilevers via smart materials technology and optimal feedback control: actuator location and power consumption issues. Smart Materials and Structures 1998;7:833. https://doi.org/10.1088/0964-1726/7/6/011.

[95] Wang Q, Quek ST. Flexural vibration analysis of sandwich beam coupled with piezoelectric actuator. Smart Materials and Structures 2000;9:103. https://doi.org/10.1088/0964-1726/9/1/311.

[96] Wang Q, Quek ST, Sun CT, Liu X. Analysis of piezoelectric coupled circular plate. Smart Materials and Structures 2001;10:229.

[97] Hagood NW, McFarland AJ. Modeling of a Piezoelectric Rotary Ultrasonic Motor. IEEE Transactions on Ultrasonics, Ferroelectrics and Frequency Control 1995;42:210–24. https://doi.org/10.1109/58.365235.

[98] Heyliger PR, Ramirez G. Free vibration of laminated circular piezoelectric plates and discs. Journal of Sound and Vibration 2000;229:935–56. https://doi.org/10.1006/JSVI.1999.2520.

[99] Xu SX, Koko TS. Finite element analysis and design of actively controlled piezoelectric smart structures. Finite Elements in Analysis and Design 2004;40:241–62. https://doi.org/10.1016/S0168-874X(02)00225-1.

[100] He XQ, Ng TY, Sivashanker S, Liew KM. Active control of FGM plates with integrated piezoelectric sensors and actuators. International Journal of Solids and Structures 2001;38:1641–55. https://doi.org/10.1016/S0020-7683(00)00050-0.

[101] Huang XL, Shen HS. Vibration and dynamic response of functionally graded plates with piezoelectric actuators in thermal environments. Journal of Sound and Vibration 2006;289:25–53. https://doi.org/10.1016/J.JSV.2005.01.033.

[102] Kargarnovin MH, Najafizadeh MM, Viliani NS. Vibration control of a functionally graded material plate patched with piezoelectric actuators and sensors under a constant electric charge. Smart Materials and Structures 2007;16:1252. https://doi.org/10.1088/0964-1726/16/4/037.

[103] Brischetto S, Carrera E. Refined 2D Models for the Analysis of Functionally Graded Piezoelectric Plates: Journal of Intelligent Material Systems and Structures 2009;20:1783–97. https://doi.org/10.1177/1045389X08098444.

[104] Liang XQ, Batra RC. Changes in Frequencies of a Laminated Plate Caused by Embedded Piezoelectric Layers. AIAA Journal 1997;35:1672–3. https://doi.org/10.2514/2.9.

[105] Davis CL, Lesieutre GA. An actively tuned solid-state vibration absorber using capacitive shunting of piezoelectric stiffness. Journal of Sound and Vibration 2000;232:601–17. https://doi.org/10.1006/JSVI.1999.2755.

[106] Jin J, Batra RC. Effect of electromechanical coupling on static deformations and natural frequencies. IEEE Transactions on Ultrasonics, Ferroelectrics, and Frequency Control 2005;52:1079–93. https://doi.org/10.1109/TUFFC.2005.1503994.

[107] Askari Farsangi MA, Saidi AR. Levy type solution for free vibration analysis of functionally graded rectangular plates with piezoelectric layers. Smart Materials and Structures 2012;21:094017. https://doi.org/10.1088/0964-1726/21/9/094017.

[108] Bendine K, Boukhoulda FB, Nouari M, Satla Z. Active vibration control of functionally graded beams with piezoelectric layers based on higher order shear deformation theory. Earthquake Engineering and Engineering Vibration 2016 15:4 2016;15:611–20. https://doi.org/10.1007/S11803-016-0352-Y.

[109] Loja MAR, Mota Soares CM, Barbosa JI. Analysis of functionally graded sandwich plate structures with piezoelectric skins, using B-spline finite strip method. Composite Structures 2013;96:606–15. https://doi.org/10.1016/J.COMPSTRUCT.2012.08.010.

[110] Askari M, Brusa E, Delprete C. Design and modeling of a novel multi-beam piezoelectric smart structure for vibration energy harvesting. Mechanics of Advanced Materials and Structures 2021:1–23. https://doi.org/10.1080/15376494.2021.2001122.

[111] Wu H, Tang L, Yang Y, Soh CK. A novel two-degrees-of-freedom piezoelectric energy harvester. Journal of Intelligent Material Systems and Structures 2013;24:357–68. https://doi.org/10.1177/1045389X12457254.

[112] Toyabur RM, Salauddin M, Park JY. Design and experiment of piezoelectric multimodal energy harvester for low frequency vibration. Ceramics International 2017;43:S675–81. https://doi.org/10.1016/j.ceramint.2017.05.257.

[113] Upadrashta D, Yang Y. Trident-Shaped Multimodal Piezoelectric Energy Harvester. Journal of Aerospace Engineering 2018;31:04018070. https://doi.org/10.1061/(ASCE)AS.1943-5525.0000899.

[114] Sun S, Tse PW. Design and performance of a multimodal vibration-based energy harvester model for machine rotational frequencies. Applied Physics Letters 2017;110:243902. https://doi.org/10.1063/1.4986477.

[115] Sun S, Tse PW. Modeling of a horizontal asymmetric U-shaped vibration-based piezoelectric energy harvester (U-VPEH). Mechanical Systems and Signal Processing 2019;114:467–85. https://doi.org/10.1016/j.ymssp.2018.05.029.

[116] Castagnetti D, Radi E. A piezoelectric based energy harvester with dynamic magnification: modelling, design and experimental assessment. Meccanica 2018;53:2725–42. https://doi.org/10.1007/s11012-018-0860-0.

[117] Castagnetti D. Wideband fractal-inspired piezoelectric energy harvesters. Proceedings of the Institution of Mechanical Engineers, Part L: Journal of Materials: Design and Applications 2021. https://doi.org/10.1177/14644207211005504.

[118] Bath D, Salehian A. A novel 3D folded zigzag piezoelectric energy harvester; Modeling and experiments. Smart Materials and Structures 2019;28:025011. https://doi.org/10.1088/1361-665X/aaf15b.

[119] Fernandes E, Martin B, Rua I, Zarabi S, Debéda H, Nairn D, et al. Design, fabrication, and testing of a low frequency MEMS piezoelectromagnetic energy harvester. Smart Materials and Structures 2018;27:035017. https://doi.org/10.1088/1361-665X/aaaba5.

[120] Udvardi P, Radó J, Straszner A, Ferencz J, Hajnal Z, Soleimani S, et al. Spiral-Shaped Piezoelectric MEMS Cantilever Array for Fully Implantable Hearing Systems. Micromachines 2017;8:311. https://doi.org/10.3390/mi8100311.

[121] Liu H, Lee C, Kobayashi T, Tay CJ, Quan C. A new S-shaped MEMS PZT cantilever for energy harvesting from low frequency vibrations below 30 Hz. Microsystem Technologies 2012;18:497–506. https://doi.org/10.1007/s00542-012-1424-1.

[122] Jiang W, Wang L, Zhao L, Luo G, Yang P, Ning S, et al. Modeling and design of V-shaped piezoelectric vibration energy harvester with stopper for low-frequency broadband and shock excitation. Sensors and Actuators, A: Physical 2021;317:112458. https://doi.org/10.1016/j.sna.2020.112458.

[123] Shu YC, Lien IC, Wu WJ. An improved analysis of the SSHI interface in piezoelectric energy harvesting. Smart Materials and Structures 2007;16:2253–64. https://doi.org/10.1088/0964-1726/16/6/028.

[124] Shu YC, Lien IC. Analysis of power output for piezoelectric energy harvesting systems. Smart Materials and Structures 2006;15:1499–512. https://doi.org/10.1088/0964-1726/15/6/001.

[125] Sayyaadi H, Rahnama F. On the energy harvesting via doubly curved piezoelectric panels. Journal of Intelligent Material Systems and Structures 2016;27:2692–706. https://doi.org/10.1177/1045389X16641206.

[126] Niiranen J, Balobanov V, Kiendl J, Hosseini S. Variational formulations, model comparisons and numerical methods for Euler–Bernoulli micro- and nano-beam

models. Mathematics and Mechanics of Solids 2019;24:312–35. https://doi.org/10.1177/1081286517739669.

[127] Banks HT, Inman DJ. On damping mechanisms in beams. Journal of Applied Mechanics, Transactions ASME 1991;58:716–23. https://doi.org/10.1115/1.2897253.

[128] Pradeesh EL, Udhayakumar S. Effect of placement of piezoelectric material and proof mass on the performance of piezoelectric energy harvester. Mechanical Systems and Signal Processing 2019;130:664–76. https://doi.org/10.1016/j.ymssp.2019.05.044.

[129] Wang L, Zhao L, Jiang Z, Luo G, Yang P, Han X, et al. High accuracy comsol simulation method of bimorph cantilever for piezoelectric vibration energy harvesting. AIP Advances 2019;9. https://doi.org/10.1063/1.5119328.

[130] Brusa E, Lemma L, Benasciutti D. Vibration analysis of a Sendzimir cold rolling mill and bearing fault detection. Proceedings of the Institution of Mechanical Engineers, Part C: Journal of Mechanical Engineering Science 2010;224:1645–54. https://doi.org/10.1243/09544062JMES1540.

[131] Brusa E. Development of a sentry smart bearing as a node for connectivity and monitoring of steelmaking system. 2017 IEEE International Symposium on Systems Engineering, ISSE 2017 - Proceedings, Institute of Electrical and Electronics Engineers Inc.; 2017. https://doi.org/10.1109/SysEng.2017.8088257.

[132] Kundu S, Nemade HB. Modeling and Simulation of a Piezoelectric Vibration Energy Harvester. Procedia Engineering, vol. 144, Elsevier Ltd; 2016, p. 568–75. https://doi.org/10.1016/j.proeng.2016.05.043.

[133] Muthalif AGA, Nordin NHD. Optimal piezoelectric beam shape for single and broadband vibration energy harvesting: Modeling, simulation and experimental results. Mechanical Systems and Signal Processing 2015;54:417–26. https://doi.org/10.1016/j.ymssp.2014.07.014.

[134] Erturk A, Tarazaga PA, Farmer JR, Inman DJ. Effect of strain nodes and electrode configuration on piezoelectric energy harvesting from cantilevered beams. Journal of Vibration and Acoustics, Transactions of the ASME 2009;131:0110101–01101011. https://doi.org/10.1115/1.2981094.

[135] Anton SR, Erturk A, Inman DJ. Bending strength of piezoelectric ceramics and single crystals for multifunctional load-bearing applications. IEEE Transactions on Ultrasonics, Ferroelectrics, and Frequency Control 2012;59:1085–92. https://doi.org/10.1109/TUFFC.2012.2299.

[136] de Marqui Junior C, Erturk A, Inman DJ. An electromechanical finite element model for piezoelectric energy harvester plates. Journal of Sound and Vibration 2009;327:9–25. https://doi.org/10.1016/j.jsv.2009.05.015.

[137] Kim S, Clark WW, Wang QM. Piezoelectric Energy Harvesting with a Clamped Circular Plate: Analysis: Http://DxDoiOrg/101177/1045389X05054044 2016;16:847–54. https://doi.org/10.1177/1045389X05054044.

[138] Kim S, Clark WW, Wang QM. Piezoelectric Energy Harvesting with a Clamped Circular Plate: Experimental Study: Http://DxDoiOrg/101177/1045389X05054043 2016;16:855–63. https://doi.org/10.1177/1045389X05054043.

[139] Arrieta AF, Hagedorn P, Erturk A, Inman DJ. A piezoelectric bistable plate for nonlinear broadband energy harvesting. Applied Physics Letters 2010;97:104102. https://doi.org/10.1063/1.3487780.

[140] Solovyev AN, Duong L v. Optimization for the Harvesting Structure of the Piezoelectric Bimorph Energy Harvesters Circular Plate by Reduced Order Finite Element Analysis. Https://DoiOrg/101142/S1758825116500290 2016;8. https://doi.org/10.1142/S1758825116500290.

[141] Rahmani Naeim Abadi M, Saidi AR, Askari Farsangi MA. Piezoelectric energy harvesting via thin annular sectorial plates: an analytical approach. Archive of Applied Mechanics 2021:1–18. https://doi.org/10.1007/s00419-021-01971-9.

[142] Darabi A, Shahab S, Leamy MJ, Erturk A. Bimorph disk piezoelectric energy harvester under base excitation: electroelastic modeling and experimental validation. Https://DoiOrg/101117/122085607 2015;9431:311–27. https://doi.org/10.1117/12.2085607.

[143] Paknejad A, Rahimi G, Salmani H. Analytical solution and numerical validation of piezoelectric energy harvester patch for various thin multilayer composite plates. Archive of Applied Mechanics 2018;88:1139–61. https://doi.org/10.1007/S00419-018-1363-0/FIGURES/14.

[144] Yoon H, Youn BD, Kim HS. Kirchhoff plate theory-based electromechanically-coupled analytical model considering inertia and stiffness effects of a surface-bonded piezoelectric patch 2016. https://doi.org/10.1088/0964-1726/25/2/025017.

[145] Shukla R, Pradyumna S. Energy harvesting in variable stiffness composite piezolaminated plates. Composite Structures 2021;267:113792. https://doi.org/10.1016/J.COMPSTRUCT.2021.113792.

[146] Shin DJ, Lim DH, Koo BK, Kim MS, Kim IS, Jeong SJ. Porous sandwich structures based on BaZrTiO3–BaCaTiO3 ceramics for piezoelectric energy harvesting. Journal of Alloys and Compounds 2020;831:154792. https://doi.org/10.1016/J.JALLCOM.2020.154792.

[147] Moradi-Dastjerdi R, Behdinan K. Dynamic performance of piezoelectric energy harvesters with a multifunctional nanocomposite substrate. Applied Energy 2021;293:116947. https://doi.org/10.1016/J.APENERGY.2021.116947.

[148] Askari M, Saidi AR, Rezaei AS. On natural frequencies of Levy-type thick porous-cellular plates surrounded by piezoelectric layers. Composite Structures 2017;179:340–54. https://doi.org/10.1016/j.compstruct.2017.07.073.

[149] Askari M, Saidi AR, Rezaei AS. An investigation over the effect of piezoelectricity and porosity distribution on natural frequencies of porous smart plates. Journal of Sandwich Structures and Materials 2020;22:2091–124. https://doi.org/10.1177/1099636218791092.

[150] Sadeghi Gughari M, Saidi AR, Rezaei AS, Askari M, Naderi A. Analytical buckling response of sectorial porous plates integrated with piezoelectric layers. Applied Mathematical Modelling 2022;101:811–31. https://doi.org/10.1016/J.APM.2021.09.019.

[151] Jabbari M, Farzaneh Joubaneh E, Mojahedin A. Thermal buckling analysis of porous circular plate with piezoelectric actuators based on first order shear deformation theory. International Journal of Mechanical Sciences 2014;83:57–64.

[152] Chen D, Yang J, Kitipornchai S. Elastic buckling and static bending of shear deformable functionally graded porous beam. Composite Structures 2015;133:54–61. https://doi.org/10.1016/J.COMPSTRUCT.2015.07.052.

[153] Chen D, Yang J, Kitipornchai S. Free and forced vibrations of shear deformable functionally graded porous beams. International Journal of Mechanical Sciences 2016;108–109:14–22. https://doi.org/10.1016/J.IJMECSCI.2016.01.025.

[154] Chen D, Kitipornchai S, Yang J. Nonlinear free vibration of shear deformable sandwich beam with a functionally graded porous core. Thin-Walled Structures 2016;107:39–48. https://doi.org/10.1016/J.TWS.2016.05.025.

[155] Wu H, Yang J, Kitipornchai S. Mechanical Analysis of Functionally Graded Porous Structures: A Review. Https://DoiOrg/101142/S0219455420410151 2020;20. https://doi.org/10.1142/S0219455420410151.

[156] Rezaei AS, Saidi AR. Application of Carrera Unified Formulation to study the effect of porosity on natural frequencies of thick porous–cellular plates. Composites Part B: Engineering 2016;91:361–70. https://doi.org/10.1016/J.COMPOSITESB.2015.12.050.

[157] Moradi-Dastjerdi R, Behdinan K. Free vibration response of smart sandwich plates with porous CNT-reinforced and piezoelectric layers. Applied Mathematical Modelling 2021;96:66–79. https://doi.org/10.1016/J.APM.2021.03.013.

[158] Roundy S, Wright PK. A piezoelectric vibration based generator for wireless electronics. Smart Materials and Structures 2004;13:1131. https://doi.org/10.1088/0964-1726/13/5/018.

[159] Hall JF. Problems encountered from the use (or misuse) of Rayleigh damping. Earthquake Engineering & Structural Dynamics 2006;35:525–45. https://doi.org/10.1002/EQE.541.

[160] Rouzegar J, Abad F. Free vibration analysis of FG plate with piezoelectric layers using four-variable refined plate theory. Thin-Walled Structures 2015;89:76–83. https://doi.org/10.1016/j.tws.2014.12.010.

[161] Askari M, Brusa E, Delprete C. On the vibration analysis of coupled transverse and shear piezoelectric functionally graded porous beams with higher-order theories. The Journal of Strain Analysis for Engineering Design 2021;56:29–49. https://doi.org/10.1177/0309324720922085.

[162] Reddy JN, Cheng ZQ. Three-Dimensional Solutions of Smart Functionally Graded Plates. Journal of Applied Mechanics 2001;68:234–41. https://doi.org/10.1115/1.1347994.

[163] Wang BL, Noda N. Design of a smart functionally graded thermopiezoelectric composite structure. Smart Materials and Structures 2001;10:189. https://doi.org/10.1088/0964-1726/10/2/303.

[164] Kiani Y, Rezaei M, Taheri S, Eslami MR. Thermo-electrical buckling of piezoelectric functionally graded material Timoshenko beams. International Journal of Mechanics and Materials in Design 2011;7:185–97. https://doi.org/10.1007/S10999-011-9158-2/TABLES/5.

[165] Askari Farsangi MA, Saidi AR, Batra RC. Analytical solution for free vibrations of moderately thick hybrid piezoelectric laminated plates. Journal of Sound and Vibration 2013;332:5981–98. https://doi.org/10.1016/j.jsv.2013.05.010.

[166] Wang YQ. Electro-mechanical vibration analysis of functionally graded piezoelectric porous plates in the translation state. Acta Astronautica 2018;143:263–71.

[167] Wu N, Wang Q, Quek ST. Free vibration analysis of piezoelectric coupled circular plate with open circuit. Journal of Sound and Vibration 2010;329:1126–36. https://doi.org/10.1016/J.JSV.2009.10.040.

[168] Pradhan KK, Chakraverty S. Free vibration of Euler and Timoshenko functionally graded beams by Rayleigh–Ritz method. Composites Part B: Engineering 2013;51:175–84. https://doi.org/10.1016/J.COMPOSITESB.2013.02.027.

[169] Aydogdu M, Taskin V. Free vibration analysis of functionally graded beams with simply supported edges. Materials & Design 2007;28:1651–6. https://doi.org/10.1016/J.MATDES.2006.02.007.

[170] Su H, Banerjee JR, Cheung CW. Dynamic stiffness formulation and free vibration analysis of functionally graded beams. Composite Structures 2013;106:854–62. https://doi.org/10.1016/J.COMPSTRUCT.2013.06.029.

[171] Askari M, Brusa E, Delprete C. On wave propagation and free vibration of piezoelectric sandwich plates with perfect and porous functionally graded substrates: Journal of Intelligent Material Systems and Structures 2022. https://doi.org/10.1177/1045389X211072195.

[172] Vashishth AK, Gupta V. Wave propagation in transversely isotropic porous piezoelectric materials. International Journal of Solids and Structures 2009;46:3620–32. https://doi.org/10.1016/j.ijsolstr.2009.06.011.

[173] Qian ZH, Jin F, Lu T, Kishimoto K. Transverse surface waves in functionally graded piezoelectric materials with exponential variation. Smart Materials and Structures 2008;17:065005. https://doi.org/10.1088/0964-1726/17/6/065005.

[174] Sun D, Luo SN. Wave propagation and transient response of functionally graded material circular plates under a point impact load. Composites Part B: Engineering 2011;42:657–65. https://doi.org/10.1016/j.compositesb.2011.02.020.

[175] Sun D, Luo SN. Wave propagation of functionally graded material plates in thermal environments. Ultrasonics 2011;51:940–52. https://doi.org/10.1016/j.ultras.2011.05.009.

[176] Sun D, Luo SN. Wave propagation and transient response of a functionally graded material plate under a point impact load in thermal environments. Applied Mathematical Modelling 2012;36:444–62. https://doi.org/10.1016/j.apm.2011.07.023.

[177] Ebrahimi F, Barati MR, Haghi P. Wave propagation analysis of size-dependent rotating inhomogeneous nanobeams based on nonlocal elasticity theory. Journal of Vibration and Control 2018;24:3809–18. https://doi.org/10.1177/1077546317711537.

[178] Faroughi S, Rahmani A, Friswell MI. On wave propagation in two-dimensional functionally graded porous rotating nano-beams using a general nonlocal higher-order beam model. Applied Mathematical Modelling 2020;80:169–90. https://doi.org/10.1016/j.apm.2019.11.040.

[179] Ebrahimi F, Seyfi A. Studying propagation of wave in metal foam cylindrical shells with graded porosities resting on variable elastic substrate. Engineering with Computers 2020;1:3. https://doi.org/10.1007/s00366-020-01069-w.

[180] Gao W, Qin Z, Chu F. Wave propagation in functionally graded porous plates reinforced with graphene platelets. Aerospace Science and Technology 2020;102:105860. https://doi.org/10.1016/j.ast.2020.105860.

[181] Li C, Han Q, Wang Z, Wu X. Analysis of wave propagation in functionally graded piezoelectric composite plates reinforced with graphene platelets. Applied Mathematical Modelling 2020;81:487–505. https://doi.org/10.1016/j.apm.2020.01.016.

[182] Aminipour H, Janghorban M, Civalek O. Analysis of functionally graded doubly-curved shells with different materials via higher order shear deformation theory. Composite Structures 2020;251:112645. https://doi.org/10.1016/j.compstruct.2020.112645.

[183] Ebrahimi F, Rastgoo A. Free vibration analysis of smart annular FGM plates integrated with piezoelectric layers. Smart Materials and Structures 2008;17:015044. https://doi.org/10.1088/0964-1726/17/1/015044.

[184] Baferani AH, Saidi AR, Jomehzadeh E. An exact solution for free vibration of thin functionally graded rectangular plates. Proceedings of the Institution of Mechanical Engineers, Part C: Journal of Mechanical Engineering Science 2011;225:526–36. https://doi.org/10.1243/09544062JMES2171.

[185] Zenkour AM. On vibration of functionally graded plates according to a refined trigonometric plate theory. International Journal of Structural Stability and Dynamics 2005;5:279–97. https://doi.org/10.1142/s0219455405001581.

[186] Tadi Beni Y. Size-dependent electromechanical bending, buckling, and free vibration analysis of functionally graded piezoelectric nanobeams. Journal of Intelligent Material Systems and Structures 2016;27:2199–215. https://doi.org/10.1177/1045389X15624798.

[187] Fu Y, Wang J, Mao Y. Nonlinear vibration and active control of functionally graded beams with piezoelectric sensors and actuators. Journal of Intelligent Material Systems and Structures 2011;22:2093–102. https://doi.org/10.1177/1045389X11425277.

[188] Jandaghian AA, Rahmani O. Size-dependent free vibration analysis of functionally graded piezoelectric plate subjected to thermo-electro-mechanical loading. Journal of Intelligent Material Systems and Structures 2017;28:3039–53. https://doi.org/10.1177/1045389X17704920.

[189] Vel SS, Batra RC. Three-dimensional exact solution for the vibration of functionally graded rectangular plates. Journal of Sound and Vibration 2004;272:703–30. https://doi.org/10.1016/S0022-460X(03)00412-7.

[190] Askari M, Brusa E, Delprete C. On the vibration analysis of coupled transverse and shear piezoelectric functionally graded porous beams with higher-order theories. The Journal of Strain Analysis for Engineering Design 2021;56:29–49. https://doi.org/10.1177/0309324720922085.

[191] Rezaei AS, Saidi AR, Abrishamdari M, Mohammadi MHP. Natural frequencies of functionally graded plates with porosities via a simple four variable plate theory: An analytical approach. Thin-Walled Structures 2017;120:366–77. https://doi.org/10.1016/j.tws.2017.08.003.

[192] Zhao J, Choe K, Xie F, Wang A, Shuai C, Wang Q. Three-dimensional exact solution for vibration analysis of thick functionally graded porous (FGP) rectangular plates with arbitrary boundary conditions. Composites Part B:

Engineering 2018;155:369–81. https://doi.org/10.1016/j.compositesb.2018.09.001.

[193] Shimpi RP. Refined plate theory and its variants. AIAA Journal 2002;40:137–46. https://doi.org/10.2514/2.1622.

[194] Touratier M. An efficient standard plate theory. International Journal of Engineering Science 1991;29:901–16. https://doi.org/10.1016/0020-7225(91)90165-Y.

[195] Reddy JN. Mechanics of laminated composite plates and shells: theory and analysis. CRC Press; 2003.

[196] Rahmat Talabi M, Saidi AR. An explicit exact analytical approach for free vibration of circular/annular functionally graded plates bonded to piezoelectric actuator/sensor layers based on Reddy's plate theory. Applied Mathematical Modelling 2013;37:7664–84. https://doi.org/10.1016/j.apm.2013.03.021.

[197] Achenbach JD. Wave propagation in elastic solids,. Elsevier; 1973.

[198] Gopalakrishnan S. Wave Propagation in Materials and Structures. CRC Press; 2016. https://doi.org/10.1201/9781315372099.

[199] Barati MR, Sadr MH, Zenkour AM. Buckling analysis of higher order graded smart piezoelectric plates with porosities resting on elastic foundation. International Journal of Mechanical Sciences 2016;117:309–20. https://doi.org/10.1016/j.ijmecsci.2016.09.012.

[200] Sayyaadi H, Rahnama F, Askari Farsangi MA. Energy harvesting via shallow cylindrical and spherical piezoelectric panels using higher order shear deformation theory. Composite Structures 2016;147:155–67. https://doi.org/10.1016/j.compstruct.2016.03.035.

[201] Shufrin I, Eisenberger M. Stability and vibration of shear deformable plates - First order and higher order analyses. International Journal of Solids and Structures 2005;42:1225–51. https://doi.org/10.1016/j.ijsolstr.2004.06.067.

[202] Timoshenko S, Young D. Elements of strength of materials. New York: Van Nostrand Reinhold; 1968.

[203] Askari, M., Brusa, E. and Delprete, C., 2020, March. Electromechanical vibration characteristics of porous bimorph and unimorph doubly curved panels. In Actuators (Vol. 9, No. 1, p. 7). Multidisciplinary Digital Publishing Institute.

[204] Sayyaadi, H. and Farsangi, M.A.A., 2014. An analytical solution for dynamic behavior of thick doubly curved functionally graded smart panels. Composite Structures, 107, pp.88-102.

[205] Brusa, E (2020) Design of a kinematic vibration energy harvester for a smart bearing with piezoelectric/magnetic coupling. Mechanics of Advanced Materials and Structures 27(15): 1322–1330.

[206] Brusa, E, Carabelli, S, Carraro, F, et al. (1998) Electromechanical tuning of self-sensing piezoelectric transducers. Journal of Intelligent Material Systems and Structures 9(3): 198–209.

[207] Brusa, E, Zelenika, S, Moro, L, et al. (2009) Analytical characterization and experimental validation of performances of piezoelectric vibration energy scavengers. In: Smart sensors, actuators, and MEMS IV, Dresden, Germany, 18 May 2009, vol. 7362, p.736204. International Society for Optics and Photonics.

[208] G. De Pasquale, E. Brusa, and A. Soma, Capacitive vibration energy harvesting with resonance tuning. Symposium on Design, Test, Integration and Packaging of MEMS/MOEMS, 2009. p. 280–285.

[209] M. Scapolan, M. G. Tehrani, and E. Bonisoli, Energy harvesting using parametric resonant system due to time-varying damping, Mech. Syst. Sig. Process., vol. 79, pp. 149–165, 2016. DOI: 10. 1016/j.ymssp.2016.02.037.

Appendix A

From Fig. 2.1(a), it is remembered that the width of the beam is b, the thickness of the substrate layer is h_s and the thickness of the piezoelectric layer is h_p. In Ref. [202], the procedure of finding the position of neutral axis is described in detail. In summary:

$$h_1 = \frac{h_p^2 + nh_s^2 + 2nh_p h_s}{2h_p + 2nh_s}$$
$$h_2 = \frac{h_p^2 + nh_s^2 + 2h_p h_s}{2h_p + 2nh_s} \tag{A.1}$$
$$h_3 = \frac{nh_s^2 + nh_p h_s}{2h_p + 2nh_s}$$
$$h_a = -h_2, \quad h_b = h_1 - h_p, \quad h_c = h_1, \quad h_z = h_3, \quad n = E^s/E^p$$

in which h_1, h_2 and h_3 are the distance from the top of the piezoelectric layer to the neutral axis, the distance from the bottom of the substrate layer to the neutral axis and the distance from the middle plane of the piezoelectric layer from the neutral axis.

Appendix B

The constant coefficients of Eq. (3.20) are given as:

$$\begin{Bmatrix} a_{11}^N \\ a_{12}^N \\ a_{66}^N \end{Bmatrix} = \int_{-h-h_p}^{-h} \begin{Bmatrix} \bar{C}_{11} \\ \bar{C}_{12} \\ C_{66} \end{Bmatrix} dz + \int_{-h}^{+h} \begin{Bmatrix} Q_{11} \\ Q_{12} \\ Q_{66} \end{Bmatrix} dz + \int_{+h}^{+h+h_p} \begin{Bmatrix} \bar{C}_{11} \\ \bar{C}_{12} \\ C_{66} \end{Bmatrix} dz$$

$$\begin{Bmatrix} b_{11}^N \\ b_{12}^N \\ b_{66}^N \end{Bmatrix} = \int_{-h-h_p}^{-h} (z - \alpha z^3) \begin{Bmatrix} \bar{C}_{11} \\ \bar{C}_{12} \\ C_{66} \end{Bmatrix} dz + \int_{-h}^{+h} (z - \alpha z^3) \begin{Bmatrix} Q_{11} \\ Q_{12} \\ Q_{66} \end{Bmatrix} dz + \int_{+h}^{+h+h_p} (z - \alpha z^3) \begin{Bmatrix} \bar{C}_{11} \\ \bar{C}_{12} \\ C_{66} \end{Bmatrix} dz$$

$$\begin{Bmatrix} f_{11}^N \\ f_{12}^N \\ f_{66}^N \end{Bmatrix} = -\int_{-h-h_p}^{-h} \alpha z^3 \begin{Bmatrix} \bar{C}_{11} \\ \bar{C}_{12} \\ 2C_{66} \end{Bmatrix} dz - \int_{-h}^{+h} \alpha z^3 \begin{Bmatrix} Q_{11} \\ Q_{12} \\ 2Q_{66} \end{Bmatrix} dz - \int_{+h}^{+h+h_p} \alpha z^3 \begin{Bmatrix} \bar{C}_{11} \\ \bar{C}_{12} \\ 2C_{66} \end{Bmatrix} dz$$

$$\begin{Bmatrix} a_{11}^M \\ a_{12}^M \\ a_{66}^M \end{Bmatrix} = \int_{-h-h_p}^{-h} z \begin{Bmatrix} \bar{C}_{11} \\ \bar{C}_{12} \\ C_{66} \end{Bmatrix} dz + \int_{-h}^{+h} z \begin{Bmatrix} Q_{11} \\ Q_{12} \\ Q_{66} \end{Bmatrix} dz + \int_{+h}^{+h+h_p} z \begin{Bmatrix} \bar{C}_{11} \\ \bar{C}_{12} \\ C_{66} \end{Bmatrix} dz$$

$$\begin{Bmatrix} b_{11}^M \\ b_{12}^M \\ b_{66}^M \end{Bmatrix} = \int_{-h-h_p}^{-h} (z^2 - \alpha z^4) \begin{Bmatrix} \bar{C}_{11} \\ \bar{C}_{12} \\ C_{66} \end{Bmatrix} dz + \int_{-h}^{+h} (z^2 - \alpha z^4) \begin{Bmatrix} Q_{11} \\ Q_{12} \\ Q_{66} \end{Bmatrix} dz + \int_{+h}^{+h+h_p} (z^2 - \alpha z^4) \begin{Bmatrix} \bar{C}_{11} \\ \bar{C}_{12} \\ C_{66} \end{Bmatrix} dz$$

$$\begin{Bmatrix} f_{11}^M \\ f_{12}^M \\ f_{66}^M \end{Bmatrix} = -\int_{-h-h_p}^{-h} \alpha z^4 \begin{Bmatrix} \bar{C}_{11} \\ \bar{C}_{12} \\ 2C_{66} \end{Bmatrix} dz - \int_{-h}^{+h} \alpha z^4 \begin{Bmatrix} Q_{11} \\ Q_{12} \\ 2Q_{66} \end{Bmatrix} dz - \int_{+h}^{+h+h_p} \alpha z^4 \begin{Bmatrix} \bar{C}_{11} \\ \bar{C}_{12} \\ 2C_{66} \end{Bmatrix} dz$$

$$\begin{Bmatrix} a_{11}^P \\ a_{12}^P \\ a_{66}^P \end{Bmatrix} = \int_{-h-h_p}^{-h} z^3 \begin{Bmatrix} \bar{C}_{11} \\ \bar{C}_{12} \\ C_{66} \end{Bmatrix} dz + \int_{-h}^{+h} z^3 \begin{Bmatrix} Q_{11} \\ Q_{12} \\ Q_{66} \end{Bmatrix} dz + \int_{+h}^{+h+h_p} z^3 \begin{Bmatrix} \bar{C}_{11} \\ \bar{C}_{12} \\ C_{66} \end{Bmatrix} dz$$

$$\begin{Bmatrix} b_{11}^P \\ b_{12}^P \\ b_{66}^P \end{Bmatrix} = \int_{-h-h_p}^{-h} (z^4 - \alpha z^6) \begin{Bmatrix} \bar{C}_{11} \\ \bar{C}_{12} \\ C_{66} \end{Bmatrix} dz + \int_{-h}^{+h} (z^4 - \alpha z^6) \begin{Bmatrix} Q_{11} \\ Q_{12} \\ Q_{66} \end{Bmatrix} dz + \int_{+h}^{+h+h_p} (z^4 - \alpha z^6) \begin{Bmatrix} \bar{C}_{11} \\ \bar{C}_{12} \\ C_{66} \end{Bmatrix} dz$$

$$\begin{Bmatrix} f_{11}^P \\ f_{12}^P \\ f_{66}^P \end{Bmatrix} = -\int_{-h-h_p}^{-h} \alpha z^6 \begin{Bmatrix} \bar{C}_{11} \\ \bar{C}_{12} \\ 2C_{66} \end{Bmatrix} dz - \int_{-h}^{+h} \alpha z^6 \begin{Bmatrix} Q_{11} \\ Q_{12} \\ 2Q_{66} \end{Bmatrix} dz - \int_{+h}^{+h+h_p} \alpha z^6 \begin{Bmatrix} \bar{C}_{11} \\ \bar{C}_{12} \\ 2C_{66} \end{Bmatrix} dz$$

$$\begin{Bmatrix} a_{55}^{Q} \\ a_{55}^{R} \end{Bmatrix} = \int_{-h-h_p}^{-h} C_{55}{K_s}^2(1-3\alpha z^2)\begin{Bmatrix} 1 \\ z^2 \end{Bmatrix} dz + \int_{-h}^{+h} Q_{55}{K_s}^2(1-3\alpha z^2)\begin{Bmatrix} 1 \\ z^2 \end{Bmatrix} dz + \int_{+h}^{+h+h_p} C_{55}{K_s}^2(1-3\alpha z^2)\begin{Bmatrix} 1 \\ z^2 \end{Bmatrix} dz \tag{B.1}$$

Also, the coefficients α_N, α_M and α_P are given below for both parallel and series connections:

For parallel:

$$\{\alpha_N, \alpha_M, \alpha_P\} = -\int_{-h-h_p}^{-h} \left(\frac{\bar{e}_{31}}{h_p}\right)\{1, z, z^3\}\, dz + \int_{+h}^{+h+h_p} \left(\frac{\bar{e}_{31}}{h_p}\right)\{1, z, z^3\} dz \tag{B.2}$$

For series:

$$\{\alpha_N, \alpha_M, \alpha_P\} = +\int_{-h-h_p}^{-h} \left(\frac{\bar{e}_{31}}{2h_p}\right)\{1, z, z^3\}\, dz + \int_{+h}^{+h+h_p} \left(\frac{\bar{e}_{31}}{2h_p}\right)\{1, z, z^3\} dz \tag{B.3}$$

The coefficients X_{mn}^{i} and s_{mn}^{i} ($i = u_0, v_0, \psi_x, \psi_y, w_0$) in Eq. (27) are given in Eqs. (A.4) to (A.6) for both cases of FSDT and TSDT:

$$\begin{aligned} \left\{X_{mn}^{u_0}, X_{mn}^{v_0}\right\} &= \alpha_N C_{mn}\left\{\frac{1}{\beta_n}, \frac{1}{\beta_m}\right\} \\ \left\{s_{mn}^{u_0}, s_{mn}^{v_0}\right\} &= -\bar{e}_{31} C_{mn}\left\{\frac{1}{\beta_n}, \frac{1}{\beta_m}\right\} \end{aligned} \tag{B.4}$$

For FSDT case:

$$\left\{X_{mn}^{\psi_x}, X_{mn}^{\psi_y}\right\} = \alpha_M C_{mn} \left\{\frac{1}{\beta_n}, \frac{1}{\beta_m}\right\}$$
$$\left\{s_{mn}^{\psi_x}, s_{mn}^{\psi_y}\right\} = -\bar{e}_{31}\hat{h} C_{mn} \left\{\frac{1}{\beta_n}, \frac{1}{\beta_m}\right\}$$
$$X_{mn}^{w_0} = s_{mn}^{w_0} = 0 \tag{B.5}$$

For TSDT case:

$$\left\{X_{mn}^{\psi_x}, X_{mn}^{\psi_y}\right\} = (\alpha_M - \alpha\alpha_P) C_{mn} \left\{\frac{1}{\beta_n}, \frac{1}{\beta_m}\right\}$$
$$\left\{s_{mn}^{\psi_x}, s_{mn}^{\psi_y}\right\} = -\bar{e}_{31}(\hat{h} - \alpha\tilde{h}) C_{mn} \left\{\frac{1}{\beta_n}, \frac{1}{\beta_m}\right\}$$
$$X_{mn}^{w_0} = \frac{\alpha\alpha_P(\beta_m^2 + \beta_n^2) C_{mn}}{\beta_m\beta_n}, \qquad s_{mn}^{w_0} = -\frac{\alpha\bar{e}_{31}\tilde{h}(\beta_m^2 + \beta_n^2) C_{mn}}{\beta_m\beta_n} \tag{B.6}$$

On the other hand, the components of the stiffness matrix $[K]$ and mass matrix $[M]$ in Eq. (27) are given as:

$$K_{11} = -a_{11}^N \beta_m^2 - a_{66}^N \beta_n^2$$
$$K_{12} = -(a_{12}^N + a_{66}^N)\beta_m\beta_n$$
$$K_{13} = -b_{11}^N \beta_m^2 - b_{66}^N \beta_n^2$$
$$K_{14} = -(b_{12}^N + b_{66}^N)\beta_m\beta_n$$
$$K_{15} = -f_{11}^N \beta_m^3 - (f_{12}^N + f_{66}^N)\beta_m\beta_n^2$$
$$K_{21} = -(a_{12}^N + a_{66}^N)\beta_m\beta_n$$
$$K_{22} = -a_{66}^N \beta_m^2 - a_{11}^N \beta_n^2$$
$$K_{23} = -(b_{12}^N + b_{66}^N)\beta_m\beta_n$$
$$K_{24} = -b_{66}^N \beta_m^2 - b_{11}^N \beta_n^2$$
$$K_{25} = -f_{11}^N \beta_n^3 - (f_{12}^N + f_{66}^N)\beta_n\beta_m^2$$
$$K_{31} = -(a_{11}^M - \alpha a_{11}^P)\beta_m^2 - (a_{66}^M - \alpha a_{66}^P)\beta_n^2$$
$$K_{32} = -(a_{12}^M + a_{66}^M - \alpha a_{12}^P - \alpha a_{66}^P)\beta_m\beta_n$$
$$K_{33} = \left(-a_{55}^Q + 3\alpha a_{55}^R\right) - (b_{11}^M - \alpha b_{11}^P)\beta_m^2 - (b_{66}^M - \alpha b_{66}^P)\beta_n^2$$
$$K_{34} = -(b_{12}^M + b_{66}^M - \alpha b_{12}^P - \alpha b_{66}^P)\beta_m\beta_n$$

$$
\begin{aligned}
K_{35} &= \left(-a_{55}^{Q} + 3\alpha a_{55}^{R}\right)\beta_m - (f_{11}^{M} - \alpha f_{11}^{P})\beta_m^3 \\
&\quad - (f_{12}^{M} + f_{66}^{M} - \alpha f_{12}^{P} - \alpha f_{66}^{P})\beta_m\beta_n^2 \\
K_{41} &= -(a_{12}^{M} + a_{66}^{M} - \alpha a_{12}^{P} - \alpha a_{66}^{P})\beta_m\beta_n \\
K_{42} &= -(a_{66}^{M} - \alpha a_{66}^{P})\beta_m^2 - (a_{11}^{M} - \alpha a_{11}^{P})\beta_n^2 \\
K_{43} &= -(b_{12}^{M} + b_{66}^{M} - \alpha b_{12}^{P} - \alpha b_{66}^{P})\beta_m\beta_n \\
K_{44} &= \left(-a_{55}^{Q} + 3\alpha a_{55}^{R}\right) - (b_{66}^{M} - \alpha b_{66}^{P})\beta_m^2 - (b_{11}^{M} - \alpha b_{11}^{P})\beta_n^2 \\
K_{45} &= \left(-a_{55}^{Q} + 3\alpha a_{55}^{R}\right)\beta_n - (f_{11}^{M} - \alpha f_{11}^{P})\beta_n^3 \\
&\quad - (f_{12}^{M} + f_{66}^{M} - \alpha f_{12}^{P} - \alpha f_{66}^{P})\beta_n\beta_m^2 \\
K_{51} &= \alpha a_{11}^{P}\beta_m^3 + (2\alpha a_{66}^{P} + \alpha a_{12}^{P})\beta_m\beta_n^2 \\
K_{52} &= \alpha a_{11}^{P}\beta_n^3 + (2\alpha a_{66}^{P} + \alpha a_{12}^{P})\beta_n\beta_m^2 \\
K_{53} &= -\left(a_{66}^{Q} - 3\alpha a_{55}^{R}\right)\beta_m + \alpha b_{11}^{P}\beta_m^3 + (2\alpha b_{66}^{P} + \alpha b_{12}^{P})\beta_m\beta_n^2 \\
K_{54} &= -\left(a_{66}^{Q} - 3\alpha a_{55}^{R}\right)\beta_n + \alpha b_{11}^{P}\beta_n^3 + (2\alpha b_{66}^{P} + \alpha b_{12}^{P})\beta_n\beta_m^2 \\
K_{55} &= -\left(a_{55}^{Q} - 3\alpha a_{55}^{R}\right)\beta_m^2 - \left(a_{55}^{Q} - 3\alpha a_{55}^{R}\right)\beta_n^2 + \alpha f_{11}^{P}\beta_m^4 \\
&\quad + (\alpha f_{12}^{P} + 2\alpha f_{66}^{P} + \alpha f_{12}^{P})\beta_m^2\beta_n^2 + \alpha f_{11}^{P}\beta_n^4
\end{aligned}
\tag{B.7}
$$

And:

$$
\begin{aligned}
M_{11} &= -I_0 \\
M_{12} &= 0 \\
M_{13} &= -J_1 \\
M_{14} &= 0 \\
M_{15} &= \alpha I_3\beta_m \\
M_{21} &= 0 \\
M_{22} &= -I_0 \\
M_{23} &= 0 \\
M_{24} &= -J_1 \\
M_{25} &= \alpha I_3\beta_n \\
M_{31} &= -J_1 \\
M_{32} &= 0
\end{aligned}
$$

$$
\begin{aligned}
M_{33} &= -K_1 \\
M_{34} &= 0 \\
M_{35} &= \alpha J_4 \beta_m \\
M_{41} &= 0 \\
M_{42} &= -J_1 \\
M_{43} &= 0 \\
M_{44} &= -K_1 \\
M_{45} &= \alpha J_4 \beta_n \\
M_{51} &= \alpha I_3 \beta_m \\
M_{52} &= \alpha I_3 \beta_n \\
M_{53} &= \alpha J_4 \beta_m \\
M_{54} &= \alpha J_4 \beta_n \\
M_{55} &= -I_0 - \alpha^2 I_6 (\beta_m^2 + \beta_n^2)
\end{aligned} \tag{B.8}
$$

The coefficients Y_{mn}^{i} $(i = 1,2,3,4,5)$ in Eq. (33) are given as:

$$
\begin{aligned}
Y_{mn}^{1} &= B_{11} X_{mn}^{u_0} + B_{12} X_{mn}^{v_0} + B_{13} X_{mn}^{\psi_x} + B_{14} X_{mn}^{\psi_y} + B_{15} X_{mn}^{w_0} \\
Y_{mn}^{2} &= B_{21} X_{mn}^{u_0} + B_{22} X_{mn}^{v_0} + B_{23} X_{mn}^{\psi_x} + B_{24} X_{mn}^{\psi_y} + B_{25} X_{mn}^{w_0} \\
Y_{mn}^{3} &= B_{31} X_{mn}^{u_0} + B_{32} X_{mn}^{v_0} + B_{33} X_{mn}^{\psi_x} + B_{34} X_{mn}^{\psi_y} + B_{35} X_{mn}^{w_0} \\
Y_{mn}^{4} &= B_{41} X_{mn}^{u_0} + B_{42} X_{mn}^{v_0} + B_{43} X_{mn}^{\psi_x} + B_{44} X_{mn}^{\psi_y} + B_{45} X_{mn}^{w_0} \\
Y_{mn}^{5} &= B_{51} X_{mn}^{u_0} + B_{52} X_{mn}^{v_0} + B_{53} X_{mn}^{\psi_x} + B_{54} X_{mn}^{\psi_y} + B_{55} X_{mn}^{w_0}
\end{aligned} \tag{B.9}
$$

Appendix C

The coefficients a_i^{pq} $(i = 1, 2, \dots, 13)$, β_i^{pq} $(i = 1, 2, \dots, 4)$, and μ_i^{pq} $(i = 1, 2, \dots, 4)$ in transverse (or d_{31}) mode are defined as:

In the SC electrical condition:

$$\begin{pmatrix} a_1^{31} \\ a_4^{31} \\ a_7^{31} \end{pmatrix} = \int_{-t_c-t_p}^{-t_c} \begin{pmatrix} 1 \\ z \\ f(z) \end{pmatrix} C_{11}\, dz + \int_{-t_c}^{+t_c} \begin{pmatrix} 1 \\ z \\ f(z) \end{pmatrix} Q_{11}\, dz + \int_{+t_c}^{+t_c+t_p} \begin{pmatrix} 1 \\ z \\ f(z) \end{pmatrix} C_{11}\, dz$$

$$\begin{pmatrix} a_2^{31} \\ a_5^{31} \\ a_8^{31} \end{pmatrix} = -\int_{-t_c-t_p}^{-t_c} \begin{pmatrix} 1 \\ z \\ f(z) \end{pmatrix} zC_{11}\, dz - \int_{-t_c}^{+t_c} \begin{pmatrix} 1 \\ z \\ f(z) \end{pmatrix} zQ_{11}\, dz - \int_{+t_c}^{+t_c+t_p} \begin{pmatrix} 1 \\ z \\ f(z) \end{pmatrix} zC_{11}\, dz$$

$$\begin{pmatrix} a_3^{31} \\ a_6^{31} \\ a_9^{31} \end{pmatrix} = \int_{-t_c-t_p}^{-t_c} \begin{pmatrix} 1 \\ z \\ f(z) \end{pmatrix} f(z)C_{11}\, dz + \int_{-t_c}^{+t_c} \begin{pmatrix} 1 \\ z \\ f(z) \end{pmatrix} f(z)Q_{11}\, dz + \int_{+t_c}^{+t_c+t_p} \begin{pmatrix} 1 \\ z \\ f(z) \end{pmatrix} f(z)C_{11}\, dz$$

$$a_{10}^{31} = \int_{-t_c-t_p}^{-t_c} [f'(z)]^2 C_{55}\, dz + \int_{-t_c}^{+t_c} [f'(z)]^2 Q_{55}\, dz + \int_{+t_c}^{+t_c+t_p} [f'(z)]^2 C_{55}\, dz$$

$$\begin{pmatrix} a_{11}^{31} \\ a_{12}^{31} \\ a_{13}^{31} \end{pmatrix} = \begin{pmatrix} 0 \\ 0 \\ 0 \end{pmatrix}$$

$$\begin{pmatrix} \mu_1^{31} \\ \mu_2^{31} \\ \mu_3^{31} \end{pmatrix} = \int_{-t_c-t_p}^{-t_c} \begin{pmatrix} 1 \\ z \\ f(z) \end{pmatrix} \frac{4e_{31}}{t_p} \left[\frac{-2z - 2t_c - t_p}{t_p} \right] dz - \int_{+t_c}^{+t_c+t_p} \begin{pmatrix} 1 \\ z \\ f(z) \end{pmatrix} \frac{4e_{31}}{t_p} \left[\frac{2z - 2t_c - t_p}{t_p} \right] dz$$

$$\mu_4^{31} = 0$$

$$\mu_5^{31} = \int_{-t_c-t_p}^{-t_c} \frac{8\Xi_{33}}{(t_p)^2} dz + \int_{+t_c}^{+t_c+t_p} \frac{8\Xi_{33}}{(t_p)^2} dz$$

$$\begin{pmatrix} \beta_1^{31} \\ \beta_2^{31} \\ \beta_3^{31} \end{pmatrix} = \begin{pmatrix} 0 \\ 0 \\ 0 \end{pmatrix}$$

$$\beta_4^{31} = \int_{-t_c-t_p}^{-t_c} f'(z)\, e_{15} \left[1 - \left(\frac{-2z - 2t_c - t_p}{t_p} \right)^2 \right] dz + \int_{+t_c}^{+t_c+t_p} f'(z)\, e_{15} \left[1 - \left(\frac{2z - 2t_c - t_p}{t_p} \right)^2 \right] dz$$

$$\beta_5^{31} = -\int_{-t_c-t_p}^{-t_c} \Xi_{11} \left[1 - \left(\frac{-2z - 2t_c - t_p}{t_p} \right)^2 \right] dz - \int_{+t_c}^{+t_c+t_p} \Xi_{11} \left[1 - \left(\frac{2z - 2t_c - t_p}{t_p} \right)^2 \right] dz$$

$$\begin{pmatrix} b_1^{31} \\ b_3^{31} \\ b_4^{31} \\ b_5^{31} \\ b_6^{31} \\ b_8^{31} \\ b_9^{31} \end{pmatrix} = \begin{pmatrix} 0 \\ 0 \\ 0 \\ 0 \\ 0 \\ 0 \\ 0 \end{pmatrix}$$

$$b_2^{31} = \int_{-t_c-t_p}^{-t_c} f'(z)(e_{31}+e_{15})\,dz + \int_{+t_c}^{+t_c+t_p} f'(z)(e_{31}+e_{15})\,dz$$

$$b_7^{31} = -\int_{-t_c-t_p}^{-t_c} e_{31}\,dz - \int_{+t_c}^{+t_c+t_p} e_{31}\,dz \tag{C.1}$$

In the OC electrical condition:

$$\begin{pmatrix} a_1^{31} \\ a_4^{31} \\ a_7^{31} \end{pmatrix} = \int_{-t_c-t_p}^{-t_c} \begin{pmatrix} 1 \\ z \\ f(z) \end{pmatrix} \left[C_{11} + \frac{{e_{31}}^2}{\Xi_{33}} \right] dz + \int_{-t_c}^{+t_c} \begin{pmatrix} 1 \\ z \\ f(z) \end{pmatrix} Q_{11}\,dz + \int_{+t_c}^{+t_c+t_p} \begin{pmatrix} 1 \\ z \\ f(z) \end{pmatrix} \left[C_{11} + \frac{{e_{31}}^2}{\Xi_{33}} \right] dz$$

$$\begin{pmatrix} a_2^{31} \\ a_5^{31} \\ a_8^{31} \end{pmatrix} = \int_{-t_c-t_p}^{-t_c} \begin{pmatrix} 1 \\ z \\ f(z) \end{pmatrix} \left[-zC_{11} + \frac{(t_c+t_p){e_{31}}^2}{\Xi_{33}} \right] dz - \int_{-t_c}^{+t_c} \begin{pmatrix} 1 \\ z \\ f(z) \end{pmatrix} zQ_{11}\,dz + \int_{+t_c}^{+t_c+t_p} \begin{pmatrix} 1 \\ z \\ f(z) \end{pmatrix} \left[-zC_{11} + \frac{(t_c+t_p){e_{31}}^2}{\Xi_{33}} \right] dz$$

$$\begin{pmatrix} a_3^{31} \\ a_6^{31} \\ a_9^{31} \end{pmatrix} = \int_{-t_c-t_p}^{-t_c} \begin{pmatrix} 1 \\ z \\ f(z) \end{pmatrix} \left[f(z)C_{11} + \frac{\eta_2 {e_{31}}^2}{\Xi_{33}} \right] dz + \int_{-t_c}^{+t_c} \begin{pmatrix} 1 \\ z \\ f(z) \end{pmatrix} f(z)Q_{11}\,dz + \int_{+t_c}^{+t_c+t_p} \begin{pmatrix} 1 \\ z \\ f(z) \end{pmatrix} \left[f(z)C_{11} + \frac{\eta_1 {e_{31}}^2}{\Xi_{33}} \right] dz$$

$$a_{10}^{31} = \int_{-t_c-t_p}^{-t_c} [f'(z)]^2 C_{55}\,dz + \int_{-t_c}^{+t_c} [f'(z)]^2 Q_{55}\,dz + \int_{+t_c}^{+t_c+t_p} [f'(z)]^2 C_{55}\,dz$$

$$\begin{pmatrix} a_{11}^{31} \\ a_{12}^{31} \\ a_{13}^{31} \end{pmatrix} = \int_{-t_c-t_p}^{-t_c} \begin{pmatrix} \eta_2 \\ 1 \\ t_c+t_p \end{pmatrix} \frac{f'(z)e_{15}e_{31}(z+t_c)}{\Xi_{33}}\,dz + \int_{+t_c}^{+t_c+t_p} \begin{pmatrix} \eta_1 \\ 1 \\ t_c+t_p \end{pmatrix} \frac{f'(z)e_{15}e_{31}(z-t_c)}{\Xi_{33}}\,dz$$

$$\begin{pmatrix}\mu_1^{31}\\ \mu_2^{31}\\ \mu_3^{31}\end{pmatrix} = -\int_{-t_c-t_p}^{-t_c}\begin{pmatrix}1\\ z\\ f(z)\end{pmatrix}\frac{8e_{31}}{t_p}\left(z+t_c+t_p\right)dz - \int_{+t_c}^{+t_c+t_p}\begin{pmatrix}1\\ z\\ f(z)\end{pmatrix}\frac{8e_{31}}{t_p}\left(z-t_c-t_p\right)dz$$

$$\mu_4^{31} = 0$$

$$\mu_5^{31} = \int_{-t_c-t_p}^{-t_c}\frac{8\Xi_{33}}{\left(t_p\right)^2}dz + \int_{+t_c}^{+t_c+t_p}\frac{8\Xi_{33}}{\left(t_p\right)^2}dz$$

$$\begin{pmatrix}\beta_1^{31}\\ \beta_2^{31}\\ \beta_3^{31}\end{pmatrix} = \begin{pmatrix}0\\ 0\\ 0\end{pmatrix}$$

$$\beta_4^{31} = \int_{-t_c-t_p}^{-t_c} f'(z)\, e_{15}\left[1-\left(\frac{-2z-2t_c-t_p}{t_p}\right)^2 - \frac{4(z+t_c)}{t_p}\right]dz + \int_{+t_c}^{+t_c+t_p} f'(z)\, e_{15}\left[1-\left(\frac{2z-2t_c-t_p}{t_p}\right)^2 + \frac{4(z-t_c)}{t_p}\right]dz$$

$$\beta_5^{31} = -\int_{-t_c-t_p}^{-t_c}\Xi_{11}\left[1-\left(\frac{-2z-2t_c-t_p}{t_p}\right)^2 - \frac{4(z+t_c)}{t_p}\right]dz - \int_{+t_c}^{+t_c+t_p}\Xi_{11}\left[1-\left(\frac{2z-2t_c-t_p}{t_p}\right)^2 + \frac{4(z-t_c)}{t_p}\right]dz$$

$$\begin{pmatrix}b_1^{31}\\ b_3^{31}\\ b_5^{31}\\ b_8^{31}\end{pmatrix} = \begin{pmatrix}0\\ 0\\ 0\\ 0\end{pmatrix}$$

$$b_2^{31} = \int_{-t_c-t_p}^{-t_c} f'(z)(e_{31}+e_{15})\,dz + \int_{+t_c}^{+t_c+t_p} f'(z)(e_{31}+e_{15})\,dz$$

$$\begin{pmatrix}b_4^{31}\\ b_6^{31}\\ b_9^{31}\end{pmatrix} = -\int_{-t_c-t_p}^{-t_c}\begin{pmatrix}\eta_2\\ 1\\ t_c+t_p\end{pmatrix}\frac{\Xi_{11}e_{31}(z+t_c)}{\Xi_{33}}dz - \int_{+t_c}^{+t_c+t_p}\begin{pmatrix}\eta_1\\ 1\\ -t_c-t_p\end{pmatrix}\frac{\Xi_{11}e_{31}(z-t_c)}{\Xi_{33}}dz$$

$$b_7^{31} = -\int_{-t_c-t_p}^{-t_c} e_{31}\,dz - \int_{+t_c}^{+t_c+t_p} e_{31}\,dz \tag{C.2}$$

The coefficients a_i^{pq} $(i = 1, 2, \dots, 13)$, β_i^{pq} $(i = 1, 2, \dots, 4)$, and μ_i^{pq} $(i = 1, 2, \dots, 4)$ in Shear (d_{15}) Mode are defined as

In the SC electrical condition:

$$\begin{pmatrix} a_1^{15} \\ a_4^{15} \\ a_7^{15} \end{pmatrix} = \int_{-t_c-t_p}^{-t_c} \begin{pmatrix} 1 \\ z \\ f(z) \end{pmatrix} C_{33}\,dz + \int_{-t_c}^{+t_c} \begin{pmatrix} 1 \\ z \\ f(z) \end{pmatrix} Q_{11}\,dz + \int_{+t_c}^{+t_c+t_p} \begin{pmatrix} 1 \\ z \\ f(z) \end{pmatrix} C_{33}\,dz$$

$$\begin{pmatrix} a_2^{15} \\ a_5^{15} \\ a_8^{15} \end{pmatrix} = -\int_{-t_c-t_p}^{-t_c} \begin{pmatrix} 1 \\ z \\ f(z) \end{pmatrix} zC_{33}\,dz - \int_{-t_c}^{+t_c} \begin{pmatrix} 1 \\ z \\ f(z) \end{pmatrix} zQ_{11}\,dz - \int_{+t_c}^{+t_c+t_p} \begin{pmatrix} 1 \\ z \\ f(z) \end{pmatrix} zC_{33}\,dz$$

$$\begin{pmatrix} a_3^{15} \\ a_6^{15} \\ a_9^{15} \end{pmatrix} = \int_{-t_c-t_p}^{-t_c} \begin{pmatrix} 1 \\ z \\ f(z) \end{pmatrix} f(z)C_{33}\,dz + \int_{-t_c}^{+t_c} \begin{pmatrix} 1 \\ z \\ f(z) \end{pmatrix} f(z)Q_{11}\,dz + \int_{+t_c}^{+t_c+t_p} \begin{pmatrix} 1 \\ z \\ f(z) \end{pmatrix} f(z)C_{33}\,dz$$

$$a_{10}^{15} = \int_{-t_c-t_p}^{-t_c} [f'(z)]^2 C_{55}\,dz + \int_{-t_c}^{+t_c} [f'(z)]^2 Q_{55}\,dz + \int_{+t_c}^{+t_c+t_p} [f'(z)]^2 C_{55}\,dz$$

$$\begin{pmatrix} a_{11}^{15} \\ a_{12}^{15} \\ a_{13}^{15} \end{pmatrix} = \begin{pmatrix} 0 \\ 0 \\ 0 \end{pmatrix}$$

$$\begin{pmatrix} \mu_1^{15} \\ \mu_2^{15} \\ \mu_3^{15} \end{pmatrix} = \begin{pmatrix} 0 \\ 0 \\ 0 \end{pmatrix}$$

$$\mu_4^{15} = \int_{-t_c-t_p}^{-t_c} \frac{4e_{15}f'(z)}{t_p}\left[\frac{-2z-2t_c-t_p}{t_p}\right]dz - \int_{+t_c}^{+t_c+t_p} \frac{4e_{15}f'(z)}{t_p}\left[\frac{2z-2t_c-t_p}{t_p}\right]dz$$

$$\mu_5^{15} = \int_{-t_c-t_p}^{-t_c} \frac{8\Xi_{11}}{(t_p)^2}dz + \int_{+t_c}^{+t_c+t_p} \frac{8\Xi_{11}}{(t_p)^2}dz$$

$$\begin{pmatrix}\beta_1^{15}\\ \beta_2^{15}\\ \beta_3^{15}\end{pmatrix} = \int_{-t_c-t_p}^{-t_c} \begin{pmatrix}1\\ z\\ f(z)\end{pmatrix} e_{33}\left[1-\left(\frac{-2z-2t_c-t_p}{t_p}\right)^2\right]dz + \int_{+t_c}^{+t_c+t_p} \begin{pmatrix}1\\ z\\ f(z)\end{pmatrix} e_{33}\left[1-\left(\frac{2z-2t_c-t_p}{t_p}\right)^2\right]dz$$

$$\beta_4^{15} = 0$$

$$\beta_5^{15} = -\int_{-t_c-t_p}^{-t_c} \Xi_{33}\left[1-\left(\frac{-2z-2t_c-t_p}{t_p}\right)^2\right]dz - \int_{+t_c}^{+t_c+t_p} \Xi_{33}\left[1-\left(\frac{2z-2t_c-t_p}{t_p}\right)^2\right]dz$$

$$\begin{pmatrix}b_2^{15}\\ b_4^{15}\\ b_6^{15}\\ b_7^{15}\\ b_9^{15}\end{pmatrix} = \begin{pmatrix}0\\ 0\\ 0\\ 0\\ 0\end{pmatrix}$$

$$b_1^{15} = \int_{-t_c-t_p}^{-t_c} e_{15}f''(z)\,dz + \int_{+t_c}^{+t_c+t_p} e_{15}f''(z)\,dz$$

$$b_3^{15} = \int_{-t_c-t_p}^{-t_c} e_{33}f(z)\,dz + \int_{+t_c}^{+t_c+t_p} e_{33}f(z)\,dz$$

$$b_5^{15} = \int_{-t_c-t_p}^{-t_c} e_{33}\,dz + \int_{+t_c}^{+t_c+t_p} e_{33}\,dz$$

$$b_8^{15} = -\int_{-t_c-t_p}^{-t_c} ze_{31}\,dz - \int_{+t_c}^{+t_c+t_p} ze_{31}\,dz \qquad \text{(C.3)}$$

In the OC electrical condition:

$$\begin{pmatrix} a_1^{15} \\ a_4^{15} \\ a_7^{15} \end{pmatrix} = \int_{-t_c-t_p}^{-t_c} \begin{pmatrix} 1 \\ z \\ f(z) \end{pmatrix} C_{33}\, dz + \int_{-t_c}^{+t_c} \begin{pmatrix} 1 \\ z \\ f(z) \end{pmatrix} Q_{11}\, dz + \int_{+t_c}^{+t_c+t_p} \begin{pmatrix} 1 \\ z \\ f(z) \end{pmatrix} C_{33}\, dz$$

$$\begin{pmatrix} a_2^{15} \\ a_5^{15} \\ a_8^{15} \end{pmatrix} = -\int_{-t_c-t_p}^{-t_c} \begin{pmatrix} 1 \\ z \\ f(z) \end{pmatrix} zC_{33}\, dz - \int_{-t_c}^{+t_c} \begin{pmatrix} 1 \\ z \\ f(z) \end{pmatrix} zQ_{11}\, dz - \int_{+t_c}^{+t_c+t_p} \begin{pmatrix} 1 \\ z \\ f(z) \end{pmatrix} zC_{33}\, dz$$

$$\begin{pmatrix} a_3^{15} \\ a_6^{15} \\ a_9^{15} \end{pmatrix} = \int_{-t_c-t_p}^{-t_c} \begin{pmatrix} 1 \\ z \\ f(z) \end{pmatrix} \left[C_{33} f(z) + \frac{e_{15} e_{33} \zeta_2 (z + t_c)}{\Xi_{11}} \right] dz + \int_{-t_c}^{+t_c} \begin{pmatrix} 1 \\ z \\ f(z) \end{pmatrix} f(z) Q_{11}\, dz + \int_{+t_c}^{+t_c+t_p} \begin{pmatrix} 1 \\ z \\ f(z) \end{pmatrix} \left[C_{33} f(z) + \frac{e_{15} e_{33} \zeta_1 (z - t_c)}{\Xi_{11}} \right] dz$$

$$a_{10}^{15} = \int_{-t_c-t_p}^{-t_c} \left(C_{55} [f'(z)]^2 + \frac{\zeta_2 f'(z) {e_{15}}^2}{\Xi_{11}} \right) dz + \int_{-t_c}^{+t_c} Q_{55} [f'(z)]^2\, dz + \int_{+t_c}^{+t_c+t_p} \left(C_{55} [f'(z)]^2 + \frac{\zeta_1 f'(z) {e_{15}}^2}{\Xi_{11}} \right) dz$$

$$\begin{pmatrix} a_{11}^{15} \\ a_{12}^{15} \\ a_{13}^{15} \end{pmatrix} = \begin{pmatrix} 0 \\ 0 \\ 0 \end{pmatrix}$$

$$\begin{pmatrix} \mu_1^{15} \\ \mu_2^{15} \\ \mu_3^{15} \end{pmatrix} = \begin{pmatrix} 0 \\ 0 \\ 0 \end{pmatrix}$$

$$\mu_4^{15} = -\int_{-t_c-t_p}^{-t_c} \frac{8e_{15}f'(z)}{t_p}\left[\frac{z+t_c+t_p}{t_p}\right]dz - \int_{+t_c}^{+t_c+t_p} \frac{8e_{15}f'(z)}{t_p}\left[\frac{z-t_c-t_p}{t_p}\right]dz$$

$$\mu_5^{15} = \int_{-t_c-t_p}^{-t_c} \frac{8\Xi_{11}}{(t_p)^2}dz + \int_{+t_c}^{+t_c+t_p} \frac{8\Xi_{11}}{(t_p)^2}dz$$

$$\begin{pmatrix}\beta_1^{15}\\ \beta_2^{15}\\ \beta_3^{15}\end{pmatrix} = \int_{-t_c-t_p}^{-t_c} \begin{pmatrix}1\\ z\\ f(z)\end{pmatrix} e_{33}\left[1-\left(\frac{-2z-2t_c-t_p}{t_p}\right)^2 - \frac{4(z+t_c)}{t_p}\right]dz + \int_{+t_c}^{+t_c+t_p} \begin{pmatrix}1\\ z\\ f(z)\end{pmatrix} e_{33}\left[1-\left(\frac{2z-2t_c-t_p}{t_p}\right)^2 + \frac{4(z-t_c)}{t_p}\right]dz$$

$$\beta_4^{15} = 0$$

$$\beta_5^{15} = -\int_{-t_c-t_p}^{-t_c} \Xi_{33}\left[1-\left(\frac{-2z-2t_c-t_p}{t_p}\right)^2 - \frac{4(z+t_c)}{t_p}\right]dz - \int_{+t_c}^{+t_c+t_p} \Xi_{33}\left[1-\left(\frac{2z-2t_c-t_p}{t_p}\right)^2 + \frac{4(z-t_c)}{t_p}\right]dz$$

$$\begin{pmatrix}b_2^{15}\\ b_4^{15}\\ b_6^{15}\\ b_7^{15}\\ b_9^{15}\end{pmatrix} = \begin{pmatrix}0\\ 0\\ 0\\ 0\\ 0\end{pmatrix}$$

$$b_1^{15} = \int_{-t_c-t_p}^{-t_c} e_{15}f''(z)\,dz + \int_{+t_c}^{+t_c+t_p} e_{15}f''(z)\,dz$$

$$b_3^{15} = \int_{-t_c-t_p}^{-t_c}\left(e_{33}f(z) - \frac{e_{15}\zeta_2\Xi_{33}(z+t_c)}{\Xi_{11}}\right)dz + \int_{+t_c}^{+t_c+t_p}\left(e_{33}f(z) - \frac{e_{15}\zeta_1\Xi_{33}(z-t_c)}{\Xi_{11}}\right)dz$$

$$b_5^{15} = \int_{-t_c-t_p}^{-t_c} e_{33}\,dz + \int_{+t_c}^{+t_c+t_p} e_{33}\,dz$$

$$b_8^{15} = -\int_{-t_c-t_p}^{-t_c} ze_{33}\, dz - \int_{+t_c}^{+t_c+t_p} ze_{33}\, dz \tag{C.4}$$

Appendix D

The constant coefficients of Eq. (5.13) are as:

$$\begin{Bmatrix} a_i \\ b_i \\ d_i \\ f_i \\ g_i \\ h_i \end{Bmatrix} = \int_{-h-h_p}^{-h} \begin{Bmatrix} 1 \\ z \\ f \\ z^2 \\ zf \\ f^2 \end{Bmatrix} \bar{C}_i \, dz + \int_{-h}^{+h} \begin{Bmatrix} 1 \\ z \\ f \\ z^2 \\ zf \\ f^2 \end{Bmatrix} Q_i \, dz + \int_{+h}^{+h+h_p} \begin{Bmatrix} 1 \\ z \\ f \\ z^2 \\ zf \\ f^2 \end{Bmatrix} \bar{C}_i \, dz \, , (i = 11,22)$$

$$\begin{Bmatrix} a_{66} \\ b_{66} \\ d_{66} \\ f_{66} \\ g_{66} \\ h_{66} \end{Bmatrix} = \int_{-h-h_p}^{-h} \begin{Bmatrix} 1 \\ z \\ f \\ z^2 \\ zf \\ f^2 \end{Bmatrix} C_{66} \, dz + \int_{-h}^{+h} \begin{Bmatrix} 1 \\ z \\ f \\ z^2 \\ zf \\ f^2 \end{Bmatrix} Q_i \, dz + \int_{+h}^{+h+h_p} \begin{Bmatrix} 1 \\ z \\ f \\ z^2 \\ zf \\ f^2 \end{Bmatrix} \bar{C}_i \, dz \tag{D.1}$$

$$a_{55} = \int_{-h-h_p}^{-h} C_{55}\, g^2\, dz + \int_{-h}^{+h} Q_{55}\, g^2\, dz + \int_{+h}^{+h+h_p} C_{55}\, g^2\, dz$$

For OC condition:

$$\begin{aligned}
\mu_1 &= \int_{-h-h_p}^{-h} \left[\frac{-\pi \bar{e}_{31}}{h_p}\left\{1+\cos\left(\frac{\pi(-z-h)}{h_p}\right)\right\}\right] dz \\
&\quad + \int_{+h}^{+h+h_p} \left[\frac{\pi \bar{e}_{31}}{h_p}\left\{1+\cos\left(\frac{\pi(z-h)}{h_p}\right)\right\}\right] dz \\
\hat{\mu}_1 &= \int_{-h-h_p}^{-h} \left[\frac{-\pi \bar{e}_{31}}{h_p}\left\{1+\cos\left(\frac{\pi(-z-h)}{h_p}\right)\right\}\right] z\, dz \\
&\quad + \int_{+h}^{+h+h_p} \left[\frac{\pi \bar{e}_{31}}{h_p}\left\{1+\cos\left(\frac{\pi(z-h)}{h_p}\right)\right\}\right] z\, dz \\
\tilde{\mu}_1 &= \int_{-h-h_p}^{-h} \left[\frac{-\pi \bar{e}_{31}}{h_p}\left\{1+\cos\left(\frac{\pi(-z-h)}{h_p}\right)\right\}\right] f\, dz \\
&\quad + \int_{+h}^{+h+h_p} \left[\frac{\pi \bar{e}_{31}}{h_p}\left\{1+\cos\left(\frac{\pi(z-h)}{h_p}\right)\right\}\right] f\, dz \\
\mu_2 &= \int_{-h-h_p}^{-h} e_{15}\left[\sin\left(\frac{\pi(-z-h)}{h_p}\right) - \frac{\pi(z+h)}{h_p}\right] g\, dz \\
&\quad + \int_{+h}^{+h+h_p} e_{15}\left[\sin\left(\frac{\pi(z-h)}{h_p}\right) + \frac{\pi(z-h)}{h_p}\right] g\, dz \\
\begin{Bmatrix}\lambda_1 \\ \hat{\lambda}_1 \\ \tilde{\lambda}_1\end{Bmatrix} &= \int_{-h-h_p}^{-h} \left(\frac{\bar{e}_{31}\bar{e}_{31}}{\bar{\Xi}_{33}}\right)\begin{Bmatrix}1 \\ z \\ f\end{Bmatrix} dz + \int_{+h}^{+h+h_p} \left(\frac{\bar{e}_{31}\bar{e}_{31}}{\bar{\Xi}_{33}}\right)\begin{Bmatrix}1 \\ z \\ f\end{Bmatrix} dz \\
\begin{Bmatrix}\lambda_2 \\ \hat{\lambda}_2 \\ \tilde{\lambda}_2\end{Bmatrix} &= -\int_{-h-h_p}^{-h} (h+h_p)\left(\frac{\bar{e}_{31}\bar{e}_{31}}{\bar{\Xi}_{33}}\right)\begin{Bmatrix}1 \\ z \\ f\end{Bmatrix} dz \\
&\quad + \int_{+h}^{+h+h_p} (h+h_p)\left(\frac{\bar{e}_{31}\bar{e}_{31}}{\bar{\Xi}_{33}}\right)\begin{Bmatrix}1 \\ z \\ f\end{Bmatrix} dz
\end{aligned} \tag{D.2}$$

$$\begin{Bmatrix}\lambda_3\\ \hat{\lambda}_3\\ \tilde{\lambda}_3\end{Bmatrix} = \int_{-h-h_p}^{-h} \alpha_1 \left(\frac{\bar{e}_{31}\bar{e}_{31}}{\bar{\Xi}_{33}}\right)\begin{Bmatrix}1\\ z\\ f\end{Bmatrix} dz + \int_{+h}^{+h+h_p} \alpha_0 \left(\frac{\bar{e}_{31}\bar{e}_{31}}{\bar{\Xi}_{33}}\right)\begin{Bmatrix}1\\ z\\ f\end{Bmatrix} dz$$

$$\lambda_4 = \int_{-h-h_p}^{-h} \left(\frac{e_{15}\bar{e}_{31}(z+h)}{\bar{\Xi}_{33}}\right) g\, dz + \int_{+h}^{+h+h_p} \left(\frac{e_{15}\bar{e}_{31}(z-h)}{\bar{\Xi}_{33}}\right) g\, dz$$

$$\lambda_5 = \int_{-h-h_p}^{-h} (h+h_p)\left\{\frac{e_{15}\bar{e}_{31}(z+h)}{\bar{\Xi}_{33}}\right\} g\, dz - \int_{+h}^{+h+h_p} (h+h_p)\left\{\frac{e_{15}\bar{e}_{31}(z-h)}{\bar{\Xi}_{33}}\right\} g\, dz$$

$$\lambda_6 = -\int_{-h-h_p}^{-h} \alpha_1 \left\{\frac{e_{15}\bar{e}_{31}(z+h)}{\bar{\Xi}_{33}}\right\} g\, dz - \int_{+h}^{+h+h_p} \alpha_0 \left\{\frac{e_{15}\bar{e}_{31}(z-h)}{\bar{\Xi}_{33}}\right\} g\, dz$$

For SC condition:

$$\begin{aligned}
\mu_1 &= \int_{-h-h_p}^{-h} \left[\frac{-\pi\bar{e}_{31}}{h_p}\cos\left(\frac{\pi(-z-h)}{h_p}\right)\right] dz + \int_{+h}^{+h+h_p} \left[\frac{\pi\bar{e}_{31}}{h_p}\cos\left(\frac{\pi(z-h)}{h_p}\right)\right] dz \\
\hat{\mu}_1 &= \int_{-h-h_p}^{-h} \left[\frac{-\pi\bar{e}_{31}}{h_p}\cos\left(\frac{\pi(-z-h)}{h_p}\right)\right] z\, dz + \int_{+h}^{+h+h_p} \left[\frac{\pi\bar{e}_{31}}{h_p}\cos\left(\frac{\pi(z-h)}{h_p}\right)\right] z\, dz \\
\tilde{\mu}_1 &= \int_{-h-h_p}^{-h} \left[\frac{-\pi\bar{e}_{31}}{h_p}\cos\left(\frac{\pi(-z-h)}{h_p}\right)\right] f\, dz + \int_{+h}^{+h+h_p} \left[\frac{\pi\bar{e}_{31}}{h_p}\cos\left(\frac{\pi(z-h)}{h_p}\right)\right] f\, dz
\end{aligned} \tag{D.3}$$

$$\mu_2 = \int_{-h-h_p}^{-h} e_{15}\left[\sin\left(\frac{\pi(-z-h)}{h_p}\right)\right] g\, dz + \int_{+h}^{+h+h_p} e_{15}\left[\sin\left(\frac{\pi(z-h)}{h_p}\right)\right] g\, dz$$

$$\{\lambda_i, \hat{\lambda}_j, \tilde{\lambda}_k\} = 0, i = (1,2,3,4,5,6), j = (1,2,3), k = (1,2,3)$$

The constant coefficients λ_i $(i = 7,8,..,13)$ in Eq. (5.16) are derived as:

For OC condition:

$$\lambda_7 = \int_{-h-h_p}^{-h} (e_{15}\, g - \bar{e}_{31} f')\, dz + \int_{+h}^{+h+h_p} (e_{15}\, g - \bar{e}_{31} f')\, dz$$

$$\lambda_8 = -\int_{-h-h_p}^{-h} \bar{e}_{31}\, dz - \int_{+h}^{+h+h_p} \bar{e}_{31}\, dz$$

$$\lambda_9 = \int_{-h-h_p}^{-h} \left\{\frac{\pi^2 \bar{\Xi}_{33}}{{h_p}^2} \sin\left(\frac{\pi(-z-h)}{h_p}\right)\right\} dz + \int_{+h}^{+h+h_p} \left\{\frac{\pi^2 \bar{\Xi}_{33}}{{h_p}^2} \sin\left(\frac{\pi(z-h)}{h_p}\right)\right\} dz$$

$$\lambda_{10} = -\int_{-h-h_p}^{-h} \Xi_{11}\left\{\sin\left(\frac{\pi(-z-h)}{h_p}\right) - \frac{\pi(z+h)}{h_p}\right\} dz - \int_{+h}^{+h+h_p} \Xi_{11}\left\{\sin\left(\frac{\pi(z-h)}{h_p}\right) + \frac{\pi(z-h)}{h_p}\right\} dz \quad \text{(D.4)}$$

$$\lambda_{11} = -\int_{-h-h_p}^{-h} \left(\frac{\bar{e}_{31}\Xi_{11}(z+h)}{\bar{\Xi}_{33}}\right) dz - \int_{+h}^{+h+h_p} \left(\frac{\bar{e}_{31}\Xi_{11}(z-h)}{\bar{\Xi}_{33}}\right) dz$$

$$\lambda_{12} = -\int_{-h-h_p}^{-h} \left(\frac{\bar{e}_{31}\Xi_{11}(z+h)\left(h+h_p\right)}{\bar{\Xi}_{33}}\right) dz + \int_{+h}^{+h+h_p} \left(\frac{\bar{e}_{31}\Xi_{11}(z-h)\left(h+h_p\right)}{\bar{\Xi}_{33}}\right) dz$$

$$\lambda_{13} = \int_{-h-h_p}^{-h} \left(\frac{\bar{e}_{31}\alpha_1 \Xi_{11}(z+h)}{\bar{\Xi}_{33}} \right) dz + \int_{+h}^{+h+h_p} \left(\frac{\bar{e}_{31}\alpha_0 \Xi_{11}(z-h)}{\bar{\Xi}_{33}} \right) dz$$

For SC condition:

$$\lambda_7 = \int_{-h-h_p}^{-h} (e_{15}\, g - \bar{e}_{31} f')\, dz + \int_{+h}^{+h+h_p} (e_{15}\, g - \bar{e}_{31} f')\, dz$$

$$\lambda_8 = -\int_{-h-h_p}^{-h} \bar{e}_{31}\, dz - \int_{+h}^{+h+h_p} \bar{e}_{31}\, dz$$

$$\lambda_9 = \int_{-h-h_p}^{-h} \left\{ \frac{\pi^2 \bar{\Xi}_{33}}{{h_p}^2} \sin\left(\frac{\pi(-z-h)}{h_p} \right) \right\} dz + \int_{+h}^{+h+h_p} \left\{ \frac{\pi^2 \bar{\Xi}_{33}}{{h_p}^2} \sin\left(\frac{\pi(z-h)}{h_p} \right) \right\} dz \quad \text{(D.5)}$$

$$\lambda_{10} = -\int_{-h-h_p}^{-h} \Xi_{11} \left\{ \sin\left(\frac{\pi(-z-h)}{h_p} \right) \right\} dz - \int_{+h}^{+h+h_p} \Xi_{11} \left\{ \sin\left(\frac{\pi(z-h)}{h_p} \right) \right\} dz$$

$$\lambda_i = 0, i = (11,12,13)$$

The coefficients K_{ij}'s in Eq. (5.18) are derived as:

$$\begin{aligned}
k_{11} &= -(a_{11} + \lambda_1)\beta_1^2 - a_{66}\beta_2^2 + \omega^2 I_0 \\
k_{12} &= -(a_{12} + a_{66} + \lambda_1)\beta_1\beta_2 \\
k_{13} &= j(b_{11} + \lambda_2)\beta_1^3 + j(b_{12} + 2b_{66} + \lambda_2)\beta_1\beta_2^2 + j\omega^2\beta_1 I_1 \\
k_{14} &= j(d_{11} + \lambda_3)\beta_1^3 + j(d_{12} + 2d_{66} + \lambda_3)\beta_1\beta_2^2 + j\omega^2\beta_1 J_1 \\
k_{15} &= j\mu_1\beta_1 \\
k_{21} &= -(a_{12} + a_{66} + \lambda_1)\beta_1\beta_2 \\
k_{22} &= -a_{66}\beta_1^2 - (a_{11} + \lambda_1)\beta_2^2 + \omega^2 I_0 \\
k_{23} &= j(b_{11} + \lambda_2)\beta_2^3 + j(b_{12} + 2b_{66} + \lambda_2)\beta_1^2\beta_2 - j\omega^2\beta_2 I_1
\end{aligned} \quad \text{(D.6)}$$

$$
\begin{aligned}
k_{24} &= j(d_{11}+\lambda_3)\beta_2^3 + j(d_{12}+2d_{66}+\lambda_3)\beta_1^2\beta_2 - j\omega^2\beta_2 J_1\\
k_{25} &= j\mu_1\beta_2\\
k_{31} &= -j\left(b_{11}+\hat{\lambda}_1\right)\beta_1^3 - j\left(b_{12}+2b_{66}+\hat{\lambda}_1\right)\beta_1\beta_2^2 + j\omega^2\beta_1 I_1\\
k_{32} &= -j\left(b_{12}+2b_{66}+\hat{\lambda}_1\right)\beta_1^2\beta_2 - j\left(b_{11}+\hat{\lambda}_1\right)\beta_2^3 + j\omega^2\beta_2 I_1\\
k_{33} &= -\left(f_{11}+\hat{\lambda}_2\right)\beta_1^4 - 2\left(f_{12}+2f_{66}+\hat{\lambda}_2\right)\beta_1^2\beta_2^2 - \left(f_{11}+\hat{\lambda}_2\right)\beta_2^4\\
&\quad - \omega^2 I_0 + I_2\omega^2\beta_1^2 + I_2\omega^2\beta_2^2\\
k_{34} &= -\left(g_{11}+\hat{\lambda}_3\right)\beta_1^4 - 2\left(g_{12}+2g_{66}+\hat{\lambda}_3\right)\beta_1^2\beta_2^2 - \left(g_{11}+\hat{\lambda}_3\right)\beta_2^4\\
&\quad - \omega^2 I_0 + J_2\omega^2\beta_1^2 + J_2\omega^2\beta_2^2\\
k_{35} &= -\hat{\mu}_1\beta_1^2 - \hat{\mu}_1\beta_2^2\\
k_{41} &= -j\left(d_{11}+\tilde{\lambda}_1+\lambda_4\right)\beta_1^3 - j\left(d_{12}+2d_{66}+\tilde{\lambda}_1+\lambda_4\right)\beta_1\beta_2^2\\
&\quad + j\omega^2\beta_1 J_1\\
k_{42} &= -j\left(d_{12}+2d_{66}+\tilde{\lambda}_1+\lambda_4\right)\beta_1^2\beta_2 - j\left(d_{11}+\tilde{\lambda}_1+\lambda_4\right)\beta_2^3\\
&\quad + j\omega^2\beta_2 J_1\\
k_{43} &= -\left(g_{11}+\tilde{\lambda}_2+\lambda_5\right)\beta_1^4 + 2\left(-g_{12}-2g_{66}-\tilde{\lambda}_2+\lambda_5\right)\beta_1^2\beta_2^2\\
&\quad - \left(g_{11}+\tilde{\lambda}_2-\lambda_5\right)\beta_2^4 + \omega^2 I_0 + \omega^2\beta_1^2 J_2 + \omega^2\beta_2^2 J_2\\
k_{44} &= -\left(h_{11}+\tilde{\lambda}_3-\lambda_6\right)\beta_1^4 + 2\left(-h_{12}-2h_{66}-\tilde{\lambda}_3+\lambda_6\right)\beta_1^2\beta_2^2\\
&\quad - \left(h_{11}+\tilde{\lambda}_3-\lambda_6\right)\beta_2^4 - a_{55}\beta_1^2 - a_{55}\beta_2^2 + \omega^2 I_0\\
&\quad + \omega^2 K_2\beta_1^2 + \omega^2 K_2\beta_2^2\\
k_{45} &= -(\tilde{\mu}_1+\mu_2)\beta_1^2 - (\tilde{\mu}_1+\mu_2)\beta_2^2\\
k_{51} &= -j\lambda_{11}\beta_1^3 - j\lambda_{11}\beta_1\beta_2^2\\
k_{52} &= -j\lambda_{11}\beta_1^2\beta_2 - j\lambda_{11}\beta_2^3\\
k_{53} &= -\lambda_8\beta_1^2 - \lambda_8\beta_2^2 + \lambda_{12}\beta_1^4 + 2\lambda_{12}\beta_1^2\beta_2^2 + \lambda_{12}\beta_2^4\\
k_{54} &= -\lambda_7\beta_1^2 - \lambda_7\beta_2^2 + \lambda_{13}\beta_1^4 + 2\lambda_{13}\beta_1^2\beta_2^2 + \lambda_{13}\beta_2^4\\
k_{55} &= \lambda_9 - \lambda_{10}\beta_1^2 - \lambda_{10}\beta_2^2
\end{aligned}
$$

The coefficients K'_{ij}'s in Eq. (5.30) are derived as:

$$
\begin{aligned}
k_{11} &= (a_{11}+\lambda_1)X_{12} + a_{66}X_8 + \omega^2 I_0 X_6\\
k_{12} &= (a_{12}+\lambda_1+a_{66})X_8\\
k_{13} &= -(b_{11}+\lambda_2)X_{12} - (b_{12}+\lambda_2+2b_{66})X_8 - \omega^2 I_1 X_6\\
k_{14} &= -(d_{11}+\lambda_3)X_{12} - (d_{12}+\lambda_3+2d_{66})X_8 - \omega^2 J_1 X_6\\
k_{15} &= \mu_1 X_2
\end{aligned}
\qquad \text{(D.7)}
$$

$$k_{21} = (a_{12} + \lambda_1 + a_{66})X_{10}$$
$$k_{22} = a_{66}X_{10} + (a_{11} + \lambda_1)X_4 + \omega^2 I_0 X_2$$
$$k_{23} = -(b_{12} + \lambda_2 + 2b_{66})X_{10} - (b_{11} + \lambda_2)X_4 - \omega^2 I_1 X_2$$
$$k_{24} = -(d_{12} + \lambda_3 + 2d_{66})X_{10} - (d_{11} + \lambda_3)X_4 - \omega^2 J_1 X_2$$
$$k_{25} = \mu_1 X_2$$
$$k_{31} = \left(b_{11} + \hat{\lambda}_1\right)X_{13} + \left(b_{12} + \hat{\lambda}_1 + 2b_{66}\right)X_{11} + \omega^2 I_1 X_9$$
$$k_{32} = \left(b_{12} + \hat{\lambda}_1 + 2b_{66}\right)X_{11} + \left(b_{11} + \hat{\lambda}_1\right)X_5 + \omega^2 I_1 X_3$$
$$k_{33} = -\left(f_{11} + \hat{\lambda}_2\right)X_{13} - \left(2f_{12} + 2\hat{\lambda}_2 + 4f_{66}\right)X_{11} - \left(f_{11} + \hat{\lambda}_2\right)X_5 + \omega^2 I_0 X_1 - \omega^2 I_2 X_9 - \omega^2 I_2 X_3$$
$$k_{34} = -\left(g_{11} + \hat{\lambda}_3\right)X_{13} - \left(2g_{12} + 2\hat{\lambda}_3 + 4g_{66}\right)X_{11} - \left(g_{11} + \hat{\lambda}_3\right)X_5 + \omega^2 I_0 X_1 - \omega^2 J_2 X_9 - \omega^2 J_2 X_3$$
$$k_{35} = \hat{\mu}_1(X_9 + X_3)$$
$$k_{41} = \left(d_{11} + \tilde{\lambda}_1 + \lambda_4\right)X_{13} + \left(d_{12} + \tilde{\lambda}_1 + 2d_{66} + \lambda_4\right)X_{11} + \omega^2 J_1 X_9$$
$$k_{42} = \left(d_{12} + \tilde{\lambda}_1 + 2d_{66} + \lambda_4\right)X_{11} + \left(d_{11} + \tilde{\lambda}_1 + \lambda_4\right)X_5 + \omega^2 J_1 X_3$$
$$k_{43} = -\left(g_{11} + \tilde{\lambda}_2 - \lambda_5\right)X_{13} - \left(2g_{12} + 2\tilde{\lambda}_2 + 4g_{66} - 2\lambda_5\right)X_{11} - \left(g_{11} + \tilde{\lambda}_2 - \lambda_5\right)X_5 + \omega^2 I_0 X_1 - \omega^2 J_2 X_9 - \omega^2 J_2 X_3$$
$$k_{44} = -\left(h_{11} + \tilde{\lambda}_3 - \lambda_6\right)X_{13} - \left(2h_{12} + 2\tilde{\lambda}_3 + 4h_{66} - 2\lambda_6\right)X_{11} - \left(h_{11} + \tilde{\lambda}_3 - \lambda_6\right)X_5 + a_{55}X_9 + a_{55}X_3 + \omega^2 I_0 X_1 - \omega^2 K_2 X_9 - \omega^2 K_2 X_3$$
$$k_{45} = \tilde{\mu}_1 X_9 + \mu_2 X_9 + \tilde{\mu}_1 X_3 + \mu_2 X_3$$
$$k_{51} = \lambda_{11}X_{11} + \lambda_{11}X_{13}$$
$$k_{52} = \lambda_{11}X_{11} + \lambda_{11}X_5$$
$$k_{53} = \lambda_8 X_9 + \lambda_8 X_3 + \lambda_{12}X_{13} + 2\lambda_{12}X_{11} + \lambda_{12}X_5$$
$$k_{54} = \lambda_7 X_9 + \lambda_7 X_3 + \lambda_{13}X_{13} + 2\lambda_{13}X_{11} + \lambda_{13}X_5$$
$$k_{55} = \lambda_9 X_1 + \lambda_{10}X_9 + \lambda_{10}X_3$$

where:

$$\{X_1, X_3, X_5\} = \int_0^a \int_0^b \{F_m F_n, F_m F_n'', F_m F_n''''\} F_m F_n dx dy \tag{D.8}$$

$$\{X_9, X_{11}, X_{13}\} = \int_0^a \int_0^b \{F_m'' F_n, F_m'' F_n'', F_m'''' F_n\} F_m F_n dxdy$$

$$\{X_6, X_8, X_{12}\} = \int_0^a \int_0^b \{F_m' F_n, F_m' F_n'', F_m''' F_n\} F_m' F_n dxdy$$

$$\{X_2, X_4, X_{10}\} = \int_0^a \int_0^b \{F_m F_n', F_m F_n''', F_m'' F_n'\} F_m F_n' dxdy$$

Appendix E

The coefficients Z_i and $\tilde{Z}_i$ $(i = 1,2, \dots ,6)$, β_i $(i = 1,2, \dots ,5)$, as well as ζ_i and $\tilde{\zeta}_i$ $(i = 1,2, \dots ,12)$ in Eq. (6.26) are given as:

$$Z_1 = \frac{\eta_m^2 a_{66}}{(a_{11})}$$

$$Z_2 = \frac{\eta_m (a_{12} + a_{66})}{(a_{11})}$$

$$Z_3 = \frac{\eta_m^2 (b_{12} + 2b_{66})}{-(a_{11})}$$

$$Z_4 = \frac{b_{11}}{a_{11}}$$

$$Z_5 = \frac{\eta_m^2 (d_{12} + 2d_{66})}{-(a_{11})}$$

$$Z_6 = \frac{d_{11}}{a_{11}}$$

$$\tilde{Z}_1 = \frac{\eta_m (a_{12} + a_{66})}{-a_{66}}$$

$$\tilde{Z}_2 = \frac{\eta_m^2 (a_{11})}{a_{66}}$$

$$\tilde{Z}_3 = \frac{\eta_m^3 (b_{11})}{-a_{66}}$$

$$\tilde{Z}_4 = \frac{\eta_m(b_{12} + 2b_{66})}{a_{66}}$$

$$\tilde{Z}_5 = \frac{\eta_m^3(d_{11})}{-a_{66}}$$

$$\tilde{Z}_6 = \frac{\eta_m(d_{12} + 2d_{66})}{a_{66}}$$

$$\beta_1 = \frac{\lambda_9}{-\lambda_{10}} + \eta_m^2$$

$$\beta_2 = \frac{\lambda_8}{-\lambda_{10}}$$

$$\beta_3 = \frac{\eta_m^2\lambda_8}{\lambda_{10}}$$

$$\beta_4 = \frac{\lambda_7}{-\lambda_{10}}$$

$$\beta_5 = \frac{\eta_m^2\lambda_7}{\lambda_{10}}$$

$$\xi_1 = b_{11}$$

$$\xi_2 = -\eta_m^2(b_{12} + 2b_{66})$$

$$\xi_3 = -\eta_m(b_{12} + 2b_{66})$$

$$\xi_4 = +\eta_m^3(b_{11})$$

$$\xi_5 = -(f_{11})$$

$$\xi_6 = \{\eta_m^2(2f_{12} + 4f_{66}) + r_x N_{cr}\}$$

$$\xi_7 = \left\{-\eta_m^4(f_{11}) - \eta_m^2 r_y N_{cr}\right\}$$

$$\xi_8 = -(g_{11})$$

$$\xi_9 = \{\eta_m^2(2g_{12} + 4g_{66}) + r_x N_{cr}\}$$

$$\xi_{10} = \left\{-\eta_m^4(g_{11}) - \eta_m^2 r_y N_{cr}\right\}$$

$$\xi_{11} = \hat{\mu}_1$$

$$\xi_{12} = -\eta_m^2\hat{\mu}_1$$

$$\tilde{\xi}_1 = d_{11}$$

$$\tilde{\xi}_2 = -\eta_m^2(2d_{66} + d_{12})$$

$$\tilde{\xi}_3 = -\eta_m(d_{12} + 2d_{66})$$

$$\tilde{\xi}_4 = \eta_m^3(d_{11})$$

$$\tilde{\xi}_5 = -(g_{11})$$
$$\tilde{\xi}_6 = \{\eta_m^2(2g_{12} + 4g_{66}) + r_x N_{cr}\}$$
$$\tilde{\xi}_7 = \{-\eta_m^4(g_{11}) - \eta_m^2 r_y N_{cr}\}$$
$$\tilde{\xi}_8 = -(h_{11})$$
$$\tilde{\xi}_9 = \{\eta_m^2(2h_{12} + 4h_{66}) + (a_{55} + r_x N_{cr})\}$$
$$\tilde{\xi}_{10} = \{-\eta_m^4(h_{11}) - \eta_m^2(a_{55} + r_y N_{cr})\}$$
$$\tilde{\xi}_{11} = (\tilde{\mu}_1 + \mu_2)$$
$$\tilde{\xi}_{12} = -\eta_m^2(\tilde{\mu}_1 + \mu_2) \quad \text{(E.1)}$$

The coefficients α_i and $\tilde{\alpha}_i$ ($i = 1,2, \ldots ,9$), as well as Z_i and $\tilde{Z}_i$ ($i = 8,9 \ldots ,14$) in Eqs. (6.27) to (6.30) are given as:

$$\alpha_1 = (\xi_1 Z_4 + \xi_5)$$
$$\alpha_2 = (\xi_1 Z_6 + \xi_8)$$
$$\alpha_3 = (\xi_1 Z_1 + \xi_1 Z_2 \tilde{Z}_1 + \xi_2 + \xi_3 \tilde{Z}_1)$$
$$\alpha_4 = (\xi_1 Z_2 \tilde{Z}_2 + \xi_3 \tilde{Z}_2 + \xi_4)$$
$$\alpha_5 = (\xi_1 Z_2 \tilde{Z}_3 + \xi_3 \tilde{Z}_3 + \xi_7 + \xi_{11}\beta_3)$$
$$\alpha_6 = (\xi_1 Z_2 \tilde{Z}_4 + \xi_1 Z_3 + \xi_3 \tilde{Z}_4 + \xi_6 + \xi_{11}\beta_2)$$
$$\alpha_7 = (\xi_1 Z_2 \tilde{Z}_5 + \xi_3 \tilde{Z}_5 + \xi_{10} + \xi_{11}\beta_5)$$
$$\alpha_8 = (\xi_1 Z_2 \tilde{Z}_6 + \xi_1 Z_5 + \xi_3 \tilde{Z}_6 + \xi_9 + \xi_{11}\beta_4)$$
$$\alpha_9 = (\xi_{11}\beta_1 + \xi_{12})$$
$$\tilde{\alpha}_1 = (\tilde{\xi}_1 Z_4 + \tilde{\xi}_5)$$
$$\tilde{\alpha}_2 = (\tilde{\xi}_1 Z_6 + \tilde{\xi}_8)$$
$$\tilde{\alpha}_3 = (\tilde{\xi}_1 Z_1 + \tilde{\xi}_1 Z_2 \tilde{Z}_1 + \tilde{\xi}_2 + \tilde{\xi}_3 \tilde{Z}_1)$$
$$\tilde{\alpha}_4 = (\tilde{\xi}_1 Z_2 \tilde{Z}_2 + \tilde{\xi}_3 \tilde{Z}_2 + \tilde{\xi}_4)$$
$$\tilde{\alpha}_5 = (\tilde{\xi}_1 Z_2 \tilde{Z}_3 + \tilde{\xi}_3 \tilde{Z}_3 + \tilde{\xi}_7 + \tilde{\xi}_{11}\beta_3)$$
$$\tilde{\alpha}_6 = (\tilde{\xi}_1 Z_2 \tilde{Z}_4 + \tilde{\xi}_1 Z_3 + \tilde{\xi}_3 \tilde{Z}_4 + \tilde{\xi}_6 + \tilde{\xi}_{11}\beta_2)$$
$$\tilde{\alpha}_7 = (\tilde{\xi}_1 Z_2 \tilde{Z}_5 + \tilde{\xi}_3 \tilde{Z}_5 + \tilde{\xi}_{10} + \tilde{\xi}_{11}\beta_5)$$
$$\tilde{\alpha}_8 = (\tilde{\xi}_1 Z_2 \tilde{Z}_6 + \tilde{\xi}_1 Z_5 + \tilde{\xi}_3 \tilde{Z}_6 + \tilde{\xi}_9 + \tilde{\xi}_{11}\beta_4)$$
$$\tilde{\alpha}_9 = (\tilde{\xi}_{11}\beta_1 + \tilde{\xi}_{12})$$

$$Z_8 = \frac{\left(\frac{\alpha_3}{\alpha_2} - \frac{\tilde{\alpha}_3}{\tilde{\alpha}_2}\right)}{-\left(\frac{\alpha_1}{\alpha_2} - \frac{\tilde{\alpha}_1}{\tilde{\alpha}_2}\right)}$$

$$Z_9 = \frac{\left(\frac{\alpha_4}{\alpha_2} - \frac{\tilde{\alpha}_4}{\tilde{\alpha}_2}\right)}{-\left(\frac{\alpha_1}{\alpha_2} - \frac{\tilde{\alpha}_1}{\tilde{\alpha}_2}\right)}$$

$$Z_{10} = \frac{\left(\frac{\alpha_5}{\alpha_2} - \frac{\tilde{\alpha}_5}{\tilde{\alpha}_2}\right)}{-\left(\frac{\alpha_1}{\alpha_2} - \frac{\tilde{\alpha}_1}{\tilde{\alpha}_2}\right)}$$

$$Z_{11} = \frac{\left(\frac{\alpha_6}{\alpha_2} - \frac{\tilde{\alpha}_6}{\tilde{\alpha}_2}\right)}{-\left(\frac{\alpha_1}{\alpha_2} - \frac{\tilde{\alpha}_1}{\tilde{\alpha}_2}\right)}$$

$$Z_{12} = \frac{\left(\frac{\alpha_7}{\alpha_2} - \frac{\tilde{\alpha}_7}{\tilde{\alpha}_2}\right)}{-\left(\frac{\alpha_1}{\alpha_2} - \frac{\tilde{\alpha}_1}{\tilde{\alpha}_2}\right)}$$

$$Z_{13} = \frac{\left(\frac{\alpha_8}{\alpha_2} - \frac{\tilde{\alpha}_8}{\tilde{\alpha}_2}\right)}{-\left(\frac{\alpha_1}{\alpha_2} - \frac{\tilde{\alpha}_1}{\tilde{\alpha}_2}\right)}$$

$$Z_{14} = \frac{\left(\frac{\alpha_9}{\alpha_2} - \frac{\tilde{\alpha}_9}{\tilde{\alpha}_2}\right)}{-\left(\frac{\alpha_1}{\alpha_2} - \frac{\tilde{\alpha}_1}{\tilde{\alpha}_2}\right)}$$

$$\tilde{Z}_8 = \frac{\left(\frac{\alpha_3}{\alpha_1} - \frac{\tilde{\alpha}_3}{\tilde{\alpha}_1}\right)}{-\left(\frac{\alpha_2}{\alpha_1} - \frac{\tilde{\alpha}_2}{\tilde{\alpha}_1}\right)}$$

$$\tilde{Z}_9 = \frac{\left(\frac{\alpha_4}{\alpha_1} - \frac{\tilde{\alpha}_4}{\tilde{\alpha}_1}\right)}{-\left(\frac{\alpha_2}{\alpha_1} - \frac{\tilde{\alpha}_2}{\tilde{\alpha}_1}\right)}$$

$$\tilde{Z}_{10} = \frac{\left(\frac{\alpha_5}{\alpha_1} - \frac{\tilde{\alpha}_5}{\tilde{\alpha}_1}\right)}{-\left(\frac{\alpha_2}{\alpha_1} - \frac{\tilde{\alpha}_2}{\tilde{\alpha}_1}\right)}$$

$$\tilde{Z}_{11} = \frac{\left(\frac{\alpha_6}{\alpha_1} - \frac{\tilde{\alpha}_6}{\tilde{\alpha}_1}\right)}{-\left(\frac{\alpha_2}{\alpha_1} - \frac{\tilde{\alpha}_2}{\tilde{\alpha}_1}\right)}$$

$$\tilde{Z}_{12} = \frac{\left(\frac{\alpha_7}{\alpha_1} - \frac{\tilde{\alpha}_7}{\tilde{\alpha}_1}\right)}{-\left(\frac{\alpha_2}{\alpha_1} - \frac{\tilde{\alpha}_2}{\tilde{\alpha}_1}\right)}$$

$$\tilde{Z}_{13} = \frac{\left(\frac{\alpha_8}{\alpha_1} - \frac{\tilde{\alpha}_8}{\tilde{\alpha}_1}\right)}{-\left(\frac{\alpha_2}{\alpha_1} - \frac{\tilde{\alpha}_2}{\tilde{\alpha}_1}\right)}$$

$$\tilde{Z}_{14} = \frac{\left(\frac{\alpha_9}{\alpha_1} - \frac{\tilde{\alpha}_9}{\tilde{\alpha}_1}\right)}{-\left(\frac{\alpha_2}{\alpha_1} - \frac{\tilde{\alpha}_2}{\tilde{\alpha}_1}\right)} \qquad \text{(E.2)}$$

Appendix F

The coefficients β_i $(i = 1, 2, 3, 4)$ and η_j $(j = 1, 2)$ are obtained as follows:

$$\beta_1 = \int_{-h-h_{pb}}^{-h} e_{15} dz + \int_{+h}^{+h+h_{pt}} e_{15} dz$$

$$\beta_2 = \int_{-h-h_{pb}}^{-h} e_{31} dz + \int_{+h}^{+h+h_{pt}} e_{31} dz$$

$$\beta_3 = \int_{-h-h_{pb}}^{-h} \frac{8\Xi_{33}}{{h_{pb}}^2} dz + \int_{+h}^{+h+h_{pt}} \frac{8\Xi_{33}}{{h_{pt}}^2} dz \tag{F.1}$$

SC condition:

$$\beta_4 = -\int_{-h-h_{pb}}^{-h} \Xi_{11} \left[1 - \left(\frac{-2z - 2h - h_{pb}}{h_{pb}}\right)^2\right] dz - \int_{+h}^{+h+h_{pt}} \Xi_{11} \left[1 - \left(\frac{2z - 2h - h_{pt}}{h_{pt}}\right)^2\right] dz$$

$$\eta_1 = \eta_2 = 0 \tag{F.2}$$

OC condition:

$$\beta_4 = -\int_{-h-h_{pb}}^{-h} \Xi_{11}\left[1-\left(\frac{-2z-2h-h_{pb}}{h_{pb}}\right)^2-\frac{4(z+h)}{h_{pb}}\right]dz - \int_{+h}^{+h+h_{pt}} \Xi_{11}\left[1-\left(\frac{2z-2h-h_{pt}}{h_{pt}}\right)^2+\frac{4(z-h)}{h_{pt}}\right]dz$$

$$\eta_1 = \int_{-h-h_{pb}}^{-h} \frac{-\Xi_{11}e_{31}(z+h)}{\bar{\Xi}_{33}}dz + \int_{+h}^{+h+h_{pt}} \frac{-\Xi_{11}e_{31}(z-h)}{\bar{\Xi}_{33}}dz$$

$$\eta_2 = \int_{-h-h_{pb}}^{-h} \frac{\Xi_{11}e_{31}(z+h)(h+h_{pb})}{\Xi_{33}}dz + \int_{+h}^{+h+h_{pt}} \frac{-\Xi_{11}e_{31}(z-h)(h+h_{pt})}{\Xi_{33}}dz \tag{F.3}$$

The constant coefficients a_{ij}, b_{ij}, d_{ij}, p_{ij} and q_{ij} are expressed as follows:

$$\{a_{11}, b_{11}, d_{11}\} = \int_{-h-h_{pb}}^{-h} C_{11}^{p}\{1, z, z^2\}dz + \int_{-h}^{+h} C_{11}^{s}\{1, z, z^2\}dz + \int_{+h}^{+h+h_{pt}} C_{11}^{p}\{1, z, z^2\}dz + \{\zeta_1, \zeta_2, \zeta_3\}$$

$$\{a_{12}, b_{12}, d_{12}\} = \int_{-h-h_{pb}}^{-h} C_{12}^{p}\{1, z, z^2\}dz + \int_{-h}^{+h} C_{12}^{s}\{1, z, z^2\}dz + \int_{+h}^{+h+h_{pt}} C_{12}^{p}\{1, z, z^2\}dz + \{\zeta_1, \zeta_2, \zeta_3\}$$

$$\{p_{11}, q_{11}\} = \int_{-h-h_{pb}}^{-h} \{1, z\}\left(\frac{C_{11}^{p}}{R_x}+\frac{C_{12}^{p}}{R_y}\right)dz + \int_{-h}^{+h} \{1, z\}\left(\frac{C_{11}^{s}}{R_x}+\frac{C_{12}^{s}}{R_y}\right)dz + \int_{+h}^{+h+h_{pt}} \{1, z\}\left(\frac{C_{11}^{p}}{R_x}+\frac{C_{12}^{p}}{R_y}\right)dz + \{\zeta_4, \zeta_5\}$$

$$\begin{aligned}\{p_{11}^{'}, q_{11}^{'}\} &= \int_{-h-h_{pb}}^{-h} \{1, z\}\left(\frac{C_{12}^{p}}{R_x} + \frac{C_{11}^{p}}{R_y}\right) dz \\ &+ \int_{-h}^{+h} \{1, z\}\left(\frac{C_{11}^{s}}{R_x} + \frac{C_{12}^{s}}{R_y}\right) dz \\ &+ \int_{+h}^{+h+h_{pt}} \{1, z\}\left(\frac{C_{11}^{p}}{R_x} + \frac{C_{12}^{p}}{R_y}\right) dz + \{\zeta_4, \zeta_5\} \\ \{a_{66}, b_{66}, d_{66}\} &= \int_{-h-h_{pb}}^{-h} C_{66}^{p}\{1, z, z^2\} dz + \int_{-h}^{+h} C_{66}^{s}\{1, z, z^2\} dz \\ &+ \int_{+h}^{+h+h_{pt}} C_{66}^{p}\{1, z, z^2\} dz \\ a_{55} &= \int_{-h-h_{pb}}^{-h} K_s C_{55}^{p} dz + \int_{-h}^{+h} K_s C_{55}^{s} dz + \int_{+h}^{+h+h_{pt}} K_s C_{55}^{p} dz \end{aligned} \tag{F.4}$$

SC condition:

$$\zeta_1 = \zeta_2 = \zeta_3 = \zeta_4 = \zeta_5 = 0 \tag{F.5}$$

OC condition:

$$\begin{aligned}\{\zeta_1, \zeta_2, \zeta_3\} &= \int_{-h-h_{pb}}^{-h} \frac{{e_{31}}^2}{\Xi_{33}}\{1, (-h-h_{pb}), (-h-h_{pb})z\} dz \\ &+ \int_{+h}^{+h+h_{pt}} \frac{{e_{31}}^2}{\Xi_{33}}\{1, (h+h_{pt}), (h+h_{pt})z\} dz \\ \{\zeta_4, \zeta_5\} &= \int_{-h-h_{pb}}^{-h} \left(\frac{1}{R_x} + \frac{1}{R_y}\right)\left\{\frac{{e_{31}}^2}{\Xi_{33}}, \frac{{e_{31}}^2}{\Xi_{33}} z\right\} dz \\ &+ \int_{+h}^{+h+h_{pt}} \left(\frac{1}{R_x} + \frac{1}{R_y}\right)\left\{\frac{{e_{31}}^2}{\Xi_{33}}, \frac{{e_{31}}^2}{\Xi_{33}} z\right\} dz \end{aligned} \tag{F.6}$$

Furthermore, the coefficients β_i $(i = 5, 6, 7, 8, 9)$ for both SC and OC conditions are defined as follows:

SC condition:

$$\begin{aligned}\{\beta_5, \beta_6\} &= \int_{-h-h_{pb}}^{-h} \{1, z\}\frac{4e_{31}}{h_{pb}}\left(\frac{-2z-2h-h_{pb}}{h_{pb}}\right) dz \\ &- \int_{+h}^{+h+h_{pt}} \{1, z\}\frac{4e_{31}}{h_{pt}}\left(\frac{2z-2h-h_{pt}}{h_{pt}}\right) dz\end{aligned}$$

$$\beta_7 = \int_{-h-h_{pb}}^{-h} e_{15}\left[1-\left(\frac{-2z-2h-h_{pb}}{h_{pb}}\right)^2\right]dz + \int_{+h}^{+h+h_{pt}} e_{15}\left[1-\left(\frac{2z-2h-h_{pt}}{h_{pt}}\right)^2\right]dz$$

$$\beta_8 = \beta_9 = 0 \tag{F.7}$$

OC condition:

$$\{\beta_5, \beta_6\} = \int_{-h-h_{pb}}^{-h} \{1, z\}\frac{-8e_{31}(z+h+h_{pb})}{{h_{pb}}^2}dz - \int_{+h}^{+h+h_{pt}} \{1, z\}\frac{-8e_{31}(z-h-h_{pt})}{{h_{pt}}^2}dz$$

$$\beta_7 = \int_{-h-h_{pb}}^{-h} e_{15}\left[1-\left(\frac{-2z-2h-h_{pb}}{h_{pb}}\right)^2-\frac{4(z+h)}{h_{pb}}\right]dz + \int_{+h}^{+h+h_{pt}} e_{15}\left[1-\left(\frac{2z-2h-h_{pt}}{h_{pt}}\right)^2 + \frac{4(z-h)}{h_{pt}}\right]dz$$

$$\{\beta_8, \beta_9\} = \int_{-h-h_{pb}}^{-h} \{1, (-h-h_{pb})\}\frac{e_{31}e_{15}(z+h)}{\Xi_{33}}dz + \int_{+h}^{+h+h_{pt}} \{1, (h+h_{pt})\}\frac{e_{31}e_{15}(z-h)}{\Xi_{33}}dz \tag{F.8}$$